



DIPARTIMENTO DI INGEGNERIA CIVILE, UNIVERSITÀ DEGLI STUDI DI SALERNO

CORSO DI DOTTORATO IN RISCHIO E SOSTENIBILITÀ DEI SISTEMI
DELL'INGEGNERIA CIVILE, EDILE ED AMBIENTALE
XXXI Ciclo

Application of inverse analysis to geotechnical problems, from soil behaviour to large deformation modelling

Applicazione dell'analisi inversa a problemi geotecnici, dal
comportamento del terreno alla modellazione di grandi deformazioni

ING. (DOTT.) POOYAN GHASEMI

Relatore:
PROF. ING. SABATINO CUOMO

Coordinatore
PROF. ING. FERNANDO
FERATERNALLI

Correlatore:
PROF. ING. MICHELE CALVELLO

Correlatore estero:
DOTT. ING. MARIO MARTINELLI
DELTARES, DELFT, PAESI BASSI

“What we observe is not nature in itself. But, nature exposed to our method of questioning”

W. Heisenberg



In copertina: note sull'eventuale immagine in copertina

Application of inverse analysis to geotechnical problems, from soil behaviour to large deformation modelling

Copyright © 2005 Università degli Studi di Salerno – via Ponte don Melillo, 1 – 84084 Fisciano (SA), Italy – web: www.unisa.it

Proprietà letteraria, tutti i diritti riservati. La struttura ed il contenuto del presente volume non possono essere riprodotti, neppure parzialmente, salvo espressa autorizzazione. Non ne è altresì consentita la memorizzazione su qualsiasi supporto (magnetico, magnetico-ottico, ottico, cartaceo, etc.).

Benché l'autore abbia curato con la massima attenzione la preparazione del presente volume, Egli declina ogni responsabilità per possibili errori ed omissioni, nonché per eventuali danni dall'uso delle informazioni ivi contenute.

Finito di stampare il 14/01/2019

TABLE OF CONTENST

TABLE OF CONTENST	i
LIST OF FIGURES	iv
LIST OF TABLES.....	xi
AKNOWLEDGMENT.....	xiii
ABSTRACT	xiv
ABOUT THE AUTHOR.....	xvi
1 INTRODUCTION	1
1.1 Layout of the thesis	2
2 LITERATURE REVIEW	4
2.1 Inverse analysis and the geotechnical problems.....	5
2.2 Analysis and simulation of flow-like landslides.....	7
2.3 Simulation of penetration problems	10
3 MATERIALS AND METHODS.....	12
3.1 Inverse analysis algorithms.....	13
3.1.1 Error Definition and Normalization	14
3.1.2 Optimisation Algorithm	19
3.2 MPM formulation.....	25
3.2.1 Basic concepts.....	25
3.2.2 3D, two phase single MP.....	29
3.2.3 Axisymmetric one phase formulation (Galavi et al., 2018)	33
3.2.4 Numerical aspects and alternatives in MPM	38
3.3 Constitutive models.....	43
3.3.1 Mohr-Coulomb.....	43
3.3.2 Mohr-Coulomb Hardening Soil	44
3.3.3 Hypoplastic model	48
3.4 Smoothed Particle Hydrodynamics.....	54
3.4.1 Basic concept	54
3.4.2 Features of the model used.....	56
3.5 Combination of different numerical approaches for back-	
analysis of landslides.....	58
4 MODELLING OF LABORATORY TESTS	60

4.1	Estimation of Baskarp Sand hypo plastic parameters (Sweden)	61
4.1.1	Soil description and available data	61
4.1.2	Model calibration.....	61
4.1.3	Model results versus experimental data.....	63
4.1.4	Validation towards an oedometer test.....	69
4.2	Hypoplastic parameter estimation for Northen Sea Sand (Belgium).....	71
4.2.1	Soil Description	71
4.2.2	Calibration and parameters estimation.....	73
4.2.3	Static triaxial tests	73
4.2.4	Parametric Analysis on the intergranular parameters.....	77
4.2.5	Calibration of hypoplastic parameters regarding model capacity	81
4.3	Hypoplastic parameter estimation for North-Wich Coal (Australia).....	86
4.3.1	Soil Description and available data	86
4.3.2	Estimation of Hypoplastic model parameters.....	87
4.4	Conclusions	92
5	INVERSE ANALYSIS APPLIED TO CONE PENETRATION TEST MODELLING	94
5.1	data.....	95
5.1.1	Chamber tests in loose, dense and layered soil (Tehrani et al 2017)	95
5.1.2	Centrifuge test experiment of jacked pile installation (Stoevelaar 2011)	98
5.1.3	Offshore CPT field data (Fugro 2015).....	99
5.2	Simulation of CPT using Mohr-Coulomb constitutive model	102
5.2.1	Sensitivity analysis on Mohr-Coulomb parameters.....	102
5.2.2	Calibration of chamber CPT experiments (Tehrani et al 2017)	111
5.3	Simulation of cpt using hardening soil model	121
5.3.1	Numerical difficulties with state variable dependent constitutive models	123
5.3.2	Calibration of CPT on loose, dense and layered soil samples (loose over dense).....	124
5.4	simulation of cpt using hypoplastic model	126

5.4.1	Simulation of a centrifuge test of a jacket pile installation 127	
5.4.2	Simulation of an in-situ CPT in Northern sea sand.....	132
6	MODELLING OF SMALL SCALED SLOPES.....	142
6.1	Simulation of dry small scaled experiment of dry granular propagation.....	143
6.1.1	Case study.....	143
6.1.2	Selected Observations.....	145
6.1.3	MPM Model.....	145
6.1.4	Sensitivity analysis.....	148
6.1.5	Calibrated MPM simulation.....	149
6.2	Modelling a retrogressive slope failure including soil liquefaction.....	152
6.2.1	Case study.....	152
6.2.2	MPM Modelling.....	154
6.2.3	Simulation of the Slope using Lab tests outcomes.....	155
6.2.4	Recalibration of the parameters.....	156
6.3	Conclusions.....	163
7	SIMULATION OF A RAINFALL-INDUCED LANDSLIDE IN HONG KONG.....	164
7.1	Description and soil features.....	165
7.2	SPH modelling of landslide propagation.....	173
7.2.1	The adopted procedure and data set.....	173
7.2.2	Definition of parametric studies.....	179
7.2.3	Observations Selection.....	181
7.2.4	Two phase propagation analysis.....	185
7.3	Slope stability analysis using LEM.....	193
7.4	MPM analysis using two phase formulation.....	197
7.4.1	Effect of soil cohesion.....	197
7.4.2	Effect of basal friction angle.....	200
7.5	Conclusions.....	203
8	CONCLUDING REMARKS.....	205
9	BIBLIOGRAPHY.....	210

LIST OF FIGURES

Figure 3-1, Visualization of the error between observations and simulations for different geotechnical problem (a) Cone Penetration Tests (b) Landslide propagation (c) Lab tests.	15
Figure 3-2 , Examples of desired error intervals for the results of drained triaxial tests.	16
Figure 3-3 Parameter optimization algorithm flowchart (modified from [8]).....	21
Figure 3-4 Spatial discretisation of a continuum body with nodes of the computational mesh and material points (After [72])......	27
Figure 3-5 MPM algorithm for a single calculation step of a time increment: (a)map information from MPs to nodes, (b)solve balance equations, (c)map velocity field to MPs, and (d) update position of MPs.(After [72]).....	28
Figure 3-6 Overview of multi-phase MPM approaches (After [72])	29
Figure 3-7 Scheme of volume if each particles in MPM Axisymmetric	34
Figure 3-8 Flow chart illustrating the contact algorithm after ([57])	41
Figure 3-9 The correction of acceleration and velocity in contact. a) Without correction b) with correction.	42
Figure 3-10, H-S yield surfaces.....	45
Figure 3-11, Scheme of hypoplastic model in each part of material shear module degradation (modified from [90])	51
Figure 3-12, Adopted hypoplastic parameters for Hochstetten Sand (Niemunis and Herle 1997).....	52
Figure 3-13, Hypoplastic prediction of undrained cyclic triaxial tests using the parameters of the Hochstetten sand ([89]).....	53
Figure 3-14, SPH particle approximations in a two-dimensional problem domain.	55
Figure 3-15, Framework of inverse analysis for a rainfall induced landslide adopting LEM, SPH and MPM models.....	59
Figure 4-1. Model results using parameters calibrated in INV 01.....	64
Figure 4-2 Model results using parameters calibrated in INV 02.....	65

Figure 4-3 Model results using parameters calibrated in INV 03.....	66
Figure 4-4 Model results using parameters calibrated in INV 04.....	67
Figure 4-5 Model results using parameters calibrated in INV 05.....	69
Figure 4-6 Performance of obtained parameter in oedometer test.....	70
Figure 4-7 Particle size distribution curve for Eem/Kreftenheye sand [101].....	71
Figure 4-8 the outcome of 3rd step of for the three CID tests.....	75
Figure 4-9 The outcome of 3rd step of calibration for the CIU test.....	76
Figure 4-10 The outcome of 4th step of calibration in terms of one CIU test, Stiffness degradation curve.....	76
Figure 4-11 Effect of Parameter h_s on Cyclic mobility.....	77
Figure 4-12 Effect of Parameter n on Cyclic mobility.....	78
Figure 4-13 Effect of Parameter e_{d0} on Cyclic mobility.....	78
Figure 4-14 Effect of Parameter e_{i0} on Cyclic mobility.....	78
Figure 4-15 Effect of Parameter α on Cyclic mobility.....	79
Figure 4-16 Effect of Parameter β on Cyclic mobility.....	79
Figure 4-17 Effect of Parameter m_R on Cyclic mobility.....	79
Figure 4-18 Effect of Parameter β_r on Cyclic mobility.....	80
Figure 4-19 Effect of Parameter R_{max} on Cyclic mobility.....	80
Figure 4-20 Effect of Parameter χ on Cyclic mobility.....	80
Figure 4-21 comparing S-N cyclic resistance curve of experiment with Artificial S-N resistance curve of simulation in terms of original and modified parameters set.	83
Figure 4-22 comparison of initial and modified intergranular parameters in reproducing the stiffness degradation curve.....	83
Figure 4-23 Simulation of CTXL5 using the calibrated parameters of the hypoplastic model.....	84
Figure 4-24 Simulation of CTXL8 using the calibrated parameters of the hypoplastic model.....	85
Figure 4-25 Results of strain-controlled CIU triaxial tests: a) effective stress paths, b) state diagram (data from Eckersley, 1990).....	86
Figure 4-26, Simulations versus observations of CIU tests.	89
Figure 4-27, Performance of adopted ISG parameters a) simulation of stiffness degradation curve for Test NP-2 . b) Simulation of Cyclic triaxial test with low deviatoric stress ratio ($q/p' = 0.1$).....	91
Figure 5-1, Grain size distribution of the # 2Q-ROK sand.....	96
Figure 5-2, Direct shear test results on #2Q-ROK sand ([111]).....	97

Figure 5-3 Outcome of chamber test experiments ([109]).....	98
Figure 5-4, Centrifuge chamber for pile installation experiment	99
Figure 5-5 Experiment output for Jacked pile installation ([110]).....	99
Figure 5-6 CPT results and observations used to calibrate the soil model	100
Figure 5-7, Triaxial tests on samples extracted from borehole BH-WFS2- 5 ([101]).....	101
Figure 5-8, Scheme of the MPM model of CPT.....	103
Figure 5-9, Results of the MPM model at penetration depths 2D and 6D: a) deviatoric strain; b) deviatoric stress	105
Figure 5-10, Results of the parametric analysis: cone resistance pressure vs. dimensionless depth.....	107
Figure 5-11, Parameter values during the regression analysis when it is conducted to calibrate on one parameter at the time: a) soil stiffness, E; b) friction angle, ϕ	110
Figure 5-12, Parameter values during the regression analysis when it is conducted to calibrate both parameters simultaneously: a) soil stiffness, E; b) friction angle, ϕ	110
Figure 5-13, Error function during the regression analysis when it is conducted to calibrate parameters E and ϕ simultaneously.	111
Figure 5-14, Cone resistance profile with depth for the initial and optimal values of the input parameters in the regression analysis conducted to calibrate parameters E and ϕ simultaneously.	111
Figure 5-15 Discretization mesh used in the MPM model of the CPT	113
Figure 5-16 Effect of the mesh size on the model output	113
Figure 5-17, simulation of CPT on the loose sample.....	115
Figure 5-18, Simulated tip resistance over the iterations.....	117
Figure 5-19, a) relation between volumetric strain and deviatoric strain in the case of two sets of parameters b) deviatoric strain around the cone and shaft after 20 cm of penetration.	118
Figure 5-20, Model error function over the iterations.	118
Figure 5-21, Horizontal displacement of particle at the depth of 20 cm. a) starting value b) optimal model.....	119
Figure 5-22, Model for simulation of CPT in layered soil, loose over dense layer	120
Figure 5-23, Simulation of the CPT on the layered sample, T1LOD, loose over dense	121

Figure 5-24, Instability while using MPM-MIXED integration method	123
Figure 5-25, Simulation of CPT using MPM-MP+GP and initial parameters value. a) Loose sample b) dense sample	124
Figure 5-26, Calibration of the hardening soil model with CPT using modified dilation angles and fine mesh a) Loose sample b) Dense Sample	125
Figure 5-27, Simulation of CPT on the layered sample using hardening soil model	126
Figure 5-28, MPM model for centrifuge experiment of pile installation a) initial stress using K0 Procedure b) stress initialization using the gravity acceleration equal to 40g	127
Figure 5-29, Effect of intergranular parameters on the vertical effective stress of the soil domain while pile is 18 cm penetrated a) suggested IGS parameters b) IGS parameters value suggested by Wegener and Herle (2013)	128
Figure 5-30 Outcome of MPM model adopting INV02 for hypoplastic main parameters and suggested IGS parameters ([59])	129
Figure 5-31 Outcome of the modified set of parameter	130
Figure 5-32 Vertical effective stress when the pile is 18 cm penetrated. a) Parameters of INV02 b) Modified parameter (hs=100mPa)	131
Figure 5-33 Simulation of lab tests using modified parameters, a) oedometer test, b) triaxial tests of INV02 in Chapter 3	132
Figure 5-34 Scheme of the MPM model of CPT.	134
Figure 5-35 Comparison between CPT data and computed tip resistance for initial and calibrated values of the input parameters	136
Figure 5-36 Results of regression at each iteration: values of parameters and objective function.	137
Figure 5-37 MPM results: direction of horizontal and vertical displacement at end of penetration for the initial (a) and calibrated models (b)	139
Figure 5-38 Comparison between experimental data from triaxial tests and hypoplastic model results for the initial and calibrated values of the input parameters	140
Figure 5-39 Comparison between CPT observations and computed tip resistance for the 5 simulations of the parametric analysis	141
Figure 6-1 Schematic of the flume used for propagation tests of granular flows [121].	143

Figure 6-2 Overview of the experimental results achieved in the flume test considered herein [121].	144
Figure 6-3 Observations, at time equal to 1.5 s, along the longitudinal cross-section of the flume used to calibrate the MPM model.	145
Figure 6-4 Scheme of computational domain.	146
Figure 6-5 Experimental observations and results of the initial MPM simulation at the end of the test.	146
Figure 6-6 Result of model calibration by regression using observations at time $t = 1.5$ s.	150
Figure 6-7 Comparison between model results and experimental observations.	151
Figure 6-8 Results of flume test #7 (from Eckersley, 1990): failure and post-failure stages.	154
Figure 6-9, MPM model and its initial condition, with the indication of the (moving) tracking points (P1-P5) and the (fixed) control Zones (1-3).	155
Figure 6-10, Displacements and deviatoric shear strains computed at different times depending on the initial void ratio. In the Zone 1, at $t=0$, e_p : 0.51 (a), 0.55 (b), 0.61 (c).	156
Figure 6-11, Displacements and deviatoric shear strains computed at different times for: a) $\alpha= 0.34$ (original set of parameters) b) $\alpha= 0.10$ (modified set of parameters).	158
Figure 6-12, Effect of Parameter α on mobilized friction angle.	158
Figure 6-13, Evolution of the control points (P1-P5) in the e - p' plot during the slope instability process.	159
Figure 6-14, Mean effective stresses during the three slope instability stages.	161
Figure 6-15, Pore water pressure and mean effective stress simulated over time at the tracked zones.	162
Figure 6-16, Point P1 tracked over time: a) current and critical void ratios; b) mean effective stress.	162
Figure 7-1 (a) Plan view of landslide of topography contours of debris thickness (b) Landslide debris in plan and section views	166
Figure 7-2 Typical stratigraphy through the landslide site ([122]).	166
Figure 7-3 Hourly rainfall intensities from 11 to 13 August 1995 ([122])	167
Figure 7-4 Probable sequence of the events ([122])	168

Figure 7-5 Groundwater regime ([122]).....	169
Figure 7-6 Geological cross section of the slope before that landslide occurred ([122])	170
Figure 7-7 Direct shear test results for altered tuff with kaolinite veins (a) and for weathered volcanic joints (b) ([122]).	171
Figure 7-8 Water retention curves ([125]).....	172
Figure 7-9 Procedure employed to calibrate the input parameters of a numerical model that simulates the propagation of a landslide.....	176
Figure 7-10 Location of the landslide deposition height observations used to compute the objective functions for model calibration: a) plan view (modified from [122]); b) cross-section.	178
Figure 7-11 Parametric study 1: comparison between observations and computed results for observation set 1 (a) and observation set 2 (b)....	181
Figure 7-12 Parametric study 1: model error variance vs. value of model parameter, $\tan \phi_b$, for the 13 observation sets employed in the analysis.	182
Figure 7-13 Step 1 optimization analysis: value of model parameter (a) and model error variance (b) at each iteration of performed regression.	185
Figure 7-14 Parametric study 2: comparison between observation set 1 and computed results for three values of model parameter $\tan \phi_b$ and five values of model parameter c_v	189
Figure 7-15 Parametric study 2: model error variance vs. value of model parameters, $\tan \phi_b$ and c_v , for observation sets 01 (a), 12 (b) and 13 (c).	190
Figure 7-16 Parametric studies 3 and 4: (a) comparison between observation set 1 and computed results considering $\tan \phi_b = 0.55$ and five values of model parameters ρ_w^{rel} and h_w^{rel} , (b) model error variance vs. values of model parameters for observation set 1.....	191
Figure 7-17 Values of calibrated parameters and model error variance at each iteration of the regression: (a) calibration of parameter $\tan \phi_b$; (b) calibration of parameters $\tan \phi_b$ and ρ_w^{rel}	192
Figure 7-18 Soil height contour lines for the best-fit parameter estimates: (a) calibration of parameter $\tan \phi_b$; (b) calibration of parameters $\tan \phi_b$ and ρ_w^{rel}	193
Figure 7-19, The Calculation mesh used in the seepage analysis	194

Figure 7-20, Factor of safety changing in time with different suction and permeability values	196
Figure 7-21, (a) Critical slip surface at failure time; (b) Suction distribution at failure time	197
Figure 7-22, (a) Calculation mesh for the MPM analysis; (b) Geometry of the slope for the MPM simulations.	198
Figure 7-23, Deviatoric strain distribution for three simulations with different cohesion values.....	200
Figure 7-24, comparison of the outcome of case 3 with final the geometry of landslide	201
Figure 7-25 Results of the inverse analysis	202
Figure 7-26, optimal model obtained through the inverse analysis and comparison with initial one.....	203
Figure 7-27, comparison of the optimal model with final geometry of landslide	203

LIST OF TABLES

Table 3-1, Hardening-Soil input parameters	46
Table 3-2, Possible range of parameters of Hypoplastic model, suggested by [91].....	51
Table 4-1. Triaxial tests used for model calibration.	61
Table 4-2 Inverse analyses performed.....	63
Table 4-3 Calibrated parameters compared to [99].	63
Table 4-4 Calibration stages along with adopted observations, variable parameter and method of parameters determination.....	72
Table 4-5 Considered range for main parameters and outcome of calibration in stage 3.....	74
Table 4-6 Considered range for intergranular parameters and outcome of calibration in stage 4.....	77
Table 4-7, qualitative sensitivity of the CTXL test to the hypoplastic model parameters	81
Table 4-8 Final calibrated parameters of the hypoplastic model for Kreftenheye sand.....	84
Table 4-9, Estimated values of the parameters for the hypoplastic constitutive model.....	89
Table 5-1 Summary of studies for CPT modelling.....	94
Table 5-2, the chamber tests on the #2Q-ROK ([109]).....	95
Table 5-3 Triaxial tests on samples extracted from borehole BH-WFS2-5.....	100
Table 5-4 Input parameter values of the parametric analysis	104
Table 5-5, Main statistical indicators of the sensitivity analysis.....	108
Table 5-6 Size of elements in discretization mesh used in the MPM Mohr-Coulomb of the CPT.....	112
Table 5-7 Values of the calibrated parameters at each iteration of the regression.....	117
Table 5-8, Estimated parameters value of hardening soil model based on [85].	122

Table 5-9 Input parameters of the adopted hypoplastic model	135
Table 5-10 Values of the hypoplastic model parameters in the parametric analysis	140
Table 6-1 Composite scaled sensitivities of the model input parameters	148
Table 7-1 Soil materials properties (data from [122]).....	171
Table 7-2 Sets of observations used for model calibration.....	177
Table 7-3 Material schematization, rheological laws, values of the input parameters and number of simulations performed for the parametric analyses.....	180
Table 7-4 Linear correlation coefficients between the parameters of the rheological law, computed from the variance-covariance matrix for the following values of the parameters:	180
Table 7-5, Seepage and slope analyses inputs.....	196
Table 7-6, Initial input parameters in the MPM simulation of the slope	199

ACKNOWLEDGMENT

I was not able to carry this research unless with great support, sympathy and patience of my advisors Prof. Sabatino Cuomo and Prof. Michele Calvello who managed well three years of my career. I should also admit that what I achieved in my PhD was not possible without help, support and doctorine of my external supervisor Dr. Mario Martinelli. I also should be grateful to be partially supervised by Dr. Vahid Galavi who transferred lots of knowledge and ideas to me.

I did not find enough words to appreciate the favors of Prof. Settimio Ferlisi in all aspects of my life during these three and half years of PhD.

I also thank the chair of Geotechnical lab of University of Salerno, Prof. Leonardo Cascini, the head of international exchange office of civil engineering department Prof. Salvatore Barba as well as the head of the doctoral school, Dr. Giovanni Salzano and the Deltares managers; Harm Aantjes, Dr. Ahmed Elkadi and Ipo Ritesma for their kind favors, supports and allowing me to fulfil my research in their teams and organizations. I would like to acknowledge also Prof. Majid Hassanizadeh from Utrecht Universities for his consultancy and help. I would like to appreciate the patience and support of my new colleagues particularly Professor Tobias Mörz and Dr. Majid Goodarzi in Marum.

I would like to show gratitude to my friends in Salerno , such as my Best friend Dr. Gaetano Pecoraro who has been always beside of me in both happy and sad moments, from the beginning of my stay in Italy till last min. As a foreign student in south of Italy, I am very happy to find great friends in Unisa Geotechnical Lab such as Dr. Dario Peduto, Antonio Marchese, Maria Grazia Stoppiello, , Maria Rosaria Scoppettuolo, Angela Di Perna, Mariantonia Santoro and Dr. Gianfranco Nicodemo, Dr. Luca Picullo , Dr. Vittoria Capobianco, Dr. Ilaria Redina and Dr. Mariagiovanna Moscariello, Ing. Vitto Foresta, Ing. Mauro Forte, as well as my close friends in salerno, Ing. Francesco Montone and Hannes Amberger who always helped me and my wife in various aspects of our stay in Italy.

I also thank my friends and colleagues in Deltares and Anura 3D research community to make a great memory for me during those 9 months stay in the Netherland. Thanks to Dr. Alex Rohe, Dr. Francesca Ceccato and Dr. Faraz Sadeghi Tehrani for their consultancy, thanks to Dirk De Lange, Mike Woning, Thomas Bles, Dr. Margareet Van Marle, Wie Lee Lin and Sara Faghigh Naini.

I would like to express my gratitude to the family of Ferullo and especially " il mio padrino Ettore e' la mia madrina Rosa Desiderio" who always take care of me and my wife like our parents. At the end, I wish to thanks my wife for her perseverance, support and help during these years.

ABSTRACT

Large deformation analysis has become recently centre of attraction in geotechnical design. It is used to predict geotechnical boundary value problems such as, excessive movement of soil masses like landslides or soil-structure interaction like pile installations. Wrong understanding and simulation of each mentioned problem could lead to significant costs and damages, therefore, robust approaches of modelling are needed. Throughout the past decades many numerical methods aiming to simulate large deformations have been introduced as for example, Discrete Element Method (DEM), Smooth Particle Hydrodynamics (SPH), Updated Lagrangian Finite Element Method (UL-FEM) and Material Point Method (MPM). They are varying in basic theories, capabilities and accuracy. But, the complexity is the feature which is quite common in all them and it is attributed to the unclear response of soil body under excessive deformations. As a result these methods are involving many uncertainties in input parameters. Determination of these parameters is always difficult, because reproducing large deformations in the laboratory is difficult and needs advanced and expensive facilities. As a result the introduction of a methodology for estimation of the model parameters adopted for large deformation analysis is extremely needed.

Inverse analysis approaches have proved to be able to overcome complex engineering problem in different fields. In geotechnical engineering, inverse analysis is typically employed to back-calculate the input parameter set of a model to best reproduce monitored observations. Accordingly, its application attempts to clarify the effective soil conditions and allows for an update of the design based on the in-situ measurements. Numerous researches have been fulfilled to evaluate the performance of this approach in geotechnical problem, however, rarely the application of this methodology to the problems involving large deformations have been addressed.

This thesis is addressing these issues by combining inverse analysis methods with advanced numerical methods and soil constitutive models. The proposed methodology is applied to two popular large deformation engineering problem i.e. landslides and soil-structure interaction,

particularly cone penetration tests modelling. Different case studies are addressed; two methods of Smoothed Particle Hydrodynamic and Material Point Method are adopted as numerical models, depending on the case study. Similarly, various constitutive models ranging from the simple Mohr-Coulomb to the advanced ones such as Hardening soil and Hypoplastic model are employed. The employed inverse analysis algorithm also varies by the type of the numerical models and required computation time of the forward model. Particularly, two algorithm are selected, a gradient-based method (modified Gauss-Newton method) and an evaluation based one (Species- based Quantum Particle Swarm Optimization).

In each case the strength and shortcoming of the adopted methods as well as the role played by the adopted benchmarks and the type of observation in model calibration is assessed. A concept of in-situ recalibration of the model is defined and its importance is highlighted. This method is used to determine advanced constitutive model parameters using in-situ tests and geometrical observations.

As a conclusion, the research shows how using an inverse analysis algorithm may improve the modelling of geotechnical problems involving large deformations and, particularly, facilitate model calibration and discovering the shortcoming and strength of the numerical models.

ABOUT THE AUTHOR

Pooyan Ghasemi earned a Master of Science in Seismic Geotechnical Engineering at the University of Tehran (Iran) in 2012 with a dissertation on "Experimental study of remediation measures of anchored sheet pile quay walls using soil compaction". He conducted experimental (shaking table test) and numerical (Finite Element Method) investigation on the remediation measures of anchored sheet pile quay walls that are embedded in the liquefaction-susceptible soil. After his master degree, he started working in Hexa consulting Engineer Company where he has gained some professional experiences in designing of roadways and railways infrastructures such as bridges, tunnels, retaining walls, etc.

Since December 2015, he was awarded a PhD position by the Laboratory of Geotechnical Engineering at University of Salerno. Meanwhile, he has been also a visiting scholar at Deltares (The Netherlands) for almost 9 months working on applications of the material point method to geotechnical problems and on the implementation of inverse analysis algorithms in the MPM code. He also was partially involved in JIP-SIMON project, a Joint Industry Project on the Simulation of installation of offshore Monopile. During the PhD and mentioned project, he earned valuable skills in program developing, advanced numerical methods, Constitutive models, and laboratory and in-situ tests data interpretations.

By the time of finalizing his PhD, he has joined MARUM, Centre for Marine Environmental Science, Bremen-Germany, in order to work within a research project about offshore wind turbine foundations.

1 INTRODUCTION

Soil characterization and estimation is the first step in geotechnical design and engineering. It is not exaggerating if one says the core of geotechnical engineering is site characterisation. Because, proper, certain and accurate determination of the soil properties leads to the efficient design and subsequently significant cost reduction. On the other hand recent design approaches are highly coupled with risk assessment and mitigation which requires a reliable prediction of site or nature response to the human or atmospheric induced disturbance. Such predictions could be carried out through the numerical modelling.

Many geotechnical problems involve large deformation and large movement of soil mass. As examples of such problems, landslides and pile driving could be quoted. The analysis of such a problem is challenging, and need to be simulated using numerical methods developed for large deformation modelling. To name few, the Arbitrary Lagrangian Eulerian Finite Element Method (ALE), the Coupled Eulerian-Lagrangian (CEL) or particle-based methods such as Smoothed Particle Hydrodynamics (SPH) or Material Point Method (MPM). They are varying in basic theories, capabilities and accuracy. But, the complexity is the feature which is quite common in all them and it is attributed to the unclear response of soil body under excessive deformations. As a result these methods are involving many uncertainties in input parameters. Determination of these parameters is always difficult. Moreover, in order to simulate the elaborated circumstances, adopting the advanced numerical method is needed. Advanced numerical methods which usually involve a large number of parameters mostly need to be coupled with soil advanced constitutive model able to reproduce soil hydro-mechanical behaviour properly. However, difficulties in determination of both numerical and constitutive parameters might undermine the practicability of advanced numerical models. Therefore, many engineers still are willing to rely on the empirical methods to predict the geotechnical problem whilst those methods are not enough accurate in many cases.

1.INTRODUCTION

In the thesis, an attempt has been carried out to first of all show how the inverse analysis technique could be used to determine the soil constitutive and numerical parameters. Secondly, a comprehensive methodology on the application of inverse analysis to the landslide flow slide in both failure and propagation stage is proposed. In addition, a novel methodology is going to be presented by which the soil parameters of advanced constitutive models could be determined based on the results of laboratory and in-situ tests (cone penetration tests) while adopting inverse analysis technique. The benefit, challenges and drawbacks of adopted methodology would be discussed.

To reach the aforementioned aims, the needs of a robust method to large deformation modelling are indisputable. Accordingly, two recently developed numerical methods adopted for large deformation phenomenon have been addressed: 1) SPH, which has been used to simulated the propagation stage of a landslide case study, 2) Material point method, which is a novel robust numerical approach able to cover both failure and large strain of the material. In this thesis, MPM has been used to simulate two different geotechnical problems, 1) flow-like landslide case studies covering the initiation of failure until end of the propagation, 2) Simulation of Cone Penetration Tests (CPTs) in sandy soils.

1.1 LAYOUT OF THE THESIS

The second chapter consists of a brief literature review on the application of inverse analysis approach in geotechnical problems. In addition, the chapter presents a brief review on the studies fulfilled on the numerical simulation of the geotechnical problems addressed in theses thesis, i.e. retrogressive failure and flow-like landslide in a slope, landslide propagation and also simulation of cone penetration tests.

In the third chapter, the material and methods used in this study are introduced, starting from the ingredients of inverse analysis including the error definitions and optimization algorithms. Then, the adopted numerical methods i.e. the Material Point Method (MPM), Smoothed Particles Hydrodynamic (SPH), are described. In addition, the three adopted constitutive models in this study are discussed. At the end, a general framework in order to apply inverse analysis to landslide soil

characterisation through the usage of various numerical methods is introduced.

In the fourth chapter, the automatic parameter estimation of advanced constitutive model using REV and lab data is presented, proposed method is applied to estimate the hypoplastic constitutive model in terms of three different cohesion-less material. The adopted laboratory data includes both cyclic and monotonic tests

The fifth chapter of this study is devoted to the in-situ soil parameters estimation through the application of inverse analysis to the material point method model of cone penetration tests. First, the feasibility of the method would be checked by employing a simple constitutive model. Then, the methodology is applied to two advanced constitutive models. The benefit and shortcomings of the method would be discussed.

In the sixth chapter, the automated inverse analysis procedures are used to calibrate the MPM models of two well-instrumented laboratory experiments on reduced-scale slopes, respectively dealing with (1) long run-out soil propagation and (2) large slope deformation. The first laboratory test reproduces a soil mass rapidly propagating along an inclined plane and depositing over a flat area. The second test refers to a retrogressive slope instability combined with soil liquefaction.

In the seventh chapter, a real rainfall induced landslide is addressed. The framework introduced in the last section of chapter 3 is adopted to combine the inverse analysis algorithm with three different numerical methods of LEM, SPH, and MPM. At the end the hydraulic and mechanical parameters of the soil which leads to the best reproductions of landslide triggering and propagation stage are estimated and reported.

2 LITERATURE REVIEW

In this chapter some of the studies related to geotechnical problems addressed in this thesis are reviewed. The studies are presented in three different sections. First, the state of art related to the applications of inverse analysis to the geotechnical problem is presented.

Two main geotechnical problems of this study are the landslides and the Cone Penetration Tests (CPT). The literature on these two topics is widely extended. Therefore, just few studies related to the simulation of these two problems are discussed here. In the Sec. 2.2 a summary of studies related to the simulation of flow slides and retrogressive failure is discussed. In Sec.2.3 a brief literature review on the simulation of penetration problems using different numerical method is performed.

2.1 INVERSE ANALYSIS AND THE GEOTECHNICAL PROBLEMS

[1] presented one of the first geotechnical back-analysis, where the identification of rock mass parameters during a tunnel excavation was carried out. The least squares criterion was used to define the objective function, while a direct method was applied to minimize it.

In [2] and [3], back-analyses applied to earth dam problems were studied. Subsequently, [4] presented some remarks on back-analysis and characterization problems in geomechanics.

Simultaneously to the trend initiated by [4], a Japanese group (formed by the universities of Kobe, Kyoto and Tokyo) was strongly working on the field of back-analysis applied to geotechnics. Several back-analyses for tunnel excavations were performed by [5] and [6], as well as for consolidation and test embankments on soft clay deposits in [7].

Since the advent of numerical methods like Finite Element Method (FEM), the adaptation of the back-analysis in geotechnical problem become more popular, the methodology was applied to different problems to determine various kind of model input parameters from soil mechanical properties to hydraulic parameters. In addition different kinds of observation regarding the objective problem were employed. Having a general view on the literature implies that, as the models are getting more complicated, tend to use automatic calibration rather than conventional back-analysis has increased.

In the geotechnical community, always there is a distinction between the soil behaviour in lab and field condition. Traditionally, soil parameters have been obtained from laboratory tests. However, in many cases samples used in laboratory tests do not represent the whole soil profile. In addition to that, sample extraction itself causes some disturbance and changes of the soil properties that are difficult to quantify. This fundamental distinction has also influenced the researches fulfilled using inverse analysis technique so that, the automatic calibration of the parameters could be classified in two groups. 1) Automatic parameter estimation based on lab data. 2) Automatic parameter estimation based on the field data. Obviously, these two categories are altered in the model being used to simulate the objective data. The former consists in single element or constitutive modelling while the latter is involving a boundary value problem modelling.

2. LITERATURE REVIEW

As for the first group of mentioned research, the main benefit of inverse analysis technique rises when dealing with an advanced constitutive model involving large number of input parameters. For example, many researchers have been carried out using different approach of inverse engineering to determine the parameters of cam clay. [8] calibrated the model using Modified Guass Newton Method. The model parameters also estimated using lab data and neural network by [9], [10] identified the cam clay model parameters using lab data and particle swarm optimization method (PSO). Obviously, automatic parameters estimation for simple constitutive model with little number of parameters based on lab data does not worth hassling like Mohr-coulomb model in which the parameters can be estimated based on the interpretation of the lab data and the executing of the model and iterative procedure is not needed.

In the second category of application (Application to the boundary value problem), the aim is to estimate the soil parameters for in-situ condition and find the optimal value of parameters which yields the best matches between model and real field data. In this category, the application even to the simple constitutive model is very beneficial because, even the estimation of in-situ parameters for simple model is not an easy tasks. In the previous studies, many researches focused on application of inverse analysis to the excavation such as [11] in which the parameters were estimated from inclinometer data, [12] discussed the advantages and disadvantages of using genetic algorithms and self-learning simulations for inverse analysis in a deep urban excavation. Finally, in [13], a simple synthetic tunnel excavation was used to illustrate the potential of the hybrid methodology to parameter estimation.

In addition to the excavation, back-analysis and inverse engineering have been always employed in slope stability and landslide studies. The previous studies mainly devoted to determine the soil parameters by back-analysing of the failure surface and factor of safety. Started by [14] and then followed by [15] who used the pore water pressure information to back-analysis of landslide. [16] for the first time encountered the high correlation of the parameters and admitted the different combination of C and ϕ may lead to similar failure surface.

Inverse modelling has been employed for different slope stability and landslide study ([17] [18]; [19]; [20]). The majority of the research conducted on this topic has focused on landslide triggering employing the hydraulic response of the slope, such as measures from piezometers, as observations to identify the model soil properties ([21]; [22]).

Landslide propagation behaviour, although a subject of broad and current interest (e.g., [23]; [24]; [25]), has rarely been coupled with inverse analysis algorithms explicitly considering the geometric characteristics of the slope as observation values, which may include ground displacements and run-out soil heights (e.g., [26]). This kind of data is particularly useful for the simulation of the propagation stage of landslides. Concerning that, for a well-posed inverse analysis problem, it is very important to choose proper sets of observations - not always an easy task to perform. The propagation stage modelling of a landslide requires a numerical model capable to simulate large deformations. Since such these methods are becoming more popular and developed. Investigation on the practicality of inverse analysis methods to calibrate these models are required .

Large deformation numerical methods also provided the possibility of the penetration problem modelling like cone penetration tests or pile driving ([27], [28]and [29]). This gives a good opportunity to estimate the in-situ soil parameters using the data recorded during penetration process. [30] shows that adopting inverse analysis helps to overcome the complexity of the soil-density and strength relation in field condition.

As it was mentioned, the inverse analysis has been applied in many research to estimate the soil parameters either using field data or laboratory testing data. But, rarely the parameter estimation using simultaneously are both types investigated. In this case, the real influence, robustness, performance and shortcoming of the model remain unknown. This researches aims to advertise the inverse analysis approach not only as a tool to back-analysis of a phenomenon, but also a useful tool for prediction and future design. Thus, in the scope of this thesis, a general overview to both lab data and the corresponding field data is addressed with particular attention to the boundary value problems involving large deformations.

2.2 ANALYSIS AND SIMULATION OF FLOW-LIKE LANDSLIDES

Rainfall-induced instability mechanisms of real and reduced-scale slopes may consist in development of successive shear bands, progressive or

2. LITERATURE REVIEW

retrogressive landslides induced by (or causing) soil static liquefaction, associated to large deformations of soil. Slope geometry, and the initial and boundary conditions within a slope are key factors for these processes [31]. Flume tests performed on reduced-size slope models provided pioneering measurements of the build-up of pore water pressure after slope failure [32]. Such tests were later extended to complex groundwater conditions, including infiltration from ground surface and/or a downwards/upwards water spring from the bedrock to the tested soil layer [33]. On the other hand, centrifuge tests on artificial-real-size slopes pointed out that the transition from slide to flow is caused by local failures producing a variation in the slope geometry [34]. This mechanism is related to transient localized pore-water pressures that are not associated to the development of undrained conditions, but originated by contrast in soils' permeability, combination of particular hydraulic boundary conditions and stratigraphical settings. Experimental evidences show that the transition from slide to flow can occur both for loose and dense soils. Even, decreasing pore-water pressures were measured during the post-failure stage due to soil large deformations and soil volume increase [35]; [36].

The evolution of pore water pressure and shear strength mobilized upon deformation, the transition from slide to flow, and the post-failure build-up of pore water pressure depend on the soil constitutive behaviour. Laboratory tests performed on REV (Representative Elementary Volume) proved that instability and failure are two different behaviours of soils that exhibit non-associated flow rule [37]. Although both may lead to catastrophic events, they are not synonymous. In loose fine sands and silts with relatively low permeability, a small disturbance in load or even small amounts of volumetric creep may produce undrained conditions, and consequently instability of the soil mass. As long as the soil remains drained, it will remain stable in the region of potential instability. In particular, in very loose cohesionless materials the excess pore water pressure may increase immediately and cause the effective stress to drop rapidly leading to soil liquefaction [38]. The development of total or partial undrained conditions upon shearing is the main cause of high pore-water pressures, as observed in REV laboratory tests such as consolidated isotropically undrained triaxial tests (CIU), consolidated anisotropically undrained triaxial tests (CAU), constant shear drained triaxial tests (CSD). The build-up of pore pressures is relevant for soils

having low density index, fine grain size, low hydraulic conductivity and subjected to high deformation rate, as reviewed by [31].

Accurate simulation of soil behaviour requires necessarily advanced constitutive models. However, model calibration is neither easy, as the parameters are generally several, nor objective, as calibration is usually based on expert-judgement. This is an open issue, especially for slope stability.

On the other hand, the analysis of slope behaviour can be conducted through a variety of approaches, considering slope geometric configuration, soil behaviour and specific triggering factors and mechanisms. [39] showed that the drained failure of shallow covers subjected to rainfall can be satisfactorily simulated by either well-known Limit Equilibrium Methods (LEMs) [40]; or more sophisticated Finite Element Method (FEM) analyses [41]. The accurate simulation of both pore water pressure evolution and increase in strain rate necessarily requires advanced constitutive model, such as the Generalized Plasticity model [31]. In such cases deformations are either neglected (LEM) or generally considered as "small" (FEM), which may be a reasonable hypothesis when pre-failure and failure are the only issues of the analysis. The simulation of the overall evolution of slope geometry and the related large deformations requires other approaches such as extended versions of FEM (e.g. Finite Element Method with Lagrangian Integration Points, FEM-LIP, [42]; [43], meshless methods such as Smooth Particle Hydrodynamics (SPH, e.g. [44]; [45], or other methods like DEM (Discrete Element Method; e.g. [46]).

The Material Point Method (MPM) was recently used to simulate: progressive failure of river levees [47]; retrogressive and progressive slope failures induced by excavation [48]; progressive failure and post-failure behaviour for a deep-seated rockslide with a similar geometry to Vajont landslide [49]; dam break flows with different initial aspect ratios [50]; and landslide propagation [51]. However, the literature still lacks contributions which combine MPM slope simulation, the use of advanced soil constitutive model and the calibration of the model by inverse analysis and some recent contributions were recently proposed.

2.3 SIMULATION OF PENETRATION PROBLEMS

The numerical simulation of cone penetration tests (CPT) is always a hot topic for large deformation numerical studies. The majority of the research investigated on the simulation of CPT tests in the cohesive material (Clay). Fully undrained or partially drained condition are expected for these material. In saturated clays and other fine-grained soils, the test is carried out at a penetration rate that does not permit drainage, therefore the cone resistance may be interpreted as a measure of the undrained shear strength of the soil. Some of the valuable studies on the numerical modelling of CPT in clayey material are as follows;

[52] adopted the ALE method with 4-noded interface elements at the soil-cone contact. He carried out undrained total stress analyses with Tresca material model. He considered the effects of the soil stiffness, the roughness of the cone and the initial stress state. [53] adopted the CEL method to simulate cone penetration in clay.

[54] compared the performance three numerical analysis approaches capable of accounting for large deformations in simulation of cone penetration tests. They compared the implicit re-meshing and interpolation technique by small strain (RITSS), an efficient Arbitrary Lagrangian–Eulerian (EALE) implicit method and the Coupled Eulerian–Lagrangian (CEL). In all the cases, Clayey soils rather than sands were explored, allowing focus on comparison of the performance of the three numerical approaches without the additional complication of a constitutive relationship that appropriately captures the behaviour of sandy soils. It was concluded that the three methods yield similar results for the quasi-static penetration problems. In the CEL analysis the penetration velocity and critical time step need to be selected carefully, while the re-meshing interval requires attention in the two selected implicit methods. the result obtained with the CEL show dependency on element size (even very fine mesh was used in the region concerned) and differs from those predicted with the EALE and RITSS. The exact solution for this problem is not known.

[55] employed the implicit quasi-static MPM formulation with 3-noded triangular interface elements to perform undrained total and effective stress analysis of cone penetration. His results are in good agreement with those of van den [52] and [56] [57] repeated the same study using explicit time integration scheme MPM formulation.

The simulation of penetration in sandy soils seems to be more challenging. On one side, the instability of the model regarding the absence of the cohesion is more likely; secondly, the shear strength of sand requires more complicated failure criterion rather than those of Tresca model.

Accurate numerical modelling of cone penetration in sand requires a constitutive model that captures stress- and state-dependent response of the soil. [58] shows that the use of a very complex constitutive model to realistically simulate cone penetration in sand can be extremely challenging, keeping in mind that the problem involves high mesh distortion and frictional contact in finite element analysis.

[27] also evaluates the effect of analysis parameter choices on the stability and efficiency of modelling cone penetration into sand

Since the material point method shows acceptable performance in simulation of cone penetration test in Clay [55] and [57], [29] adopted this method to simulate a jacked pile installation in sand. The study clearly shows the challenges in input parameters and necessity to recalibration of the soil constitutive model parameters.

A big challenge in the adopted MPM model by Phuong was the high computation times for simulation few centimetre penetrations. That was due to the fact that, they adopted a 3D MPM formulation. Then, [59] presented axisymmetric MPM formulation which reduced significantly the required computational time.

In this study the axisymmetric MPM model of [59] would be employed to simulate the cone penetration tests in sandy soil, since the computation times are expected to be less than previous models, this thesis can focus on the challenges and performance of constitutive model for CPT modelling in sand and the parameter estimation as well, which is quite missing in the previous researches.

3 MATERIALS AND METHODS

In this chapter, the materials and methodology used in this thesis are presented. Sec.3.1 describes the inverse analysis concepts in details. Its ingredients and elements along with their alternatives to be employed are discussed. It would be explained the main elements of the algorithm are Forward model (herein the numerical methods and constitutive models), error definition and optimization methods. Thus, as for the forward model, Sec. 3.2 is devoted to explain the material point method concept and its formulation for two phase material and one phase in axisymmetric condition. In addition, another numerical method adopted in this thesis (Smoothed Particles Hydrodynamic) is briefly presented in Sec.3.4

Sec.3.3 explains the constitutive models employed in various context of this thesis, a simple model of Mohr-Coulomb, Hardening Soil as a semi complex model and Hypoplastic model as a complex model. The strength and weakness of each model along with their difficulties to be used in material point method formulation are also discussed

At the end of this chapter, a framework would be proposed by which the inverse analysis is applied to a rainfall induced landslide. One can use this framework to combine three different models of LEM (Limit Equilibrium Method), SPH and MPM to determine the soil hydromechanical properties and calibrate the models

3.1 INVERSE ANALYSIS ALGORITHMS

Inverse analysis consists in an iterative procedure to estimate the model input that produces the closest output to the user expectation. In other words, an inverse analysis algorithm is searching a set of input parameters that makes the minimum possible difference between the model outcome and the observations. These differences may be called the error, model error function, or objective function. Thus, the best input of the forward model is the one that minimizes the error function. Optimization problems can be classified based on the type of constraints, nature of design variables, physical structure of the problem, nature of the equations involved, deterministic nature of the variables, permissible value of the design variables, separability of the functions and number of objective functions [60].

Classification based on the existence of constraints

- Constrained optimization problems which are subject to one or more constraints.
- Unconstrained optimization problems in which no constraints exist

Classification based on the nature of the design variables

- Parameter or static optimization problems: the objective is to find a set of design parameters that make a prescribed function of these parameters minimum or maximum subject to certain constraints.
- Trajectory or dynamic optimization problems: the objective is to find a set of design parameters, which are all continuous functions of some other parameter that minimizes an objective function subject to a set of constraints.

Classification based on the physical structure of the problem.

- An optimal control problem is a mathematical programming problem involving a number of stages, where each stage evolves from the preceding stage in a prescribed manner. The problem is to find a set of control or design variables such that the total objective functions over all stages is minimized subject to a set of constraints on the control and state variables.

3. MATERIALS AND METHODS

- The problems which are not optimal control problems are called non-optimal control problems.

Classification based on the nature of the equations involved.

- Linear programming problem: if the objective function and all the constraints are linear functions of the design variables.
- Nonlinear programming problem: if any of the functions among the objectives and constraint functions is nonlinear.

Based on the mentioned type of the problem, the best type of optimization algorithm should be chosen. Apart from the mathematical point of view, the time of the computation becomes a relevant issue when the forward model is a numerical model. In this thesis two different kinds of optimization methods are used for different applications and purposes.

- 1) When the forward model is not time consuming, such as for the simulation of a single element model, performing a high number of iterations is not an issue, therefore a particle swarm optimization algorithm is used.
- 2) When the forward model is time consuming, the number of iteration needed to solve the problem must be minimized, therefore a gradient based optimization method is used.

Later in this chapter, the two optimization methods employed in this thesis will be presented and discussed.

3.1.1 Error Definition and Normalization

One of the most important elements of inverse analysis is the definition of a proper Model Error Function. Generally, the Model Error Function can be defined as a function reporting the fit between model outcomes and observations. The main inherent feature of all optimization methods is that they use some iterative procedures to minimize the Model Error Function. If we think at the observations as curves, a simple definition of the Model Error Function (MEF) could be the area between the curve representing the simulation and the observed curve. Figure 3-1 illustrates schematically this approach of error definition.

Depend on the employed optimisation algorithm, the Model Error Function could be defined as a vector or as a scalar. Usually gradient based optimization methods are compatible with a vector error based on least squared error quantification approaches. On the other hand, methods like Genetic algorithms or Particle Swarm methods incorporate a scalar error in their formulation.

A challenge in defining a proper Model Error Function arises when the observations to be used vary in type and magnitude. In this case, the errors corresponding to each type of observation should be normalized and properly weighted.

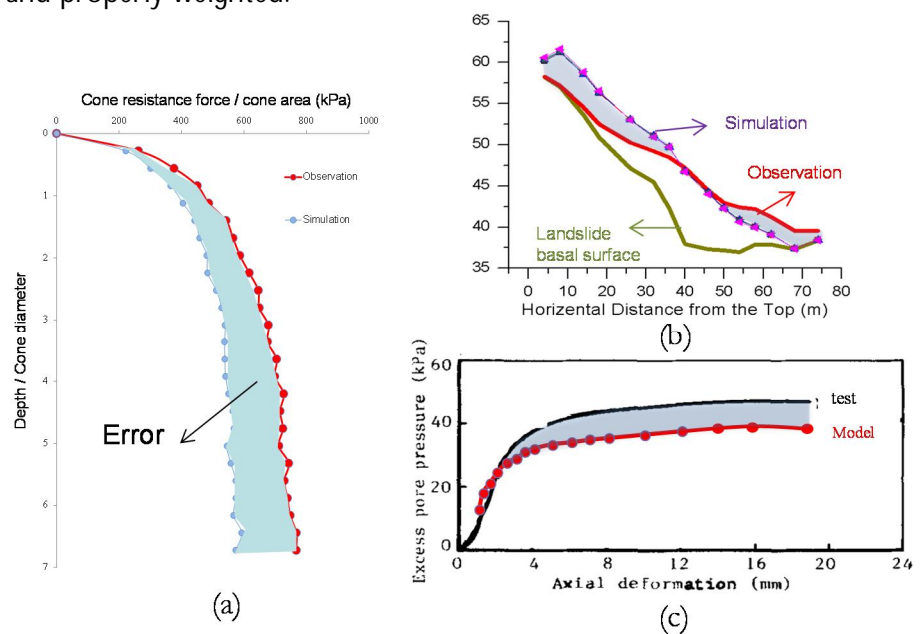


Figure 3-1, Visualization of the error between observations and simulations for different geotechnical problem (a) Cone Penetration Tests (b) Landslide propagation (c) Lab tests.

3.1.1.1 Weighting methods

When different types of observations or observations with significantly different magnitudes are used, the computation of the total error of the

3. MATERIALS AND METHODS

model, quantifying the misfit between simulated and experimental results, necessarily calls for the normalization of the observations. To overcome the challenge of observations with different units, [8] suggested to normalize the observations by the measurement error of the experiments so as to compute a dimensionless error for each observation. Most of the time, however, the error of the measurements is either not reported or not known. In such a case, the normalization could be performed in terms of the maximum desired mismatch between observations and simulated results.

For example, in the case of drained triaxial tests, usually the following two curves are of interest: deviatoric stress versus axial strain, and volumetric strain versus axial strain. It is possible to define an interval representing an acceptable range of model prediction corresponding to the observations reported in those two planes. To compute a total dimensionless error, the observations could be normalized referring to the width of that interval at each observation point.

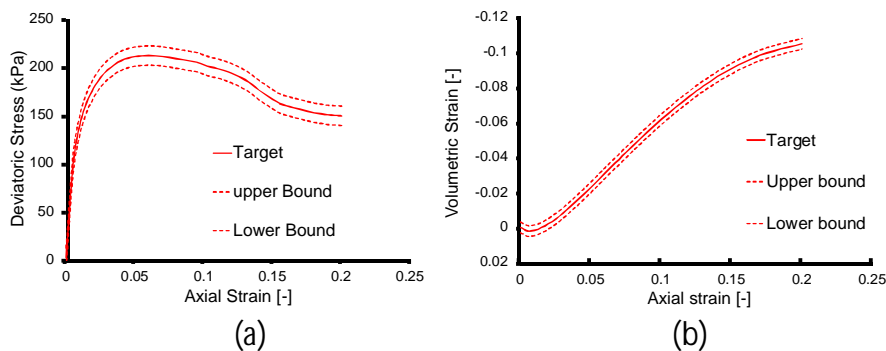


Figure 3-2 , Examples of desired error intervals for the results of drained triaxial tests.

The advantages of the mentioned approach are the following,

- 1) It provides a visual representation of acceptable errors
- 2) For each considered "curve" each observation can be normalized adopting a different normalization value
- 3) More emphasis can be attributed to some parts of the curve by using smaller desired error intervals in those parts

Another challenge in the definition of the error function is related to the different magnitude of the observations. For example, in order to calibrate the parameters of constitutive models using lab tests data, different tests with various initial stress levels are typically carried out. In these cases, since the aim of calibration is to find a set of parameter values that matches all of the tests simultaneously, the errors of each curve must be properly weighted.

3.1.1.2 Error definition of lab data curve fitting

There are different approaches available for weighting the observations to be used in an inverse analysis algorithm. One of them could be the normalization of each experimental curve considering the values of the observations reported in that curve such as, for instance, the minimum, the medium or the maximum value of the considered observations.

For example, in order to define the error function to calibrate a series of triaxial tests, the error function (EF) could be defined as the sum of the error functions of each considered experimental curve, $EF(k)$:

$$EF = \sum_{k=1}^N EF(k) \quad (3-1)$$

$$EF(k) = \sum_{i=1}^{m_k} e_k^2(i) \quad (3-2)$$

$$e_k(i) = [(y_k(i) - y'_k(i))w_k(i)] \quad (3-3)$$

where: N is the number of experimental curves considered, m_k is the number of observations adopted to define the k -th experimental curve, $e_k(i)$ is the weighted residual related to the i -th observation of the k -th experimental curve, $y_k(i)$ is the value of the i -th observation of the k -th experimental curve, $y'_k(i)$ is the value computed by the model which corresponds to the i -th observation of the k -th experimental curve, $w_k(i)$ is the weight assigned to the i -th observation of the k -th experimental curve.

The weights were assigned to produce dimensionless weighed residuals, $e_k(i)$, so that the error functions of the considered experimental curves, $EF(k)$, can be summed to produce a global dimensionless error function,

3. MATERIALS AND METHODS

EF. The weight assigned to the *i*-th observation of the *k*-th experimental curve is thus defined as follows:

$$w_k(i) = \frac{1}{s_k(i)} \quad (3-4)$$

If the weights assigned to all the observations of a given experimental curve are equal, i.e. they do not depend on the value of the *i*-th observation of that curve, the expression used to quantify the acceptable error of the *k*-th experimental curve, s_k , can be the following:

$$s_k(i) = s_k = r_k \max(y_k) \quad (3-5)$$

where: r_k is the dimensionless tolerance coefficient of the *k*-th experimental curve, $\max(y_k)$ is the maximum observed value of the *k*-th experimental curve.

Considering the above relationships, Eq. 1 can be expressed as follows:

$$EF = \sum_{k=1}^N \frac{1}{[r_k \max(y_k)]^3} \sum_{i=1}^{m_k} [y_k(i) - y'_k(i)]^2 \quad (3-6)$$

3.1.1.3 Error definition for boundary value problem and scattered observations

When the calibration of a boundary value problem such as the simulation of cone penetration tests or a landslide is of interest, single scattered or non-continue observations need to be employed. Since the single simulation of a numerical boundary problem is usually time consuming, it is typically convenient to adopt a gradient based optimisation algorithm to calibrate the model. Gradient based methods usually work with a squared weighted error function $S(\underline{b})$, often called objective function, expressed by:

$$S(\underline{b}) = [\underline{y} - \underline{y}'(\underline{b})]^T \underline{\omega} [\underline{y} - \underline{y}'(\underline{b})] = \underline{e}^T \underline{\omega} \underline{e} \quad (3-7)$$

where \underline{b} is a vector containing values of the number of parameters to be estimated; \underline{y} is the vector of the observations being matched by the regression; $\underline{y}'(\underline{b})$ is the vector of the computed values which correspond

to observations; ω is the weight matrix; and e is the vectors of residuals, i.e. the differences between model prediction and observation.

A commonly used indicator of the overall magnitude of the weighted residuals, which allows a direct comparison of results deriving from inverse analyses employing different sets of observations, is the model error variance, s^2 :

$$s^2 = \frac{S(b)}{ND - NP} \quad (3-8)$$

where ND is the number of observations, and NP is the number of estimated parameters.

3.1.2 Optimisation Algorithm

There are a number of other issues that affect proper calibration of a numerical model by inverse analysis, including: the number of parameters to be optimized, the interdependence of the model parameters within the framework of the constitutive model, the number of observations, the type of system under consideration, and the adopted optimization algorithm ([8]). Optimization algorithms can be classified in a variety of ways, for instance differentiating between deterministic and probabilistic algorithms or between gradient-based and derivative-free methods. A recent review of optimization techniques widely used in geotechnical engineering is presented by [61]. [62] showed the capability of Modified Gauss Newton Method as a gradient based method in the geotechnical problem. Among the stochastic techniques, Particle Swarm Optimization (PSO) has been shown to provide valuable results in various inverse geotechnical problems, including parameter identification of constitutive models ([63]; [64]; [10]; [65]). However, being trapped in the local minima is always a matter when using these two optimization methods. In this thesis, addition to the modified Gauss Newton Method, a modification of PSO which is thought to have less possibility of local minimum (SQPSO) is adopted.

3.1.2.1 Modified Guess Newton Method

In this section a gradient based model calibration algorithm implemented in UCODE 2014 [66], a computer code designed to allow

3. MATERIALS AND METHODS

inverse modelling and parameter estimation problem, would be described. UCODE has initially been developed for ground-water models, but it can be effectively used in geotechnical modelling because it works with any application software that can be executed in batch mode. Its model-independency allows the chosen numerical code to be used as a "closed box" in which modifications only involve model input values. This is an important feature of UCODE, in that it allows one to develop a procedure that can be easily employed in practice and in which the engineer will not be asked to use a particular forward or inversion algorithm. Figure 3-3 shows a detailed flowchart of the parameter optimization algorithm used in UCODE. Note that the minimization requires multiple runs of the Forward model.

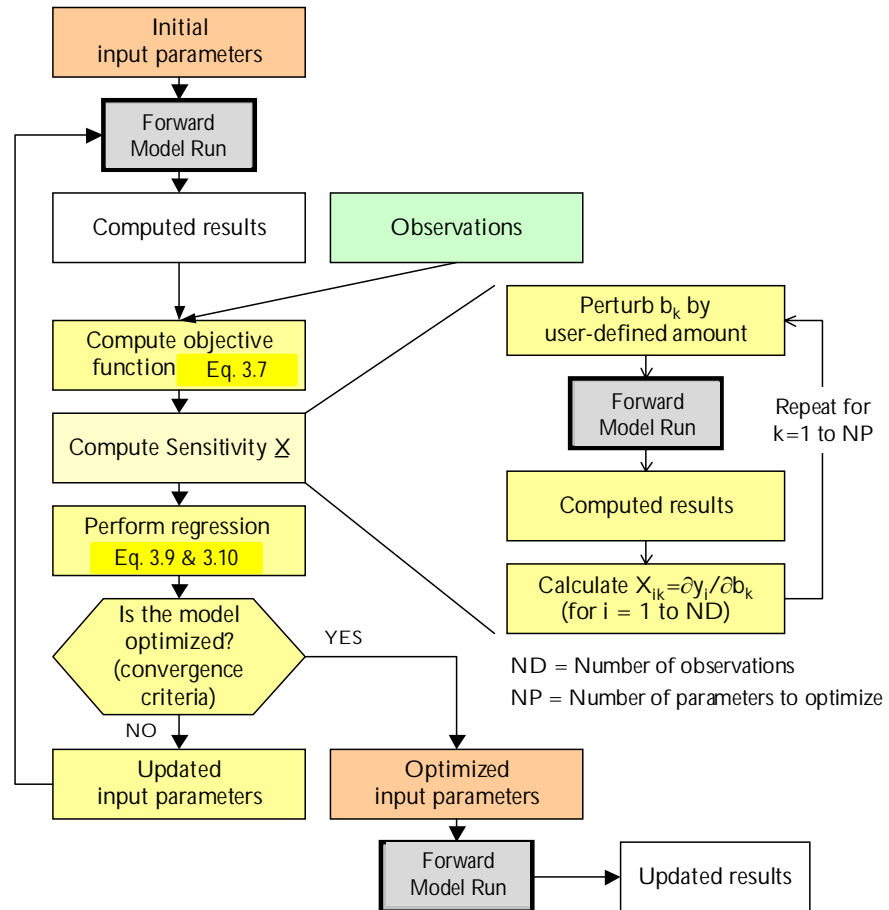


Figure 3-3 Parameter optimization algorithm flowchart (modified from [8])

In UCODE the weighted least-squares objective function is used and The modified Gauss-Newton method used by UCODE to update the input parameters is expressed as:

$$\left(\underline{C}^T \underline{X}^T_r \underline{\omega} \underline{X}_r \underline{C} + \underline{I}m_r \right) \underline{C}^{-1} \underline{d}_r = \underline{C}^T \underline{X}^T_r \underline{\omega} \left(\underline{y} - \underline{y}'(\underline{b}_r) \right) \quad (3-9)$$

$$\underline{b}_{r+1} = \rho_r \underline{d}_r + \underline{b}_r \quad (3-10)$$

3. MATERIALS AND METHODS

where $\Delta \mathbf{b}_r$ is the vector used to update the parameter estimates \mathbf{b}_r ; r is the parameter estimation iteration number; \mathbf{X}_r is the sensitivity matrix ($X_{ij} = \partial y_i / \partial b_j$) evaluated at parameter estimate \mathbf{b}_r ; \mathbf{C} is a diagonal scaling matrix with elements c_{jj} equal to $1/\sqrt{(\mathbf{X}_r^T \mathbf{W} \mathbf{X}_r)_{jj}}$; \mathbf{I} is the identity matrix; m_r is a parameter used to improve regression performance; and ρ_r is a damping parameter.

For problems with large residuals and a large degree of nonlinearity, the term $\mathbf{X}_r^T \mathbf{W} \mathbf{X}_r$ is replaced by $\mathbf{X}_r^T \mathbf{W} \mathbf{X}_r + R_r$ [67] to help convergence when the objective function changes less than 0.01 over three regression iterations.

Multiple runs of the forward model are required to update the input parameters at a given iteration because the sensitivity matrix \mathbf{X}_r is computed using a perturbation method. At any iteration every input parameter b_k is independently perturbed by a fractional amount to compute the results' response to its change. Sensitivities are calculated by forward or central differences approximations. For these approximations each iteration requires $(NP+1)$ and $(2NP+1)$ runs, respectively, to estimate a new set of updated parameters, where NP is the number of parameters optimized simultaneously. Computation time may become an issue for very complicated finite element models, depending on how much time is needed for a single model run.

At a given iteration, after performing the modified Gauss-Newton optimization ((3-9) and (3-10)), UCODE decides whether the updated model is optimized according to two convergence criteria. The parameter estimation is said to converge if either:

- i) the maximum parameter change of a given iteration is less than a user-defined percentage of the value of the parameter at the previous iteration;
- ii) The objective function, $S(\mathbf{b})$, changes less than a user-defined amount for three consecutive iterations.

When the model is optimized the final set of input parameters is used to run the model one last time and produce final "updated" results.

3.1.2.2 Input parameters statistics

The relative importance of the input parameters being simultaneously estimated can be defined using parameter statistics, including the sensitivity of the predictions to changes in parameters values, the variance-covariance matrix, confidence intervals and coefficients of variation.

Different quantities can be used to evaluate the sensitivity of the predictions to parameters changes. One percent sensitivities, dss_{ij} , scaled sensitivities, ss_{ij} , and composite scaled sensitivities, css_j , can be used for the purpose. These sensitivities are defined in Eq.(3-11) to (3-12), respectively.

$$dss_{ij} = \frac{\partial y'_i}{\partial b_j} \frac{b_j}{100} \quad (3-11)$$

$$ss_{ij} = \left(\frac{\partial y'_i}{\partial b_j} \right) b_j \omega_{ii}^{1/2} \quad (3-12)$$

$$(3-13) \quad css_j = \left[\sum_{i=1}^{ND} \left(\left(\frac{\partial y'_i}{\partial b_j} \right) b_j \omega_{ii}^{1/2} \right)^2 \right]^{1/2} / ND \quad (3-13)$$

where y'_i is the i^{th} simulated value; y_i/b_j is the sensitivity of the i^{th} simulated value with respect to the j^{th} parameter; b_j is the j^{th} estimated parameter; ω_{ij} is the weight of the i^{th} observation

One percent scaled sensitivities represent the amount that the simulated value would change if the parameter value increased by one percent. Scaled sensitivities are dimensionless quantities that can be used to compare the importance of different observations to the estimation of a single parameter or the importance of different parameters to the calculation of a simulated value. Composite scaled sensitivities indicate the total amount of information provided by the observations for the estimation of one parameter.

3. MATERIALS AND METHODS

The reliability and correlation of parameter estimates can be analyzed by using the variance-covariance matrix, $\underline{V}(\underline{b}')$, for the final estimated parameters, \underline{b}' , calculated as:

$$\underline{V}(\underline{b}') = s^2 (\underline{X}^T \underline{\omega} \underline{X})^{-1} \quad (3-14)$$

where s^2 is the error variance; \underline{X} is the sensitivity matrix; and $\underline{\omega}$ is the weight matrix.

The diagonal elements of matrix $\underline{V}(\underline{b}')$ equal the parameter variances, the off-diagonal elements equal the parameter covariance. Parameter variances are most useful when used to calculate two other statistics: confidence intervals for parameter values and coefficients of variation. Parameter covariance can be used to calculate correlation coefficients.

A linear confidence interval for each parameter b_j can be calculated as follows (Hill 1994):

$$b_j \pm t \left(n, 1.0 - \frac{\alpha}{2} \right) \sigma_{b_j} \quad (3-15)$$

where $t(n, 1.0 - \alpha/2)$ is the student-t statistic for n degrees of freedom and a significant level of α ; and σ_{b_j} is the standard deviation of the j^{th} parameter.

Coefficients of variation, cov_i , are equal to:

$$\text{cov}_i = \frac{\sigma_i}{b_i} \quad (3-16)$$

where σ_i is the standard deviation of parameter b_i .

Correlation coefficients are calculated by:

$$\text{cor}(i, j) = \frac{\text{cov}(i, j)}{\text{var}(i)^{1/2} \text{var}(j)^{1/2}} \quad (3-17)$$

where $\text{cor}(i, j)$ indicate the correlation between the i^{th} and j^{th} parameter; $\text{cov}(i, j)$ equal the off-diagonal elements of $\underline{V}(\underline{b}')$; and $\text{var}(i)$ and $\text{var}(j)$ refer to the diagonal elements of $\underline{V}(\underline{b}')$.

A confidence interval is a range that has a stated probability of containing the true value of the estimated variable. The width of the

confidence interval can be thought of as a measure of the likely precision of the estimate, with narrow intervals indicating greater precision. The coefficients of variation provide dimensionless numbers with which the relative accuracy of different parameter estimates can be compared. Correlation coefficients close to -1.0 and 1.0 are indicative of parameters that cannot be uniquely estimated with the observations used in the regression.

3.1.2.3 *Species-based Quantum Particle Swarm Optimization*

The adopted SQPSO algorithm in this thesis was proposed by [68]. SQPSO is a population-based evolutionary technique created by combining a Quantum Particle Swarm Optimization (QPSO) algorithm and the speciation concept. QPSO is the quantum model of PSO ([69]), in which the particle dynamics follow quantum mechanics rules. By applying the notion of species in QPSO, the population (solution) is classified into some groups based on the Euclidean distance. Group search improves the performance of SQPSO against the potential problem of being trapped in local optimum points when large search spaces are used.

A detailed description of the algorithm is available in [68], as well as a comprehensive analysis of the exploration ability and solution quality of SQPSO in relation to several standard functions and a practical, power-engineering-related task. And comparing the results of the SQPSO with those obtained using other methodologies; in [68] outlined the convenience of adopting a SQPSO algorithm for stability, convergence and accuracy. The results obtained by [70] [71] with different operational limitations and variables confirmed that SQPSO is a very reliable tool for solving complex practical problems.

3.2 MPM FORMULATION

3.2.1 Basic concepts

The material point method (MPM) can be considered as an extension of the standard Finite Element Method. This approach avoids mesh

3. MATERIALS AND METHODS

distortion by combining the advantages of Lagrangian and Eulerian method, and it can simulate large deformation problems with history-dependent materials. In MPM the continuum body is represented by a set of Lagrangian points, called material points (MPs) Figure 3-4. The MPs keeps and carries all physical properties of the continuum such as stresses, strains, density, momentum, material parameters and other state parameters, whereas the background mesh is used to solve the balance equations without storing any permanent information.

One of the basic and most important features of MPM is that the mass of each MP remains strictly constant which implies that mass conservation is automatically satisfied, whilst the volume of the MP can change enabling material compression or extension. In standard MPM, mass is considered to be concentrated at the corresponding MP and the computational mesh is equivalent to a conventional finite element (FE) mesh. It is constructed to cover the full domain of the problem, including empty spaces into which MPs are expected to move during computation so called empty elements.

The discretised momentum balance equations are typically solved at the nodes of this computational mesh, whereas mass conservation and constitutive equations are solved at the MPs. The information required to solve the balance equations on the computational mesh is transferred from the MPs to the nodes of the mesh at any step of the analysis by using shape functions.

After solving the balance equations by using an incremental time integration scheme the quantities carried by the MPs are updated by interpolation of the mesh results, using the same shape functions. Large deformations are modelled by moving MPs through the background mesh.

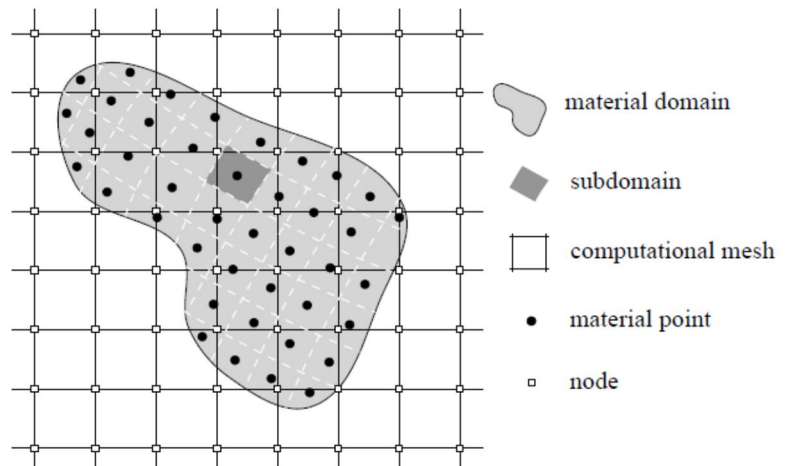


Figure 3-4 Spatial discretisation of a continuum body with nodes of the computational mesh and material points (After [72]).

The MPM algorithm for a single calculation step of a time increment is illustrated in Figure 3-5. At the beginning of each step, the components of the momentum balance equations are defined by projecting information from the MPs to the nodes of the computational mesh by means of shape functions (Figure 3-5 a). The equations of motion are solved for the nodal accelerations (Figure 3-5b). In the next stage, the nodal velocities are projected back to the particles (Figure 3-5c). Based on the velocity, the strain increment is calculated at the particle location and the stress state is updated. In the last step, the particle position is updated throughout the background mesh (Figure 3-5d).

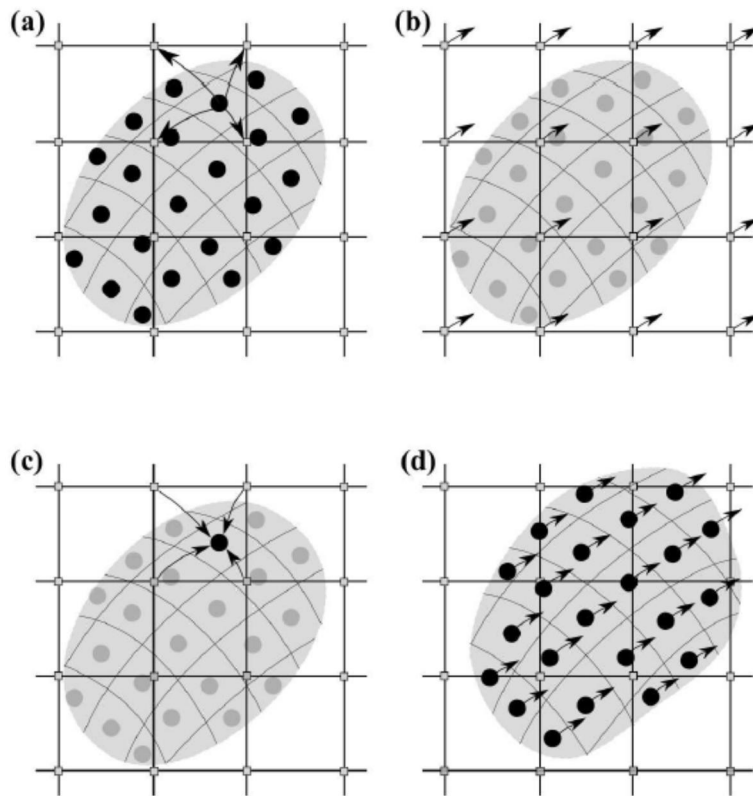



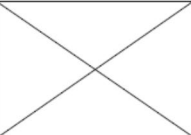

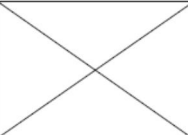


Figure 3-5 MPM algorithm for a single calculation step of a time increment: (a)map information from MPs to nodes, (b)solve balance equations, (c)map velocity field to MPs, and (d) update position of MPs.(After [72])

Soil is a mixture of three constituents (solid, liquid and gas) that interact with each other determining the mechanical and hydraulic response of the material. However, taking rigorously into account these interactions may be in many cases unnecessarily complicated, computationally expensive, and even not feasible for engineering applications. Figure 3-6 shows the concept of multiple constituents used in MPM. The columns represent the number of phases of the continuum and the rows the number of MP sets describing each phase. Dry soil, pure liquid and saturated soil in fully drained or undrained conditions can be modelled with the one-phase single-point formulation. In this case only, one set of MPs is needed to carry all required information of the material. On the other hand, in the two-phase single-point approach, the saturated porous

media are discretised by a single set of MPs which moves through the mesh according to the solid velocity field. Each MP describes a representative volume element of fully saturated soil, carrying the information of both phases, solid and liquid together. While the MPs are attached to the solid skeleton giving a Lagrangian description of its movement, an Eulerian approach with respect to the solid represents the motion of the liquid phase. In the three-phase single-point approach, the soil is considered as a material composed of three distinct constituents, i.e. solid, liquid and gas. The solid phase constitutes the solid skeleton of the porous media, while liquid and gas phases fill the voids. All phases are combined in a single MP and the balance and momentum equations are formulated and numerically solved as aforementioned. In this thesis depends of the case study, one phase, two phase and using single MPs have been adopted, the other possible schemes are out of the scope of this thesis.

	one-phase	two-phase	three-phase
single-point			
double-point			

solid
 liquid
 gas

Figure 3-6 Overview of multi-phase MPM approaches (After [72])

3.2.2 3D, two phase single MP

The material point formulation is already described in details in [28] and [51] However, it is summarized in this section for the sake of clarity. Based on the extended Biot theory [73], the conservation of mass and conservation of momentum are solved within a so called VS-VL scheme [74], in which the accelerations of water phase and solid skeleton are the

3. MATERIALS AND METHODS

primary unknown variables. In the following, "VS" and "VL" refer to the velocity of solid and liquid respectively.

By considering incompressible solid grains and disregarding the spatial variations in densities and porosity, equation represents the conservation of mass of the saturated soil. It is also known as storage equation:

$$\frac{\partial p_L}{\partial t} = \frac{K_L}{n} \left[(1-n) \frac{\partial v_{s,j}}{\partial x_j} + n \frac{\partial v_{L,j}}{\partial x_j} \right] \quad (3-18)$$

where p_L is liquid pressure, K_L is the liquid bulk modulus, and n is the soil porosity. On the other hand, the conservation of momentum of liquid (written per unit volume of liquid) and mixture are expressed as follows, respectively equation (3-18) and (3-19).

$$n(\rho_L \frac{dv_{L,j}}{dt} - \frac{\partial p_L}{\partial x_j} - \rho_L g_j) + \frac{n^2 \rho_L g}{k} (v_{L,j} - v_{s,j}) = 0 \quad (3-19)$$

where p_L is liquid pressure, K_L is the liquid bulk modulus, and n is the soil porosity. On the other hand, the conservation of momentum of liquid (written per unit volume of liquid) and mixture are expressed as follows, respectively equations

$$(1-n)\rho_s \frac{dv_{s,j}}{dt} + n\rho_L \frac{dv_{L,j}}{dt} = \frac{\partial \sigma_{ij}}{\partial x_j} + \rho_{sat} g_j \quad (3-20)$$

where ρ_s is the density of solid, ρ_L is density of liquid, ρ_{sat} is the density of the mixture and k is the Darcy permeability.

The above equations are solved numerically by those following steps (1-10).

- 1) The discrete system of equations can be written as:

$$\mathbf{M}_{L,i}^t \mathbf{a}_{L,i}^t = \mathbf{f}_{L,i}^{ext,t} + \mathbf{f}_{L,i}^{grav,t} - \mathbf{f}_{L,i}^{int,t} - \mathbf{f}_{L,i}^{drag,t} \quad (3-21)$$

$$\mathbf{M}_{S,i}^t \mathbf{a}_{S,i}^t = \mathbf{f}_i^{ext,t} + \mathbf{f}_i^{grav,t} - \mathbf{f}_i^{int,t} - \overline{\mathbf{M}}_{L,i}^t \mathbf{a}_{L,i}^t \quad (3-22)$$

Where

$$\mathbf{M}_{L,i}^t = \sum_{el=1}^{N_{el,i}} \sum_{p=1}^{N_p} N_i^T(\xi_p^t) m_{L,p} \quad (3-23)$$

$$\mathbf{M}_{S,i}^t = \sum_{el=1}^{N_{el,i}} \sum_{p=1}^{N_p} N_i^T(\xi_p^t) (1 - n_p^t) m_{S,p} \quad (3-24)$$

$$\bar{\mathbf{M}}_{L,i}^t = \sum_{el=1}^{N_{el,i}} \sum_{p=1}^{N_p} N_i^T(\xi_p^t) n_p^t m_{L,p} \quad (3-25)$$

$$\mathbf{f}_{L,i}^{grav,t} = \sum_{el=1}^{N_{el,i}} \sum_{p=1}^{N_p} N_i^T(\xi_p^t) \mathbf{f}_{L,p}^{grav} \quad (3-26)$$

$$\mathbf{f}_{L,i}^{trac,t} = \sum_{el=1}^{N_{el,i}} \sum_{p=1}^{N_p} N_i^T(\xi_p^t) \mathbf{f}_{L,p}^{trac,t} \quad (3-27)$$

$$\mathbf{f}_{L,i}^{trac,t} = \sum_{el=1}^{N_{el,i}} \sum_{p=1}^{N_p} N_i^T(\xi_p^t) \mathbf{f}_{L,p}^{trac,t} \quad (3-28)$$

$$\mathbf{f}_{L,i}^{drag,t} = \sum_{el=1}^{N_{el,i}} \sum_{p=1}^{N_p} \frac{n_p^t m_{L,p} \mathbf{g}}{k_p^t} N_i(\xi_p^t) \quad (3-29)$$

$$\mathbf{f}_i^{grav,t} = \sum_{el=1}^{N_{el,i}} \sum_{p=1}^{N_p} N_i^T(\xi_p^t) \mathbf{f}_p^{grav} \quad (3-30)$$

$$\mathbf{f}_i^{trac,t} = \sum_{el=1}^{N_{el,i}} \sum_{p=1}^{N_p} N_i^T(\xi_p^t) \mathbf{f}_p^{trac,t} \quad (3-31)$$

$$\mathbf{f}_i^{int,t} = \sum_{el=1}^{N_{el,i}} \sum_{p=1}^{N_p} \mathbf{B}_i^T(\xi_p^t) \sigma_p^t \Omega_p^t \quad (3-32)$$

The following masses are calculated and assigned to the particles:

$$m_{L,p} = \rho_L \Omega_p^{t=0}, \quad m_{S,p} = \rho_S \Omega_p^{t=0} \quad \text{and} \quad m_p = \rho_{sat} \Omega_p^{t=0} \quad (3-33)$$

The corresponding body forces are calculated from the masses associated with each particle as follows:

$$\mathbf{f}_{L,p}^{grav} = m_{L,p} \mathbf{g}, \quad \mathbf{f}_{S,p}^{grav} = m_{S,p} \mathbf{g} \quad \text{and} \quad \mathbf{f}_p^{grav} = m_p \mathbf{g} \quad (3-34)$$

In the mentioned equations, \bar{N} is the shape function, subscript S refers to solid skeleton, subscript L refers to the liquid phase, i refer to the

3. MATERIALS AND METHODS

node index and subscript p refers to the particle index. σ and σ' are total and effective stress tensor respectively and m is the symbol of mass. The term ξ_p^t is referring to the local position of particles in element. The term Ω_p is the representative of particles volume and B is the strain–displacement matrix which has the form of:

$$B^T = \begin{bmatrix} \frac{\partial N_i}{\partial x_1} & 0 & 0 & \frac{\partial N_i}{\partial x_2} & 0 & \frac{\partial N_i}{\partial x_3} \\ 0 & \frac{\partial N_i}{\partial x_2} & 0 & \frac{\partial N_i}{\partial x_1} & \frac{\partial N_i}{\partial x_3} & 0 \\ 0 & 0 & \frac{\partial N_i}{\partial x_3} & 0 & \frac{\partial N_i}{\partial x_2} & \frac{\partial N_i}{\partial x_1} \end{bmatrix} \quad (3-35)$$

- 2) The Euler-Cromer scheme is used to integrate the equations in time. So, acceleration at nodes (obtained through equations A-4 and A-5) are used to update the velocities of material points MP using shape function. therefore, for both phase of liquid and solid separately;

$$v_p^{t+\Delta t} = v_p^t + \sum_{i=1}^{N_p} \Delta t \bar{N}_i(\xi_p^t) a_i^t \quad (3-36)$$

- 3) The updated nodal velocity of solid $V_{S,i}^{t+\Delta t}$ and liquid $V_{L,i}^{t+\Delta t}$ are then calculated from the updated material point momentum solving these equations.

$$m_{S,i} v_{S,i}^{t+\Delta t} = \sum_{p=1}^{N_p} (1-n) m_{S,p} v_{S,p}^{t+\Delta t} \bar{N}_i^T(\xi_p^t) \rightarrow v_{S,i}^{t+\Delta t} \quad (3-37)$$

$$m_{L,i}^t V_{L,i}^{t+\Delta t} = \sum_{p=1}^{N_p} n m_{L,p} V_{L,p}^{t+\Delta t} \bar{N}_i^T(\xi_p^t) \rightarrow v_{L,i}^{t+\Delta t} \quad (3-38)$$

- 4) Nodal incremental displacements can be calculated by integrating the nodal velocity and subsequently the incremental strain would be obtained.

$$\Delta u_i^{(t+\Delta t)} = \Delta t v_i^{(t+\Delta t)} \quad (3-39)$$

- 5) Strain for both liquid and solid phase at MP are calculated as

$$\Delta \boldsymbol{\varepsilon}^{(t+\Delta t)} = \mathbf{B}(\boldsymbol{\xi}_p^t) \mathbf{v}^{t+\Delta t} \Delta t \quad (3-40)$$

pore water pressure and strain are calculated at material point.

$$\Delta p_{L,p}^{t+\Delta t} = \frac{K_{L,p}}{n} [(1-n) \Delta \boldsymbol{\varepsilon}_{vol,S} + n \Delta \boldsymbol{\varepsilon}_{vol,L}] \quad (3-41)$$

where, Δp_L is increment of pore water pressure and n is porosity, $\Delta \boldsymbol{\varepsilon}_{vol,S}$ and $\Delta \boldsymbol{\varepsilon}_{vol,L}$ are the volumetric strain at the MP for the solid and liquid phase respectively.

- 6) Effective stress would be calculated using constitutive model.

$$\boldsymbol{\sigma}_p^{t+\Delta t} = f(\Delta \boldsymbol{\varepsilon}_p^{t+\Delta t}, \boldsymbol{\sigma}_p^t, \mathbf{e}) \quad (3-42)$$

Where, $\boldsymbol{\sigma}_p^t$ and \mathbf{e} are the initial the initial stress and state variable respectively.

- 7) Pore water pressure and total stress would be updated

$$p_{L,p}^{t+\Delta t} = p_{L,p}^t + \Delta p_{L,p}^{t+\Delta t} \quad (3-43)$$

$$\boldsymbol{\sigma}_p^{t+\Delta t} = \boldsymbol{\sigma}_p^{t+\Delta t} + p_{wp}^{t+\Delta t} \quad (3-44)$$

- 8) Displacement and the position of particle are updated

$$\mathbf{u}_p^{t+\Delta t} = \mathbf{u}_p^t + \sum_{i=1}^{N_n} \bar{\mathbf{N}}_i(\mathbf{x}_p) \Delta \mathbf{u}_i^{t+\Delta t} \quad (3-45)$$

$$\mathbf{x}_p^{t+\Delta t} = \mathbf{x}_p^t + \sum_{i=1}^{N_n} \bar{\mathbf{N}}_i(\mathbf{x}_p) \Delta \mathbf{u}_i^{t+\Delta t} \quad (3-46)$$

- 9) Volumes associated with MP are updated using the volumetric strain increment

$$\Omega_p^{t+\Delta t} = (1 + \Delta \boldsymbol{\varepsilon}_{vol,p}^{t+\Delta t}) \quad (3-47)$$

- 10) At this step, particles are moved through the mesh

3.2.3 Axisymmetric one phase formulation (Galavi et al., 2018)

In this section, the formulation of a 2-dimensional axisymmetric material point method together with the overall procedure for one calculation step is described, more detailed explanation could be found in [59]. The main differences with the conventional plain strain formulations that, in

axisymmetric MPM, the volume of each material point is a representative of one radian of a ring around the axis of symmetric (Figure 3-7)

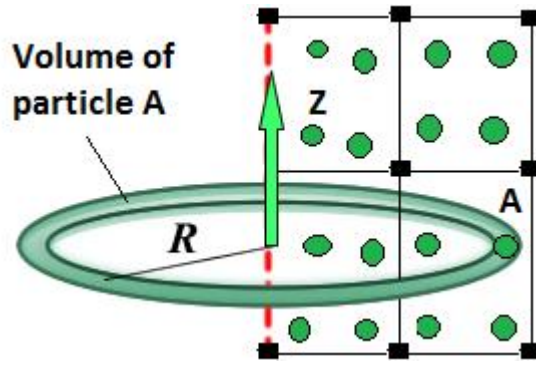


Figure 3-7 Scheme of volume if each particles in MPM Axisymmetric

3.2.3.1 Strains in an axisymmetric geometry

[75] described three examples in which three dimensional geotechnical engineering problems can be expressed by a two dimensional axisymmetric formulation, namely (a) a pile under torsional load; (b) a pile under vertical load; (c) hollow cylinder samples subject to torsion. This section covers the second case where the piles are subjected to a vertical load. In this case, the strain tensor has four non-zero components as follows ϵ_{rr} (radial strain), ϵ_{zz} (vertical strain), ϵ_{rz} (shear strain) and $\epsilon_{\theta\theta}$ (circumferential strain) in the cylindrical coordinate system. This means that there is one more non-zero strain component in the 2D axisymmetric compared to the 2D plane strain, namely $\epsilon_{\theta\theta}$. The displacements in the cylindrical coordinate system are denoted as u_r and u_z . The strain components are related to the displacements through the following relationships:

$$\epsilon_{rr} = \frac{\partial u_r}{\partial r} \quad (3-48)$$

$$\epsilon_{zz} = \frac{\partial u_z}{\partial z} \quad (3-49)$$

$$\gamma_{rz} = 2\epsilon_{rz} = \left(\frac{\partial u_r}{\partial z} + \frac{\partial u_z}{\partial r} \right) \quad (3-50)$$

$$\varepsilon_{\theta\theta} = \frac{u_r}{r} \quad (3-51)$$

where r is the radial distance between the material point and the axis of symmetry. It should be noted that the mechanical sign convention is used in this study, which means that tensile strains are positive.

In the finite element method, strains are related to the displacements as:

$$\boldsymbol{\varepsilon} = \mathbf{B}_i \mathbf{u}_i = \begin{bmatrix} \partial N_i(x_p) / \partial r & 0 \\ 0 & \partial N_i(x_p) / \partial z \\ \partial N_i(x_p) / \partial z & \partial N_i(x_p) / \partial r \\ N_i(x_p) / r & 0 \end{bmatrix} \begin{bmatrix} u_{r,i} & u_{z,i} \end{bmatrix} \quad (3-52)$$

Where u_i is a vector containing nodal displacements of node i . The matrix \mathbf{N} contains shape functions at the local location (x_p) of integration points (material points) and the matrix \mathbf{B} contains gradient of shape functions.

By expanding Eq. (3-52) the strain components in the 2D axisymmetric formulation can be expressed as:

$$(\varepsilon_{rr})_p = \sum_{i=1}^{N_n} u_{r,i} \frac{\partial N_i(x_p)}{\partial r} \quad (3-53)$$

$$(\varepsilon_{zz})_p = \sum_{i=1}^{N_n} u_{z,i} \frac{\partial N_i(x_p)}{\partial z} \quad (3-54)$$

$$(\gamma_{rz})_p = \sum_{i=1}^{N_n} \left(u_{z,i} \frac{\partial N_i(x_p)}{\partial r} + u_{r,i} \frac{\partial N_i(x_p)}{\partial z} \right) \quad (3-55)$$

$$(\varepsilon_{\theta\theta})_p = \sum_{i=1}^{N_n} u_{r,i} \frac{N_i(x_p)}{r_p} \quad (3-56)$$

in which N_n is the number of nodes of an element.

3.2.3.2 Internal forces in an axisymmetric geometry

The main difference between the 2D axisymmetric and the 2D plane strain formulations is in the matrix \mathbf{B} (Eq (3-52)), which is used to

3. MATERIALS AND METHODS

calculate internal forces and strains. The following equation is used to get the internal force:

$$f_i^{int} = \sum_{p=1}^{N_p} B_i^T(x_p) \sigma_p \Omega_p \quad (3-57)$$

where N_p is the total number of material points (integration points) within an element. Ω_p is the integration weight (volume) of material point p and σ_p is the stress tensor of material point p . The components of the internal force in the 2D axisymmetric formulation are written as

$$f_{r,i}^{int} = \sum_{p=1}^{N_p} \left\{ \left((\sigma_{rr})_p \frac{\partial N_i(x_p)}{\partial r} + (\sigma_{rz})_p \frac{\partial N_i(x_p)}{\partial z} + (\sigma_{\theta\theta})_p \frac{N_i(x_p)}{r} \right) \Omega_p \right\} \quad (3-58)$$

$$f_{z,i}^{int} = \sum_{p=1}^{N_p} \left\{ \left((\sigma_{zz})_p \frac{\partial N_i(x_p)}{\partial z} + (\sigma_{rz})_p \frac{\partial N_i(x_p)}{\partial r} \right) \Omega_p \right\} \quad (3-59)$$

3.2.3.3 Overall procedure for one calculation step in 2D axisymmetric MPM

Basically the basic of formulations are similar to the 3D formulation, however, for the sake of completeness, the formulation are rewritten here for Axisymmetric as well.

The solution procedure for one calculation step of the 2D axisymmetric MPM in drained condition is summarised here:

- 1) Lumped mass matrix at nodes are calculated from the mass of material points:

$$m_i = \sum_{p=1}^{N_p} m_p N_i(x_p) \quad (3-60)$$

where m_p is the mass of material point p . The initial mass of the material point is calculated from

$$m_p = \rho_p \Omega_p \quad (3-61)$$

and

$$\Omega_p = r_p A_p \quad (3-62)$$

where ρ_p , A_p , r_p and Ω_p are the initial density, area, radius and volume of material point p , respectively. The initial area of the

material point, A_p , is set based on the Gauss quadrature or standard quadrature which can be considered as a fraction of the element area. The volume of a material point is therefore calculated as the area of a material point multiplied by its radius r_p (Eq.(3-62))

- 2) Momentum at nodes is calculated from the momentum at the material points by a mass-weighted mapping as

$$m_i v_i = \sum_{p=1}^{N_p} m_p v_p N_i(x_p) \quad (3-63)$$

where v_i and v_p are the velocities at nodes and material points, respectively.

- 3) Acceleration at nodes are calculated by solving the following discrete system of equations

$$m_i a_i = f_i^{ext} - f_i^{int} \quad (3-64)$$

where f_i^{int} and f_i^{ext} are the internal and external force vectors. The external force vector consists of body forces and traction forces. The internal force is calculated from stresses in the material points by Eq. (3-57). The components of the internal force vector are given by Eq. (3-58) and Eq. (3-59).

- 4) Acceleration at nodes are used to update the velocities of material points using the shape functions:

$$v_p^{t+\Delta t} = v_p^t + \sum_{i=1}^{N_n} \Delta t N_i(x_p) a_i^t \quad (3-65)$$

- 5) The nodal velocities are then calculated from the updated material point velocities by solving Eq.(3-63).

- 6) The nodal incremental displacements can be calculated by integrating the nodal velocities as

$$\Delta u_i^{t+\Delta t} = \Delta t v_i^{t+\Delta t} \quad (3-66)$$

- 7) The strains and stresses are calculated at material points as

$$\Delta \epsilon_p^{t+\Delta t} = B(x_p) \Delta u_e^{t+\Delta t} \quad (3-67)$$

3. MATERIALS AND METHODS

The subscript e stands for element which means that the nodal incremental displacements of the element are used. The calculated strains can then be used for calculation of stresses using a constitutive model. The components of the strain vector in the 2D axisymmetric formulation are given by Eqs. (3-53) to (3-56).

- 8) The volume and density of particles are updated using the volumetric strain $\Delta\varepsilon_{vol}$:

$$\Omega_p^{t+\Delta t} = (1 + \Delta\varepsilon_{vol,p}^{t+\Delta t}) \Omega_p^t \quad (3-68)$$

$$\rho_p^{t+\Delta t} = \frac{\rho_p^t}{(1 + \Delta\varepsilon_{vol,p}^{t+\Delta t})} \quad (3-69)$$

- 9) Displacements and positions of material points are updated according to:

$$\mathbf{u}_p^{t+\Delta t} = \mathbf{u}_p^t + \sum_{i=1}^{N_n} N_i(x_p) \Delta \mathbf{u}_i^{t+\Delta t} \quad (3-70)$$

$$\mathbf{x}_p^{t+\Delta t} = \mathbf{x}_p^t + \sum_{i=1}^{N_n} N_i(x_p) \Delta \mathbf{u}_i^{t+\Delta t} \quad (3-71)$$

- 10) At this step, the mesh is reset and a space search is performed to find new positions of material points in the background mesh.

A similar procedure can be developed for the two-phase formulation [76] where generation and dissipation of excess pore water pressure can be simulated.

3.2.4 Numerical aspects and alternatives in MPM

Material point method always suffers from some typical numerical difficulties, mainly related to convergence issues and non-physical noise caused by the interpolation between nodes and material points (MPs). These issues are mainly related to the choice of the trail functions combined with the movement throughout the computational mesh. This problem known as Grid-crossing Error and detailed explanation of these issues and their available mitigation methods can be found in [77]. To mitigate this problem, the "MIXED Integration" method, which is described in the following, is used in this thesis. Since advanced constitutive model which include state variables, a modification of the

traditional “mixed integration” is also explored in this work, and it is called “Gauss integration Method”.

3.2.4.1 Mixed integration

The integration of internal force within one element is mostly performed by summing up the values of all MPs inside a given element. The quality of such integration depends on the location of the MPs and their quantities. In contrast to the MPM integration, the Gauss integration is based on a fixed number of integration points, similar to FEM, in an optimal location to achieve as high accuracy as possible [55] proposed to use a combination of both integration schemes to mitigate the noise produced by grid-crossing. Replacing the MPM integration by Gauss integration Eq. (3-72) gives

$$f_2^{\text{int}} \approx \sum_{q=1}^{N_q^e} \sigma_p \omega_p |J(\xi_q)| - \sum_{q=1}^{N_q^{e+1}} \sigma_p \omega_p |J(\xi_q)| \quad (3-72)$$

The computation time could be reduced if Gauss integration is done by using just one integration point. The idea is to use an averaged stress in fully filled elements by weighted averaging the MP stresses over the volume MP volumes, as follows

$$\sigma = \frac{\sum_{q=1}^{N_q^e} \sigma_p \Omega_p}{\sum_{q=1}^{N_q^e} \Omega_p} \quad (3-73)$$

In case of advanced constitutive models, the state variables are also averaged and reassigned to the particles

The Gauss integration does not seem suitable for partially filled elements as the whole element volume is used for the integration whereas the sum of the MP volumes can be smaller. Therefore, it is only recommended to apply Gauss integration if the total particle volume inside one element is at least 90% of the element volume.

3.2.4.2 *Integration weight based on the element volume*

The classical MPM and MIXED integration method has proven to be a valid numerical technique to simulate geotechnical behaviour, especially when simple constitutive models are used, since these models are related with variables less sensitive to stress oscillations, as in the case of the Von Mises criterion. In reality, the use of complex constitutive models is often needed to ensure the correct evolution of the mechanical behaviour of the soil, and therefore the issue of stress oscillations should be relevant. In MIXED integration method, the stress and state variable of particles within a full element are averaged and reassigned to the particles, since the stress of all particles become similar and constant, only one MP as a Gauss integration point could be used to perform the integration. This may lead to incompatibility between the reassigned stress and state variable.

An alternative to the conventional mixed integration is to perform integration in all of MPs and only modify the integration weight of the material points inside the element, in such a way that the summation of the volume of all particles is equal to the volume of the element. In this method neither stress nor state variables are averaged and reassigned to particles. The integration weight of the MPs within an element is calculated as:

$$W_p = \frac{V_{el}}{\sum_{p=1}^{e_p} V_p} \quad (3-74)$$

where V_{el} is the element volume and e_p is the number of material points in the element, and V_p is the volume of the particle. In this method the state variables are not averaged any more. As it was shown by [78], the usage of the modified weighting value improves the results considerably and reduces the stress oscillations, however higher number of MPs should herein be used. In this thesis from now on, this method would be called as "MPM-MP+GP"

3.2.4.3 *Contact Algorithm*

In this study, a frictional contact algorithm was adopted using a Mohr-Coulomb criterion [47], which is developed at the nodal velocity level. In

this algorithm the nodal velocity is calculated from the solution of the governing equation of each body separately and then corrected using the velocity of the combined system and the contact rule.

The contact algorithm is applied between the Lagrangian step and the Convective step. The nodal velocities are first predicted in the former step. Then, the corrected nodal velocities and accelerations are computed with the contact algorithm and these new values of nodal accelerations are employed to compute the velocities of MPs and update their positions, strains and stresses in the latter step, i.e. convective step.

The detailed formulation of this contact algorithm could be found in [77]. However, it was realized that the vertical component of acceleration and velocity of soil particles, adjacent to the contact, could cause the separation between soil particles and the basal surfaces (Figure 3-9a). Therefore, to avoid rebounding of the particles, after the correction of the velocity and acceleration by contact formulation, the vertical acceleration are set to zero for the soil along the contact. In this case the gap between two entities is significantly reduced (Figure 3-9b).

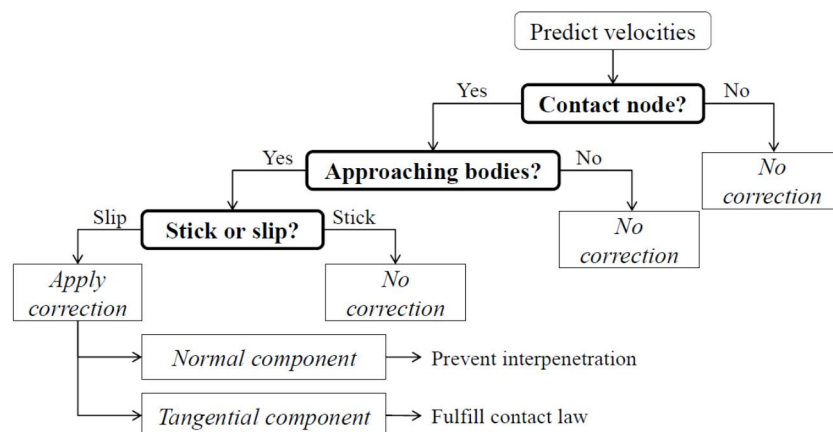


Figure 3-8 Flow chart illustrating the contact algorithm after ([57])

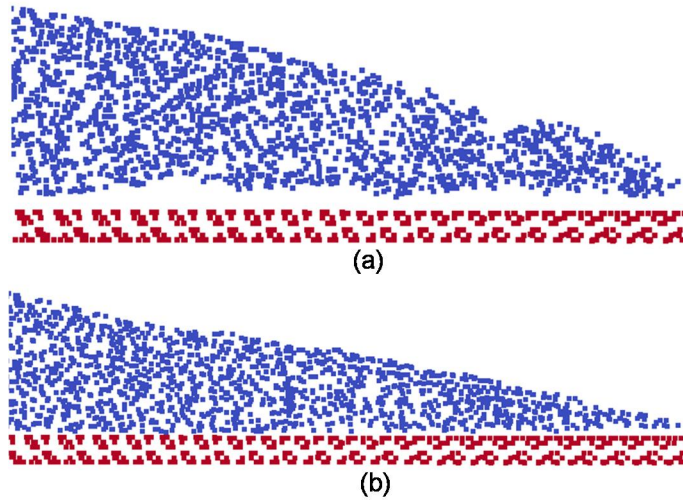


Figure 3-9 The correction of acceleration and velocity in contact. a) Without correction b) with correction.

3.2.4.4 Particle Cluster Initialization

The problem of grid crossing is always a big issue in material point method, and its mitigation become more complicated in terms of advanced constitutive model using. As it was explained in MIXED formulation, stress averaging is performed considering the volume of particles. Therefore, it could be better if the particles of domain have uniform size. In the classical MPM, the volume of particles are initialized based of the volume of initial elements, basically

$$V_p = \frac{V_e}{e_p} \quad (3-75)$$

where, the V_e is the element volume and e_p is the initial number of MPs per element. In this case, If the same number of particle per element is used to discretise the domain, the initial volume of the particles are proportion to the size of the elements, this leads to mesh size dependency of the solution in the case of non-structured mesh and more specifically more variation in the particles size.

As an alternative, the initial volume of the particles could be assigned base on the specific cluster of the domain not the volume of each mesh element. In fact, using uniform cluster, guarantees that particles have the same size. In that case the volume of each particle

$$V_p = \frac{V_d}{e_d} \quad (3-76)$$

where, v_d is the total volume of the cluster and e_d is the total number of particles in an specific cluster, in that case the particles would have the same volume independent from the element volume.

3.3 CONSTITUTIVE MODELS

3.3.1 Mohr-Coulomb

Mohr-Coulomb (MC) is a failure criterion developed by [79] with two model parameters - the cohesion c' and the friction angle ϕ' . It aims to predict the shear strength of soil only from its stress state by assuming elasticity until failure. The model is stress-path independent. This means that no history variable or state variable is required. It was subsequently transformed into a stress-strain relationship and a third parameter was included the dilatancy angle ψ . None of these parameters are coupled and the user must make sure that these are mechanically consistent.

The yield function F and the potential function P are given in Eq (3-73) and Eq (3-77) , respectively.

$$F = q - \left(\frac{c'}{\tan \phi'} + p' \right) \frac{\sin \phi'}{\cos \theta + \frac{\sin \theta \sin \phi'}{\sqrt{3}}} \quad (3-77)$$

$$P = q - (a_{pp} + p') \frac{\sin \psi}{\cos \theta + \frac{\sin \theta \sin \psi}{\sqrt{3}}} \quad (3-78)$$

where F is the yield function, P the potential function and a_{pp} the distance to the apex.

The concept of strength in MC is poorly defined as it can equally refer to the peak state or the critical state. [80] argued that it refers to the peak state and that the cohesion of granular material is a proxy for dilatancy-induced strength ($c' = \sigma'_N \tan \psi$, $\phi' = \phi'_{cs} + \psi$). Bolton suggested that the cohesion is nil and that the dilatancy-induced strength is captured by the friction angle ($c' = 0$, $\phi' = \phi'_{cs} + 0.8 \psi$, ψ).

However, the dilatancy angle ψ is a constant value, which leads to unrealistic and forever changing volumes of soil. This makes this model unsuitable for large deformation MPM simulations in some applications. More detail on this issue could be found in [81]. As the critical state conditions have to be fulfilled at large deformation simulations, the dilatancy angle must be nil and the friction angle has to be the critical state $c' = 0$, $\phi' = \phi'_{cs}$, $\psi = 0$.

According to [82], two parameters are used to describe the elastic behaviour of sands. The Poisson ratio ν is a constant and ranges from 0.15 to 0.35. The Young modulus for silica sand is the function of an effective hydrostatic pressure p'

$$E = 2(1+\nu)G_0 P_a \frac{(2.97-e)^2}{1+e} \left(\frac{p'}{p_a}\right)^{0.5} \quad (3-79)$$

where P_a is the atmospheric pressure, e is the void ratio and G_0 is a material parameter ranging from 35 to 65.

In the contrary to what [82] suggested, Mohr coulomb model describe the elastic behaviour of material only using two constant value of young module E and passion ratio ν . This implies that the predicted linear behaviour of material would be independent from the pressure level

Accordingly, two main features do not exist in conventional Mohr-coulomb model 1) Critical state condition and 2) pressure dependency of linear behaviour. In the next chapters it would be shown how this shortcoming may affect the accuracy of the results in large deformation modelling.

3.3.2 Mohr-Coulomb Hardening Soil

The Hardening Soil (HS) model is an elasto-plastic multi-yield surface model. The model includes both deviatoric and volumetric hardening. It

was originally developed by [83]. The full description of the model can be found in [83]. The model was further extended by [84] to account for small strain stiffness. In this model, failure is defined by the Mohr-Coulomb criteria. Two families of yield surfaces are considered to account for both volumetric and shear plastic strains. Figure 3-10 shows the yield surfaces of the model in p - q stress space. The model is facilitated by a yield cap surface controls the volumetric plastic strains. On this cap, the flow rule is associative. On the shearing yield surfaces, increments of plastic strain are non-associative and the plastic potential is defined to assure a hyperbolic stress-strain response for triaxial compression load conditions.

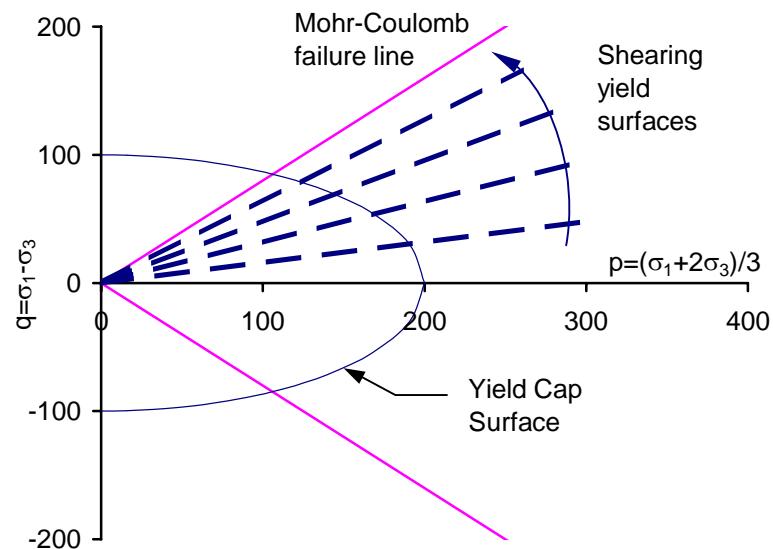


Figure 3-10, H-S yield surfaces

The H-S model input parameters are ten: ϕ , c , R_f , ψ , E_{50}^{ref} , E_{oed}^{ref} , m , E_{ur}^{ref} , ν_{ur} and k_0 . Table 3-1 shows their meaning and the standard method of their estimation. The failure parameters ϕ , c and R_f are estimated assuming a Mohr-Coulomb failure criteria. The parameter ψ is a function of the post-peak stress response of over consolidated soils (ψ is zero for normally consolidated soils). Parameters E_{50}^{ref} , m , E_{oed}^{ref} and E_{ur}^{ref} are estimated assuming the values of E_{50} , E_{oed} and E_{ur} are stress dependent ($p^{ref}=100\text{kPa}$). Parameter ν_{ur} is usually set between 0.15 and 0.3.

3. MATERIALS AND METHODS

Parameter k_0 is estimated using Jaky's empirical relationship with the peak friction angle.

Table 3-1, Hardening-Soil input parameters

Parameter	Unit	Description
E_{50}^{ref}	[MPa]	reference triaxial secant stiffness
E_{oed}^{ref}	[MPa]	reference oedometer stiffness
E_{ur}^{ref}	[MPa]	reference Young's modulus for unloading/reloading
p_{ref}	[MPa]	reference stress
ν_{ur}	[-]	unloading/reloading Poisson's ratio
m	[-]	power for stress dependency of stiffness
c'	[kPa]	effective cohesion
ϕ'	[°]	effective peak friction angle
ψ	[°]	dilation angle
R_f	[-]	failure ratio
G_0^{ref}	[MPa]	maximum reference small strain stiffness
$\gamma_{0.7}$	[-]	small strain at 70% of G_0^{ref}

[85] Introduced a series of empirical formula to initially estimate the Hardening soil parameters only based on the relative density of the sand. Even if the relative density is not precisely known, it could be estimated on the basis of very preliminary soil data. The formulas have been derived by regression analysis on a collection of soil data (general soil data, triaxial test data, oedometer test data, etc.) from [86] and others. The HSsmall model contains four different stiffness parameters, each of them quantifying the reference stiffness in a particular stress path for a

given reference stress level, p^{ref} for a detailed description of the HSsmall model and the meaning of its parameters, reference is made to [84] and [85].

For (quartz) sand, stiffness is supposed to vary linearly with relative density. The following formulas are suggested for the reference stiffness parameters, considering $p^{ref} = 100 \text{ kN/m}^2$

$$E_{50}^{ref} = 60000RD / 100 \text{ [kN/m}^2\text{]} \quad (3-80)$$

$$E_{oed}^{ref} = 60000RD / 100 \text{ [kN/m}^2\text{]} \quad (3-81)$$

$$E_{ur}^{ref} = 180000RD / 100 \text{ [kN/m}^2\text{]} \quad (3-82)$$

$$G_0^{ref} = 60000 + 68000RD / 100 \text{ [kN/m}^2\text{]} \quad (3-83)$$

The actual stiffness is stress-dependent. The rate of stress dependency, parameter m , is known to be negatively correlated with the density. The following formula is proposed for m :

$$m = 0.7 + RD / 320 \text{ [-]} \quad (3-84)$$

The following formulas are proposed for the strength-related properties:

$$\gamma_{0.7} = (2 - RD / 100) \cdot 10^{-4} \text{ [-]} \quad (3-85)$$

$$\varphi' = 28 + 12.5RD / 100 \text{ [-]} \quad (3-86)$$

$$\psi = -2 + 12.5RD / 100 \text{ [-]} \quad (3-87)$$

$$R_f = 1 - RD / 800 \text{ [-]} \quad (3-88)$$

These values should be used for drained conditions.

3.3.3 Hypoplastic model

The hypoplastic model has become popular in solving boundary value problems, e.g. for pile driving simulations [29], for soil-structure interaction issues [87] and for static liquefaction in slope using FEM [88].

In order to improve the small strain prediction [89] has added the so-called intergranular strain parameters (IGS) to eliminate ratcheting (excessive accumulation of deformation predicted for small stress cycles) and then the model was modified slightly by [90] to improve the model prediction in terms of cyclic failure. In the same studies the model parameters for different soils were reported. The main hypoplastic model formula along with the rules of its parameters are discussed with details later on

The model employs 8 main material parameters and 5 secondary parameters. The hypoplastic main equation (3-89) expresses the objective stress rate tensor $\overset{\circ}{T}_s$ as a function of the current void ratio (e), the Cauchy granular stress tensor T_s and the stretching tensor of the granular skeleton D . It could be seen from equation 2 that the stiffness of the material contains two terms, the linear part is noted by operator L and the part which is nonlinear to D is indicated as operator N so that these two operators are elaborated as equation (3-90) and (3-91), where $\hat{T}_s = T_s / tr T_s$ is granular stress ratio tensor. The factors a and F determine the critical state surface in the stress space and depend on critical frictional angle ϕ_c . Factor f_d is equal to $(e - e_d / e_c - e_d)^\alpha$ and it controls the transition to the critical state, peak friction angle and the dilative behaviour. The factor f_e controls the influence of the void ratio e on the incremental stiffness. Involving current void ratio and current critical void ratio as well as exponential parameters β as $f_e = (e / e_c)^\beta$, Factor f_b takes into account the increase of the stiffness consecutive to an increase of mean stress and it is defined as equation 5.

$$\overset{\circ}{T}_s = L(\hat{T}_s, e, D) + N(\hat{T}_s, e, D) \quad (3-89)$$

$$L(\hat{T}_s, e, D) = f_e f_b \frac{1}{tr \hat{T}_s} (F^2 D + a^2 tr(\hat{T}_s D) \hat{T}_s) \quad (3-90)$$

$$N(\hat{T}_s, e, D) = f_e f_b \frac{1}{tr \hat{T}_s} (f_d a F(\hat{T}_s + \hat{T}_s^*) \sqrt{tr D^2}) \quad (3-91)$$

$$f_b = \frac{hs}{n} \left(\frac{1+e_i}{e_i} \right) \left(\frac{e_{i0}}{e_{c0}} \right)^\beta \left(\frac{-tr T_s}{hs} \right)^{1-n} [3 + a^2 - \sqrt{3a} \left(\frac{e_{i0} - e_{d0}}{e_{c0} - e_{d0}} \right)^a]^{-1} \quad (3-92)$$

In the hypoplastic model, the void ratio in the critical state (e_c) and the corresponding mean pressure P ($P < 0$ for compression) are supposed to be connected by equation 6. This equation indeed reproduces the CSL of the material.

$$\frac{e_d}{e_{d0}} = \frac{e_i}{e_{i0}} = \frac{e_c}{e_{c0}} = \exp \left[- \left(\frac{3p}{h_s} \right)^n \right] \quad (3-93)$$

Beside the critical void ratio, the pressure dependency of 2 other characteristic void ratio of minimum e_d and maximum e_i void ratio are postulated in the same form of critical void ratio. In addition to the above mentioned characteristic void ratios, there is a model input parameter named as initial void ratio at zero pressure (e_{p0}) and it would be employed to initialize the state void ratio at the beginning of computation in a way that the initial void ratio at the initial stress level (e_p) is calculated again within the exponential function;

$$\frac{e_p}{e_{p0}} = \exp \left[- \left(\frac{3p}{h_s} \right)^n \right] \quad (3-94)$$

There are also 5 other material constants to catch the material manner in small strain, their brief description is as follow; m_R controls the initial, at very small strain, shear module upon 180° strain path reversal and in the initial loading; m_T controls the initial shear module upon 90° strain path reversal; R_{max} relates to the size of the elastic strain range; βr and χ are used to adjust the rate of degradation of the stiffness with strain.

3. MATERIALS AND METHODS

Previous studies simulating boundary value problems adopting dynamic numerical formulation [88] and [29] showed that Inter Granular Strain parameters (IGS) are needed to be used even in simulation of static loading condition. In principal, they are essential for the dynamic numerical formulations using explicit integration as the wave propagation through the soil will be reflected at each integration point. Therefore, the created noises cause some loading and unloading cycles during the simulation; so, neglecting IGS leads to the ratcheting and wrong model prediction.

Later on it will be explained how the intergranular concept would be added to the linear term of formulation to improve the model performance under the cyclic loading.

When the soil is subjected to the cyclic shearing, the irreversible rearrangement of grain skeleton causes a pore volume reduction. This leads to the accumulation of volumetric strains under drained condition or built excess pore pressure under undrained condition. Therefore, a permanent displacement or accumulated excess pore pressures exist during cyclic loading. In the hypoplastic model this behavior is reproduced by employing intergranular concept. Basically, in this model, volumetric strains or excess pore pressure accumulate during one load cycles is simulated by considering a higher hypoplastic stiffness during unloading compared with the one of "reloading" ([90]). Non usage of intergranular concept in the hypoplastic model causes a problem so called ratcheting ([89])

In this section, for the simplicity, the action of this tensor on the shear module under pure shearing is described as follow; firstly the strain range of the influence of this tensor would be specified by a constant (R_{max}) and then the normalized magnitude of intergranular strain ($\rho = \|\gamma\| / R_{max} \leq 1$) would be calculated. In the range of very small strain $\rho \ll 1$, the initial linear term of stiffness (L) (equation(3-89)) is multiplied by the parameter m_R and it forms the initial shear module G_0 . At large strain, the normalized magnitude of the intergranular strain is $\rho = 1$ and stiffness is calculated similar to the case without intergranular strain tensor. In the transition zone between very small and large strain, the stiffness would depend significantly on the interpolation function (

$[\rho^\chi m_T + (1 - \rho^\chi) m_R]$, so that the stiffness would come from multiplication of this function with nonlinear term N.

Regarding the simple mentioned mechanism of the model under monotonic shear, the involvement of each parameter in the shear module degradation curve could be schemed as Figure 3-11.

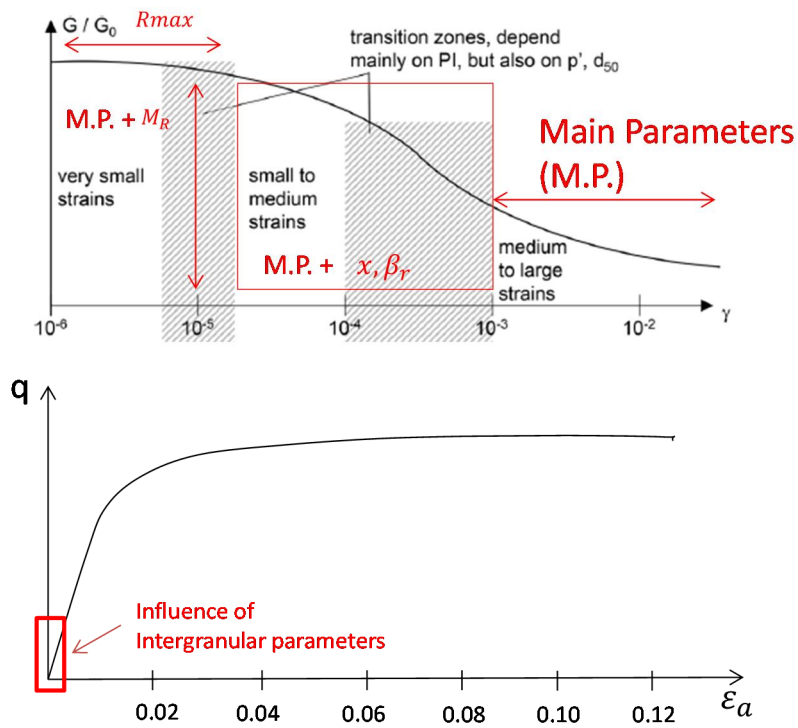


Figure 3-11, Scheme of hypoplastic model in each part of material shear module degradation (modified from [90])

Table 3-2, Possible range of parameters of Hypoplastic model, suggested by [91].

	ϕ_c	e_{i0}	e_{d0}	e_{0c}	h_s	α	β
Min	30	0.5	0.5	0.45	1.0	0.1	1
Max	36	1.1	1.1	0.98	32	0.25	2
	N	χ	m_R	m_T	R_{max}	β_r	
Min	0.18	0.7	4.5	2	2 E -05	0.09	
Max	0.29	6	16.5	16.75	1E -04	0.5	

3. MATERIALS AND METHODS

Table 3-2 shows the range of parameters suggested in [91], this range has been obtained based on the parameters value available related to a data base of different sandy soil. However, one should be aware that this range is not absolute constrain of the parameters value and it is possible to go beyond these ranges for new materials.

3.3.3.1 Performance of Hypoplastic model in cyclic loading

As an example to show the performance of the hypoplastic model in the simulation of cyclic triaxial tests, the model parameters for a test on Hochstetten sand ([89]) are considered. A stress controlled undrained triaxial test with initial confining pressure (p') of 300 kPa and deviatoric stress (q) of 40 kPa is simulated on a sample with initial void ratio of 0.695 is simulated. The predicted axial strains and mean effective stress over the cycles are shown in Figure 3-13. It can be observed that, after a certain number of cycles, i.e. 35 cycles, the sample reaches the instability point, a dramatic drop in mean effective stress happens and the soil liquefies. However, in contrast to typical results observed in many experiments ([92]), the predicted effective stress does not reach zero. Furthermore, the accumulation of axial strain takes place only towards the triaxial extension side, it does not occur in compression, and the axial strains amplitude remains almost constant. In contrast, typical results of experiments show that, after the onset of liquefaction, large axial strains happens without mobilizing any relevant shear resistance and the axial strain amplitude increases with the number of cycles.

Figure 3-12, Adopted hypoplastic parameters for Hochstetten Sand (Niemunis and Herle 1997)

ϕ_c	e_{i0}	e_{d0}	e_{0c}	h_s	α	β
33	1.05	0.55	0.95	1.00E+06	0.24	1.5
n	χ	m_R	m_T	R_{max}	β_r	
0.25	3	5	2	0.0001	0.5	

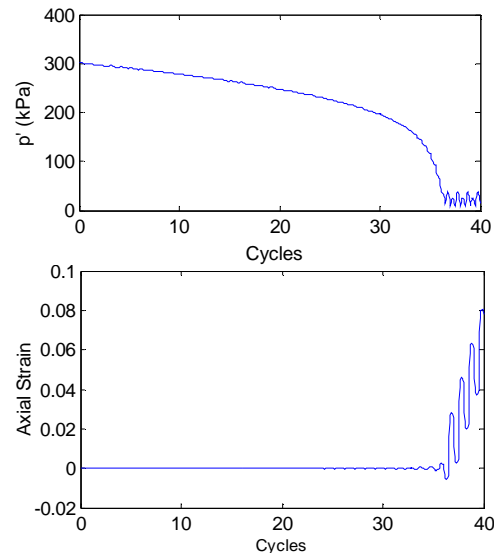


Figure 3-13, Hypoplastic prediction of undrained cyclic triaxial tests using the parameters of the Hochstetten sand ([89])

This clearly shows the limitation of the model in predicting the post-liquefaction behavior and, in general, soil response at low-stress levels. Indeed, it must be considered that after the instability point the soil loses its fabric and subsequently its stiffness. Therefore, low values of initial stiffness are expected. Yet, the current formulation of the model imposes an undesirable stiffness at the onset of the unloading phase, thus leading to accumulating strains over the cycles at constant amplitudes.

3.3.3.2 Difficulties in the using of hypoplastic model in an explicit MPM formulation.

As it was mentioned in the previous section, the hypoplastic model is suffering from the unrealistic strain accumulation while the stress level is low or the soil state is close to the instability points and this undermines the model performance under cyclic loading condition.

[78] clearly showed the existence of relatively high oscillation in classical MPM and Also the MPM-MIXED methods. Therefore there would be always an artificial cyclic load imposed on the constitutive model. As it was explained already, this oscillation would not affect the solution as soon as the constitutive relation remains linear under this small

magnitude cycles. But in the case of Hypoplastic model in which the small strain stiffness of the materials is nonlinear, the oscillations lead to the instability. The solution for this problem would be elaborated in Sec.4.3

3.4 SMOOTHED PARTICLE HYDRODYNAMICS

3.4.1 Basic concept

The core of this method is fully implied in the three words Smoothed Particle Hydrodynamics. "Smoothed" represents the smoothed approximation nature of using weighted averages of neighbouring particles for stability. "Particle" indicates that the method is established on mesh-free particle theory. The computing domain is assembled using a set of discrete particles instead of continuous entities. "Hydrodynamics" points to the fact that the SPH method was first applied to hydrodynamics problems. The basic concept of SPH is that a continuous body is represented by a set of arbitrarily distributed particles. The moving particles possess material properties. By providing accurate and stable numerical solutions for hydrodynamic equations and tracking movements of each particle, the method can describe the mechanical behaviour of an entire system. Therefore, the key facet of SPH is how to solve the partial differential equations (PDEs) using a series of arbitrarily distributed particles carrying field variables, such as mass, density, energy, and stress tensors.

The core concept of the SPH method can be summarized as follows. In the SPH model, the problem domain is replaced by a series of arbitrarily distributed particles. There is no connectivity between these particles, which reflects the mesh-free nature of this method. The major concern of this method is how to ensure the stability of numerical solutions, especially in applying the arbitrarily distributed particles to solve problems with derivative boundary conditions. One of the most important steps is to represent a function in continuous form as an integral representation using an interpolation function. This step is usually called kernel approximation. The integral has a smoothing

effect, similar to the weak form equations. In reality, the kernel approximation stabilizes numerical calculation of the SPH.

Figure 3-14 shows particle approximations in a two-dimensional problem domain Ω , with a surface S . W is the smoothing function that is used to approximate the field variables at particle i using averaged summations over particles j within the support domain with a cut-off distance of kh_i .

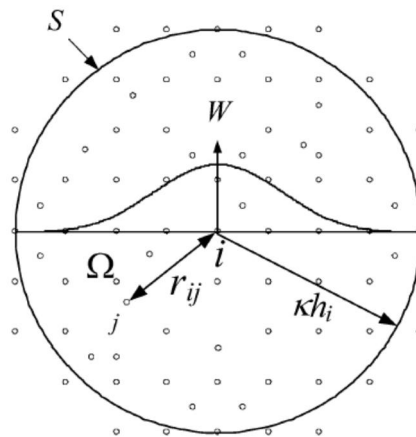


Figure 3-14, SPH particle approximations in a two-dimensional problem domain.

Another important step is that the value of a function at computing particle α is approximated using the averages of function values at all neighboring particles within the horizon of particle α generate banded or sparse discretized system. This step is termed particle approximation. The role of this approximation is to generate banded or sparse discretized system matrices, which are extremely important for calculation efficiency.

Using an explicit integration algorithm to solve differential equations can achieve fast time stepping. The time history of all field variables for all the particles can also be obtained. An appropriate method to determine the time step must be selected in the SPH method.

In summary, the mesh-free, adaptive, stable, and Lagrangian-description SPH method can be used as a dynamics problem solver.

A detailed comparison between MPM and SPH can be found in [93]. The MPM is found to have some advantages compared to SHP, e.g. in MPM spatial derivatives are calculated based on a regular computational grid, so that the time consuming neighbour searching is not required, the boundary conditions can be applied in MPM as easily as in FEM, and contact algorithms can be efficiently implemented.

3.4.2 Features of the model used

In this study, for the case study of real landslide (Chapter 7) the propagation simulation is performed through the “GeoFlow_SPH” model, which is a depth-integrated hydro-mechanical coupled model proposed by [44], based on the fundamental contributions of [6] and [41]. This model incorporates the coupling between pore pressures and the solid skeleton inside the propagating mass. In particular, a depth-integrated, coupled, mathematical model has been derived from the velocity–pressure version of the Biot–Zienkiewicz model ([41]). The equations are complemented with simple rheological equations describing soil behaviour and are discretised using Smooth Particle Hydrodynamics (SPH), which is a meshless method introduced independently by [94] and [95] for astrophysical modelling applications. GeoFlow_SPH was recently used to successfully simulate different case studies of landslide propagation involving mixtures of coarse-grained soils saturated with water, also showing bifurcation of the soil mass ([96]) or soil entrainment during the inception of debris avalanches ([42]). In most cases, a frictional-type rheology has been effectively used to schematise these case studies.

For the analyses to be performed in this thesis, two different mathematical models will be used: i) the mixed-phase model, and ii) the two-phase model.

The first schematisation can be profitably used when water and soil can be effectively approximated as a single-phase material with averaged physical and rheological properties. [41] states that the following two are the limit cases: i) flow of granular materials with high permeability, for which the consolidation time is much smaller than propagation time, hence the material behaves as “drained”; ii) flow of slurries with high

water content, for which the dissipation time for pore water pressures is much higher than the propagation time, hence the behaviour of the material can be assumed as "undrained". In both cases, the material behaviour can be approximated as mixed-phase material, for instance, by using the following frictional law:

$$\tau_b = -\rho gh \cdot \tan\phi_b \cdot \text{sgn}(\bar{v}) \quad (3-95)$$

where τ_b is the basal shear stress, g is the gravity acceleration, h is the propagating soil depth computed as perpendicular to the ground surface, ϕ_b is the basal friction angle, \bar{v} is the depth-averaged flow velocity and sgn is the sign function.

The two-phase model considers pore water pressure changes in time and space within the propagating mass during the propagation time, and two unknown variables, the velocity of the soil skeleton (v) and the pore water pressure (p_w). Both variables are defined as the sum of two components related to propagation and consolidation along the normal direction to the ground surface. The governing equations are discussed in previous studies ([44], [96]; [31]; [96]). It is worth recalling that the vertical distribution of pore water pressure is approximated using a quarter-cosinus shape function, with a zero value at the surface and zero gradient at the basal surface ([44]), while the time evolution of pore water pressure is then given by Eq.(3-97). In case of a frictional law, the basal tangential stress is now given by Eq. (3-96).

$$\frac{dp_w^b}{dt} = \frac{\pi^2}{4h^2} c_v p_w^b \quad (3-96)$$

$$\tau_b = -(\rho gh - p_w^b) \cdot \tan\phi_b \cdot \text{sgn}(\bar{v}) \quad (3-97)$$

where c_v is the consolidation coefficient, τ_b is the basal shear stress, g is the gravity acceleration, h is the propagating soil depth, ϕ_b is the basal friction angle, p_w^b is the basal pore water pressure, sgn is the sign function, and \bar{v} is the depth-averaged flow velocity. The use of the two-phase model implies that the initial pore water pressures must be assigned. This can be done by assigning the initial height of water table

relative to soil thickness (h_w^{rel}), and the ratio between the initial basal pore-water pressure and the liquefaction pressure at base of the flow (p_w^{rel}).

The importance of pore pressure dissipation during landslide propagation has been demonstrated in the literature ([44]; [97]; [98]). In the model considered herein, it is worth noting that the value of the consolidation coefficient (c_v) affects basal pore water pressure (p_w^b); the latter influences the basal shear stress (τ_b) and, in turn, both affect flow velocity (\bar{v}) and flow depth (h). Another important process, i.e. bed entrainment, will be not included in the analyses of the selected case history in Chapter 7.

3.5 COMBINATION OF DIFFERENT NUMERICAL APPROACHES FOR BACK-ANALYSIS OF LANDSLIDES

The adopted framework involves three different approaches as follows: 1) Limit Equilibrium Method (LEM) with seepage analysis to catch the observed failure surface and figure out the triggering factor and get a general insight on the landslide behaviour; 2) SPH propagation analysis to address the role and the importance of adopted observations and to obtain the rheological parameters; 3) detailed MPM analysis in order to create a unified model for both triggering and post failure as well as to characterize the numerical and mechanical soil parameters. These three different analyses are correlated together in a way that the output of some of them is used as the input of others. Figure 3-15 shows how the mentioned analyses could be incorporated and coupled together within a back-analysis of a rainfall induced landslide.

According to the figure, inverse analysis of a propagation stage of landslide using SPH model and the final landslide scheme leads to insights on the rheological parameters and also about the most relevant observations to be used for a more detailed MPM analysis. On the other hand, back-analysis of the triggering stage using LEM and adopting the observed failure surface gives insights on the slope's hydraulic features

and, specifically, on the water table at the onset of failure. At the end, a back-analysis adopting an MPM model incorporating the information obtained by the previous analyses can be able to create an optimal model to simulate the landslide from the onset of failure until the end of the propagation phase.

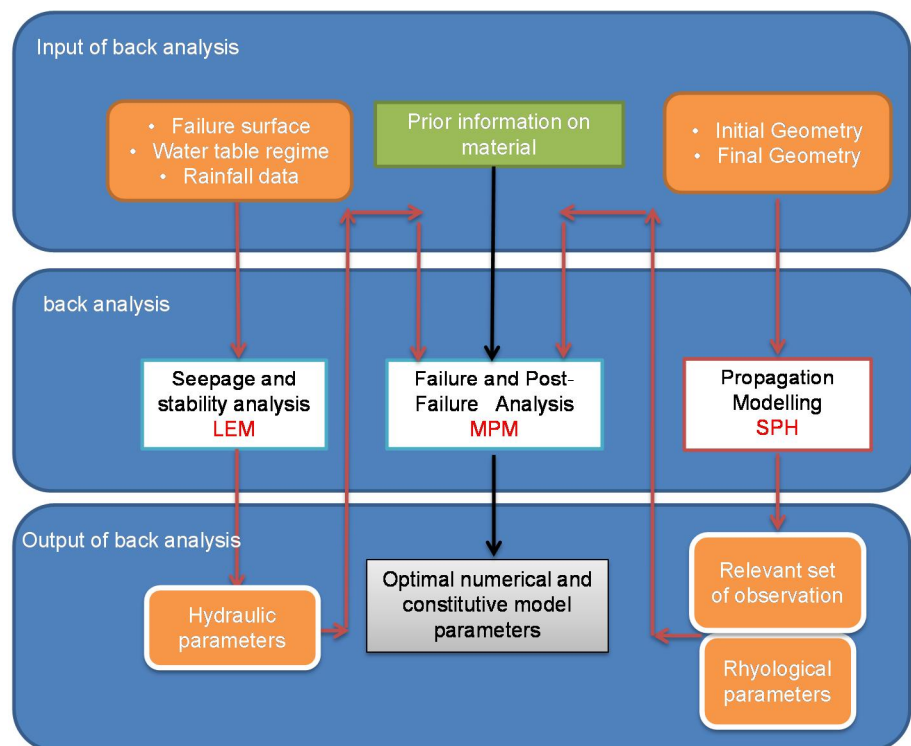


Figure 3-15, Framework of inverse analysis for a rainfall induced landslide adopting LEM, SPH and MPM models

4 MODELLING OF LABORATORY TESTS

In this chapter the parameters estimation by means of laboratory testing and inverse analysis technique would be addressed, and the constitutive model which would be used is hypoplastic model. First of all, the performance of the inverse analysis algorithm in parameters estimation of hypoplastic model parameters for a benchmark material (baskarp sand) would be checked, since the parameters of this soil is already estimated in the literature. In the next stage the proposed methodology would be applied to a sandy formation located in Northern sand sea. In that case study the intergranular parameters of model are also calibrated using cyclic triaxial tests.

In another study, the hypoplastic model parameters for an organic origin granular material (Northwich Coal) would be estimated.

The calibrated parameters in this chapter would be employed to numerical modelling of some boundary value problems in the next chapter of this thesis.

4.1 ESTIMATION OF BASKARP SAND HYPO PLASTIC PARAMETERS (SWEEDEN)

4.1.1 Soil description and available data

Baskarp sand is yellow-orange fine-grained sand deposited a few miles north of Jonkoping (Sweden) under melting of the icecap ca. 10'000 years ago. The grains are classified as angular to sub-angular. It is uniform sand with a D_{50} approximately equal to 140 μm . [99] conducted a comprehensive series of laboratory tests on samples of Baskarp sand, reporting: minimum and maximum void ratios equal to 0.58 and 1.08, respectively; critical friction angle of 30° .

Six drained triaxial tests were considered for model calibration (Table 4-1). Three tests were performed on dense specimens and three tests on loose specimens, characterized by different initial void ratio and three different confining pressures (50, 100 and 200 kPa). For each test the two $(\varepsilon_v, \varepsilon_a)$ and (q, ε_a) experimental curves were considered. Each curve was discretized considering 50 points, thus the observations were 600.

The error calculation method addressed in Sec.3.1.1 would be employed to normalize and weight the error related to each curves of each experiment

Table 4-1. Triaxial tests used for model calibration.

Test	σ'_c (kPa)	e_{initial} (-)	s_k for q (kPa)	s_k for ε_v (-)
1	50	0.59	2.3	6.4 e-4
2	100	0.60	4.2	6.4 e-4
3	200	0.60	8.3	6.0 e-4
4	50	0.70	1.5	2.5 e-4
5	100	0.84	2.7	1.3 e-4
6	200	0.81	5.1	0.4 e-4

4.1.2 Model calibration

The aim of the calibration was to estimate the following 5 parameters of the adopted hypoplastic constitutive model: h_s , n , e_{od} , α and β . Other model parameters were assumed fixed and their values were assigned as follows: e_{d0} and e_{i0} , i.e. maximum and minimum void ratio at zero pressure respectively, are set equal to 0.58 and 1.23, considering the values reported in the literature, the critical friction angle was set equal to 30° . The intergranular parameters were out of the scope of this study, since their main effect is related to the cyclic behavior and they would be elaborated in the next sections. The range of values assigned to the parameters being calibrated was assumed based on Table 3-2. It should be underlined that the starting values adopted by the inverse analysis algorithm were the lowest values of the defined range of the parameters. Inverse analysis was conducted for the triaxial tests of loose and dense specimens, separately. Table 4-2 shows the tests adopted for calibration in the five inverse analyses performed (INV 01 to INV 05).

Each calibration was conducted via 80 iterations of SQPSO, adopting a population number equal to 40. The aim of INV 01 was to check the performance of the procedure while using two tests which differs in both initial void ratio and confining pressure. INV 02 aimed at checking the performance of the procedure in the case of three triaxial tests on dense material with different confining pressures. INV 03 was based on the same idea of INV 02, considering the loose sand specimens. INV 04 and INV 05 were conducted to see the outcomes of the inverse analysis when the objective function includes two tests with similar confining pressures and different initial void ratios.

As reported in Table 4-2, the number of employed observations differs for each analysis. Therefore, the direct comparison of the values of the error functions is not possible. The obtained parameters are reported in Tab. 3, in addition to those estimated by [99].

The comparison of the parameters values estimated in the different inverse analyses shows that observations from different tests lead to relatively different optimal parameters values, although the values are often close to those reported in the literature. The value obtained in INV 03 for α and β are significantly different from those obtained with the other analyses. Similarly, α calculated by INV 05 is relatively higher than the other three estimates. The estimated values for n ranged from 0.29 to 0.41 with an average value of 0.35. The values of h_s are scattered around

a mean value of 4.9×10^6 . In all the analyses the estimated values for β are not close to the values reported by [99], who has obtained this parameter using experimental results from oedometer tests.

Table 4-2 Inverse analyses performed

Inverse analysis ID	Tests	# of observations
INV 01	4, 6	200
INV 02	1, 2, 3	300
INV 03	4, 5, 6	300
INV 04	3, 6	200
INV 05	1, 4	200

Table 4-3 Calibrated parameters compared to [99].

Parameters	α^\perp	β^\perp	hs^\perp	n^\perp	e_c^\perp
INV 01	0.13	2.48	5.33e+6	0.29	0.99
INV 02	0.15	1.57	3.39e+6	0.37	0.98
INV 03	0.10	0.21	5.29e+6	0.39	1.02
INV 04	0.15	1.31	3.06e+6	0.41	0.91
INV 05	0.17	1.88	4.90e+6	0.33	0.98
Average Values	0.15	1.55	3.37e+6	0.358	0.96
Anaraki (2008)	0.12	0.96	4.00e+6	0.42	0.93

4.1.3 Model results versus experimental data

The numerical results obtained using the model parameters calibrated in the five performed analyses, from INV 01 to INV 05, are illustrated in Figure 4-1 to Figure 4-5, respectively. The results of the model simulations adopting the parameters values indicated by [99] are also reported in each figure.

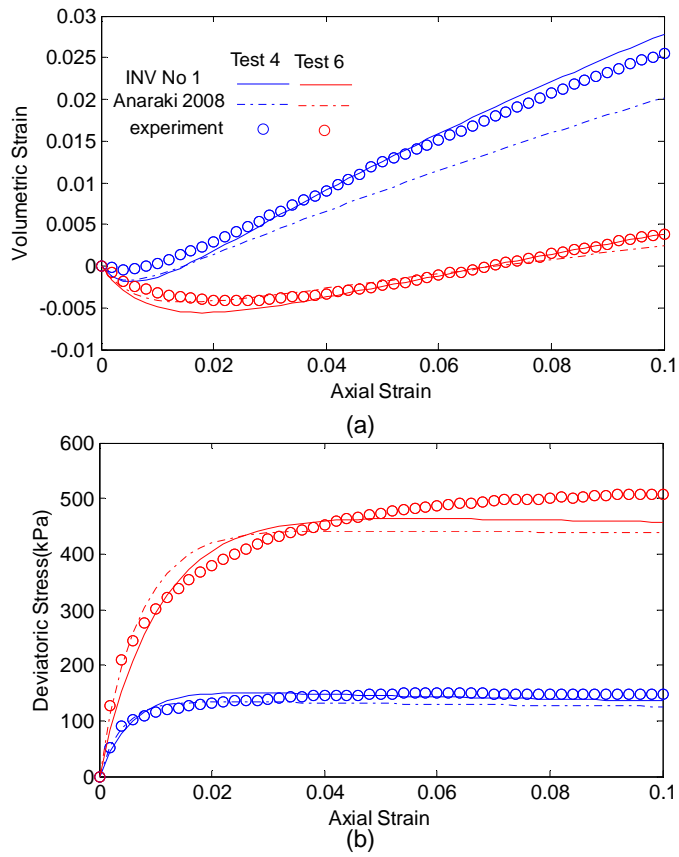


Figure 4-1. Model results using parameters calibrated in INV 01.

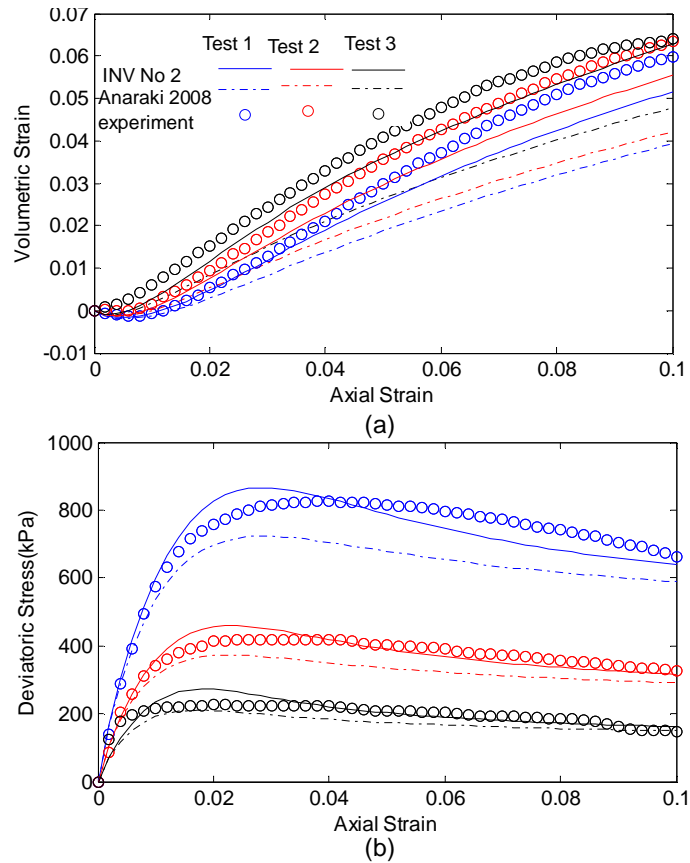


Figure 4-2 Model results using parameters calibrated in INV 02.

INV 01 and INV 03 only consider tests on loose soil samples. In the first analysis, two tests were taken into the account (tests 4 and 6). In the latter, also test 5 was considered in addition to the previous ones. The experimental data from the two tests employed in INV 01 well match the numerical simulations calibrated using those tests (Figure 4-1). On the contrary, INV 03 leads to an unsatisfactory simulated behaviour in the $(\varepsilon_v, \varepsilon_a)$ space for all the three tests (Figure 4-3). This unsatisfactory performance of the inverse analysis highlights the role played by test 5 in worsening the calibration of the model also in relation to the simulations for the other two tests. The improper calibration of this analysis could also be perceived by looking at the values of the calibrated parameters, most of which are quite different from the average values (Table 4-2).

Indeed, even adopting the parameters values suggested by [99] to model results do not reproduce the experimental volumetric strain behaviour recorded in test 5. Experimental results from test 5 should thus be considered peculiar in relation to the other test results, thus unfit as a source of observations for model calibration purposes.

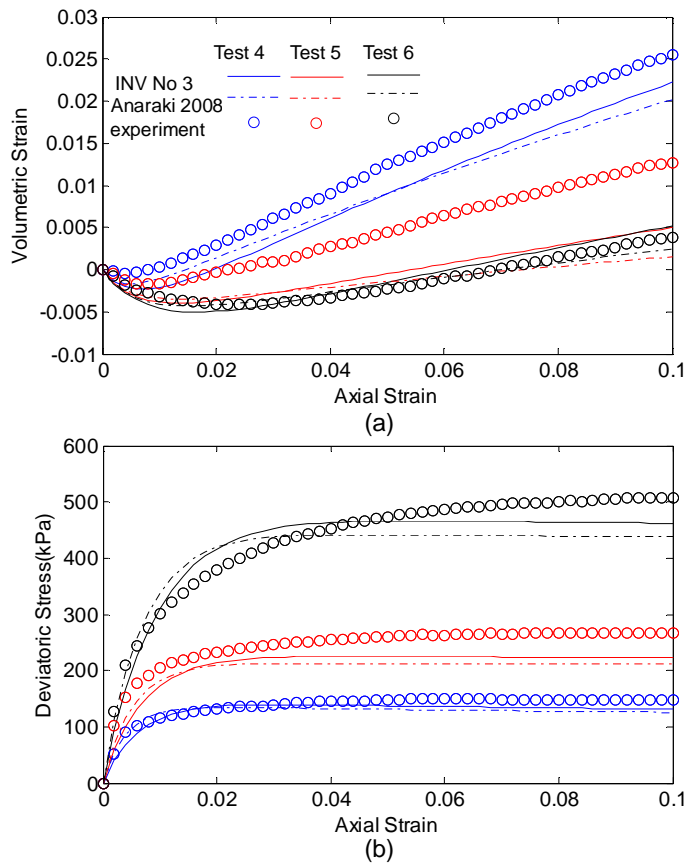


Figure 4-3 Model results using parameters calibrated in INV 03

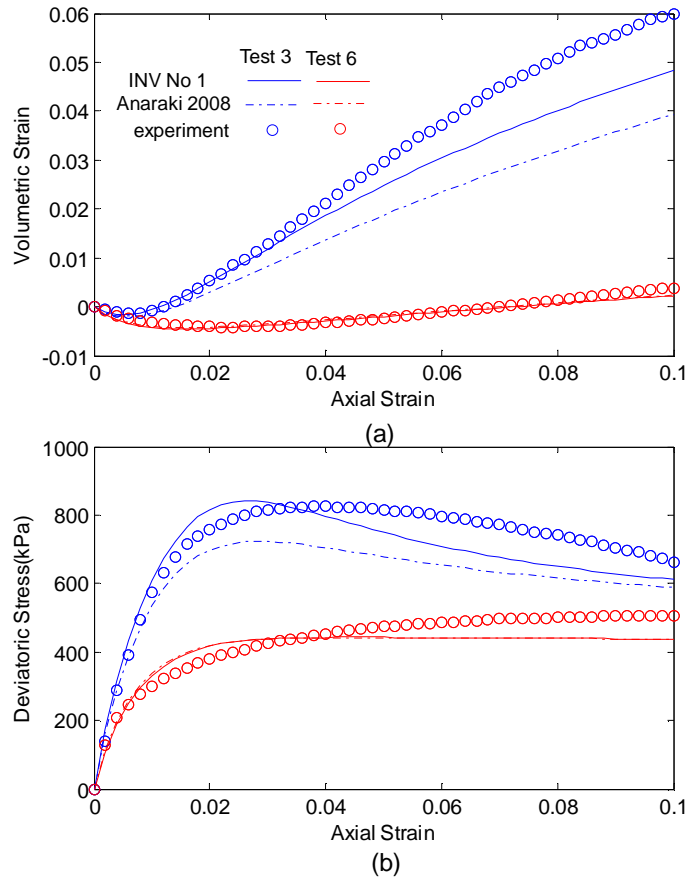


Figure 4-4 Model results using parameters calibrated in INV 04.

The outcome of the calibration performed in INV 02 resulted in a satisfactory fit between simulated and measured values for both $(\varepsilon_v, \varepsilon_a)$ and (q, ε_a) plots. However, the final predicted volumetric strains are slightly underestimated for all three tests. Nevertheless, the predicted curves are closer to the experimental data than the curves produced using the parameters values from the literature.

As mentioned before, INV 04 and INV05 were conducted to check the performance of the inverse analysis when the observations come from two tests on specimens with similar confining pressures and different initial void ratios. The curves from INV 04 (tests with a confining pressure equal to 200 kPa) are in good agreement with the experimental data, as shown in Figure 4-4. The values of the predicted peak shear

strengths are consistent with the observations. The simulated residual shear strength for test 6 is slightly lower than the value recorded in the experiment. The results of INV 05 (tests with a confining pressure equal to 50 kPa) are illustrated in Figure 4-5. The results show proper matches for the loose soil sample. For the dense sample the peak deviatoric stress is overestimated while the residual shear strength is adequately predicted.

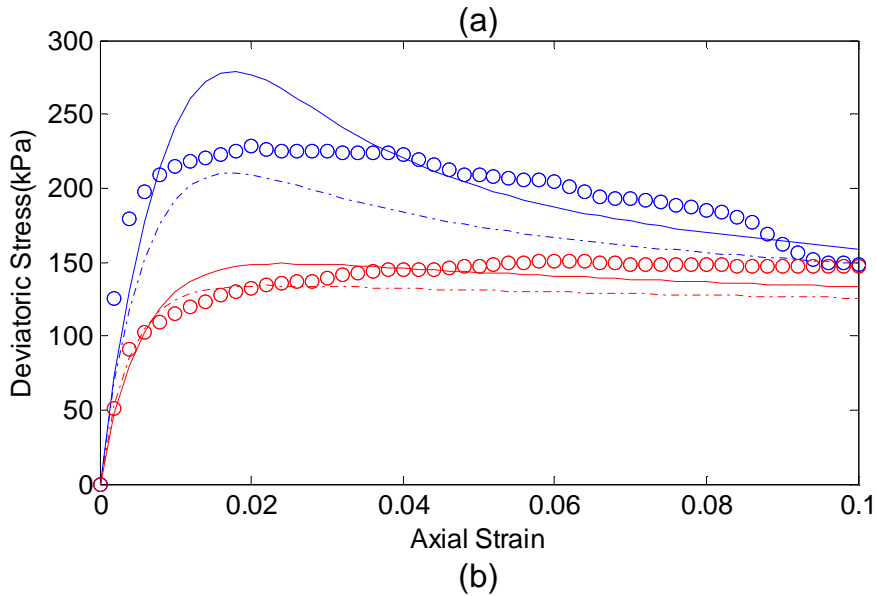
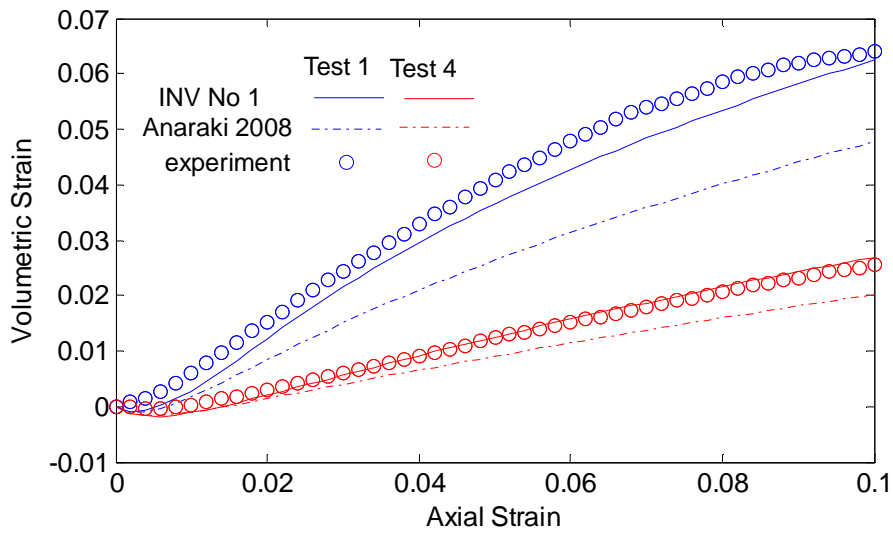


Figure 4-5 Model results using parameters calibrated in INV 05

The inverse analyses conducted adopting observations from specimens confined at lower stresses generally lead to lower estimates for parameters α and h_s . The analyses conducted adopting observations from specimens confined at higher stresses also produce higher values of the critical void ratio. The values of α obtained in the latter cases are also relatively higher than the value reported by [99]. These differences are in accordance with the dissimilarities observed in the simulation of the dilative behaviour of the three tests on dense specimens. As shown in the Figures, lower values of α produce lower dilation. The best fit between experimental data and numerical results occurs when this parameter is equal to its maximum values (0.17).

As a summary, the outcomes of all the analyses except INV 03 appear to be acceptable, although the calibrated values of β are always very different from the ones reported in the literature. In all these four cases, the modelled volumetric strains match the experimental data better than when the model is adopting the set of input parameters from the literature. The analyses also highlight that using observations from tests with similar initial void ratios and different confining pressures (INV 01 and INV 02) or similar confining pressures and different initial void ratios (INV 04 and INV 05), works similarly well. This means that all the 4 sets represent 4 solutions of the optimization algorithm, i.e. they are local minima of the objective function (error) that we are trying to minimize.

4.1.4 Validation towards an oedometer test

The four sets of input parameters of the hypoplastic constitutive model previously calibrated should be able to properly simulate triaxial test results performed on the same material also for tests on specimens that are different in both initial void ratio and confining stress level. In addition, the same set of parameters should also allow reproducing the soil behaviour along other stress paths. Therefore, the performance of achieved calibrated sets of input parameters was rechecked in the simulation of the experimental results of an oedometer test.

Figure 6 shows the oedometric response of a specimen with initial void ratio equal to 0.825 and loaded up to 5 MPa, as well as the simulated responses adopting the four good-performing sets of calibrated. According to [100], the compressive behaviour of the model is related to the parameters h , s , n and β . As shown in Figure 4-6, the parameters set estimated with the analyses INV 01 and INV 05 were not able to reproduce the measured curve correctly. Indeed, the above sets of parameters underestimate the soil stiffness. Adopting INV 04 and INV 02, the results provide a good simulation of the oedometer test. However, some small differences between the simulated and the experimental response still exist.

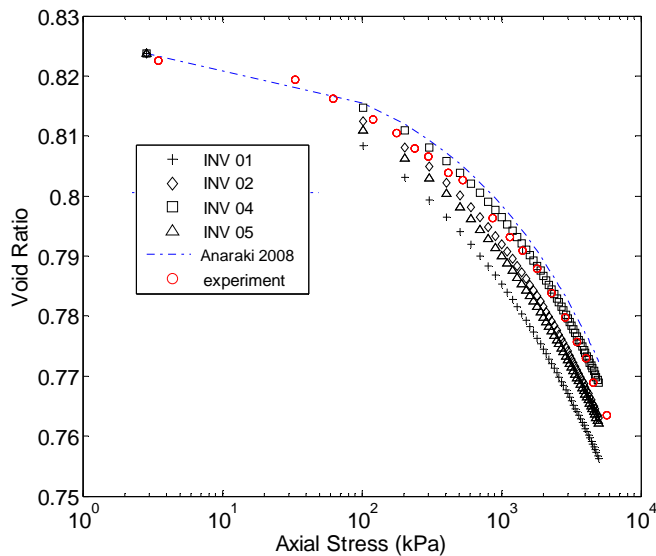


Figure 4-6 Performance of obtained parameter in oedometer test

In fact, INV04 overestimates in the oedometric test and INV02 underestimates it. It seems difficult to decide which one are the best optimal parameters. Therefore to check the accuracy of obtained value and introduce one set of parameter, other two in-verse analyses calculation were carried out in which the error function is defined as the combination of INV02 with oedometer curve and the combination of INV04 with oedometer test respectively. In the former, the obtained parameters are those which were obtained before. But, in the latter, the optimal parameters altered with respect to previous values. Therefore

the obtained values through the INV02 are more prone to simulate the material behaviour properly.

4.2 HYPOPLASTIC PARAMETER ESTIMATION FOR NORTHERN SEA SAND (BELGIUM)

4.2.1 Soil Description

All of the experimental data employed in this section are extracted from a report of [101]. In particular, this study considers the Eem/Kreftenheye sand located in the Brussels wind farm II. The soil is characterized by a relatively high stiffness. The particle distribution curve of the material is shown in Figure.2. The soil specific density is 2.65. D_{10} and D_{60} are 0.01 mm and 0.33mm, respectively. Minimum and maximum void ratios are estimated as 0.56 and 1.14, respectively.

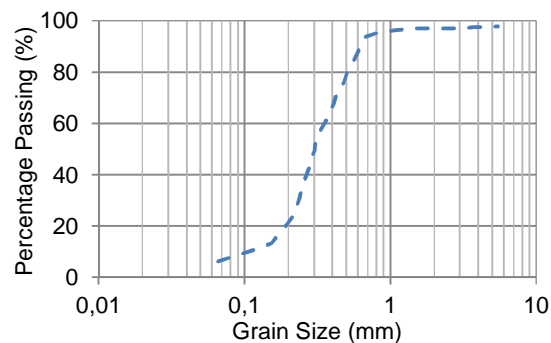


Figure 4-7 Particle size distribution curve for Eem/Kreftenheye sand [101]

The adopted data in this study are divided into four groups. I) Laboratory index tests carried on a sample extracted from borehole BH-WSF2-5. II) Three isotropic consolidated drained tests (CID) on the samples extracted from the same borehole, with different cell pressures, i.e. 80 kPa, 160 kPa and 320 kPa, and initial void ratios equal to 0.53, 0.55 and 0.54, respectively. III) A isotropic consolidated undrained test (CIU) with local strain measurement, characterized by a confining pressure of 80 kPa and an initial void ratio of 0.57. IV) Four stress-controlled cyclic triaxial tests (CTXL), with an initial confining pressure

of 80 kPa and different value of deviatoric stresses, i.e. 28 kPa, 30 kPa, 35 kPa and 48 kPa.

Based on this method, the hypoplastic model parameters are determined via three different method of experimental results interpretation. A direct method is used to determine the parameters which can be associated to a physical feature of the soil independent from the constitutive model. Curve fitting is used for two kinds of model parameters. The first group are parameters that are associated to model properties, rather than to soil physical features, and are defined only within the framework of a specific constitutive model. The second group are intrinsic soil parameters which are difficult to be determined directly from lab data. Both these groups of parameters are determined through inverse analysis methods and their optimal values are those that allow the best match between model response and experimental data. Finally, the surrogate curve method is used to further calibrate some of the model parameters not related to intrinsic soil characteristics. Yet, differently from the previous method, there is no unit set of parameters optimally reproducing the experimental response of the soil. The best parameter values are defined as those which fulfil the expectations of the user, not the real observed data. This concept will be further elaborated later.

The calibration procedure consists of 5 steps, in each step different types of lab test data are used to determine certain parameters. The overview of the process, including adopted data and calibrated parameters, is summarized in Table 4-4.

Table 4-4 Calibration stages along with adopted observations, variable parameter and method of parameters determination

Stage	Par.	Tests	data	Method
1	e_{i0} & e_{d0}	Index tests	γ_{\max} γ_{\min}	Direct
2	ϕ_c	CID	q-p'	Direct
3	$\alpha, \beta, n,$ h_s, e_{c0}	CID CIU	$q - \varepsilon_a$ $\varepsilon_v - \varepsilon_a$ $pwp - \varepsilon_a$	Curve fitting
4	$m_R, \beta_r,$ R_{max}, χ	CIU-AD	$E - \varepsilon_a$	Curve fitting
5	m_R & χ	CTLX	S-N	Surrogate curve

According to Table 4-4, the direct method is used for parameters e_{i0} , e_{d0} and ϕ_c . In particular, e_{i0} and e_{d0} assigned to the model are equal to the maximum and minimum void ratios obtained from the index test. The critical friction angle is also assigned looking at the slope of the critical state line in the q - p plane of the CID tests.

The rest of 5 main parameters are determined by curve fitting of and , for the three CID tests, as well as of and PWP- ε_a for the CIU test. This procedure is similar to that defined in Sec.4.1. At this stage of calibration, all of the intergranular parameters are set to zero. In the next step, the intergranular parameters m_R , β_r , R_{max} and χ are estimated based on the curve fitting of the stiffness degradation curve $E - \varepsilon_a$.

In the next stage parameters χ and m_R are re-estimated to improve the cyclic behaviour of the model. This stage adopts a surrogate curve concept. As it was explained before, the hypoplastic model is not able to predict the soil behaviour at low effective stress levels. Therefore, the reproduction of real experimental curves is an impossible task. The solution is to define other surrogate goals (experimental curves) that are compatible with the model capabilities.

4.2.2 Calibration and parameters estimation

4.2.3 Static triaxial tests

Sec.4.1 showed the performance of an inverse analysis method to determine the main parameters of the hypoplastic model using drained triaxial tests. As it was mentioned before, the values of parameters e_{i0} and e_{d0} correspond to the maximum and the minimum void ratios of the soil obtained by index tests, 0.59 and 1.14 respectively. Parameter ϕ_c is the slope of the critical state line in the q - p plane of the CID tests, herein obtained as 35.24° . The other 5 parameters of α , β , n , h_{s1} and e_{0c} are determined by inverse analysis of CID and CIU.

In order to perform inverse analysis on three CID tests and one CIU test, the defined error function is identical to the one explained in Sec.3.1.1. Two graphs of $q - \varepsilon_a$ and $\varepsilon_v - \varepsilon_a$, for each CID test, as well as $q - \varepsilon_a$ and $pwp - \varepsilon_a$ of the CIU test are fitted against experimental results simultaneously. The error of each curve is defined based on the

differences between observed and simulated values. These differences are normalized considering one percent of the maximum value of the curve. Finally, the objective function is obtained by summing all of the normalized weighted errors related to each curve.

The inverse analysis is performed considering the range of parameter values shown in Table 4-5. The table also reports the optimal values of the five considered parameters. The rest of the main parameters are assumed to be constant (as their deterministic values are already obtained). It should be underlined that all of the small strain parameters are assigned to zero at this stage.

Table 4-5 Considered range for main parameters and outcome of calibration in stage 3.

Parameter	Lower bound	Upper bound	Obtained value
hs	100	10 E+6	1.96E+6
n	0.01	1	0.27
α	0.1	0.5	0.17
β	0.1	3.0	2.5
e_{co}	0.59	1.14	0.69

The results of calibration of CID tests and CIU test are illustrated in Figure 4-8 and Figure 4-9. Adopting the estimated parameters leads to an appropriate agreement between simulation and experimental results. The stiffness degradation curve ($E - \varepsilon_a$, E being q/ε_a) obtained from CIU tests with local measurement is used to initially estimate the intergranular small strain parameters. The effect of each parameter on the stiffness reduction curve is explained in Sec.3.3.3.

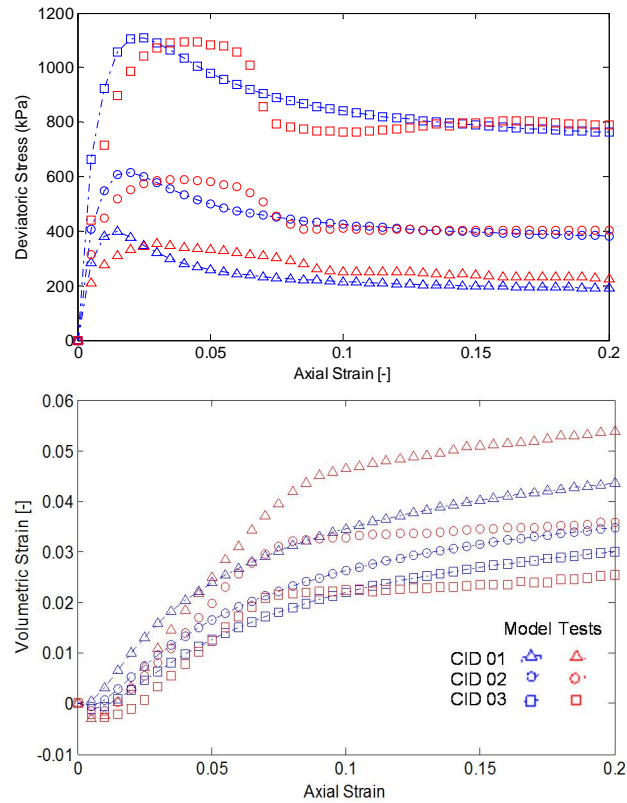


Figure 4-8 the outcome of 3rd step of for the three CID tests.

Parameters β_r and χ influence the transition part of the curve at small to medium strains. Parameter mR is a coefficient by which the initial small strain stiffness is calculated. Parameter mT is a challenging parameter to be estimated, since it has an effect only in the case of 90 degrees rotation of strain path, which does not occur in static and cyclic triaxial tests; therefore the calibration of this parameter is out of the scope of this thesis and its value is assumed to be equal to half of mR . Accordingly, with the same approach used for previous curve fitting, the $E - \varepsilon_a$ (Figure 4-10) is used as the objective curve of this step to calibrate the parameters m_R , β_r , R_{max} and χ . Since this stage of calibration only affects the small strain part of the model response, the previously predicted $q - \varepsilon_a$ and $\varepsilon_v - \varepsilon_a$, for the CID tests, and the $q - \varepsilon_a$ and $pwp - \varepsilon_a$, for

the CIU tests, still match the experimental results as before. The considered range of parameters and their optimal values are reported in Table 4-6 .

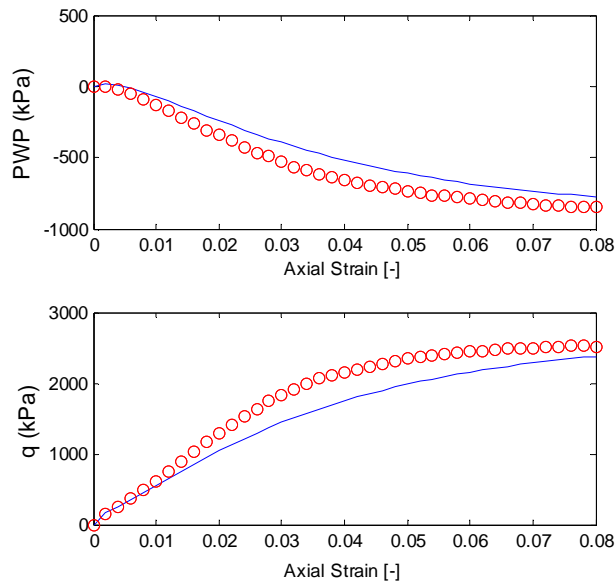


Figure 4-9 The outcome of 3rd step of calibration for the CIU test

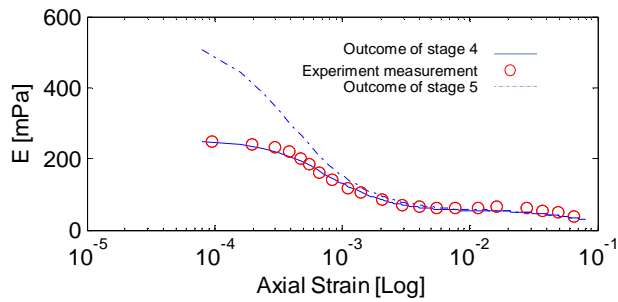


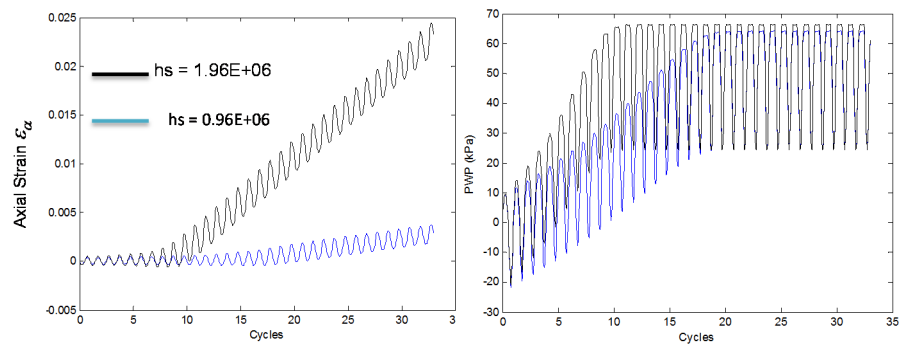
Figure 4-10 The outcome of 4th step of calibration in terms of one CIU test, Stiffness degradation curve

Table 4-6 Considered range for intergranular parameters and outcome of calibration in stage 4.

Parameter	Lower bound	Upper bound	Obtained value
χ	1	10	2.36
m_R	1	10	2.25
β_r	0.1	5	0.3
R_{max}	10e-05	5e-04	0.3

4.2.4 Parametric Analysis on the intergranular parameters

In order to have an insight on the effect and rules of parameters, a series of sensitivity analysis in terms of each individual IGS parameters was carried out. In this study, the obtained set of parameters through the previous stages (obtained value reported in Table 4-6 and Table 4-5) are considered as a base set of parameters and in each simulation on of parameters would be altered to gain the effect of individual parameters on the cyclic repose of a stress controlled cyclic triaxial with confining pressure of 80 kPa and different value of deviatoric stresses 48 kPa and void ration after consolidation equals to 0.56.

Figure 4-11 Effect of Parameter h_s on Cyclic mobility

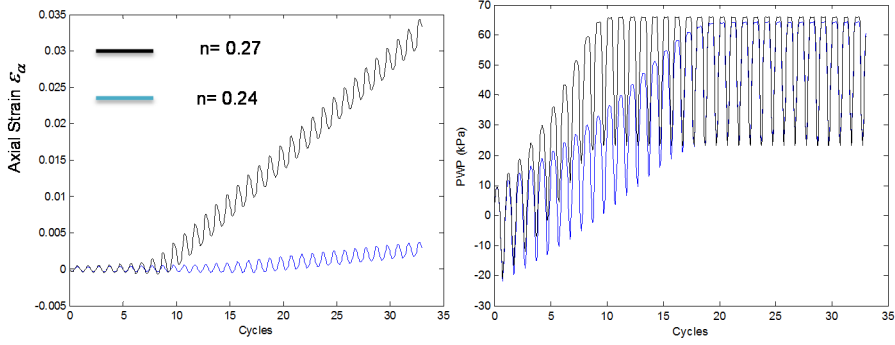


Figure 4-12 Effect of Parameter n on Cyclic mobility

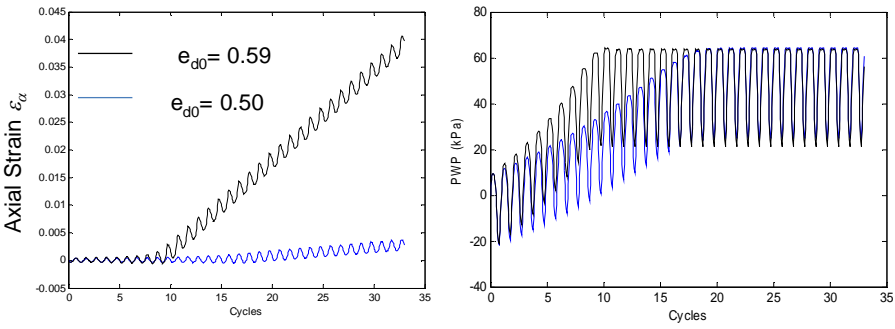


Figure 4-13 Effect of Parameter e_{d0} on Cyclic mobility

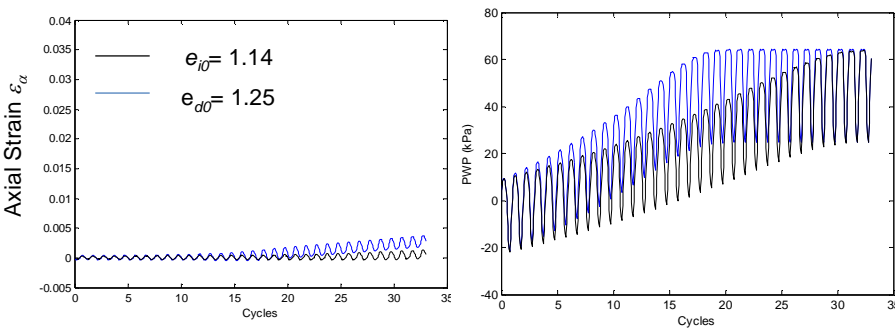


Figure 4-14 Effect of Parameter e_{i0} on Cyclic mobility

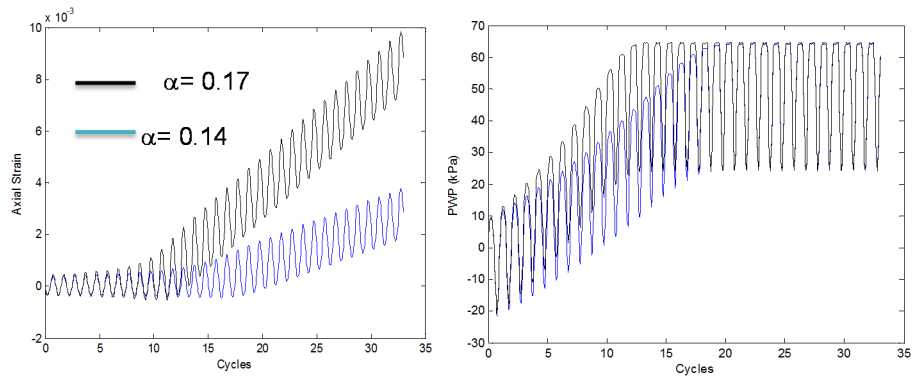


Figure 4-15 Effect of Parameter α on Cyclic mobility

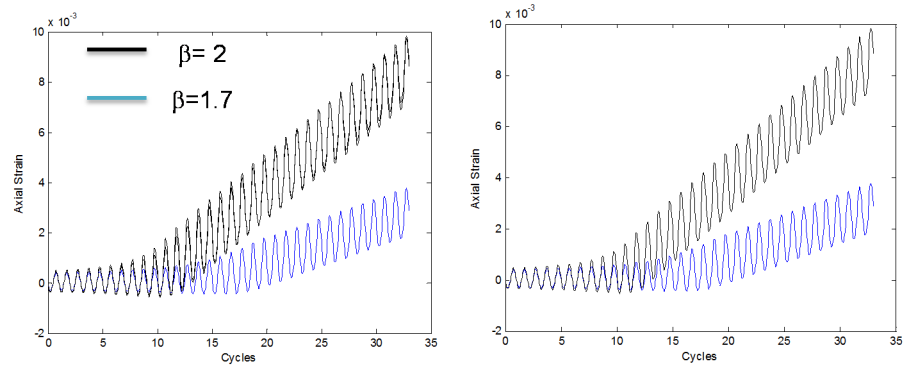


Figure 4-16 Effect of Parameter β on Cyclic mobility

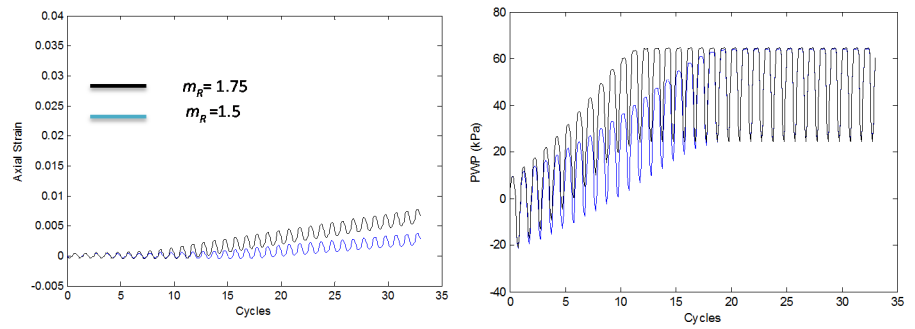


Figure 4-17 Effect of Parameter m_R on Cyclic mobility

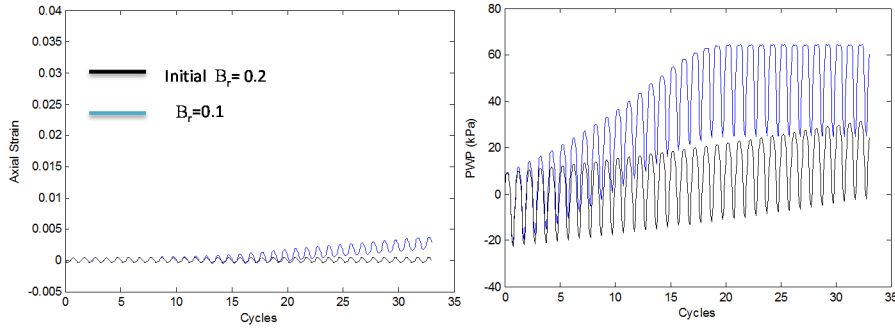


Figure 4-18 Effect of Parameter β_r on Cyclic mobility

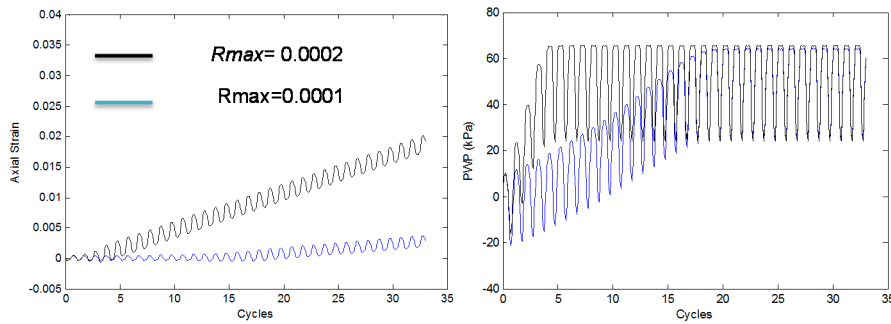


Figure 4-19 Effect of Parameter R_{max} on Cyclic mobility

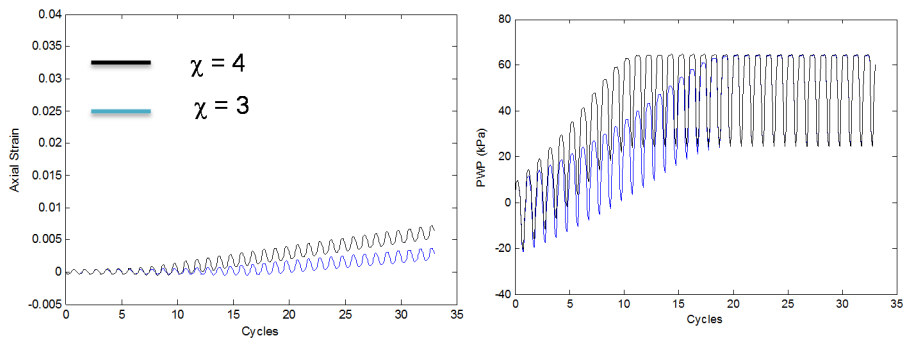


Figure 4-20 Effect of Parameter χ on Cyclic mobility

According to the Figure 4-11 to Figure 4-20, in all of the simulations the model problem mentioned in Sec.3.3.3.1 are exists .i.e, accumulation of axial strain in extension direction, and the pore water pressure is not able

to arrive to the value of initial effective confining pressure while the sample is instable. Considering those limitations, some indicators for evaluation of each parameters influence could be considered; a) number of Cyclic by which the sample would arrive to the maximum value of pore water pressure $N_{Cycle}^{Max-pwp}$, the value of maximum pore water pressure in $N_{Cycle}^{Max-pwp}$, the axial strain amplitude in that cycle and the maximum axial strain in that cycle.

The sensitivity those indicator to the hypoplastic parameters are summarized in the Table 4-7.

Table 4-7, qualitative sensitivity of the CTXL test to the hypoplastic model parameters

Parameter	strain range of Influence on Stiffness	Parameters Change	$N_{Cycle}^{Max-pwp}$	Maximum PWP value	Strain Amplitude	Maximum Strain
hs	Large & Small Strain	↓	↓	↑	↑	↑
n	Large & Small Strain	↓	↓	↑	↑	↑
e_{d0}	Large & Small Strain	↓	↓	↓	↑	↑
e_{j0}	Large & Small Strain	↓	↑	↓	↓	↓
α	Large & Small Strain	↓	↓	↑	↑	↑
β	Large & Small Strain	↓	↓	↑	↑	↑
m_R	Small Strain	↓	↓	↑	↑	↑
R_{max}	Small Strain	↓	↓	↑	↑	↑
β_f	Small Strain	↓	↑	↓	↓	↓
χ	Small Strain	↓	↓	↑	↑	↑

4.2.5 Calibration of hypoplastic parameters regarding model capacity

Generally, the liquefaction resistance of the soil could be assessed by the S-N cyclic resistance curve obtained from a series of cyclic undrained triaxial tests (CTXL) with various deviatoric stress ratios. In particular, q_{cv}/σ_r depicts the normalized cyclic deviatoric stress versus the number of cycles to failure. Based on the data adopted for this case study, failure is defined when one of the following conditions is fulfilled: I) the cyclic shear strain amplitude exceeds 3.75%; II) the excess pore water pressure exceeds 95% of the effective stress in the specimen at the start of

cycling; III) the applied cyclic shear stress drops to less than 90% of the specified value.

According to section 4.2.4, the model is not able to reproduce the experimental results when the sample is approaching low-stress levels. Thus, the defined failure criterion of experiments in terms of axial strain and pore water pressure will not happen in the model predictions. So, a new failure criterion should be defined which is compatible with the model capability. Based on this idea, the cycle in which numerical failure happens can be considered the observation to match, i.e. either the cycle at which there is a dramatic change in the trend of average axial strain or the cycle at which the pore water pressure arrives at its maximum value.

If the value of excess pore water pressure remains constant over 5 subsequent cycles, the simulation should be stopped and the failure cycle should be reported as the number of the first cycle of those 5 cycles. Considering the aforementioned definition, the normalized cyclic deviator stress versus the cycles to the numerical failure can be plotted. This curve, which can be named artificial S-N curve, represents a surrogate curve compatible with the model capability.

In the next step of model calibration (stage 5 of Table 4-4) the artificial S-N curve will be compared with the trend line of the S-N cyclic resistance curve derived from the experiments. As it can be seen, adopting the obtained parameters through the calibration of static tests creates an artificial S-N curve whose slope is far steeper than the slope of the real S-N cyclic resistance curve. Therefore, some of the parameters should be modified to improve the simulation results. To this aim, a series of sensitivity analysis on the intergranular parameters have been performed. As a result, it was understood that if the parameters m_R and χ are increased, to values equals to 5 and 3 respectively, the slope of the artificial S-N curve will be similar to the S-N cyclic resistance curve of the experiments (red line in the Figure 4-21).

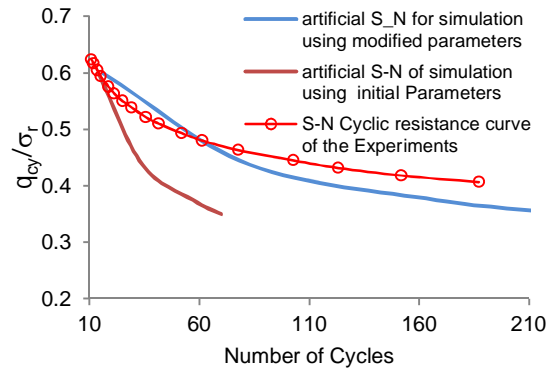


Figure 4-21 comparing S-N cyclic resistance curve of experiment with Artificial S-N resistance curve of simulation in terms of original and modified parameters set.

As it was expected, adopting the new parameters value of M_r and M_t doesn't match the stiffness reduction curve of CIU tests, in a way that the predicted initial stiffness is so far higher than experiments (dash line in Figure 4-22). This might be attributed to two main reasons: a shortcoming of the hypoplastic model; and a significant uncertainty in the small strain measurements of CIU experiments.

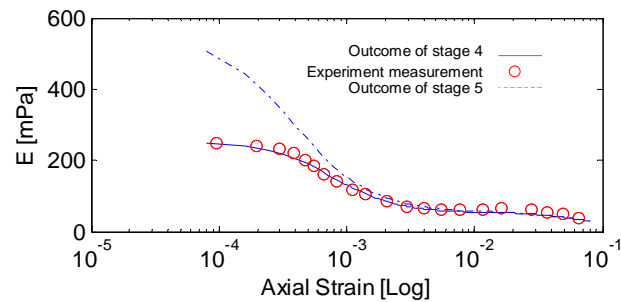


Figure 4-22 comparison of initial and modified intergranular parameters in reproducing the stiffness degradation curve

The final values of the parameters are reported in Table 4-8. Apart from the general output of the cyclic tests, i.e. S-N degradation curve, the outcome of calibrated model for two individual CTXL tests (CTXL5 and CTXL8 in the report of case study) is also shown in Figure 4-23 and

Figure 4-24. In this tests , the following is considered: for CTXL5: initial void ratio of the sample equal to 0.56, $\sigma_r=80kPa$ and $q_{cv}=48 kPa$ and as for CTXL8: void ratio of the sample equal to 0.55, $\sigma_r=80kPa$ and $q_{cv}=30 kPa$

Table 4-8 Final calibrated parameters of the hypoplastic model for Kreftenheye sand.

ϕ_c	e_{i0}	e_{d0}	e_{0c}	h_s	α	β
35.24	1.14	0.59	0.78	1.96E+06	0.17	2.5
n	χ	m_R	m_T	R_{max}	β_r	
0.27	3	5.22	$0.5m_R$	0.0001	0.3	

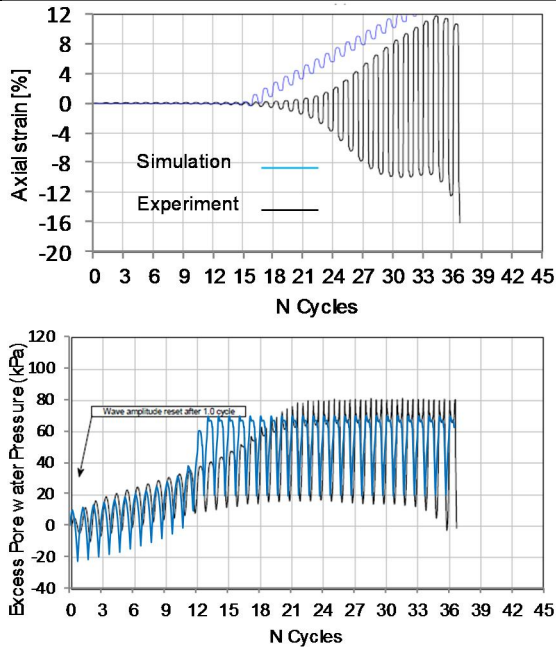


Figure 4-23 Simulation of CTXL5 using the calibrated parameters of the hypoplastic model

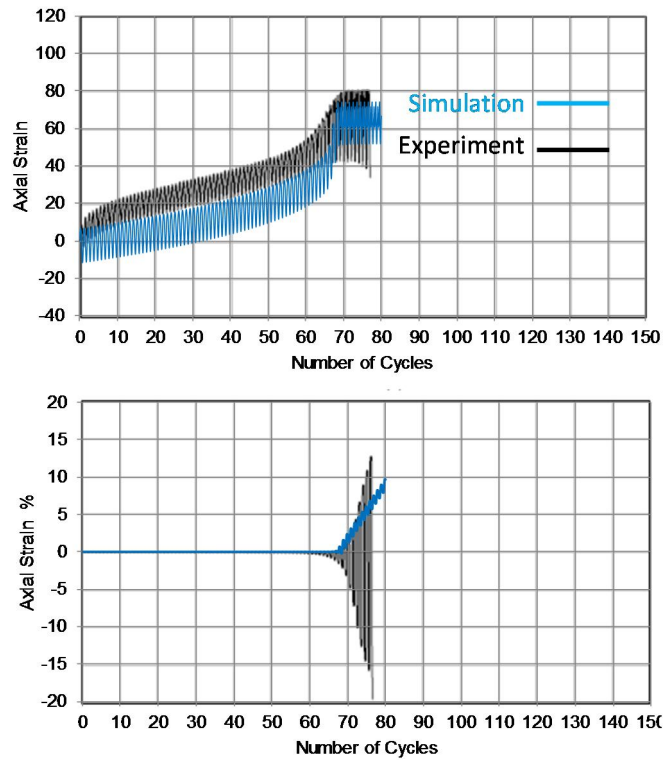


Figure 4-24 Simulation of CTXL8 using the calibrated parameters of the hypoplastic model

As it can be seen from the Figure 4-23 and Figure 4-24, the prediction of the axial strain is significantly different from the real experimental data. In terms of predicted excess pore water pressure, as it was expected, the maximum generated pore water pressure is less than the one of recorded in the experiment. On the other hand, in the CLTX5 the pore water pressure reaches its maximum value after 12 cycles, while in the tests 18 cycles are needed.

4.3 HYPOPLASTIC PARAMETER ESTIMATION FOR NORTH-WICH COAL (AUSTRALIA)

4.3.1 Soil Description and available data

This section referring to determination of hypoplastic model parameters for an organic soil material named as Northwich-coal, the experimental work of [102] and [32]. Laboratory (REV and flume) tests were performed on the Northwich coking coal, available from mines in the Bowen Basin area of northern Australia. The material ranged from fine sand and silt to gravel characterized by: a d_{10} (0.06-0.3 mm) of a similar magnitude of other materials involved in flowslides ([102]); and an extremely low specific gravity (1.34), close to the lower values typical for organic soils [103]. The maximum and minimum void ratios were equal to 0.21 and 1.23, respectively. Correspondingly, porosity ranged from 0.17 to 0.55 and the material is characterized by high values of both compressibility. Even the hydraulic conductivity is very high (0.01 m/s for loose state).

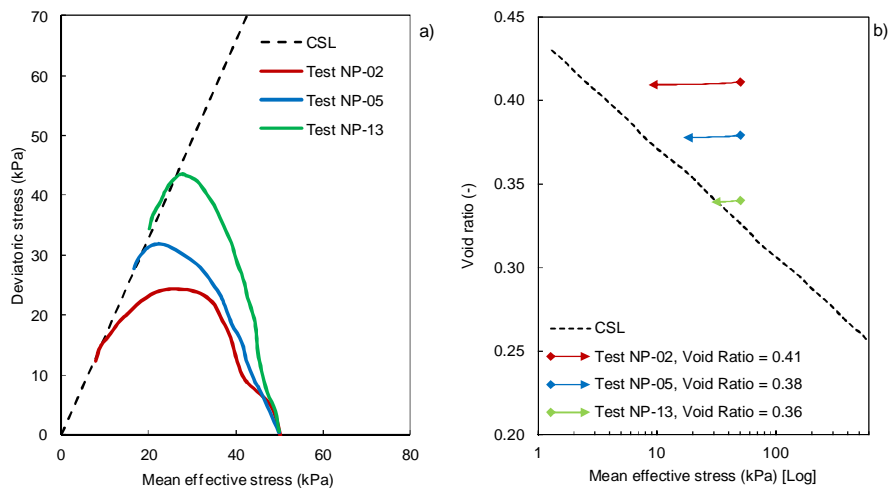


Figure 4-25 Results of strain-controlled CIU triaxial tests: a) effective stress paths, b) state diagram (data from Eckersley, 1990).

Figure 4-25 shows the results of CIU triaxial tests on specimens covering a range of initial void ratio (0.34-0.41) with an effective consolidation pressure of 50 kPa (Eckersley, 1990). The effective stress paths and the behaviour in the e - p' state diagram are very similar to those of sand with failure of loose specimens at 1-2% axial strain. The critical state friction angle (ϕ_c) was equal to 40° . Loose samples (Test NP-02 and Test NP-05) experienced: a strain softening that shifted the stress path towards the left (decreasing mean effective stress p') to the CSL; gradually decreasing stiffness due to contractive behaviour [32]; a drop in the deviatoric stress (q) after the initial peak. Such behaviour is similar to that observed for loose silty sand in undrained condition and at low confining pressure. It consists in large contractive tendencies, resulting in continuously increasing pore pressures. This stress path embodies what is generally called liquefaction [37]; [104], which is one of the principal mechanisms of flowslides [31].

4.3.2 Estimation of Hypoplastic model parameters

Six (out of eight) main model parameters could be obtained directly from available data, namely ϕ_c , h_s , n , e_{c0} , e_{i0} and e_{d0} . They were derived directly from the experimental results and prior information. Particularly, the value of the friction angle ($\phi_c = 40^\circ$), and the values of the maximum and minimum void ratios ($e_{i0}=0.21$, $e_{d0}=1.23$) were taken from Eckersley (1985, 1990). The parameters $h_s = 93$ kPa, $n=0.0785$ and $e_{c0}=0.93$ were obtained by fitting Eq.(3-93) to the CSL (Figure 4-25b) relatively low value of granular stiffness (h_s) for an organic soil like Northwich coal is justifiable. On other hand, adopting $e_{c0}=0.93$ gives the ratio of $e_{d0}/e_{c0} = 1.32$ which is comparable with that of 1.2 proposed by [105].

As it was mentioned in Sec.3.3.3.2 the intergranular parameters play roles in the simulation while using the explicit numerical scheme. Since the aim of this section is to determine the parameters of the material which are going to be employed for a boundary value problem modelling in Sec.6.2, the attention is paid here to the intergranular parameters as well.

As explained in Sec.3.3.3, the IGS leads to increase in stiffness upon unloading phase and helps to better simulation of the accumulated volumetric strain or excess pore water pressure under the real cyclic loading condition. But, in the case of the static loading condition in explicit scheme that cyclic loading is unreal and it is attributed to the

numerical noise, therefore, such a strain accumulation and built up pressure are unwanted and they lead to the early unreal failure in the system. A solution for the mentioned problem is to increase the elastic range of small strain stiffness, i.e. higher value of R_{max} , i.e. 0.0004, (the value of this parameter is 0.00001 in the case of cohesion less material, [90]. and also reduce the value of increased initial stiffness by adopting lower value of parameter m_R , $m_R < 3$ (this parameter is usually more than 5 for sands) as well as smoothing the transition part from small to large strain by adopting by considering $\chi = 1.0$. (this value is also used for sand in the literature [91]). In this case, all of small cyclic loading caused by noises in the system are covered by the elastic range of strain so that no unreal plastic strain is created in the model. Then, after the plastic tensor of the formulation is getting involved since the medium and large strain occurs. Since the higher value of R_{max} implies higher Plasticity Index, the suggested mitigation method could be interpreted like regular consideration of a small value of cohesion in the system in order to increase the numerical stability. Beside the numerical stability, this approach could be justified in geo-mechanical point of view as well. Because, the material used in this case study is a organic soil and, based on [106] and [107], which shows the very linear behaviour with negligible module redaction upon small shear strain.

Finally, only 5 parameters of α , β , β_r , m_R and m_T are still remained unknown for the material of case study for which it is expected that the results of triaxial tests would be sufficient to estimate them individually except parameter m_T which can be assumed as $0.5 m_R$ [89]. Therefore, their values were estimated by applying the inverse algorithm described in Sect. 2.4 considering the following assumptions: i) small strain stiffness is controlled by parameters m_R which $1 < m_R < 3$ to satisfy the conditions explained in previous paragraph; ii) m_T is derived parameters assuming it is equal to the maximum value between 1.0 and $0.5 m_R$. iii) based on [108], the parameter α is assumed between 0.1 and 1 and parameter β would be between 0 and 2. iv) The range of β_r is $0.1 < \beta_r < 0.3$, this range could form a quite flat shape for transition zone of the stiffness degradation curve.

Three undrained traxial tests with different initial void ratios, representing the contractive behaviour upon shearing, were taken into the account (Figure 4-25). The match between the soil response and the prediction of the hypoplastic model was analysed with reference to two

curves ($q - \varepsilon_a$) and ($p - \varepsilon_a$) for each test, ε_a being the axial strain. The observations for each curve varied from 14 points (test NP-05) to 18 points (test NP-02, test NP-13). Globally, 100 observations were used, each weighted considering a coefficient of variation equal to 0.05. The optimization was carried out through 80 iterations, not specifying a starting value of the parameters.

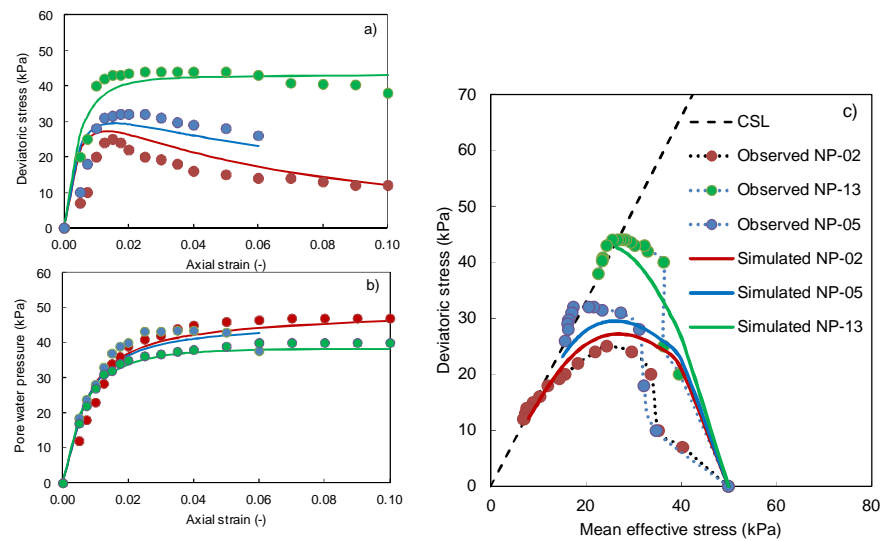


Figure 4-26, Simulations versus observations of CIU tests.

Figure 4-26 shows the satisfactory matching between the experimental data and the results of the constitutive model achieved with the optimised estimates of the soil parameters. Not only the ($q - \varepsilon_a$) and ($p - \varepsilon_a$) curves used in the objective function (Figure 4-26 a-b) but also the effective stress paths were accurately reproduced (Figure 4-26c). The final estimated parameters values are reported in Table 4-9.

Table 4-9, Estimated values of the parameters for the hypoplastic constitutive model.

ϕ_c (°)	h_s (kPa)	n	e_{c0}	e_{i0}	e_{d0}	α	β
40	93.27	0.076	0.93	1.23	0.21	0.34	1.05
m_R	m_T	R	β_r	x			
2.23	1.11	0.0004	0.12	1.0			

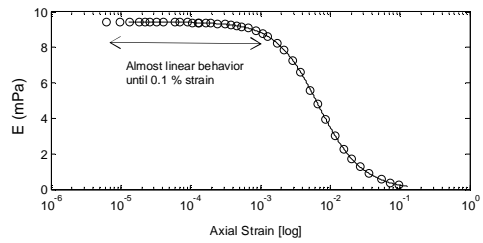
4.3.2.1 Performance of the assumed parameters value for Intergranular Strain (ISG) Parameters

As it was mentioned Sec.4.3.2, some ISG parameters of the HP model are specified before the optimization procedure and they assumed constant during the curve fitting. The main tuition of all assumption for ISG was the numerical stability upon the unwanted cyclic loading caused by numerical noises in MPM formulation. In order to check the performance of the obtained ISG parameter, two other REV simulations were fulfilled as follow. 1) Test NP-05 with focus on the small strain response while the confining 2)A Cyclic stress controlled undrained triaxial test with initial confining pressure 5 kPa (Close to the stress level of Slope) and deviatoric stress ratio $q/p' = 0.1$.i.e. $q=0.5$ kPa. Such this loading condition are similar to the oscillations occurred in MPM simulation

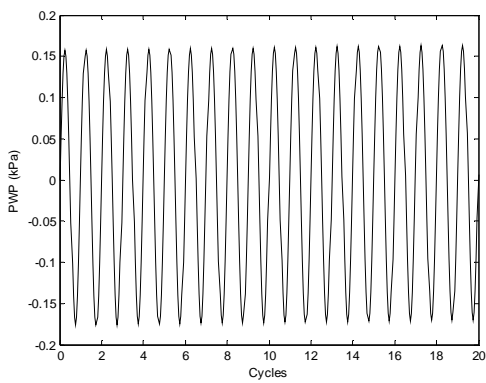
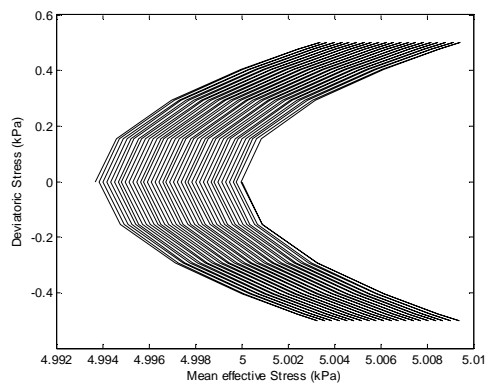
The results of these two REV simulations are shown in Figure 4-27. As it can be seen the obtained stiffness degradation are similar to those of other organic soil described by ([106]).

Figure 4-27.b also shows that, the material are stable under the low deviatoric ratio cyclic loading in a way that no significant change in mean effective stress and pore pressure could be observed over the cycles. And this is exactly what was the main aim of the used assumptions for ISG parameters selection.

4. MODELLING OF LABORATORY TESTS



(a)



(b)

Figure 4-27, Performance of adopted ISG parameters a) simulation of stiffness degradation curve for Test NP-2 . b) Simulation of Cyclic triaxial test with low deviatoric stress ratio ($q/p' = 0.1$)

4.4 CONCLUSIONS

In this chapter the parameters of hypoplastic model have been estimated using the proposed framework for three different cohesion-less materials. First of all, compatibility of the proposed methodology was examined by estimating the Baskarp sand model parameters and comparing the outcome with those parameters value obtained through the classical method of parameters determination. It was shown that, the proposed curve fitting algorithm was able to determine a set of parameters by which the simulated soil behaviour was closer to the experimental result than the response computed using parameters values reported in the literature. Secondly, it was showed the importance of the right selection of the type of tests used to provide the observations for the inverse analysis algorithm. The obtained set of calibrated parameters significantly depends on the observations used to calibrate them. For example, it appears that conducting the inverse analysis employing triaxial tests conducted on specimens subjected to higher confining pressures more likely leads to a correct estimate of the parameters. However, it should also be stated that a set of parameters providing good predictions of triaxial tests does not necessarily allow simulating oedometer tests properly. It entails that combinations of different types of laboratory tests should be used for a general calibration of constitutive model along different stress paths. In that case study no attention paid to the intergranular parameters of the model and cyclic responses.

In the next chapter of this study, the proposed methodology applied on a very challenging sandy formation in Northern Sea (Kreftenheye sand) characterised by high stiffness. In this chapter different types of laboratory tests results consists of monotonic drained and undrained triaxial tests, cyclic Undrained triaxial tests were employed in a stepwise procedure. a 5-step procedure has been introduced in order to determine all of the hypoplastic model parameters including the small strain ones. In each step of the procedure, the most relevant observations for the estimation of a certain group of parameters were used. The shortcoming of the hypoplastic model in the prediction of each adopted experimental curve was highlighted. As it was shown, the model suffers from the wrong prediction of material behavior at low stress levels, close to instability points, and for the post-failure behavior during cyclic tests. In order to calibrate the cyclic triaxial tests, the S-N curve was employed. Regarding the shortcoming of the hypoplastic model in the proper

prediction of cyclic mobility and axial strain, a new failure criterion in order to identify the numerical instability was proposed, based on a new type of curve named artificial S-N. The slope of this curve can be compared with the one obtained by experimental data and, by matching the slopes of these two curves, the most relevant model parameters which represent liquefaction resistance of the soil can be obtained.

In the last section of this chapter, the obtained experiences from the study on the two sandy formation was applied to determine the parameters of hypoplastic model for an organic origin cohesion-less material, Northwich coal, in this case a limited lab data for the material were available. Therefore, the calibration procedure had to be adjusted with respect to the available data. The main parameters of the hypoplastic model were obtained using three undrained triaxial tests and the obtained critical state line. The intergranular parameters are assumed for this material based on two hypotheses: 1) the general small strain behaviour of the organic organic materials which involves high linear elastic range 2) the compatibility of the parameters to overcome the numerical difficulties when the model is used in explicit material point method formulation, i.e. the parameters value are assumed in a way that the noises caused by numerical integration did not affect the constitutive relation under static load condition.

The parameters value for all three materials in this chapter would be employed to material point method of some boundary value problem in chapter 4 and 5.

5 INVERSE ANALYSIS APPLIED TO CONE PENETRATION TEST MODELLING

In this chapter the calibration of MPM models of cone penetration tests (CPT) is addressed. Simulation of quasi-static cone penetration tests is known as a very complicated boundary value problem since many numerical aspects are involved in the solution of the model. Yet, this problem allows to thoroughly check the response of a given constitutive model because many different stress and strain states of the material (e.g., compression, tension, small strain and shear strength, critical state conditions) are explored in different areas of the domain. In this chapter, different case studies of CPT tests using various constitutive models, ranging from a simple Mohr-Coulomb law to an advanced hypoplastic behaviour, are discussed. Different numerical factors that influence the results, such as the integration method and the mesh size, are also investigated. The MPM forward model is incorporated in the inverse analysis procedure explained in chapter 2 to create an algorithm that allows the calibration of constitutive model parameters by back analysing CPT data. The issues tackled to develop a robust, accurate and stable forward model are also discussed. The case studies presented in this chapter, along with the employed constitutive models and the adopted integration methods, are summarized in Table 5-1.

Table 5-1 Summary of studies for CPT modelling

No.	Constitutive model	CPT data	Material	Integration method
1	Mohr-Coulomb	a) Synthetic Data b) Chamber Test ([109])	a) Loose sand b) Dense Sand	MPM-MIXED
2	Hardening soil model	Chambe Test ([109])	#2Q-ROK sand	MPM-MIXED MPM-MP +GP
3	Hypoplastic model	Centrifuge chamber tests ([110]) Real field CPT data ([101])	Baskarp Sand Torgen sand (Northen sea)	MPM-MIXED MPM-MP+ GP

5.1 DATA

5.1.1 Chamber tests in loose, dense and layered soil (Tehrani et al 2017)

Tehrani (2017) carried out a valuable series of chamber tests on loose, dense and layered sandy samples. In this study, 4 of those tests are addressed. The tests are listed in Table 5-2

Table 5-2, the chamber tests on the #2Q-ROK ([109]).

Test name	Soil Profile	Layer Thickness (mm)	Relative density D_R
T1a-LOD	Loose over dense	390/610	45/85
T5-L	Loose	1,000	45
T7-D	Dense	1,000	85

In these experiments a half-circular steel chamber with three observation windows in the front polymethylmethacry wall. The diameter of the chamber is 1,680 mm while the model cone penetrometer has a diameter d_c equal to 31.75 mm, a ratio of D_c/d_c greater than 50 leads to the minimum effect of the boundary of the tests. The samples are prepared through the pluviation technics. a surcharge of 50 kPa were also applied on the top of the samples by a specially designed air-rubber balder.

In this research, coarse-grained silica sand #2Q-ROK was the main test sand. The sand is commercially available from US Silica Company in large quantities. The sand is quarried from the Oriskany sandstone deposits at Berkeley Springs, West Virginia. It has angular particles and is composed mainly of quartz (98.0%) with traces of calcite; these characteristics make it slightly more susceptible to particle crushing than other silica sands. The maximum and minimum densities of the sands were determined based on ASTM D4254 and ASTM D4253. They are 0.66 and 0.99 respectively. D_{50} of the soil in estimated as 0.78 mm ([111]).

[111] estimated the peak and critical-state friction angles of #2Q-ROK sand from direct shear tests conducted in a 60mm square shear box.

Two series of test were performed, one in loose sand (with density of $32\pm 3\%$) and the other in dense sand (with density of $78\pm 3\%$). The tests were conducted with normal stress ranging from 60 to 442 kPa. The estimated peak friction angle (ϕ_p) under these testing conditions is 40.3 degrees and the critical-state friction angle (ϕ_c) is 32.3 degrees. The test results are shown in Figure 5.3.

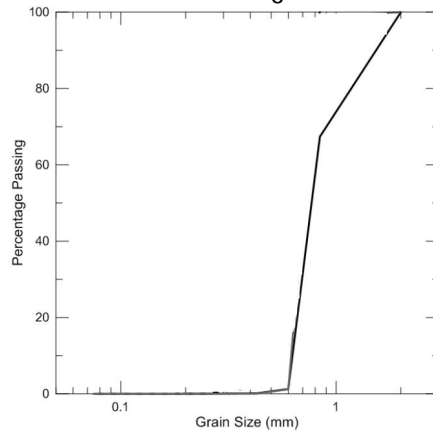


Figure 5-1, Grain size distribution of the # 2Q-ROK sand

5. INVERSE ANALYSIS ON THE CONE PENETRATION TESTS
MODELLING

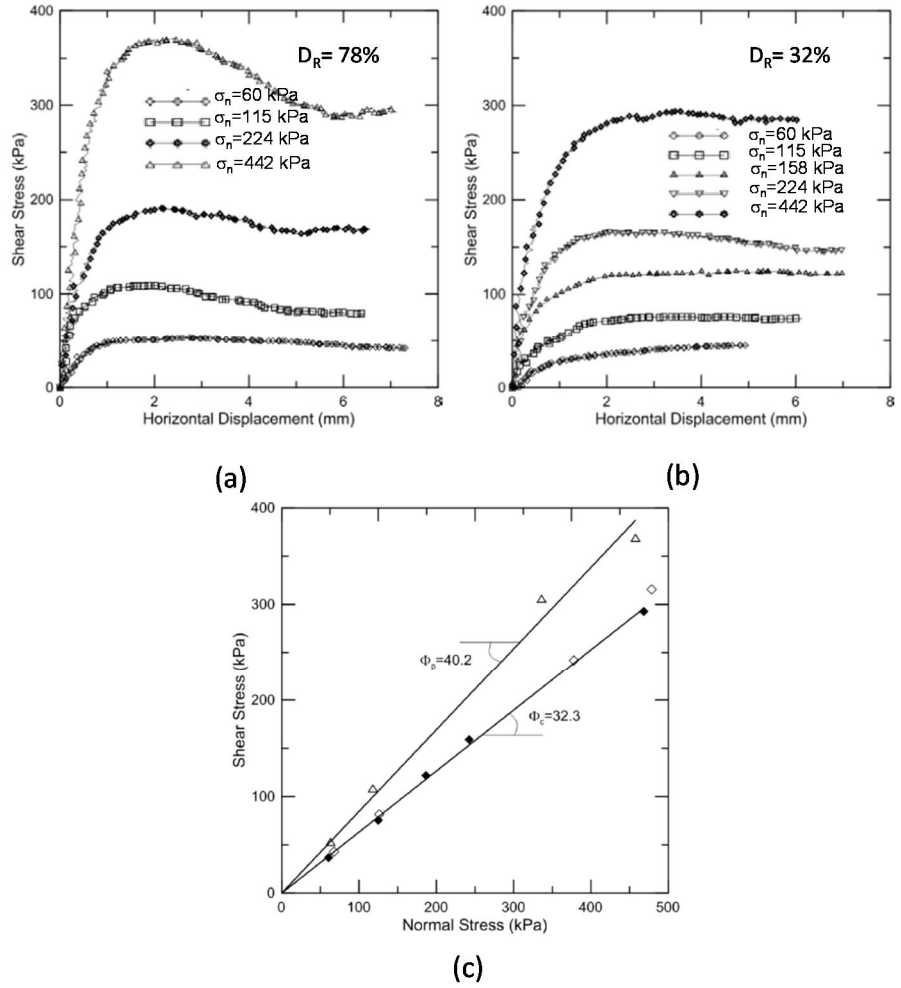


Figure 5-2, Direct shear test results on #2Q-ROK sand ([111])

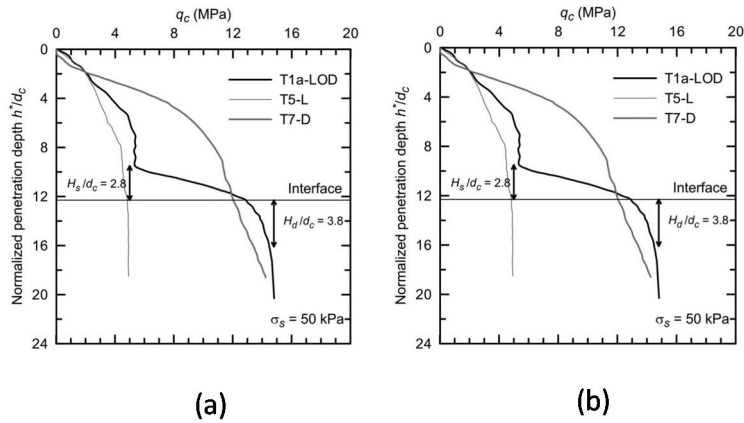


Figure 5-3 Outcome of chamber test experiments ([109])

5.1.2 Centrifuge test experiment of jacked pile installation (Stoevelaar 2011)

The test was conducted in the Deltares geotechnical unit. Figure 5-4 shows the properties of the experiment. The diameter of the chamber is 60 cm and the sample height is 40 cm. The cone tip had a length of 300 mm with a diameter 11.3 mm. The pile is pushed to the soil monotonically with the constant velocity of 0.02m/s while the gravity acceleration of 80g was applied. The soil material used in the tests is the Baskarp sand introduced in Sec.4.1. The preparation of this soil was done by using wet sand raining to make a loose sample. Next, the required density is achieved by a controlled drop of the model container ([112]). The experiment with relative densities of 38% is addressed in this thesis (Test 5 in [110]). In the selected test no grain crushing was observed. The tip resistance at 12D depth of the penetration is recorded as 0.47 MPa while the ultimate cone resistance at 24D is recorded as 0.81 MPa.

5. INVERSE ANALYSIS ON THE CONE PENETRATION TESTS MODELLING

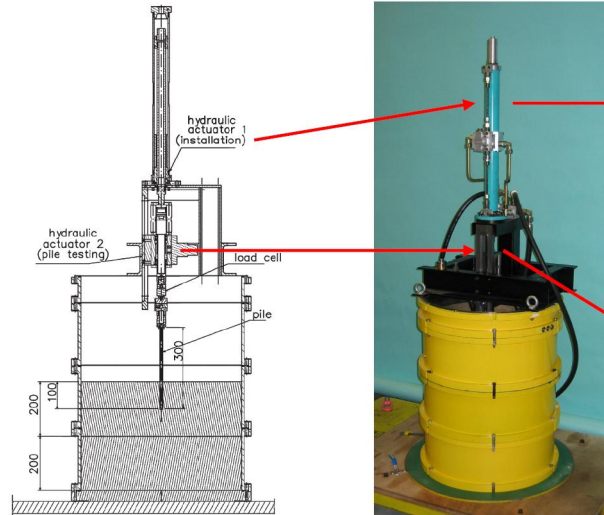


Figure 5-4, Centrifuge chamber for pile installation experiment

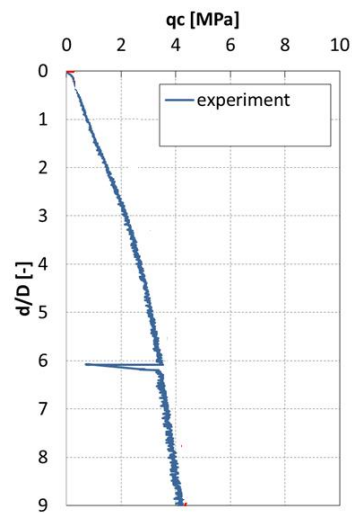


Figure 5-5 Experiment output for Jacked pile installation ([110])

5.1.3 Offshore CPT field data (Fugro 2015)

The data used in this study come from a confidential database from Fugro related to the Brussels Wind farm II Project ([113]). The data refer to a offshore sandy formation, known as Tongeren sand, and in particular to a CPT carried out 10 m below the seabed (Figure 5-6).

Results from three isotropically-consolidated drained triaxial tests are shown in Figure 5-7, conducted on samples collected 21 m below the seabed in a nearby borehole. The index tests results indicate that the minimum and maximum void ratios of the soil are equal to 0.35 and 1.37, respectively. The void ratio of the material on site, obtained in the laboratory on a sample extracted from the borehole in which the CPT was conducted, is 0.62. Figure 5-6 shows that the CPT tip resistance reaches a steady state condition after about 40 cm of cone penetration. Triaxial tests have also been used to determine the initial values of the soil model parameters (Table 5-3). The outcome of these triaxial tests are shown in Figure 5-7.

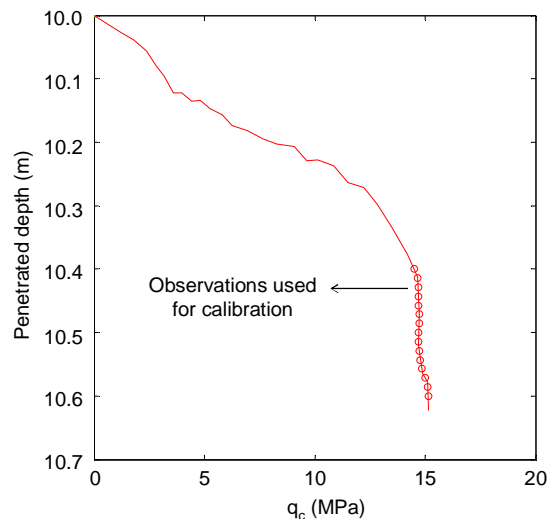


Figure 5-6 CPT results and observations used to calibrate the soil model

Table 5-3 Triaxial tests on samples extracted from borehole BH-WFS2-5.

Test number	Initial void ratio	Confining pressure (kPa)
1	0.57	190
2	0.52	380
3	0.49	760

5. INVERSE ANALYSIS ON THE CONE PENETRATION TESTS MODELLING

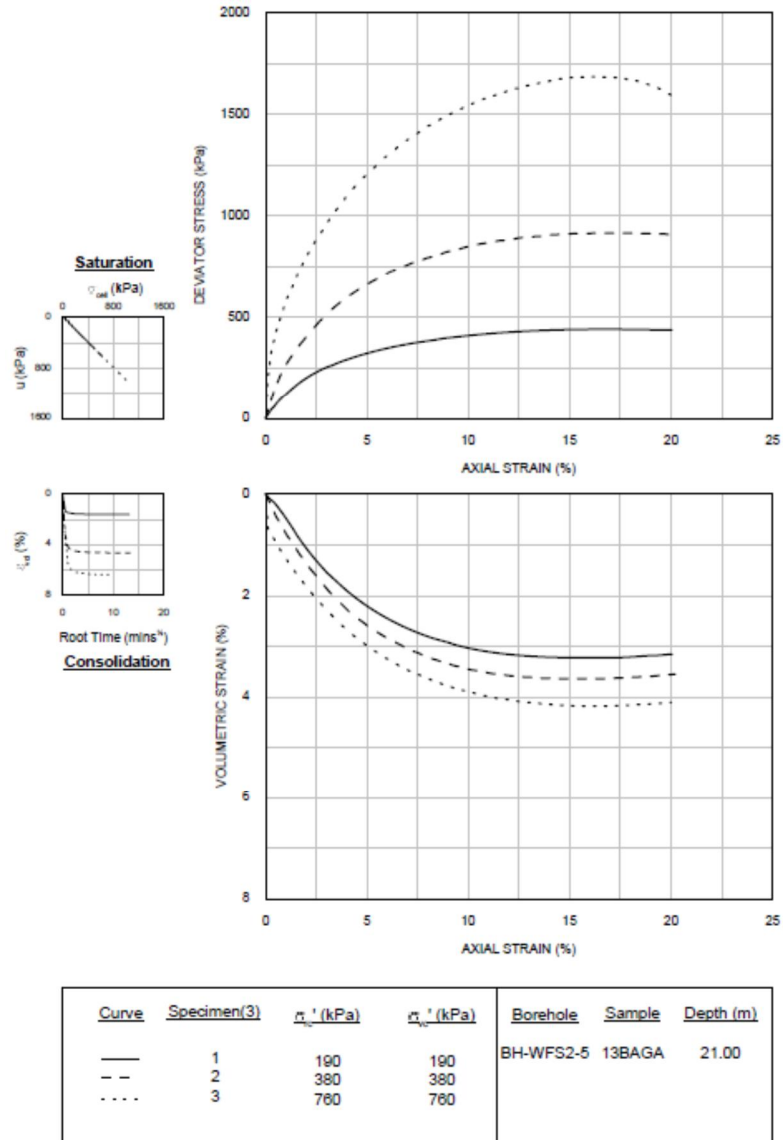


Figure 5-7, Triaxial tests on samples extracted from borehole BH-WFS2-5 ([101]).

5.2 SIMULATION OF CPT USING MOHR-COULOMB CONSTITUTIVE MODEL

In this section, the MPM simulation of the cone penetration tests adopting a simple Mohr-Coulomb constitutive model is addressed. At the beginning, sensitivity analyses on the model parameters are carried out to evaluate the effect of each parameter on the numerical results. In the next stage, the capability of the inverse analysis algorithm introduced in chapter 2 in the back analysis of the tip resistance is checked. To this aim, a synthetic case study has been set up, using the model results of a "base" simulation as observations and, in particular, the cone resistance values computed at 24 different depths. The results of the performed sensitivity, parametric and inverse analyses highlights few important aspects related to the use of optimization algorithms to calibrate the input parameters of MPM models of CPTs. Finally, the simulation of a series of well documented chamber tests conducted by ([109]) is addressed and the optimal parameters for modelling of CPT chamber tests on loose, dense and layered sandy soil is discussed.

5.2.1 Sensitivity analysis on Mohr-Coulomb parameters

The MPM schematization adopted to implement the CPT boundary value problem is shown in Figure 5-8. The finite mesh has a total of 3992 elements including the initially inactive elements. The inactive elements above the soil surface may be activated during the calculation process if material points move into the empty space they occupy. Triangular elements with a linear interpolation of the displacements are used. The number of material points is 13,810.

5. INVERSE ANALYSIS ON THE CONE PENETRATION TESTS MODELLING

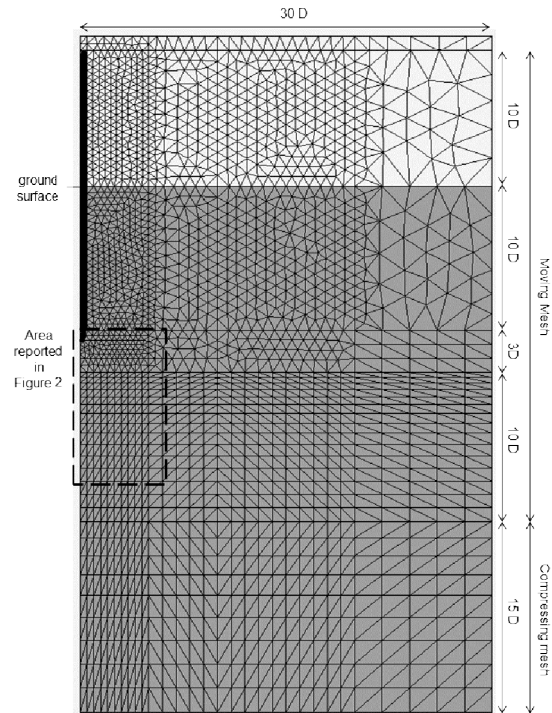


Figure 5-8, Scheme of the MPM model of CPT.

The numerical simulations are performed using an axisymmetric geometry. To avoid boundary effects, the side boundary is placed at a distance of $30 D$ from the symmetry line (D being the diameter of the cone). This space is divided in three parts with mesh sizes getting larger and the number of particles per elements decreasing as the distance from the symmetry line increases. Displacements at the side boundary are constrained in the radial direction and free in the vertical direction. The bottom boundary is fully fixed. The stresses in the soil are initialized using a typical K_0 -procedure and a surcharge of 10 kPa is applied at the ground surface, equivalent to a 1 m thick soil layer above that surface. The cone penetrometer "pile" is modelled as a rigid body penetrating into the soil. The pile, which is initially embedded below the soil surface for a length equal to $10 D$, is pushed into the soil for an additional $7 D$. The penetration of the pile into the soil is modelled by applying a prescribed velocity, herein equal to 0.02 m/s , a value common in standard practice. The MPM moving mesh concept is adopted in all

simulations ([28]). This technic would help to fix the contact surfaces on some specific nodes; therefore, the contact node detection algorithm which is used in regular MPM contact formulation ([114]) is not needed. However, more advanced method based on penalty function in order to cope with the detection problem has recently been developed [115], but it is out of the scope of this thesis. The cone is slightly curved at the transition from shaft to conical to avoid numerical difficulties due to locking. The simulations are performed considering a submerged one-phase material in drained conditions.

The values of the soil parameters assumed for the base case ("Base") are considered representative of the behaviour of loose well-graded sands. A contact algorithm is used to model the frictional contact between the pile and the soil. The adopted friction angle value (11°), is representative of a sand to polished steel contact ([116]). Considering the above conditions, the time needed to run one model simulation is equal to 20'.

Table 5-4 Input parameter values of the parametric analysis

ID	E	ν	c	ϕ	ψ	n
Base	6000	0.2	1	30	0	0.2
SET1	4000	0.2	1	30	0	0.2
SET2	8000	0.2	1	30	0	0.2
SET3	6000	0.15	1	30	0	0.2
SET4	6000	0.25	1	30	0	0.2
SET5	6000	0.2	2	30	0	0.2
SET6	6000	0.2	5	30	0	0.2
SET7	6000	0.2	1	27	0	0.2
SET8	6000	0.2	1	33	0	0.2
SET9	6000	0.2	1	30	-1	0.2
SET10	6000	0.2	1	30	1	0.2
SET11	6000	0.2	1	30	0	0.15
SET12	6000	0.2	1	30	0	0.25

Figure 5-9 shows the deviatoric strain and the deviatoric stress at penetration depths equal to two and six times the cone diameter, for the portion of mesh highlighted in Figure 5-8. The cone is pushed to its final depth from an initial position below the ground surface. This was done

5. INVERSE ANALYSIS ON THE CONE PENETRATION TESTS MODELLING

for two main reasons: to avoid numerical instabilities related to the presence of significant strains at low stress levels; to reduce the computational time, given that multiple iterations of the model are needed for the inverse analysis.

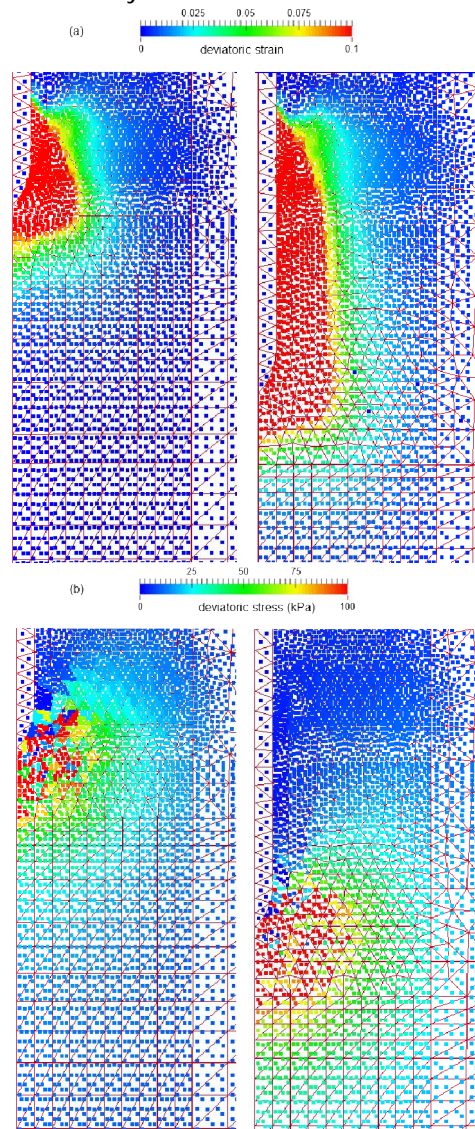


Figure 5-9, Results of the MPM model at penetration depths 2D and 6D: a) deviatoric strain; b) deviatoric stress

At the beginning of the simulation the soil mainly deforms from the initial position of the cone to about 2 to 3 D below and around the tip of the cone. As expected, no noticeable deformations are observed in the rest of the domain, including in the material particles along the CPT shaft above the initial position of the cone. The inner portion of this volume, extending for about 1 D below the tip and about 2 D laterally, exhibits deformations of the order of 10%. At the end of the simulation it is very clear that the soil deformations follow downward, as expected, the cone displacements. The highest deformations influenced a volume of soil extending from the initial position of the cone to about 2 to 3 D below its final position. The values of the deviatoric stress are less homogeneous around the cone, yet the size of the soil volume influenced by significant stresses extends laterally and downwards in a similar way at both penetration depths. These values are consistent with data reported in the literature (e.g. [117]).

The values of the cone tip pressure are plotted in Figure 5-10 as a function of the cone penetrometer depth (see "Base" simulation). As expected the cone resistance monotonically increases with depth with a trend asymptotically reaching, after a penetration depth of about 4 to 6 diameters, an almost constant value. The final value of the ratio between the resistance force and the cone area is equal to about 700 kPa, which can be associated to the average cone resistance within the soil layer extending from the initial position of the cone to about 2 D below the cone tip. Therefore, as already mentioned, the model only allows to retrieve a single force representative of the average cone resistance in a layer of soil about 10 D thick. This value is comparable to the values reported by [118] for the sand with a similar stress state.

A parametric analysis is carried out to evaluate the sensitivity of the cone resistance profile to changes in the values of the model input parameters. Table 5-4 shows the values of the parameters adopted. Besides the base case, 12 simulations were conducted by de-creasing and increasing, one at the time, the values of the six input parameters keeping the rest of them constant. The minimum and maximum parameter values were defined considering reasonable ranges around the base case for the considered soil type. The results of the 13 numerical simulations are plotted in Figure 5-10 in a graph showing the modelled cone resistance versus the ratio between the penetration depth and the cone diameter. All the simulations produce a cone resistance pressure non-linearly in-creasing with depth and reach a maximum value of cone

5. INVERSE ANALYSIS ON THE CONE PENETRATION TESTS MODELLING

resistance before the final penetration depth. This behaviour confirms that the depth reached by the numerical model is adequate. Only four simulations (sets 1, 2, 7 and 8) significantly differ from the base case, while the rest produce similar cone resistance results at all depths. This in turn means that the model results are mainly sensitive to only two input parameters, i.e. E (sets 1 and 2) and ϕ (sets 7 and 8).

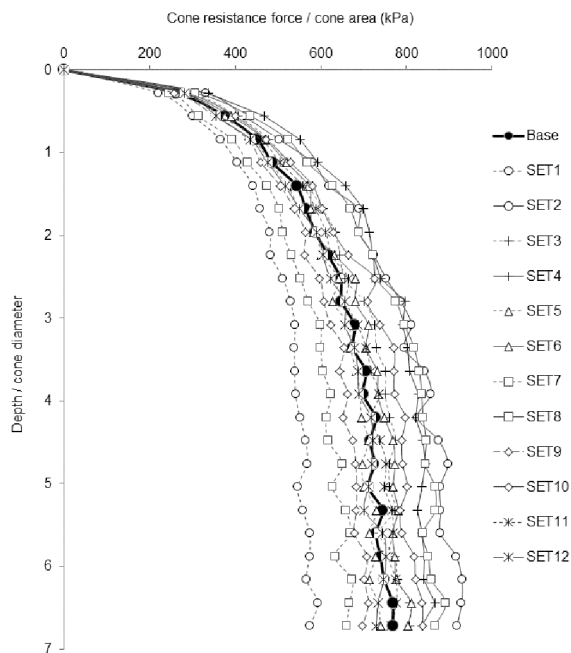


Figure 5-10, Results of the parametric analysis: cone resistance pressure vs. dimensionless depth.

In the next stage, the inverse analysis algorithm described in Sec.2.1.2.1 is used to calibrate the input parameters of the constitutive law adopted in the MPM model of the CPT. It's worth noting that the parameter optimization requires multiple runs of the MPM code, i.e. a number of iterations for the convergence of the regression analysis.

The results of the parametric analysis indicate that the two input parameters mostly affecting the MPM model results are E and ϕ . The inverse analysis is thus carried out to evaluate the capability of a gradient-based optimization algorithm to estimate the optimal value of these two input parameters, given a set of observations coming from the

results of a CPT. To this aim, a synthetic case study has been set up, using the model results of the “base” simulation as observations and, in particular, the cone resistance values computed at 24 different depths (Figure 5-14).

Table 5-5 shows the main statistical indicators resulting from a set of eight sensitivity analyses performed for different initial values of the two input parameters. The soil stiffness (E), and the friction angle (ϕ), are respectively ranging from 4000 kPa to 8000 kPa and from 27° to 33°. The values of the composite scale sensitivities (css), indicate that the model results are sensitive to both parameters for all the considered values. The values of the correlation coefficients, ranging from 0.92 to 0.96 for six of the eight considered cases, indicate that the two parameters are, in most cases, very highly correlated. The latter indicates that it is unlikely that they can be estimated simultaneously within a single regression analysis. Considering the previous results, the first two regression analyses only consider one parameter at the time (Figure 4). Two initial values are considered for each one of the parameters. In both cases and for both parameters, the regression converges to the optimal “true” values using a small number of iterations, from 2 to 4. The capability of the optimization algorithm to find the global minimum of the error function is thus proved, irrespective of the initial values assumed for the parameter being calibrated.

Table 5-5, Main statistical indicators of the sensitivity analysis

E	ϕ	css(E)	css(E)	correlation coefficient
(kPa)	(°)			
4000	27	4.32	9.91	0.78
4000	33	7.09	12.32	0.92
5000	28.5	5.72	13.09	0.94
5000	31.5	7.4	14.49	0.96
7000	28.5	6.02	18.44	0.92
7000	31.5	8.04	19.67	0.92
8000	27	6.64	18.81	0.95
8000	33	11.62	25.3	0.75

5. INVERSE ANALYSIS ON THE CONE PENETRATION TESTS MODELLING

The results are different, as expected, when both the input parameters are calibrated simultaneously. Two initial set of values are herein considered, respectively assuming the two parameter values are either both higher than the optimal ones ("upper bound" simulation) or both lower than the optimal ones ("lower bound" simulation). It's worth noting that the two sets are the only ones for which the sensitivity analysis did not yield correlation coefficients between E and ϕ higher than 0.9. The results are presented by showing the values of the parameters (Figure 5-12) and the related error functions (Figure 5-13) at each iteration of the regression analysis until the final convergence of the optimization algorithm. In the lower bound simulation the optimization ends when the error function assumes almost negligible values, i.e. the solution converges towards a global minimum representing the true solution of the case study. On the contrary, in the upper bound simulation the optimization algorithm finds a solution that represents a local minimum of the error function with values of the two input parameters very different from the optimal values of the case study. Despite that, also in this case the error function decreases significantly during the optimization and reaches a minimum value of 2.65 after only two iterations, 1.00 being the value of the error function consistent with the accuracy of the information conveyed by the observations. The latter can be visually confirmed by looking at the cone resistance profile with depth (Figure 5-14), which is much better than the initial one and not too different from the base case. In this case, the optimization got "trapped" in a local minimum of the error function possibly because the two parameters, moderately correlated when the regression started, became highly correlated after one iteration (being E close to 8000 kPa and ϕ close to 27°) and the gradient-based methods do not perform satisfactorily in calibrating multiple parameters when this happens.

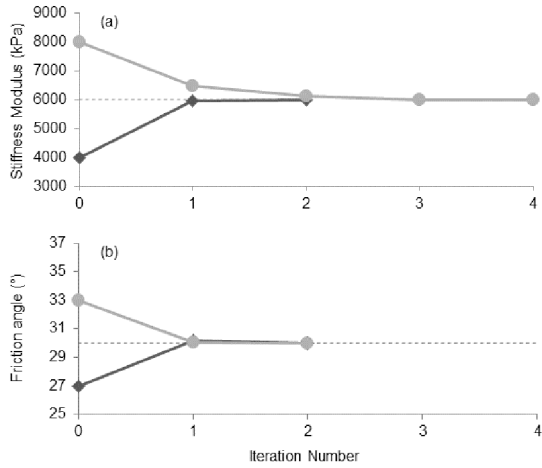


Figure 5-11, Parameter values during the regression analysis when it is conducted to calibrate on one parameter at the time: a) soil stiffness, E ; b) friction angle, ϕ .

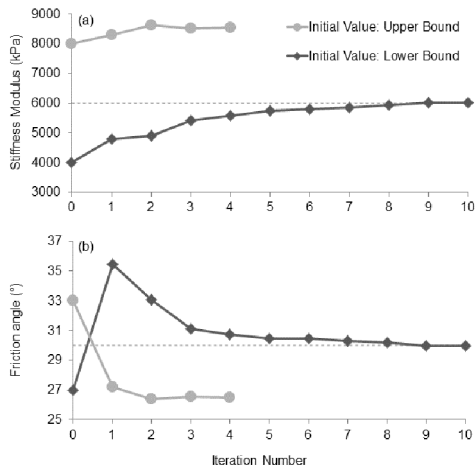


Figure 5-12, Parameter values during the regression analysis when it is conducted to calibrate both parameters simultaneously: a) soil stiffness, E ; b) friction angle, ϕ .

5. INVERSE ANALYSIS ON THE CONE PENETRATION TESTS MODELLING

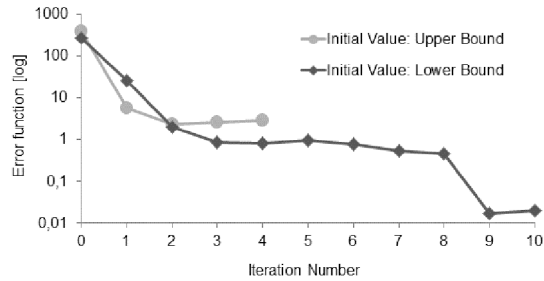


Figure 5-13, Error function during the regression analysis when it is conducted to calibrate parameters E and ϕ simultaneously.

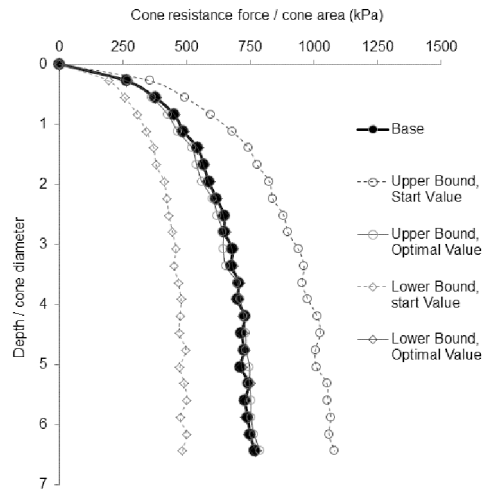


Figure 5-14, Cone resistance profile with depth for the initial and optimal values of the input parameters in the regression analysis conducted to calibrate parameters E and ϕ simultaneously.

5.2.2 Calibration of chamber CPT experiments (Tehrani et al 2017)

The aim of this section is to simulate and replicate the outcome of the chamber tests conducted on two homogenous samples (T1L and T2D) and on a layered sample (TLOD). As discussed in the previous sections, parameters E and ϕ have the major influence on calculated tip resistance. On the other hand it was shown that the calibration of the

model in terms of both parameters simultaneously is unlikely to converge to the unique set of values because of their high correlation coefficient. Therefore, in order to calibrate the camber tests data, it is better to assume some parameters constant and calibrate the other parameters. Accordingly, different group of inverse analysis vary in assumed fixed and variable parameters and in order to obtain the optimal parameters of the model could be performed. In this case, ϕ is assigned to the model equal to those obtained through direct shear testing, i.e. 32° and 40° for loose and dense samples, respectively.

Before starting to calibrate the constitutive model parameters, a mesh sensitivity analysis has been carried out to have an insight on the accuracy and robustness of the model.

Similar to the previous section, an axisymmetric MPM model with MIXED integration is used. At first, the Mohr-Coulomb constitutive model is adopted and the sensitivity analysis in terms of mesh size is carried out. Two discretising meshes (fine and coarse mesh) are employed Figure 5-15. Their properties are reported in Table 5-6. In the table, the dimensions are normalized to the cone diameter. The cluster particle initialization technics is used to have identical discretization in terms of material particles. The domain is divided in 5 parts, the highest number of particle is adopted in the cluster close to the cone (axis of symmetry) and their numbers are reducing by the distance from the axis of symmetry. The sensitivity analysis in terms of mesh size is carried out while the adopted parameters for soil models are the following: $\phi=40^\circ$, $\nu=0.3$, $\psi=5$, $E=35000$ kPa. Computational times for 2 cm penetration of the cone are 15 and 35 min, respectively for fine and coarse meshes.

Table 5-6 Size of elements in discretization mesh used in the MPM Mohr-Coulomb of the CPT

No.	Name	#N elements of cone	Compressing Mesh blow TIP (A)+		Shaft (B)		Compressing Mesh far from TIP (C)		Non active (D)	
			H	W	H	W	H	W	H	W
1	fine	10	1.13	0.12	0.12	0.33	1.13	0.70	1.18	0.70
2	Coarse	3	1.13	0.33	0.54	0.25	1.17	1.13	1.17	1.13

+ . Each zone are depicted in Figure 5-15
H. Height of the elements normalized to the cone diameter (dc)
w. width of elements normalized to the cone diameter (dc)

5. INVERSE ANALYSIS ON THE CONE PENETRATION TESTS MODELLING

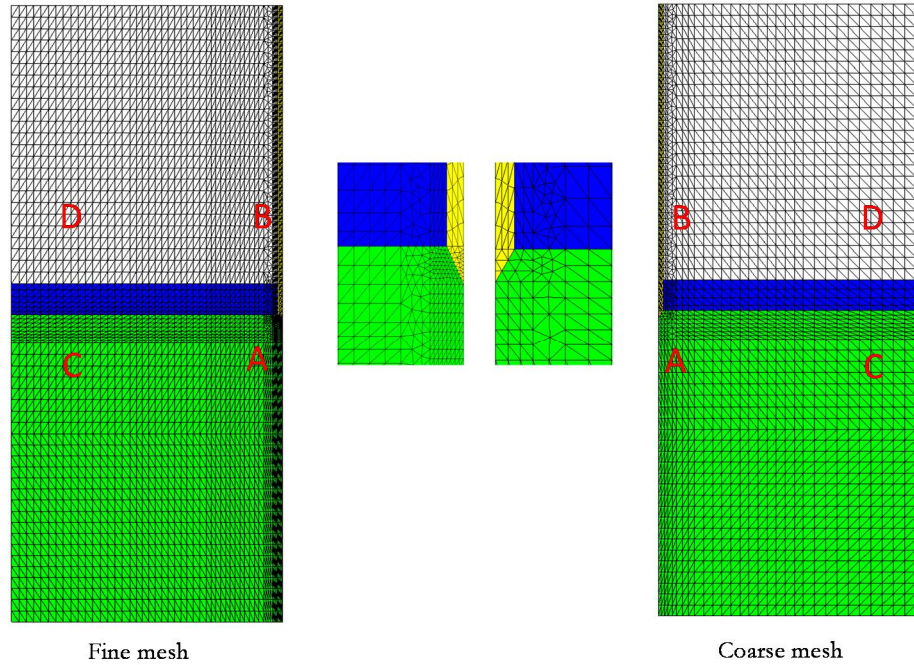


Figure 5-15 Discretization mesh used in the MPM model of the CPT

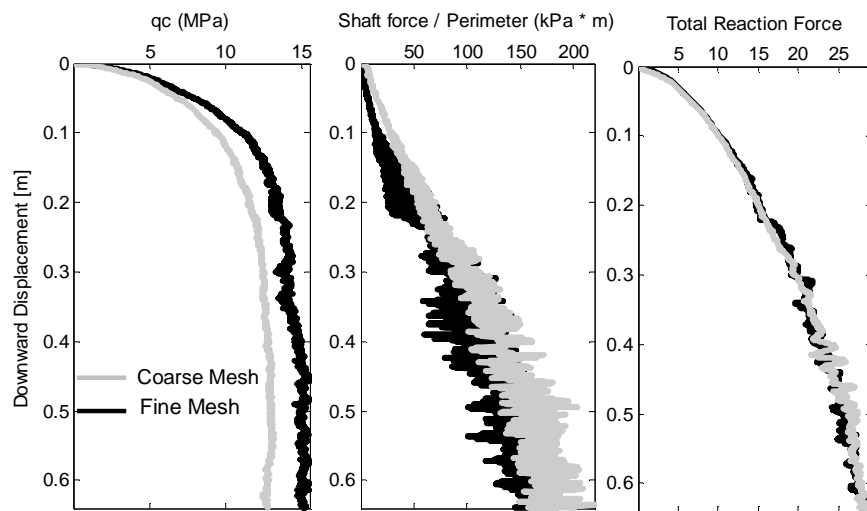


Figure 5-16 Effect of the mesh size on the model output

Figure 5-16, shows the comparison of outcomes of the model, in terms of course and fine mesh sizes, for the predicted tip resistance, shaft resistance and total force resistance (TIP + shaft). It can be observed that the model outcome is insensitive to the mesh size. The slight differences in the results are not related to the mechanical computations of the models but to an available accuracy in the algorithms which recorded the tip and shaft resistance. Indeed, the summation of them (total force) are identical in both schemes, thus implying a robustness of the model regarding the mesh size. Therefore, the coarse mesh could be used for the further simulations because of its lower required computational time.

In order to simulate test on the loose sample T1, the friction angle equal to the critical friction angle, 32° , has been used. The dilation angle of the soil is considered as zero. Stress in the model is initialized via k_0 procedure, assuming the $K_0=0.5$. The 50kPa top surcharge is modelled by putting a thin elastic layer (10 cm) at the top of the soil having the porosity of 0.5 and G_s equals to 100000, in this way the weight of this layer imposes 50 kPa to the bottom layer and therefore the stress level is identical to the one in the experiments. The young module E is initially assumed as 27000 kPa, considering E_{50} from the direct shear tests results, and the Poisson ratio ν is 0.3.

Figure 5-17 shows the tip resistance of the model for test T1a. There is a good agreement between experimental and numerical results. However, the resistance at the beginning of penetration, up to depth of 10 cm, is over estimated by the model. The reason of this mismatch is further discussed later in this thesis.

5. INVERSE ANALYSIS ON THE CONE PENETRATION TESTS MODELLING

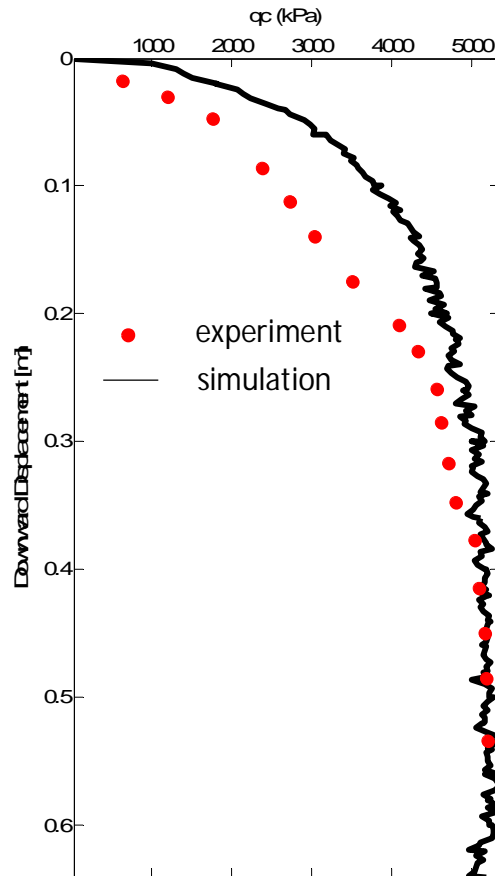


Figure 5-17, simulation of CPT on the loose sample

In the next step, the test on the homogenous dense sample is simulated. According to Bolton (1996) dilation of the dense sample is unavoidable, therefore, differently from the previous case, herein parameter ψ is unlikely to be equal to zero. To calibrate the experiment T2D, an inverse analysis similar to the previous case has been carried out in which the goal parameters are young module E and the dilation angle ψ . The soil friction angle is considered fixed and equal to the one of direct shear tests, i.e. 40° . The rest of the parameters are also fixed and similar to the loose sample model. Starting value of E is 45000 kPa equal to the E_{50} obtained from direct shear test. The starting value for ψ is assumed as 8° , equal to the difference between peak and critical friction angles

obtained from direct shear tests. The adopted observations are 18 points extracted from the q_c curve; a unit value of the weight is used for all the observations.

The inverse analysis algorithm converged after 6 iterations satisfying the second convergence criterion, i.e. changes in error function are less than 5 percent in the three subsequent iterations. The parameters adopted in each iteration are reported in Table 5-7. The optimization algorithm reduced both of the parameters and the optimal value of $E=40000$ kPa and $\psi=1$. Obtained low value for dilation angle could be attributed to the wrong prediction of dilation of the soil at large strains by the Mohr-Coulomb model, as it was discussed in Chapter 2 of this study. Soil volume at large strains is zero (Critical state condition), yet, the Mohr-Coulomb model is not able to reproduce the critical state condition. When a high value is assigned to the dilation angle of the soil, the volume of the material is always increasing over shearing and this leads to significant mismatches with real soil behaviour at large strains which are happening around the cone (Figure 5-19). The soil around the cone is experiencing the deviatoric strain of more than 400%. Based on the literature, in the reality, after 50% of deviatoric strain the volume changes reach to the zero ([119]). This feature is missing in a standard Mohr-Colomb constitutive model and this causes the overestimation of the volumetric strains and dilation of the soil at large strains (Figure 5-19a). The effect of the dilation angle can also be shown by comparing the area of the zone around the cone in which the particles show more than 2 mm radial displacement, herein called disturbed zone (Figure 5-19b). It can be observed that the disturbed zone in terms of $\psi=1$ is much bigger than the one with lower dilation angle.

The results of each analysis (q_c) is shown in Figure 5-18. It can be seen that, the starting parameters value leads to very high cone resistance with respect to the reality. Also, none of the simulations predicted the earlier stage of penetration properly so that the trend of the q_c curve is totally higher than the real one. Another shortcoming of the simulation is that, in all the cases, the tip resistance remains relatively constant after reaching the steady state (depth of 25 cm), while the real q_c is always slightly increasing over the depth of penetration. This mismatch is related to the fact that Mohr-Coulomb is an independent stress model,

5. INVERSE ANALYSIS ON THE CONE PENETRATION TESTS
MODELLING

and thus it cannot incorporate increment of material stiffness due to the increase of stress over depth.

Table 5-7 Values of the calibrated parameters at each iteration of the regression.

Set of parameters	E (mPa)	ψ
Starting value	45000	10
Iteration 1	45000	5
Iteration 2	35000	5
Iteration 3	45000	1
Iteration 4	35000	2
Iteration 5	35000	1
Iteration 6	40000	1

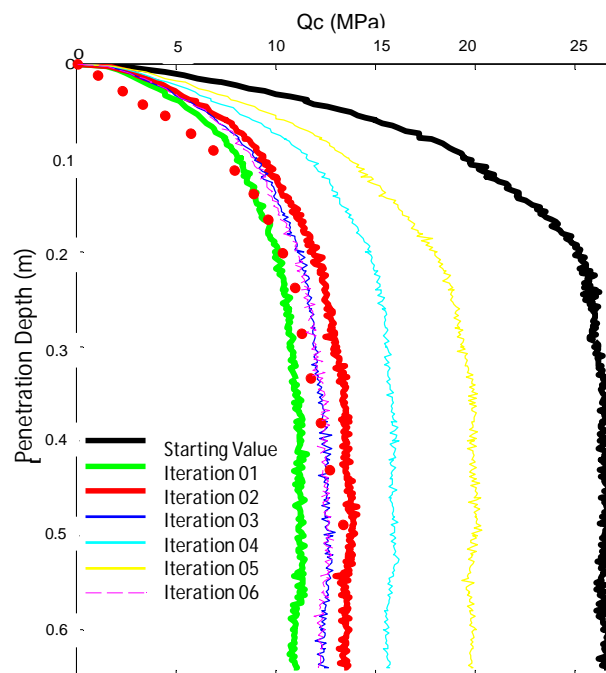


Figure 5-18, Simulated tip resistance over the iterations

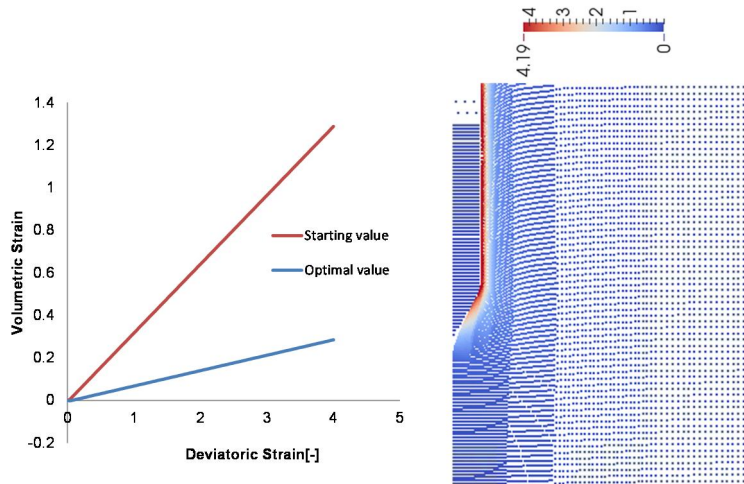


Figure 5-19, a) relation between volumetric strain and deviatoric strain in the case of two sets of parameters b) deviatoric strain around the cone and shaft after 20 cm of penetration.

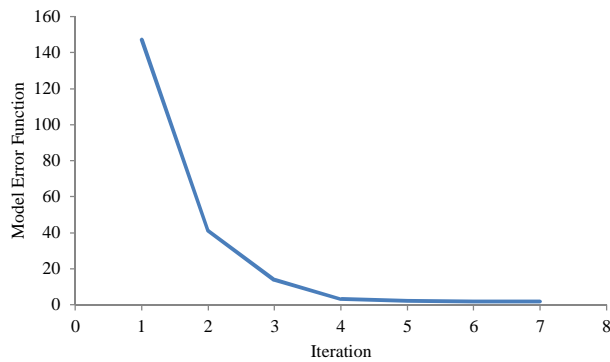


Figure 5-20, Model error function over the iterations.

5. INVERSE ANALYSIS ON THE CONE PENETRATION TESTS MODELLING

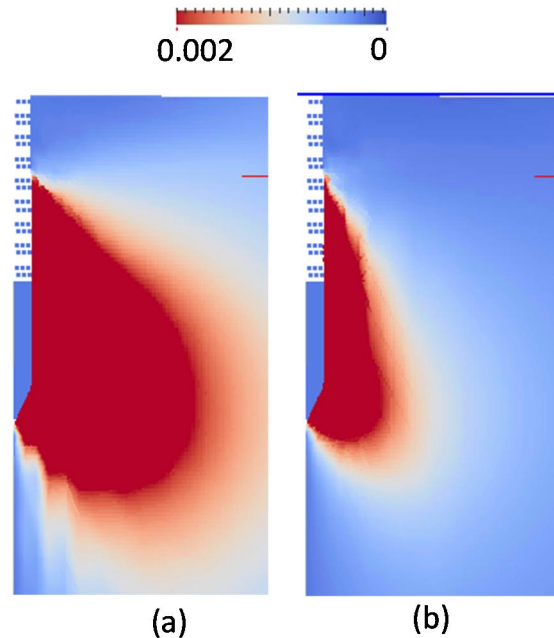


Figure 5-21, Horizontal displacement of particle at the depth of 20 cm. a) starting value b) optimal model

In the next stage the simulation on layered sample, T1LOD of [109] is carried out. The model is shown in Figure 5-22. The soil model parameters of each layer are assigned equal to the corresponding optimal ones. Therefore, the Young modules of the loose layer $E_L = 27000$ kPa and the dense layer $E_D = 40000$ kPa are initially assigned equal to the value determined through the calibration of homogenous samples. The simulation shows that the cone resistance is underestimated in the dense layer and in the transition part from loose to dense layer. In order to improve the simulations, an inverse analysis to recalibrate the Young module E_D has been carried out. The optimal parameter value is $E_D = 50000$ kPa. The outcome of this calibration is also shown in Figure 5-23. The predicted final cone resistance for both layers are in good agreement with experimental results. Although the transition part in dense layer is now well fitted, the cone resistance of the loose part is slightly over estimated.

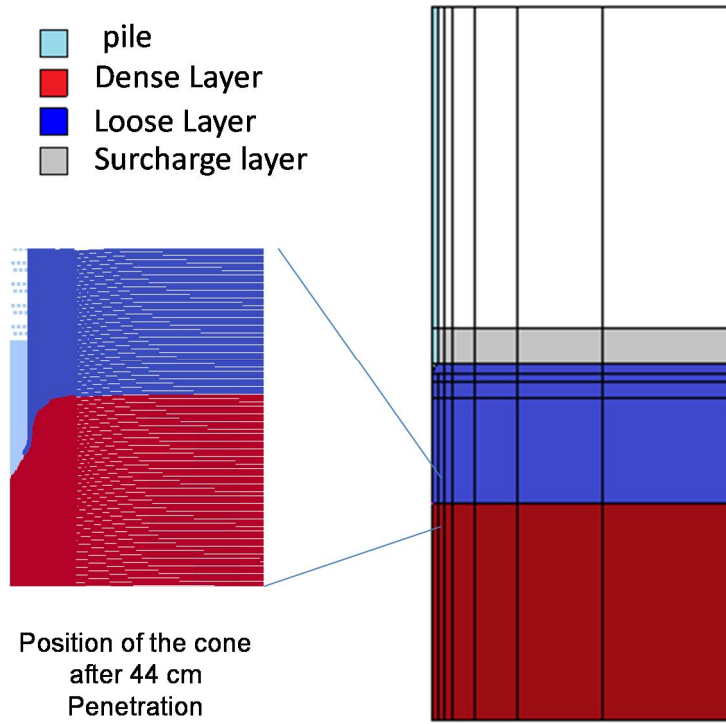


Figure 5-22, Model for simulation of CPT in layered soil, loose over dense layer

5. INVERSE ANALYSIS ON THE CONE PENETRATION TESTS MODELLING

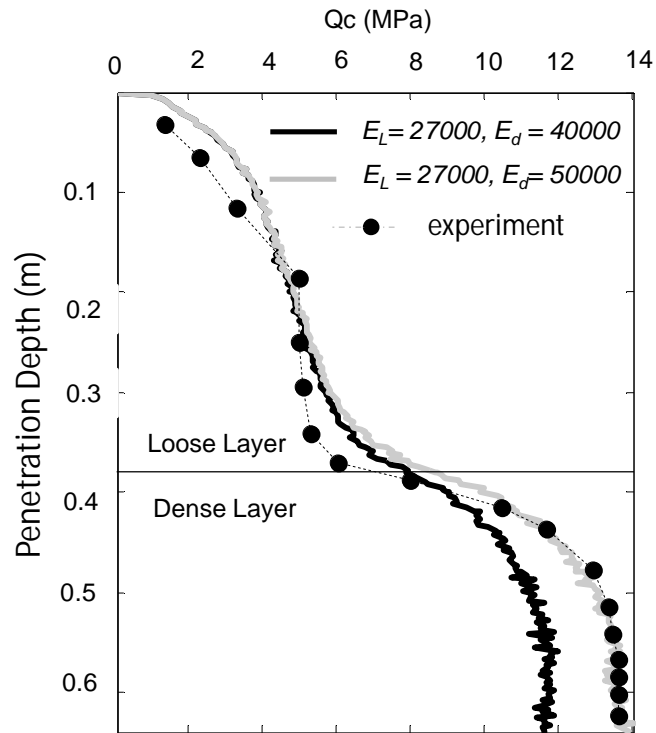


Figure 5-23, Simulation of the CPT on the layered sample, T1LOD, loose over dense

5.3 SIMULATION OF CPT USING HARDENING SOIL MODEL

As it was shown in the previous section, MPM model of cone penetration tests using a Mohr-Coulomb constitutive model was not able to reproduce the increase of cone resistance with respect to the stress increment. The main reason is the fact that the stiffness of the material does not vary with the stress level. To cope with this challenge, the Hardening soil model explained in Sec.3.3.2 is adopted here. The CPT data simulated are CPT chamber tests carried out by [109].

The hardening-soil parameters were explained in detail in Sec. 3.3.2. . The main model parameters value could be initially assumed regarding

the empirical relation addressed in Sec. 3.3.2. Accordingly the soil parameters for three relatively density of 45%, 85% and 88% are obtained as shown in Table 4.8.

Table 5-8, Estimated parameters value of hardening soil model based on [85].

Parameter		Dense		
		Loose	85	88
RD	%	45	85	88
E_{50}^{ref}	[MPa]	27	51	52800
E_{oed}^{ref}	[MPa]	27	51	52800
E_{ur}^{ref}	[MPa]	81	153	158400
p_{ref}	[MPa]	0.1	0.1	0.1
n_{ur}	[-]	0.2	0.2	0.2
m	[-]	0.55	0.43	0.425
c'	[MPa]	0	0	0
φ'	[°]	33.6	38.6	39
ψ	[°]	3.6	8.6	9
R_f	[-]	0.94	0.89	0.89
G_0^{ref}	[MPa]	90.6	117.8	119840
$g_{0.7}$	[-]	0.000155	0.000115	0.000112

It can be observed that the peak friction angle obtained from empirical relation for the dense soil is less than the one of direct shear test, i.e. 40°. The differences could be related to the differences of outcomes between

5. INVERSE ANALYSIS ON THE CONE PENETRATION TESTS MODELLING

triaxial and direct shear tests since the addressed empirical relation here are based on the results of triaxial tests, while the value of 40 degrees is the outcome of direct shear tests. According to [120] triaxial tests usually produce lower values of friction angle.

5.3.1 Numerical difficulties with state variable dependent constitutive models

At the beginning, the simulations conducted in the previous section are repeated, using the hardening soil model and a MPM-Mixed integration method. As it can be seen, for both fine and coarse meshes, numerical instability or divergence occurred, as the cone resistance drops after a while (Figure 4.23).

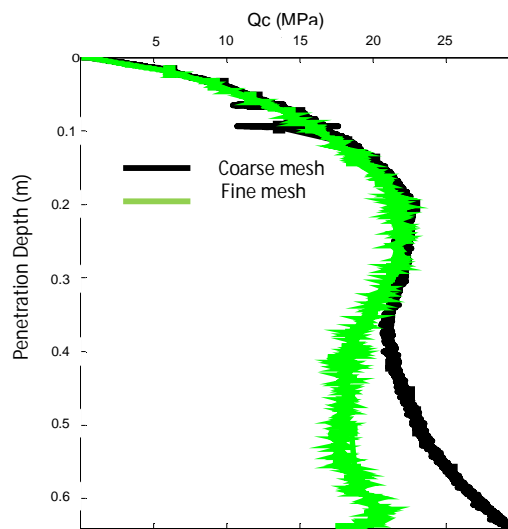


Figure 5-24, Instability while using MPM-MIXED integration method

A comprehensive investigation has been carried out to solve the problem and finally it was discovered that the problem is due to the averaging of the state variable within each element. This problem did not rise when Mohr-Coulomb was adopted. In the hardening soil model, the stiffness of the particles has a relation with the stress level of the particles, thus, high gradients of the stress around the cone lead to high gradients of the

stiffness of the particles and high gradients of state variables. Therefore, using MPM-MIXED, which involves replacing the state variables of all particles inside an element with their averaged value over the element, leads to the numerical instability. As an alternative, the simulations are repeated using MPM-MP +GP i.e. adopting the integration weight based on the element volume (Sec.3.2.4.2). It was concluded that the simulations are numerically stable using the latter approach.

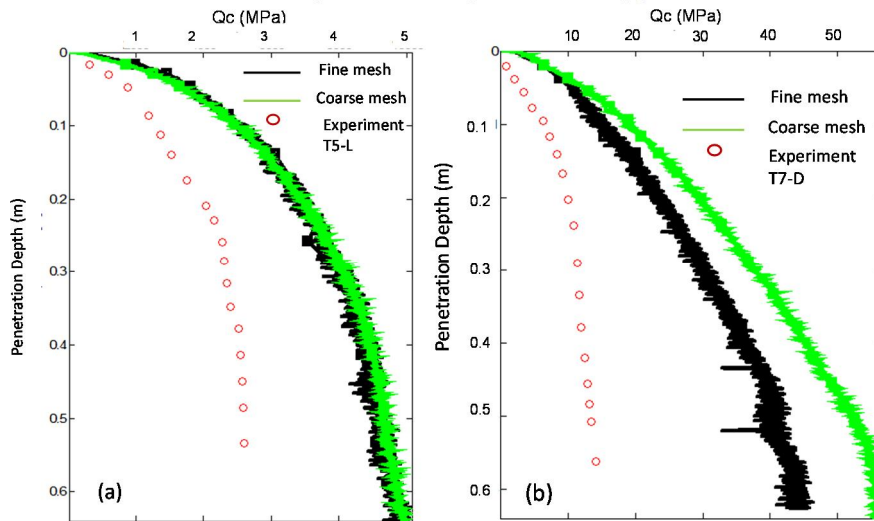


Figure 5-25, Simulation of CPT using MPM-MP+GP and initial parameters value. a) Loose sample b) dense sample

5.3.2 Calibration of CPT on loose, dense and layered soil samples (loose over dense)

According to Figure 5-25 the simulations for both loose and dense sample are overestimating the cone resistance. Moreover, for the dense material the mesh size dependency of the model outcome can also be observed. Parameters corresponding to dense soil produces sharp gradient of the stiffness around the cone (lower value of exponent m of the model). Thus, to well perform the explicit computation, the domain around the cone should be discretised using finer elements size.

In the hardening soil model, similarly to Mohr-Coulomb, the critical state condition is also missing, therefore, as it was explained in the previous section, high values of the dilation angle lead to the over estimation of q_c . Hence, dilation angles of 0 and 1° are assigned to the

5. INVERSE ANALYSIS ON THE CONE PENETRATION TESTS MODELLING

loose and dense models, respectively. From now on, the set of parameters with reduced dilation angle is called modified set. Figure 5-26 shows that the simulations with the modified dilation angle are in good agreement with the experimental outcome.

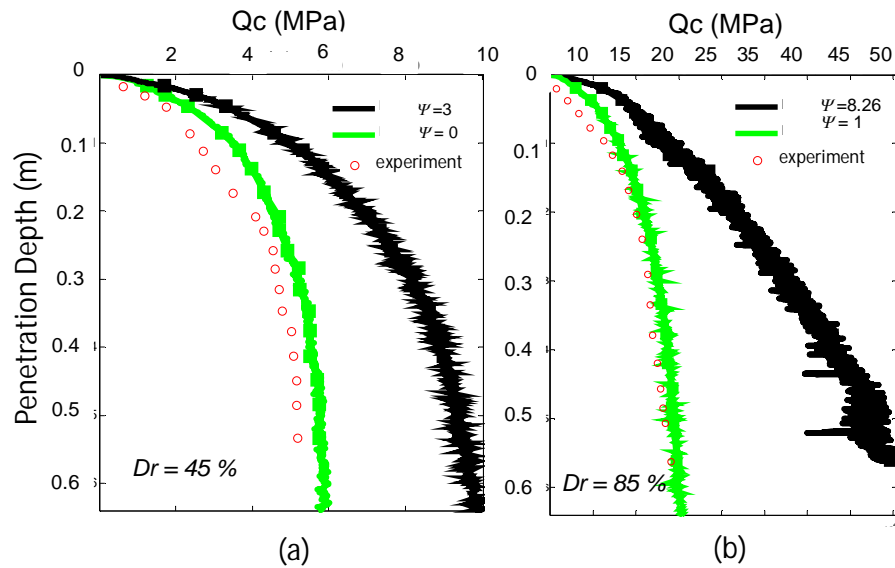


Figure 5-26, Calibration of the hardening soil model with CPT using modified dilation angles and fine mesh a) Loose sample b) Dense Sample

In the next stage, the layered sample (loose over dense) is simulated. The modified set of parameters that well matched the homogenous tests is initially employed. It can be observed that, the employed sets of parameters are underestimating the cone resistance in the dense layer. This was also confirmed in the case of the Mohr-Coloumb constitutive model. The reason of the mismatches could be related to issue related to the sample preparation before the experiment (personal conversation with the corresponding author of [109]). Particularly, the simulations are not able to fit the cone resistance in the transition zone from loose to dense layer. i.e. green line in Figure 5-27.

A sensitivity analysis considering only the relative density of the dense layer has been conducted. In a way that, for each selected relative density the parameters of the hardening soil are derived through Eq.(3-80) to Eq.(3-88). In fact, in this analysis the relative density of the bottom

layer is the only main variable and the hardening soil parameters are derivative parameters and all the parameters of the loose layer are constant. Finally, it was found that the adopting the parameters value associated with the relative density of 88% for the bottom layer significantly improve the matches between simulations and observation. However, similarly to the Mohr-Coulomb case, the transition zone of the loose layer is overestimated. It should be underlined that, the dilation angle for the dense layer, similar to the homogenous case, is assigned 1 degree.

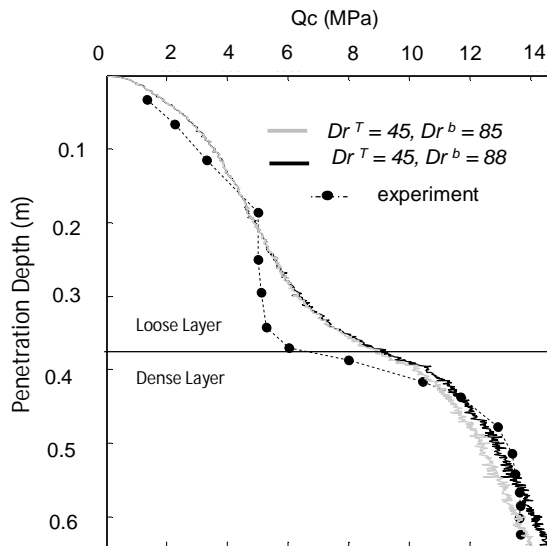


Figure 5-27, Simulation of CPT on the layered sample using hardening soil model

5.4 SIMULATION OF CPT USING HYPOPLASTIC MODEL

It was shown in the previous sections, in order to well reproduce the soil behaviour around the cone during the penetration when adopting the Mohr-Coulomb and the hardening soil constitutive laws, a low value of dilation angle should be employed. In this section a hypoplastic model, which considers the main features of the critical state theory and can well simulate the soil volume change at large deformations, is employed to

5. INVERSE ANALYSIS ON THE CONE PENETRATION TESTS MODELLING

model the cone penetration tests. As it was mentioned before, the hypoplastic model involves large number of input parameters, thus, the calibration of all of the parameters by inverse analysis considering only CPT results is not possible. To cope with this problem, the parameters determined via lab data tests (methods explained in Chapter3) are assumed as starting values of the calibration, which is aimed at adjusting the values of some of the relevant parameters.

5.4.1 Simulation of a centrifuge test of a jacket pile installation

The axisymmetric MPM formulation while using MPM-MP + GP is used here. At the beginning, the stress of the sample is initialized through a K0 procedure, assuming $K_0 = 0.5$ and 1g gravity acceleration. Then a quasi-static calculation is performed while the gravity multiplier is applied and it is increased to 40g. Figure 5-28 shows the vertical effective stress of the sample before and after the quasi-static calculation. After reaching the equilibrium, a penetration with the constant velocity of 0.02 m/s is applied.

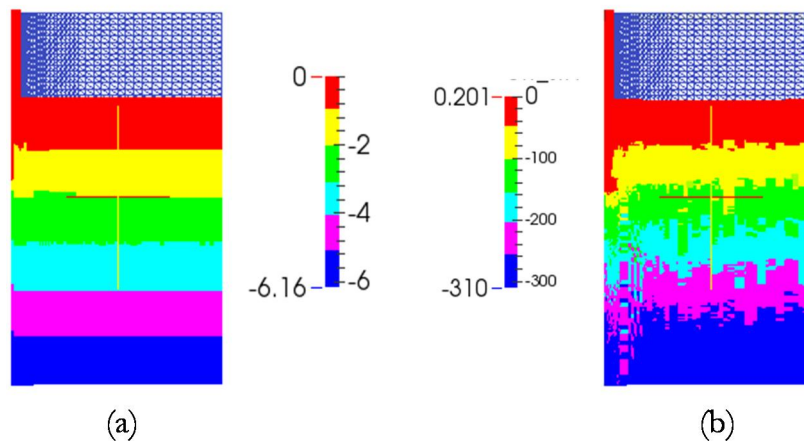


Figure 5-28, MPM model for centrifuge experiment of pile installation a) initial stress using K0 Procedure b) stress initialization using the gravity acceleration equal to 40g .

The hypoplastic model is adopted to simulate the soil model behaviour. The main parameters values are those of INV 02 determined in Sec. 4.1.

As it was explained in chapter 3, the intergranular parameters of the model should be assigned in a way that prevents the numerical instability caused by the explicit scheme., assigning a relatively high value to parameters R_{max} causes small noises of state variables and stresses. On the other hand, to readjust the small strain stiffness of the material, the stiffness multiplier M_R should be reduced to the value of 5. Thus, these values are assigned to the intergranular (IGS) parameters: $R_{max} = 0.0002$, $\beta_r=1$, $\chi=3$, $m_R=5$, $m_T=2$. The adopted IGS values, rather than the ones suggested by [90] show a more stable outcome. Figure 5-29 shows the numerical instability in the case of high value of M_R and high sensitivity of the model to the values of intergranular parameters. This is in contradiction with the intergranular concept that is supposed to show influence only in dynamic problems and not in quasi static boundary value problems like cone penetration testing.

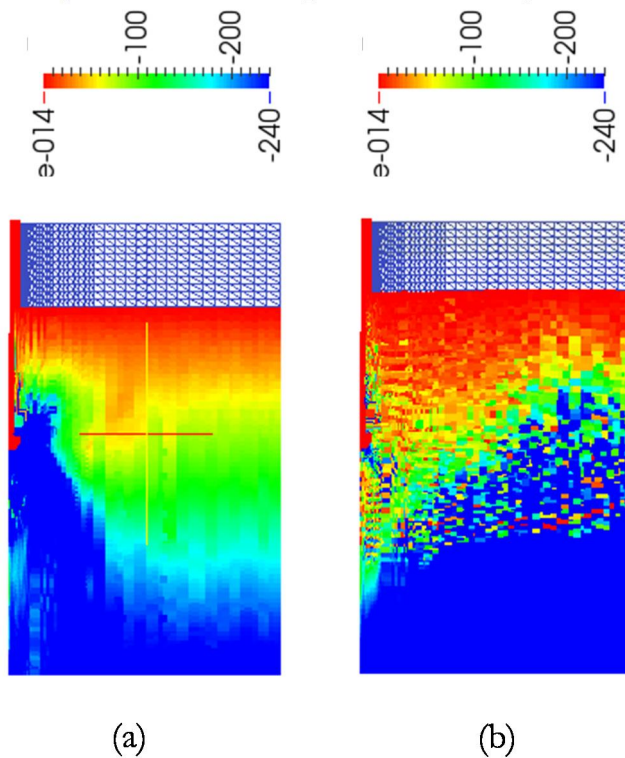


Figure 5-29, Effect of intergranular parameters on the vertical effective stress of the soil domain while pile is 18 cm penetrated a) suggested IGS parameters b) IGS parameters value suggested by Wegener and Herle (2013).

5. INVERSE ANALYSIS ON THE CONE PENETRATION TESTS
MODELLING

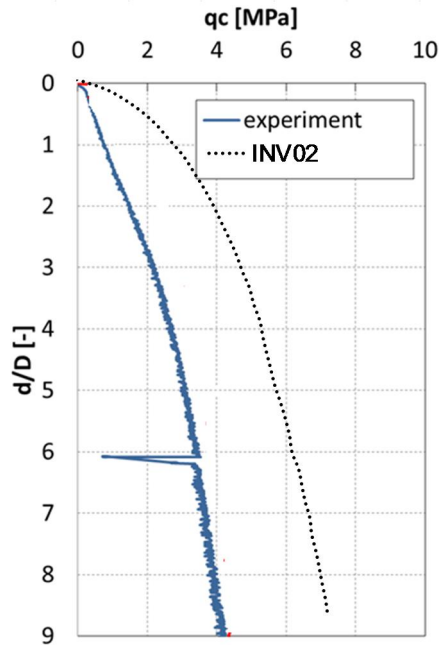


Figure 5-30 Outcome of MPM model adopting INV02 for hypoplastic main parameters and suggested IGS parameters ([59])

Figure 5-30 shows the calculated tip resistance using the current suggested set of IGS parameters; it is obvious that the simulation is overestimating the experimental results. Higher predicted cone resistance is also reported by [27] which simulated cone penetration tests in sand using an hypoplastic model and the Updated Lagrangian finite element method. The high simulated tip resistance might be due to the high assigned stiffness of the material. In the hypoplastic formulation (Sec. 3.3.3) the initial stiffness of the material is calculated as the multiplication of parameter M_r and the soil stiffness at large strain. According to [90], while high value of M_r is used, the value of parameters h_s should not be more than 1000 MPa. Therefore, a re-calibration in terms of parameter h_s was carried. It was concluded that, adopting $h_s = 100$ MPa, predicts the cone resistance more closed to the experiment outcome (Figure 5-31).

Figure 5-32 also depict the outcome of those two created model in the contour of effective vertical stresses. The higher value of h_s leads to an immediate increase of stress in a very large area below the tip. While the

lower one causes an increase of stress over a bubble around the tip. Later on in this study it would be shown that, the latter model's outcome is the most adequate for simulating cone penetration tests.

The three triaxial tests adopted to perform INV02 in Sec.4.1 and the oedometer tests in the same section are re simulated adopting the modified value of $h_s = 100 \text{ MPa}$. As it can be seen in Figure 5-33, the model prediction is not fit with experiment any more so that low stiffness of the predicted behaviour could be observed

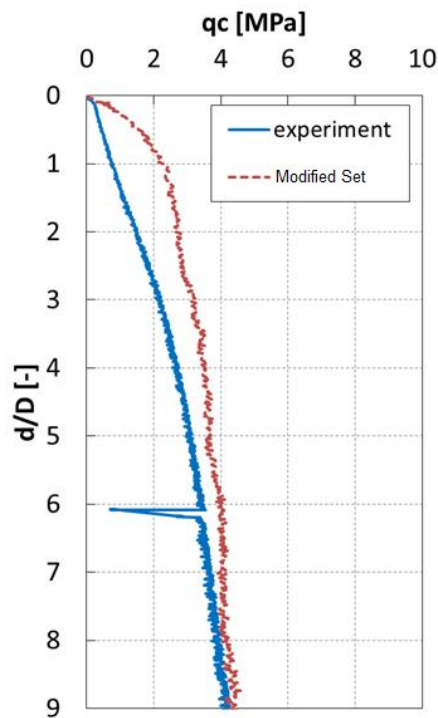


Figure 5-31 Outcome of the modified set of parameter

5. INVERSE ANALYSIS ON THE CONE PENETRATION TESTS
MODELLING

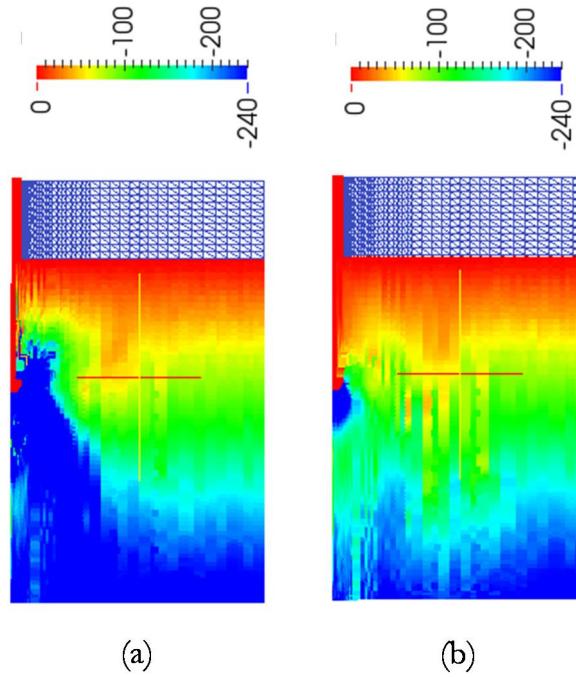


Figure 5-32 Vertical effective stress when the pile is 18 cm penetrated. a) Parameters of INV02 b) Modified parameter ($h_s=100\text{mPa}$)

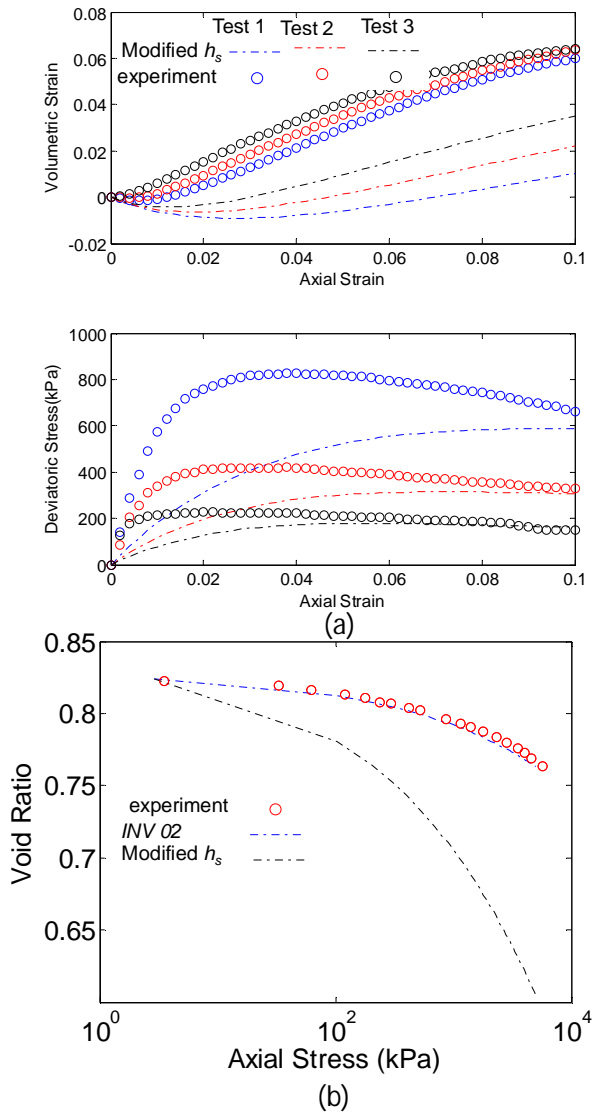


Figure 5-33 Simulation of lab tests using modified parameters, a) oedometer test, b) triaxial tests of INV02 in Chapter 3

5.4.2 Simulation of an in-situ CPT in Northern sea sand.

5. INVERSE ANALYSIS ON THE CONE PENETRATION TESTS MODELLING

Figure 5-34 shows the MPM schematization adopted to simulate the CPT boundary value problem. The background mesh has a total of 9936 elements including the initially inactive elements (in grey in the Figure). The effect of mesh size was not analyzed in this study and MPM-MP+GP (Sec 3.2.4.2) method was employed. The inactive elements are activated during the calculation if material points move into the space they occupy. Triangular elements with linear interpolation of the displacements are used. The number of material points is 105120. The MPM moving mesh concept is adopted in all simulations ([28]). The numerical simulations are performed using an axisymmetric geometry. To avoid boundary effects, the side boundary is placed at a distance of 30 D from the symmetry line (the diameter of the cone D is 3.57 cm). This space is divided in three parts with mesh sizes getting larger and number of particles per elements decreasing as the distance from the symmetry line increases. Displacements at the side boundary are constrained in the radial direction and free in the vertical direction. The bottom boundary, placed at a distance of 30 D from the initial position of the cone tip, is fully fixed. The simulations are performed considering a submerged one-phase material in drained conditions. Stresses in the soil are initialized using a typical K0-procedure. Considering that the 10 m thick soil located above the cone does not significantly interact with the shaft yet it affects the initial stresses in the domain around the cone, it is modelled considering a 10 D thick (36 cm) layer of hypoplastic material overlaid by a 10 cm thick layer of elastic material with the following properties: Young modulus equal to 1000 kPa; Poisson ratio equal to 0.0; and very high density proportional to the ratio between the real thicknesses of the soil layer above the cone and the modelled one. In this case, a material density of 887.8 kN/m³ is needed to simulate 9.64 m of submerged sand imposing an effective stress at the bottom of the elastic material equal to 92 kPa. The cone penetrometer "pile" is modelled as a rigid body penetrating into the soil with a prescribed velocity equal to 0.02 m/s, a value common in standard practice. A contact algorithm is used to model the frictional contact between the pile and the soil. The adopted friction angle value (11°), is representative of a sand to polished steel contact ([116]). Considering the above conditions, the time needed to run one model simulation is approximatively equal to 8 h.

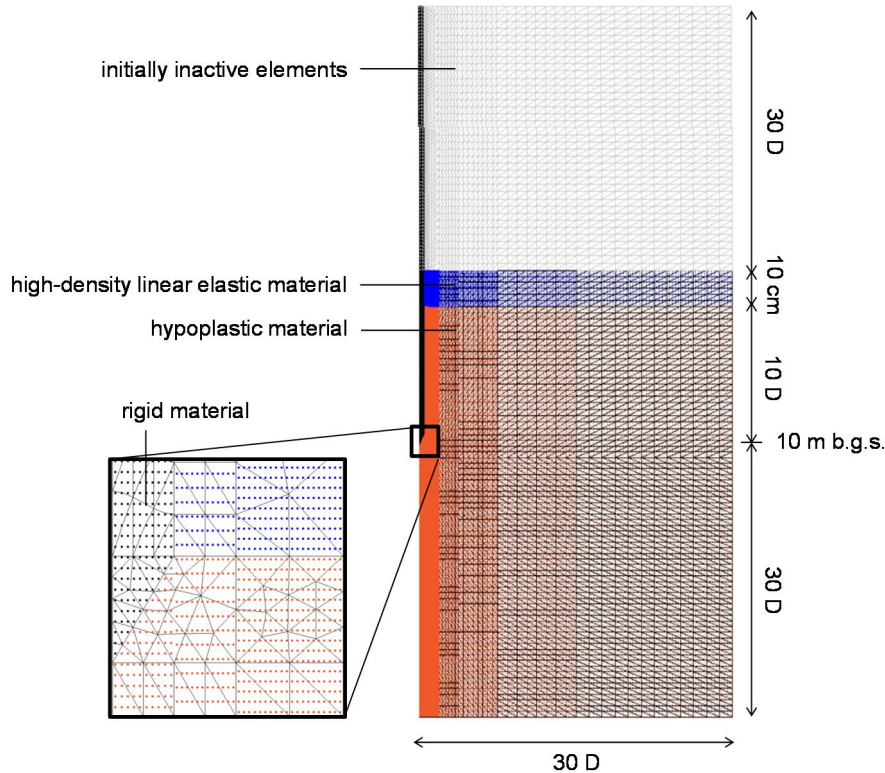


Figure 5-34 Scheme of the MPM model of CPT.

The initial values for the hypoplastic model parameters are obtained using the curve fitting of the result of three available triaxial tests similar to the methodology explained in Sec.4.1 of this thesis. Accordingly the estimated parameters are written in Table 5-9 and the result of curve fitting is shown in Figure 5-35. In the applied procedure, similar to the Sec.4.1 and Sec.4.2., Parameters e_{d0} and e_{i0} are assigned considering the e_{\max} and e_{\min} of index tests. The intergranular parameters are assuming in a way to preventing the numerical instability similar to the previous cases. Therefore, 5 main parameters of h_s , α , β , n , e_c were estimated via curve fitting procedure. The values of estimated parameters via curve fitting of triaxial tests are reported in Table 5-9. In the next stage, the 5 main variable parameters of the model are recalibrated to make a best fit with the CPT data. The curve fitting is carried out using inverse analysis employing a modified Gauss-Newton method (Sec.3.1.2.1)

5. INVERSE ANALYSIS ON THE CONE PENETRATION TESTS MODELLING

As mentioned before, each CPT forward model takes about 8 hours. To reduce at a minimum the time required for the regression, all of perturbed simulations are executed in parallel at each iteration. Two convergence criteria are used to conclude the optimisation: (i) maximum parameter change lower than a user-defined percentage of the parameter value at the previous iteration, herein equal to 5%; or (ii) objective function change lower than a user-defined amount for three consecutive iterations, herein equal to 0.05.

Table 5-9 Input parameters of the adopted hypoplastic model

Parameter	Initial value	CPT Re-Calibrated
ϕ_c	31°	no
e_{i0}	0.37	no
e_{d0}	1.35	no
e_{c0}	1	Yes
α	0.012	Yes
β	0.14	Yes
h_s	1.5E+5 kPa	Yes
n	0.24	Yes
β_r	0.4	no
R_{max}	0.0002	no
M_r	1.5	no
M_t	1.2	no
χ	1	no

The initial values of the 13 hypoplastic model parameters were estimated, as already mentioned, by curve fitting the stress strain response of three drained triaxial compression tests. More details on the optimization procedure adopted to determine the initial values of the parameters are reported in Sec.4.1. Five of these parameters (see Table 5-9) have then been further calibrated to minimize the fit between CPT experimental data and MPM model results, using the procedure described in the previous section. Figure 5-35 show that the calibrated model, differently from the initial model, adequately simulates the final tip resistance of the CPT. Figure 5-36 shows the values of the 5 calibrated parameters, as well as the value of the objective function defined in Eq.(3-8), at each iterations of the regression. The calibration procedure converged after only 7 iterations, when the regression convergence criterion is satisfied. The lowest value of the objective function, almost three orders of magnitude lower than its initial value, is reached at iteration 4. The results indicate that the optimal values of the

five calibrated parameters (see also Table 5-10) are always higher than their initial values. The parameter undergoing the highest variation from its initial estimate is the granular stiffness, h_s .

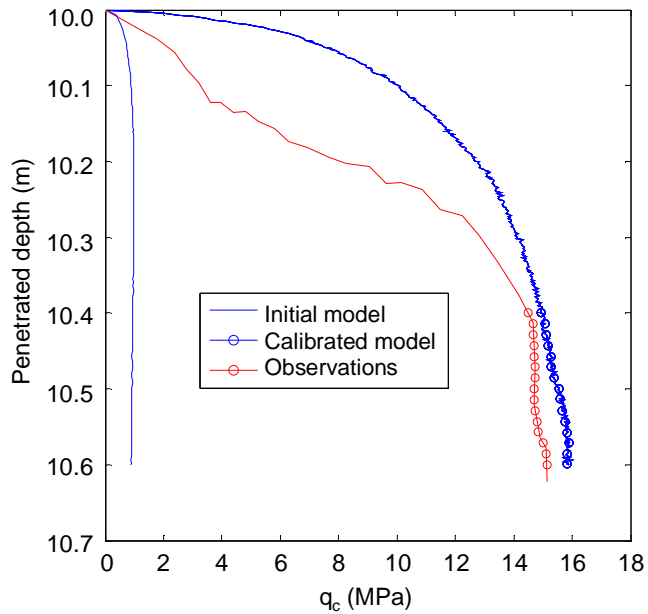


Figure 5-35 Comparison between CPT data and computed tip resistance for initial and calibrated values of the input parameters

5. INVERSE ANALYSIS ON THE CONE PENETRATION TESTS MODELLING

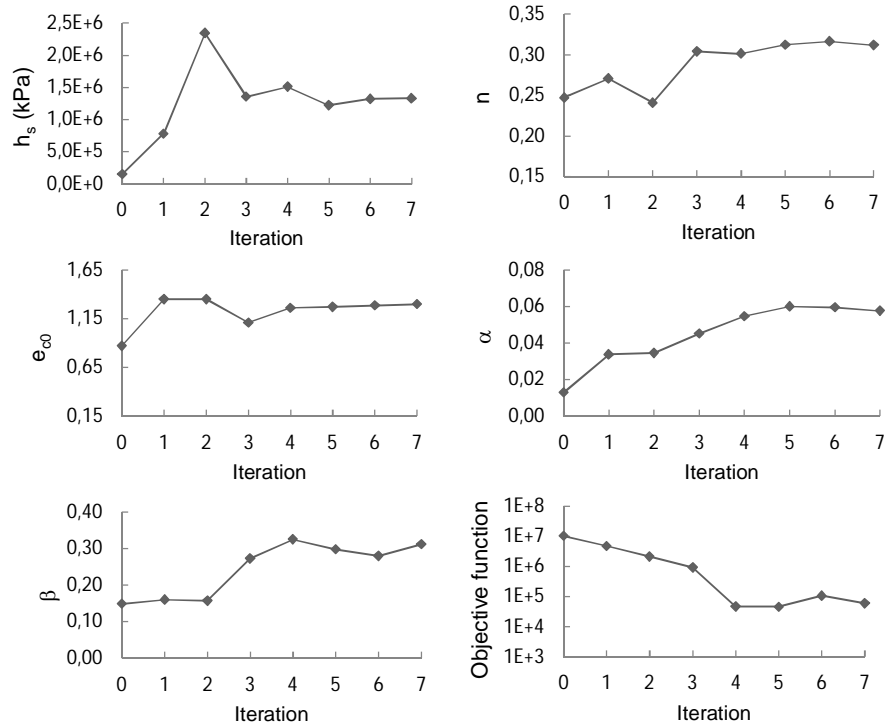


Figure 5-36 Results of regression at each iteration: values of parameters and objective function.

Figure 5-37 illustrates the direction of the particle movements at the end of penetration, for both the initial and calibrated MPM simulations. As expected, the particles close to the cone are always moving downwards, yet the shape of the lump of soil accompanying the cone varies significantly in the two cases, being wider in the calibrated model. The latter model is also characterized by a significantly larger area around the cone affected by outward horizontal displacements as well as by smaller deformations in the upper part of the soil. These differences could be attributed to the fact that the set of parameters adopted in the two cases (Table 5-10) relate to a contractive behaviour upon shearing, for the initial simulation, and to a dilative behaviour, for the calibrated simulation. This can be easily seen at representative elementary volume scale, for instance by looking at the simulations of the three triaxial test from Table 5-9 (Figure 5-38). In fact, the comparison between the experimental data and the model results indicate that the calibrated

values of the input parameters do not adequately reproduce the tests. However, this is not surprising because the void ratio of the soil samples tested in the laboratory is lower than the void ratio of the sand tested in-situ with the CPT.

A final check on the significance of the set of calibrated parameters for the MPM simulation of the CPT is performed by means of a parametric analysis (Table 5-10). Five simulations are considered in which the base case is the initial simulation and the five hypoplastic parameters are then individually changed, one by one, starting from their calibrated values. Figure 5-39 shows the comparison between observed and computed tip resistance for the 5 simulations of the parametric analysis. Somewhat unexpectedly, only two of the five parameters (h_s and α) produce results that differ from the base case. The results, besides showing that 2 parameters are more important than the other three, seem to suggest a strong correlation among the input parameters, i.e. cross-dependency effect, and a markedly non-linear behaviour of the MPM model in reproducing the CPT tip resistance. In other words, they highlight the importance of the simultaneous calibration of all the considered parameters and, therefore, the usefulness of adopting, to this purpose, an automated inverse analysis algorithm rather than a trial-and-error calibration approach.

5. INVERSE ANALYSIS ON THE CONE PENETRATION TESTS MODELLING

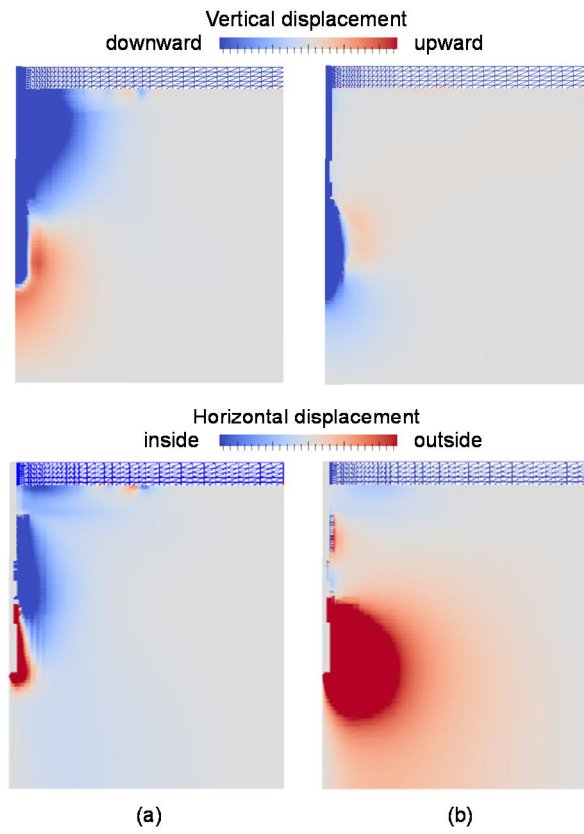


Figure 5-37 MPM results: direction of horizontal and vertical displacement at end of penetration for the initial (a) and calibrated models (b).

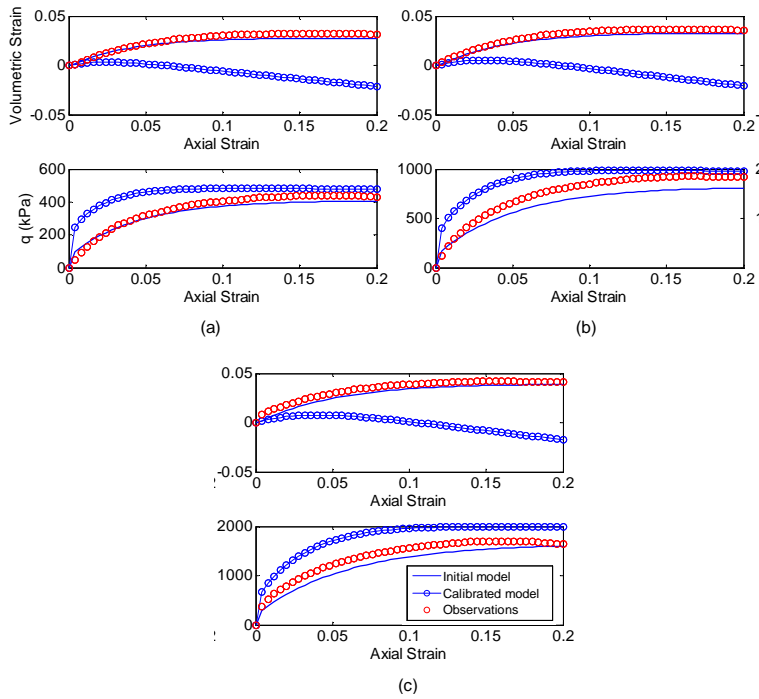


Figure 5-38 Comparison between experimental data from triaxial tests and hypoplastic model results for the initial and calibrated values of the input parameters.

Table 5-10 Values of the hypoplastic model parameters in the parametric analysis

Parameter	Initial values	Calibrated values	Simulation A	Simulation B	Simulation C	Simulation D	Simulation E
h_s	1.5E+5	1.5E+6	1.5E+6	1.5E+5	1.5E+5	1.5E+5	1.5E+5
n	0.25	0.30	0.25	0.30	0.25	0.25	0.25
e_{c0}	0.87	1.26	0.87	0.87	1.26	0.87	0.87
α	0.01	0.05	0.01	0.01	0.01	0.05	0.01
β	0.15	0.32	0.15	0.15	0.15	0.15	0.32

5. INVERSE ANALYSIS ON THE CONE PENETRATION TESTS MODELLING

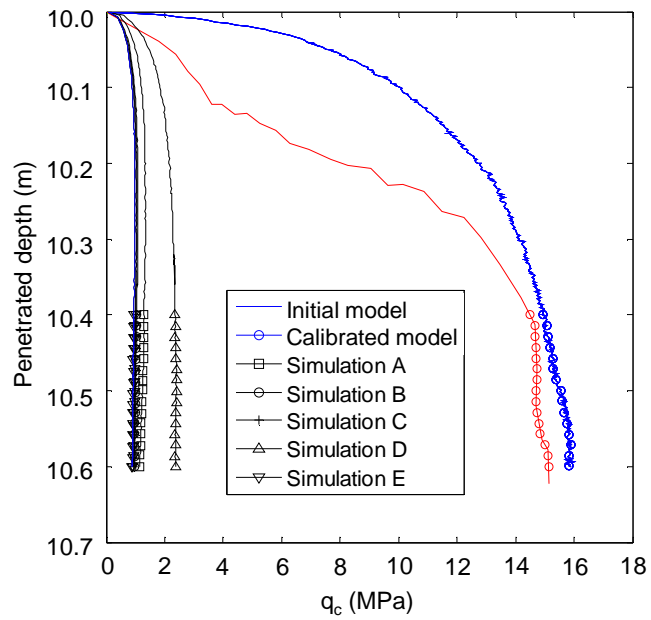


Figure 5-39 Comparison between CPT observations and computed tip resistance for the 5 simulations of the parametric analysis

6 MODELLING OF SMALL SCALED SLOPES

In this chapter, automated inverse analysis procedures are used to calibrate the MPM models of two well-instrumented laboratory experiments on reduced-scale slopes, respectively dealing with (1) slope deformation and (2) long run-out soil propagation. The first laboratory test refers to a retrogressive slope instability combined with soil liquefaction. The second test reproduces a soil mass rapidly propagating along an inclined plane and depositing over a flat area.

Depending on the specific tasks of the MPM analysis, different approaches can be used to model the soil mechanical behaviour. The Hypoplasticity model is used for the slope deformation test, while a Mohr-Coulomb model is employed to capture the dynamic behaviour of a fast-moving soil mass propagating over a non-deformable frictional surface. In both cases, the model parameters are assessed by means of inverse analysis.

6.1 SIMULATION OF DRY SMALL SCALED EXPERIMENT OF DRY GRANULAR PROPAGATION

6.1.1 Case study

Small scale experiments with flows of dry sand were carried out by [121]. The material propagated through a rectangular flume with a bed surface, inclined 31.4° , joined to a horizontal runout surface by a curved section with a 10 cm radius of curvature (Figure 6-1).

A vertical gate spanning the entire flume width (20 cm) was positioned in the uppermost part of the slope. About 290 cm^3 of loosely packed, well-sorted and well-rounded dry sand was placed behind the gate ensuring a horizontal soil surface.

The bulk density of the soil was approximated as 1600 kg/m^3 . The flume bed was surfaced with Formica. The static bed frictional angles measured using tipping table tests of sand sliding across the Formica was reported as $29^\circ \pm 1.4^\circ$. The internal friction angle of the sand was reported equal to $40^\circ \pm 1^\circ$.

The experiment started by suddenly opening the entire gate. The flow accelerated, elongated, and thinned rapidly after the gate opened. A non-invasive optical shadowing technique was used to measure the soil thickness during and after the flow.

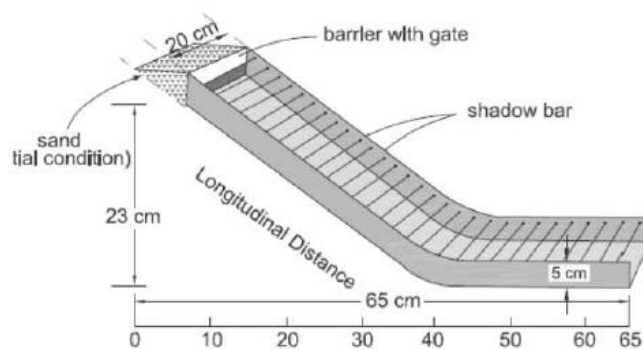


Figure 6-1 Schematic of the flume used for propagation tests of granular flows [121].

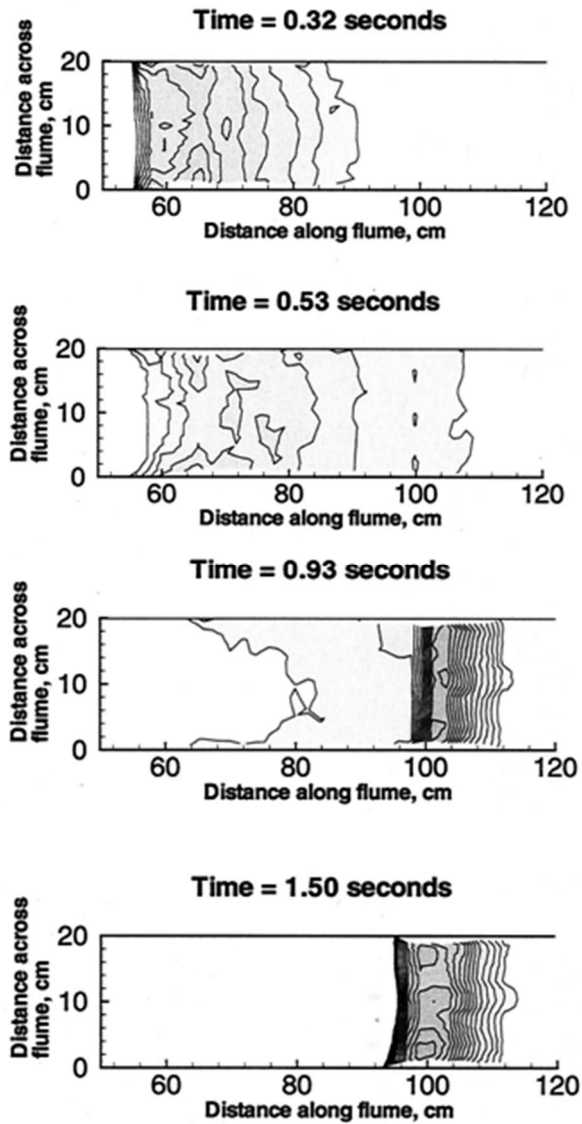


Figure 6-2 Overview of the experimental results achieved in the flume test considered herein [121].

When the leading edge of the flow reached the break in slope located 37.5 cm downslope from the gate, the sand that first reached the

depositional area was only slightly pushed forward by subsequently arriving sand.

In the experiment considered herein, the sand deposition was complete 1.5 s after the flow release. Sand thicknesses normal to the flume bed are reported by Denlinger and Iverson (2001) at 0.32 s, 0.53 s, 0.93 s and 1.5 s after the gate released (Figure 6-2).

6.1.2 Selected Observations

The longitudinal cross-sections of the propagating soil have been drawn, at different experimental times, using the contour lines presented in Figure 6-2. On the other hand, Figure 6-3 shows, as an example, the cross section highlighting the base of the apparatus and the position of the soil at the end of the test, corresponding to an experimental time equal to 1.5 s.

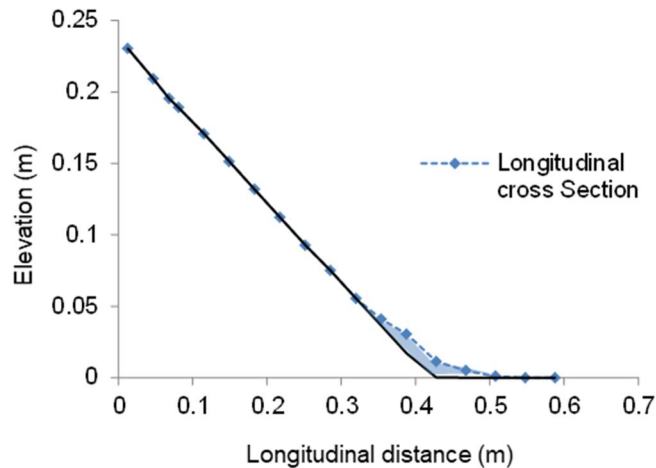


Figure 6-3 Observations, at time equal to 1.5 s, along the longitudinal cross-section of the flume used to calibrate the MPM model.

6.1.3 MPM Model

The MPM model was created adopting the Anura3D MPM code. The domain was discretized by 12'555 elements (Figure 6-4). The material points representing the soil are initially positioned in a relative small area located in the uppermost portion of the mesh comprising 440 elements. Each one of these elements initially contains 4 material points. The

experimental gate was simulated by applying horizontal fixities at the right boundary of the soil domain. To initialize the soil stresses, a quasi-static calculation was carried out at the beginning of the simulation. Subsequently, the horizontal fixities were removed and the soil was allowed to propagate downwards along the slope.

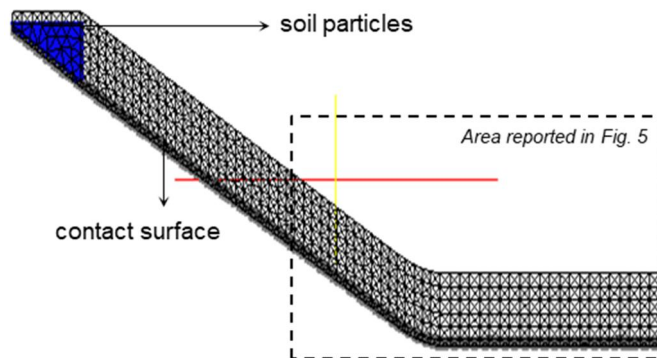


Figure 6-4 Scheme of computational domain.

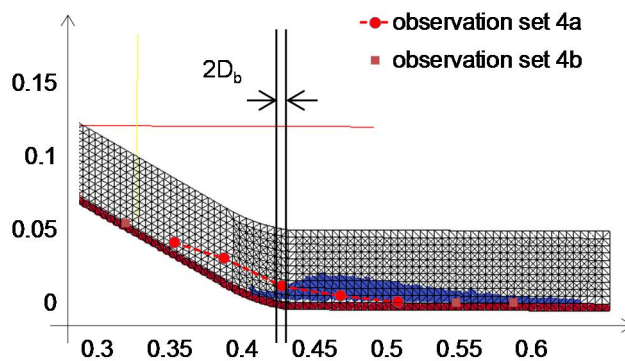


Figure 6-5 Experimental observations and results of the initial MPM simulation at the end of the test.

An elastic perfectly plastic constitutive law is used to simulate the behavior of the soil. The constitutive model is based on the Mohr-Coulomb failure criterion and adopts 5 input parameters: stiffness modulus (E); Poisson's ratio (ν); cohesion (c); friction angle (ϕ); and dilatancy angle (ψ). In addition to these, two other parameters are also needed to define the initial conditions of the soil: porosity (n); and specific gravity of the soil grains (G_s). The contact with the base of the

6. MODELLING OF SMALL SCALED SLOPES

experimental apparatus was simulated adopting a frictional law with a single input parameter: the contact coefficient (μ).

The values of the input parameters of the initial numerical simulation were determined considering the values of the sand properties reported by Delinger and Iverson (2001) and the results of a numerical simulation already performed, for the same case study, by Ceccato and Simonini (2016). They are equal to: $E=1000$ kPa, $\nu=0.3$, $c=0$, $\phi=40^\circ$, $\psi=0$, $n=0.4$, $G_s=2.65$.

Considering the above conditions, the time needed to run one model simulation is approximately equal to 60'. The comparison between the experimental observations and the results of the initial MPM simulation is reported in Figure 5 considering the position of the soil at the end of the test, i.e. experimental time equal to 1.5 s. The numerical results of the MPM model are "stored", at the end of each time step, at the location of the material points, which are of course moving within the mesh during the simulation. On the contrary, the 18 points used as observations for a given experimental time (Fig. 3) are fixed in space. A purposefully defined numerical algorithm is herein used to extract the values of the elevations of the MPM material points corresponding to the adopted observations. Buffer zones having a width equal to D_b are defined at the location of each observation, i.e. longitudinal distance X_i , as follows:

$$X_{i_min} = X_i - D_b \quad (6-1)$$

$$X_{i_max} = X_i + D_b \quad (6-2)$$

where: X_{i_min} is initial longitudinal distance of the buffer zone for the i-th observation; X_{i_max} is final longitudinal distance of the buffer zone for the i-th observation.

As depicted in Figure 6-5, the numerical value to compare to the elevation of the i-th observation, at any given experimental time, is equal to the maximum elevation of all the material points falling within the corresponding buffer zone at that time.

6.1.4 Sensitivity analysis

The relative importance of the input parameters being simultaneously estimated by the adopted inverse analysis algorithm can be defined using: statistics representative of the sensitivity of the predictions to changes in parameters values; and statistics derived from the variance-covariance matrix.

Among the statistics able to evaluate the sensitivity of the predictions to parameters changes, the composite scaled sensitivities, css_j (equation (3-13)). To this aim, all the available elevation data (72 observations) have been considered. reports the values of the composite scaled sensitivities for 7 of the 8 input parameters of the MPM model. Parameter c is not considered in the sensitivity analysis as its value is always assumed to be zero. The values of css were computed considering the input parameters values of the initial numerical simulation. The perturbations were always set to 1% of the parameter values. The results of the sensitivity analysis clearly indicate that the input parameter whose changes have the highest impact on the model results is the contact coefficient, μ . Not surprisingly, among the 5 parameters used in the constitutive law adopted to simulate the soil behaviour, the highest composite scaled sensitivity value refers to the friction angle, ϕ .

Table 6-1 Composite scaled sensitivities of the model input parameters

Parameter	Value	Perturbation	css
E	1000 kPa	0.01	5.59
ν	0.3	0.01	6.89
c	0	None	-
ϕ	40°	0.01	9.58
ψ	0.1	0.01	4.28
n	0.4	0.01	5.21
G_s	2.65	0.01	5.80
cc	0.40	0.01	29.43

The results of the sensitivity analysis also indicate that the input parameters are not highly correlated among themselves. To this aim, the parameter statistics to look at are the correlation coefficients, $cor(i,j)$ (equation (3-17)).

The highest correlation coefficient values are reported for the correlation between parameters E and ϕ (-0.60), between parameters n and ψ (-0.55) and between parameters n and ψ (0.47). The absolute values are always significantly lower than 0.8, thus indicating that only mild correlations exist between some of the input parameters.

Based on the results of the sensitivity analysis, it has been chosen to calibrate only the two input parameters to which the model results are most sensitive, i.e. the contact coefficient between the soil and the base of the apparatus and the soil friction angle.

6.1.5 Calibrated MPM simulation

The values of two model parameters, ϕ and μ , are calibrated adopting the regression analysis algorithm described in section 2.3. To this aim, many different sets of observations have been used, considering that elevation data of the propagating soil are available at four experimental stages corresponding to the following times: 0.32 s, 0.53 s, 0.93 s and 1.5 s (Figure 6-2). For each experimental time, the 18 elevation points adopted to describe the soil surface profile along a longitudinal cross-section have been further subdivided in two classes, in relation to whether the observations refer to areas with or without soil. This distinction allows to differentiate between experimental data carrying information of the absolute value of the soil depth at a given location (i.e. observation sets a) and data only reporting the "absence" of soil at that location (i.e. observation sets b). Six inverse analyses have been performed considering the following observation sets: all the available elevation data (72 observations), type-a elevation data (36 observations), and single stage elevation data from each one of the four experimental stages considered (18 observations). Contrarily to what one may have expected, the best results have not been obtained when all the observations are used. Indeed, the largest objective function reduction refers to the regression analysis conducted using only the soil elevation values at the end of the propagation, i.e. observation sets 4a and 4b (Figure 6).

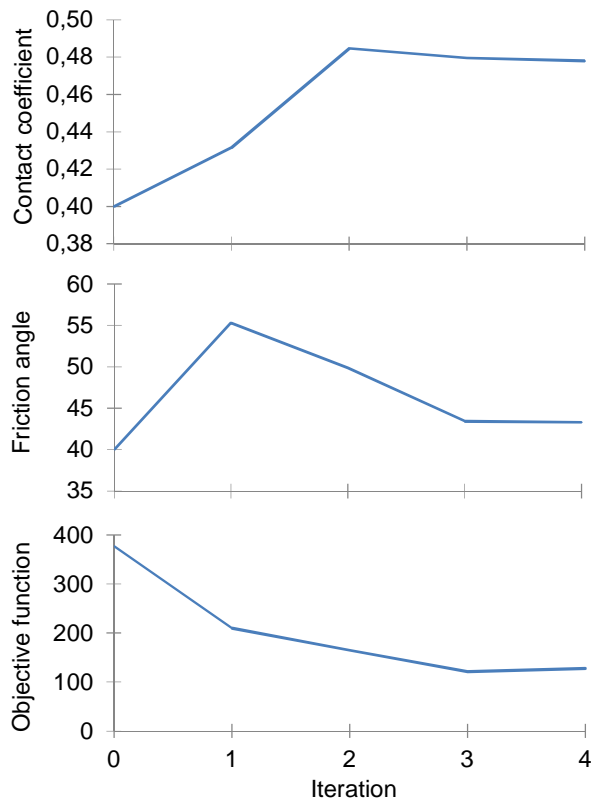


Figure 6-6 Result of model calibration by regression using observations at time $t = 1.5$ s.

In particular, the best fit between computed and experimental data is obtained, in this case, by increasing the values of both the parameters being calibrated: from 40° to 43.43 for parameter ϕ , and from 0.40 to 0.48 for parameter μ . Figure 6-7 shows the comparison between the observations and the results of the model for all the four experimental stages. The latter are reported for both the initial simulation and the calibrated one, i.e. best performing inverse analysis. The improvement of the model in reproducing the final cross section of the soil mass (i.e. observation time 1.5 s) is manifest.

6. MODELLING OF SMALL SCALED SLOPES

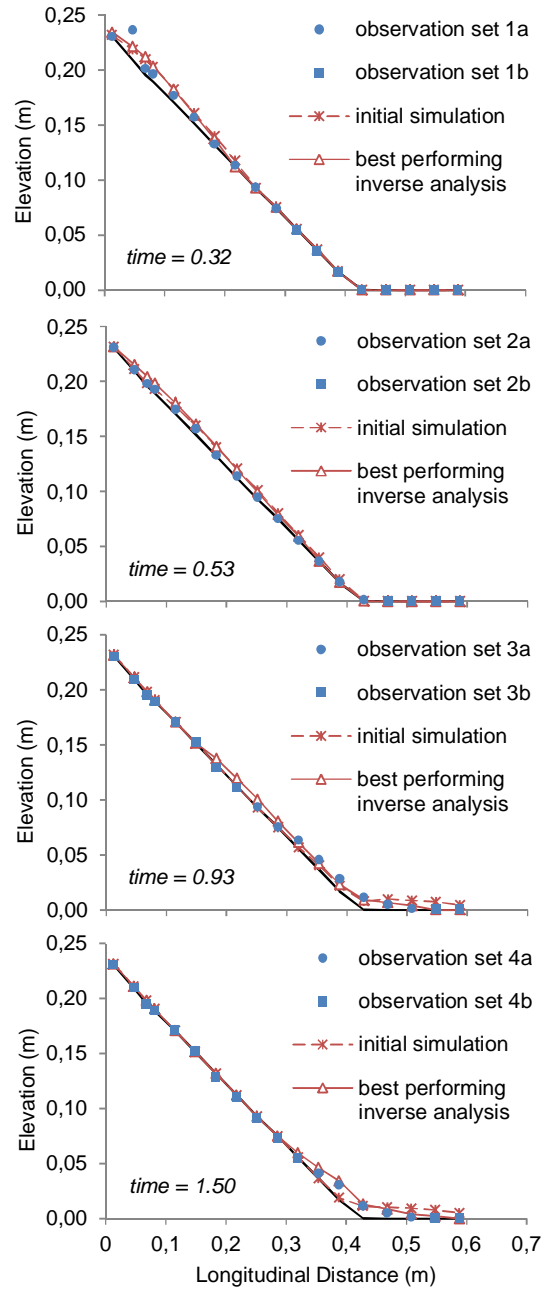


Figure 6-7 Comparison between model results and experimental observations.

The success of the inverse analysis is verified by the fact that the calibrated model is almost perfectly reproducing the position of the deposited soil mass and only slightly over-predicting the soil deposition heights. It is important to note, however, that the calibrated model is not able to adequately reproduce the evolution of the soil during propagation (i.e. observation times 0.32s, 0.53s, 0.93 s). In other words, the adopted MPM model can be calibrated to adequately predict the final condition of the soil mass but it is not able to adequately reproduce, at the same time, both the evolution and the final deposition characteristics of the debris flow. This is due to the inherent limitations of the constitutive elastic-perfectly plastic law adopted to model the propagating soil mass using a continuum modelling approach, as is already reported in the literature (e.g. [81]). The latter is further confirmed by the fact that the optimal inverse analysis does not use all the observations, but only the ones related to the final deposition stage of the soil mass.

Despite these limitations, the considered example shows that simple frictional constitutive models, if well calibrated, can be used to reproduce the most relevant outcome of dry debris flows, the position of the soil mass at its final deposition stage. This finding is comforting for a series of reasons, mainly related to the potential use of MPM models to simulate real debris flows: (1) the computational time needed to run MPM models employing complex elasto-plastic constitutive laws can be too demanding, (2) soil height data related to intermediate stages of the soil propagation are not easy to retrieve outside the laboratory, and (3) the final position of the soil mass is the "observation" most typically adopted by analysts evaluating the performance of a propagation model simulating real granular flows.

6.2 MODELLING A RETROGRESSIVE SLOPE FAILURE INCLUDING SOIL LIQUEFACTION

6.2.1 Case study

Flowslide flume tests performed by [32] is considered here to investigate static liquefaction and the role of the initial relative density in relation to the slope failure and to the post-failure behaviour. Detailed observations

6. MODELLING OF SMALL SCALED SLOPES

were acquired for failure initiation, acceleration and flowsliding in 1 m tall slopes constructed in a glass-sided tank. The slope angle was fixed at 36° and the floor was extended to 1.5 m beyond the toe. Water was injected in the slope from a constant head tank located behind it, through a wire cage filled with coarse gravel to facilitate the inflow. Seepage towards the toe brought the slope to failure. Direct sliding of the slope along the coal/floor interface was inhibited by #80 waterproof sand-paper glued to the floor, with an interface friction angle equal to $30-36^\circ$. Several tests with different relative density were conducted. This section of the thesis focuses on the results of experiment n. 7 in which the slope experienced a rapid retrogressive flowslide (Figure 6-8). Failure started by shallow sliding adjacent to the glass in the area of the saturated coal. The 1st Stage comprised two fairly distinct shallow slides over a 4 s period, each extending rapidly uphill by slipping of the overstepped dry coal face. In the 2nd Stage a 0.2 m thick slab, comprising the whole face, failed moving the previous debris ahead. In the 3rd Stage, a deep compound slide initiated, pushing the previously failed material horizontally, with the whole mass decelerating and coming to rest.

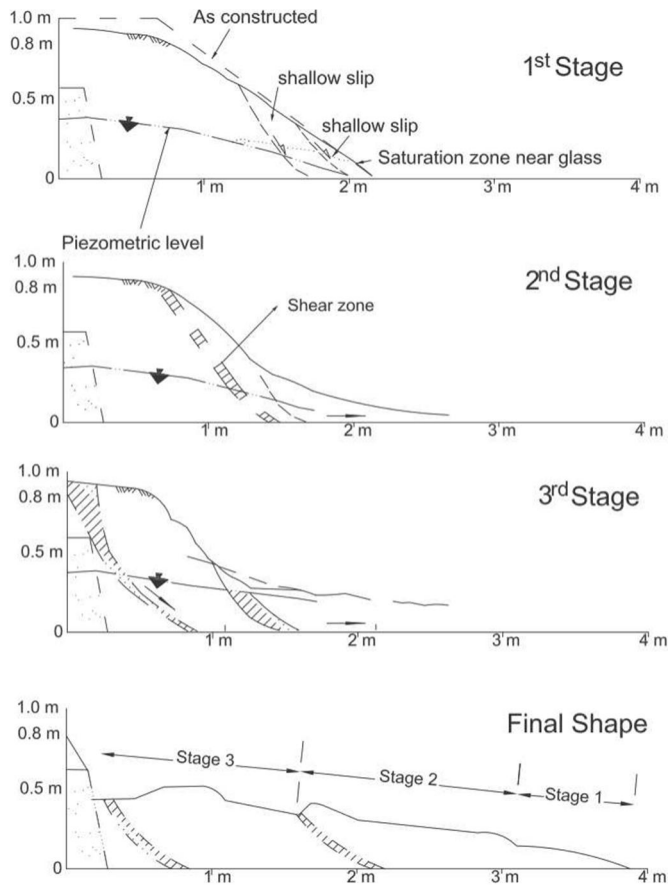


Figure 6-8 Results of flume test #7 (from Eckersley, 1990): failure and post-failure stages.

6.2.2 MPM Modelling

MPM modelling of the slope test was based on two main assumptions: i) the simulation was initialized starting from the critical water table observed at failure during the experiment, ii) matric suction was assumed negligible and disregarded. Thus, the slope scheme was schematised in two layers: a dry (upper) layer simulated by a single-phase material, and a (lower) saturated layer simulated by a two phase materials separately considering the solid skeleton and the liquid (Figure 6-9). The plywood floor was simulated by a linear elastic material above which a frictional

6. MODELLING OF SMALL SCALED SLOPES

contact algorithm was applied (3.2.4.3), considering a friction coefficient equal to 0.5 (Eckersley, 1990). The computational mesh was composed of 4-nodes unstructured tetrahedral elements; 4 material points were initialized in each element.

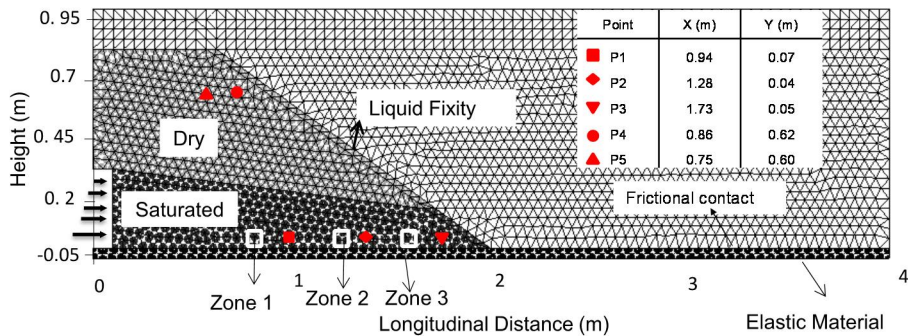


Figure 6-9, MPM model and its initial condition, with the indication of the (moving) tracking points (P1-P5) and the (fixed) control Zones (1-3).

6.2.3 Simulation of the Slope using Lab tests outcomes

The material parameters for hypoplastic model have been determined in Sec. 4.3, those value are initially used to simulate the slope failure. Yet, the void ratio of material at the onset of failure is still unknown. In the model e_{p0} was used to compute (Eq.(3-93)) the void ratio at the onset of failure (e_p), whose value in the Zone 1 was assumed as representative of the slope response. Figure 6-10 shows the shear strains computed in different cases. The lower the initial void ratio, the worse the final deep-seated failure was simulated, and the shorter was the computed run-out. For $e_p=0.61$, the simulation was able to qualitatively reproduce the main observations, such as the retrogressive failure mode, the three slope instability stages and the final shape of the slope (Figure 6-8). The main difference with the observed behaviour of the slope concerns the formation of the deep shear band, which started progressing backwards when the shallow shear sliding was not yet completely developed.

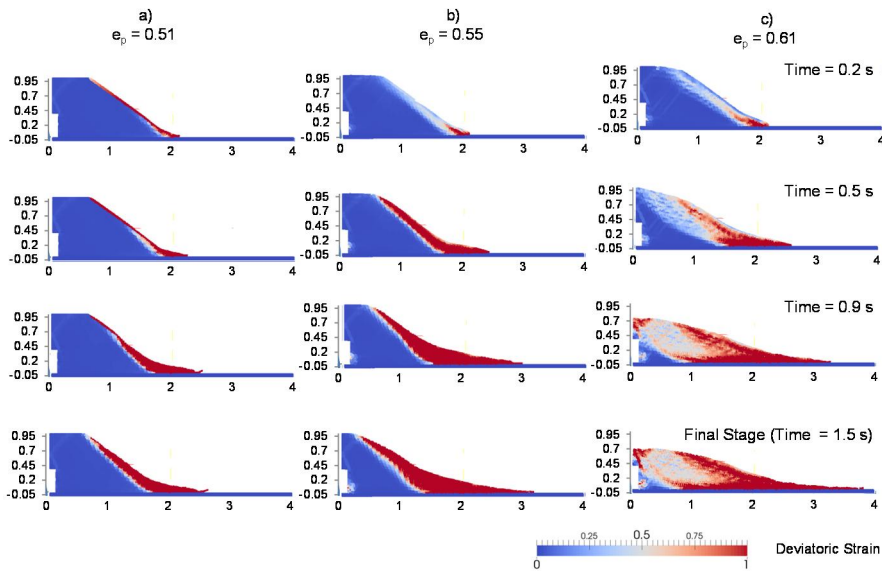


Figure 6-10, Displacements and deviatoric shear strains computed at different times depending on the initial void ratio. In the Zone 1, at $t=0$, e_p : 0.51 (a), 0.55 (b), 0.61 (c).

6.2.4 Recalibration of the parameters

Since the sequence of excess pore water pressure was coherent with what expected, the mentioned mismatch could be attributed to the fact that the parameters estimation was based only on undrained tests with a confining pressure equal to 50 kPa, while the average mean effective stress at the base of the slope was much lower (about 4.0 kPa). In this regard, it is well known that soil strength parameters may be related to the average stress level. More specifically, the stress dependency of the frictional and dilation angle for sand was firstly highlighted by [119], who showed that very low mean stresses lead to higher frictional angle values. On the other hand, as it was mentioned before, [105] showed that the parameter has a direct effect on the mobilized friction angle. Therefore, in order to reproduce the correct strength behaviour of the material at a stress of level close to what it is going to experience the model in a crucial part of the slope, further calibration was required. Based on what [29] also suggested, special attention should be given to the parameter α . About this issue, Sec. 4.1 showed that the optimal value for parameter

obtained considering a curve fitting procedure of elemental test results is significantly influenced by the stress level of the adopted observations. For all these reasons parameter α . Should be recalibrated again.

A parametric analysis was conducted with α . Ranging from 0.05 to 0.58. By reducing α the behaviour of both the saturated layer and the dry layer was well simulated for the entire slope instability phenomenon, as a rapid continuous retrogressive movement develops along a non-circular (or compound) slip surface (Figure 6-11). Firstly, shallow sliding occurred at the toe, later extending rapidly upwards because of the mobilization of the over-steepened dry material. Then, the slip surface continuously evolved towards the rear of the slope, as experimentally observed. The effect of the parameter α . on the results of undrained triaxial test simulation was additionally investigated. Some REV models of undrained triaxial tests with initial void ration of 0.61 and confining pressure of 4.34 kpa, i.e, state condition of the soil at the base of the slope, are created. A sensitivity analysis in terms of parameter α was carried out. it was observed that reduction in this parameter increases the modelled peak deviatoric stress, leads to higher mobilized friction angles at low strains while the critical friction angle are converging to the unique value at large strain and is consistent with that used in the slope simulations (i.e. 40°) (Figure 6-12). The new set of constitutive model parameters is called "modified set" from here onward.

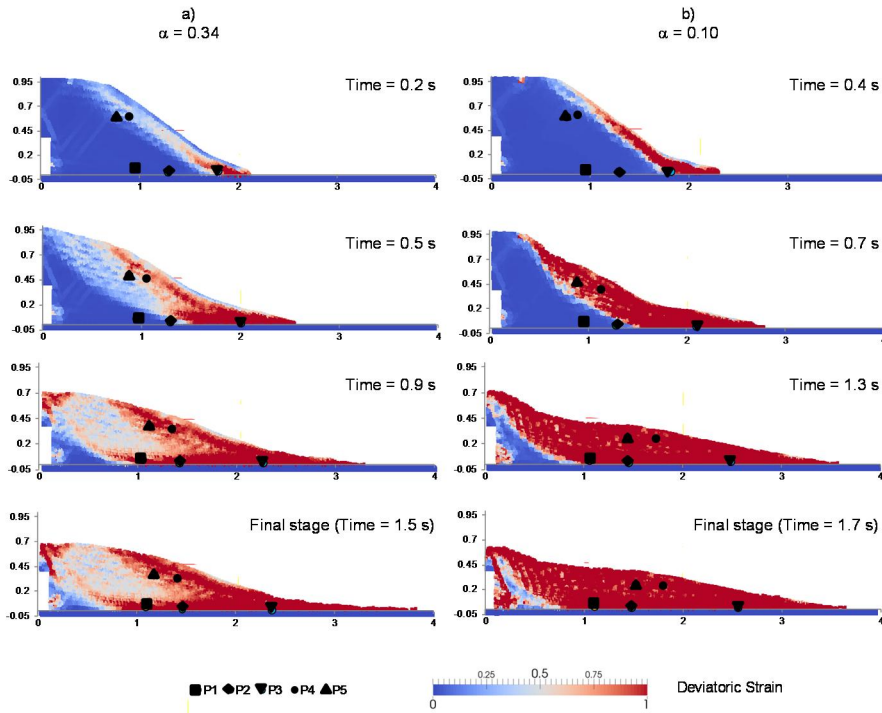
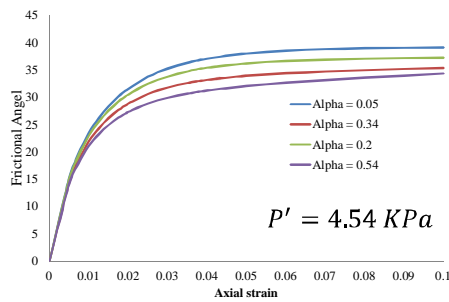


Figure 6-11, Displacements and deviatoric shear strains computed at different times for: a) $\alpha = 0.34$ (original set of parameters) b) $\alpha = 0.10$ (modified set of parameters).



(b)

Figure 6-12 , Effect of Parameter α on mobilized friction angle.

Based on the satisfactory results achieved using the “modified set” of parameters, a detailed inspection of the slope behaviour was carried out.

6. MODELLING OF SMALL SCALED SLOPES

The path in the (e-p') diagram was elaborated for the 5 control points (Figure 6-13). At P3 (located at the toe of the slope) the mean effective stress significantly reduced while the void ratio remained almost constant. This implied a first local undrained shearing (1st stage). The latter then proceeded progressively towards the rear of the slope, and with a significant build-up of pore pressure due to soil contractancy. Point P2 reached the CSL with both the mean effective stress and void ratio noticeably decreasing (2nd stage). The reduction of mean effective stress could be due to: i) change in slope geometry after the first failure, so that a thin layer at the slope surface was relocated with a reduction of vertical effective stress; ii) rising of excess pore water pressure caused by undrained shearing, commonly described as static liquefaction. In the 3rd stage of slope instability point P1 reached the CSL, similarly to the points P2 and P3, showing a significant reduction of the mean effective stress. Finally, the points located in the dry part of the slope (P4 and P5) reached the CSL mainly by means of a reduction in void ratio and slight changes in effective stress.

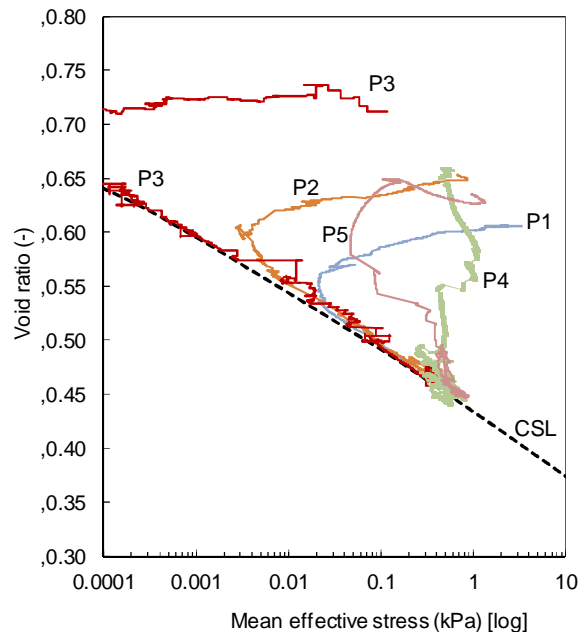


Figure 6-13, Evolution of the control points (P1-P5) in the e-p' plot during the slope instability process.

Contouring of the mean effective stress (p') is reported in Figure 6-14 at different times to indicate how much and where the localized shear bands with low value of p' evolved inside the slope during the large deformations process.

Figure 6-15 shows the changes of pore water pressure recorded over time in the three fixed Zones Z1-Z2-Z3. At the onset of each stage of slope instability, the pore water pressures reached their maximum value while the mean effective stress reached a nil value and liquefaction occurred. Afterwards, the excess pore water pressure vanished, due to consolidation, and the material gained higher effective stresses and thus a shear strength. Thus, the modelling was able to reproduce not only the transition from solid-like to fluid-like behaviour (liquefaction) but also the opposite process during the material propagation and deposition.

As last insight, the attention was focused at P1 where, in a first stage, the void ratio remained almost constant, and the mean effective stress reduced slightly without vanishing completely (Figure 6-16). At time equal to 1.0 s, the void ratio started decreasing and the declining rate of effective stress changed. The point at which the void ratio started to change and the dramatic drop in stress initiated could be considered an instability point. Afterwards, the mean effective stress decreased rapidly and the material liquefied when the stress became zero. It should be underlined that the slight reduction of mean effective stress before the instability point was due to the changes in the geometry of the slope that happened in the previous failure stages. Another important insight was the fact that the particle did not reach the critical state, i.e. the situation in which void ratio and critical void ratio converge, until time equal to 1.3 s, which is quite far from the initiation of liquefaction and instability. This clearly proved the distance between the instability and failure states of the material.

6. MODELLING OF SMALL SCALED SLOPES

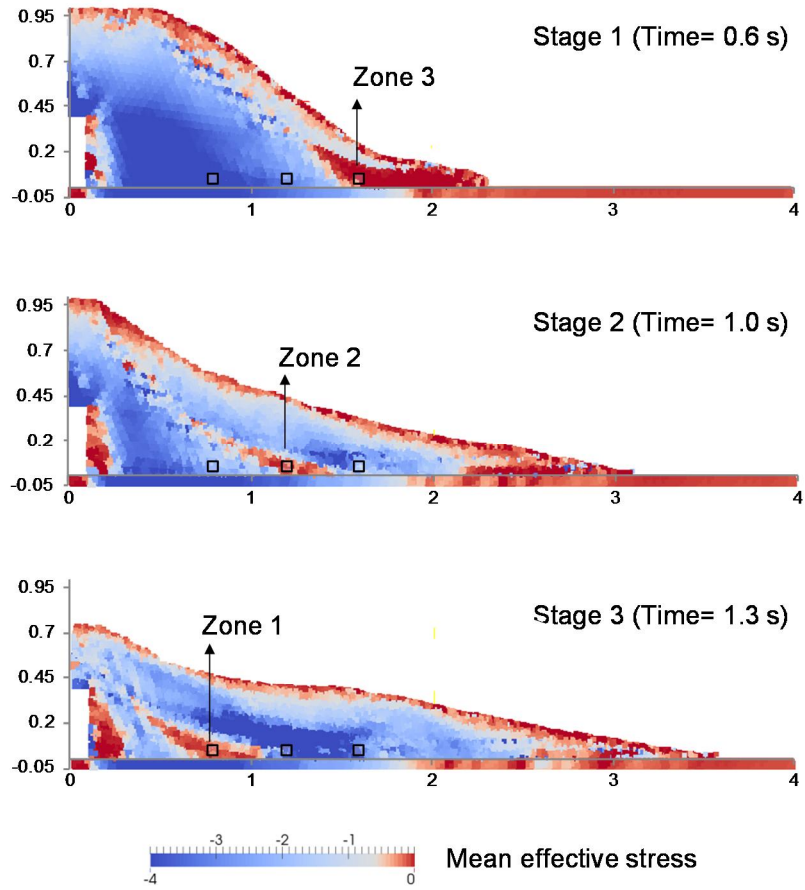


Figure 6-14, Mean effective stresses during the three slope instability stages

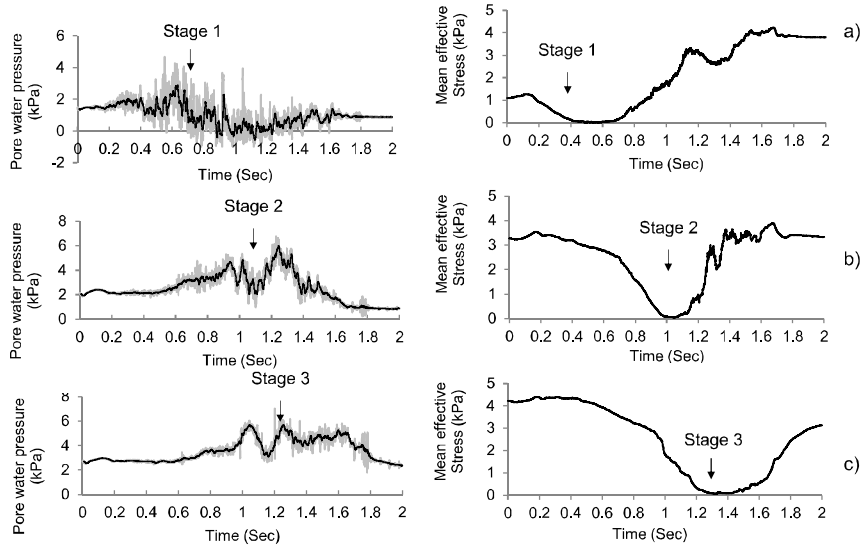


Figure 6-15, Pore water pressure and mean effective stress simulated over time at the tracked zones.

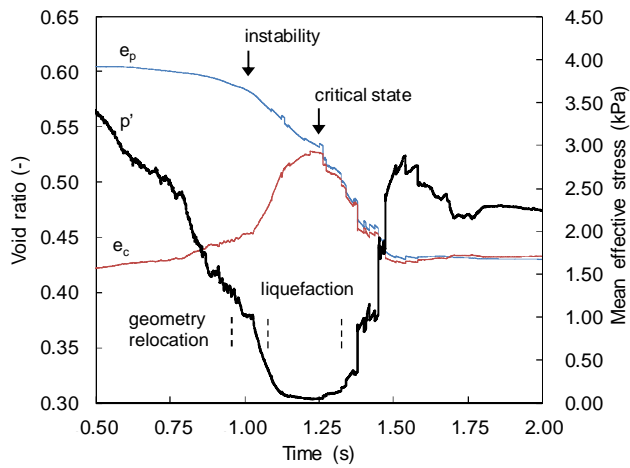


Figure 6-16, Point P1 tracked over time: a) current and critical void ratios; b) mean effective stress.

6.3 CONCLUSIONS

Two modelling examples of laboratory slope tests were provided to show how inverse analysis approaches can be effectively used for the calibration of MPM models that are able to reproduce complex slope evolution scenarios. Particularly, a progressive-retrogressive failure including soil liquefaction and a fast large run-out propagation problem were satisfactorily simulated. In both cases, inverse analysis was used but with different scopes. For the slope case the used constitutive model included several parameters to be estimated. Therefore, inverse analysis was used to calibrate the mechanical soil parameters from triaxial tests, and those parameters were then used for the MPM model of the boundary value problem. On the other hand, for the flume test, inverse analysis was directly used to calibrate a relatively simple MPM model of the slope, adopting an elastic perfectly plastic constitutive law to simulate the propagating soil mass and a purely frictional law to model the contact between the soil and the base of the experimental apparatus. The two case studies show that inverse analysis can contribute to enhance the potential of MPM modelling. More generally, MPM models calibrated using reduced-scale laboratory slopes can be used to analyse the effect played by some soil parameters on landslide triggering and propagation.

7 SIMULATION OF A RAINFALL-INDUCED LANDSLIDE IN HONG KONG

In this chapter a well-known rainfall induced landslide is investigated using back-analysis and inverse analysis. First of all the Hong Kong case study and the available data are presented and discussed, then the mentioned frame work in Sec.3.5 is adopted to back-analysis the landslide and calibrates the model.

7.1 DESCRIPTION AND SOIL FEATURES

On 12-13 August 1995, a landslide occurred at Fei Tsui Road in Chai Wan, Hong Kong (HK), during intense rainfall related to the passing of a typhoon. The Geotechnical Engineering Office (GEO) of HK investigated the landslide and the results of this investigation are reported in [122]. The Fei Tsui Road landslide, with a volume of about 14000 m³, is one of the largest and most mobile cut slope failures reported in Hong Kong over the last few decades. That is why this case study has caught the attention of many other researchers. For example, [23] adopted the Lagrangian Galerkin finite element method to simulate its propagation stage. In another research, [48] used data from this landslide to validate the accuracy of their suggested model, which adopted an apparent friction varying during the landslide motion. [123] depicted the qualitative match between the available information measured from the Fei Tsui Road landslide and the results of their landslide propagation modelling conducted by means of a mesh-less numerical method.

The geology of the landslide area comprises weathered volcanic rock overlain by a layer of fill about 3 m thick at the top of the slope. The weathered rock includes completely to slightly decomposed tuff, whose thickness ranges from about 4 m on the eastern side of the landslide area to about 11 m on the western side. A comprehensive series of geotechnical laboratory tests was conducted on soil samples retrieved during the ground investigation to identify the main soil properties of the weathered tuff. The average strength parameters of this layer, through which the basal surface of the landslide developed, are: shearing resistance (φ') equal to 29° and cohesion intercept (c') equal to zero. Based on the available information, it was postulated that two groundwater regimes existed at the site at the time of the landslide, a regional groundwater table within the rock mass below the altered tuff layer, and a perched water table in the weathered volcanic soil overlying the altered tuff layer. [122] Reported that the groundwater table was unlikely to have been above the base of the landslide at the time of the failure, and hence it could not have had any significant effect on the landslide. Yet, the perched groundwater regime operating in the altered tuff layer and in the ground above is likely to have been an important factor in causing the landslide. This issue will be discussed later in more detail.

7. SIMULATION OF A RAINFALL-INDUCED LANDSLIDE IN HONG KONG

Figure 7-1 shows the plan view and the cross section of the landslide debris ([122]). The slope before landslide occurred had a maximum height of about 27 m and an overall slope angle of about 60°. The failure occurred at the highest part of the cut-slope along a section about 50–60 m long. The main scarp was 15 m behind the original cut-slope crest (Figure 7-2).

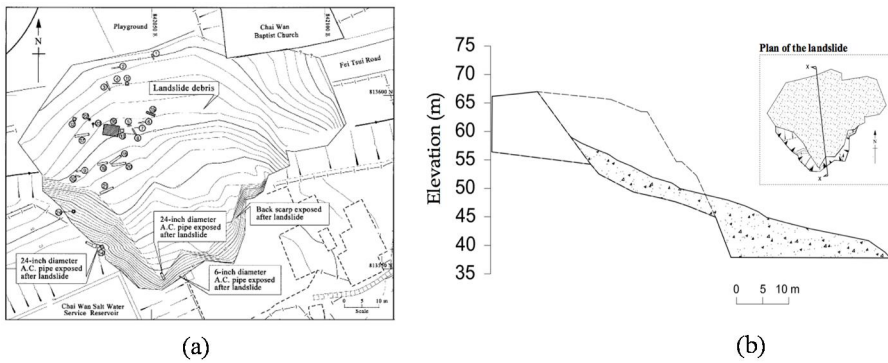


Figure 7-1 (a) Plan view of landslide of topography contours of debris thickness
(b) Landslide debris in plan and section views

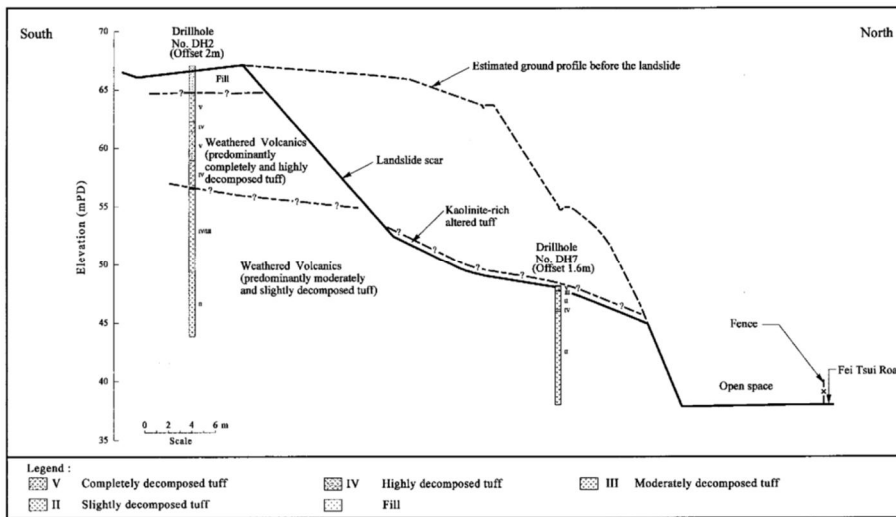
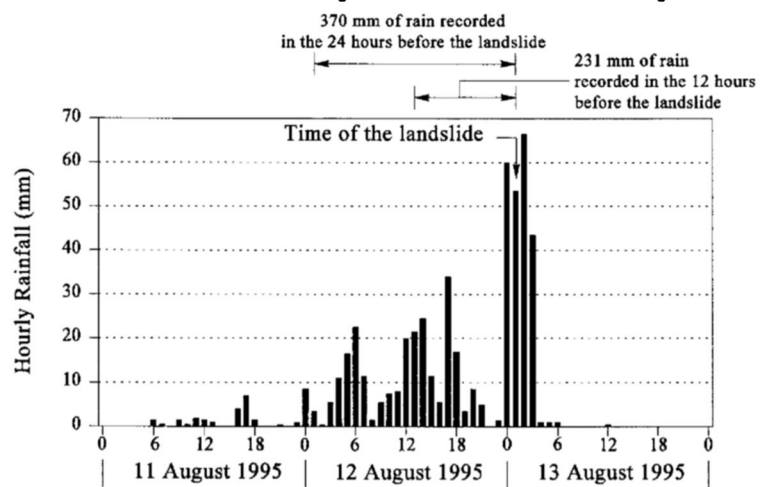


Figure 7-2 Typical stratigraphy through the landslide site ([122])

The failure is likely to be principally related to the presence of the extensive altered tuff layer that governed the landslide, which has not been commonly observed in other landslides in Hong Kong. The persistent and weak altered tuff layer, which was about 15 m below the crest of the cut slope, is thought to have rendered the large deep failure possible. The landslide occurred after a period of exceptional prolonged rainfall that was the heaviest recorded near the site since 1979. The hourly rainfalls from 11 to 13 August 1995 are shown in Figure 7-3.



(b) Hourly Rainfall Intensities from 11 to 13 August 1995

Figure 7-3 Hourly rainfall intensities from 11 to 13 August 1995 ([122])

The heavy rain is likely to have led to the development of a perched water table above the altered tuff layer. This scenario is supported by site observations and it is consistent with the hydrogeological regime at the site. A rise in the perched water table would have increased the water pressure in the altered tuff and resulted in a reduction of the material shear strength and thus culminated in the landslide (Figure 7-4).

7. SIMULATION OF A RAINFALL-INDUCED LANDSLIDE IN HONG KONG

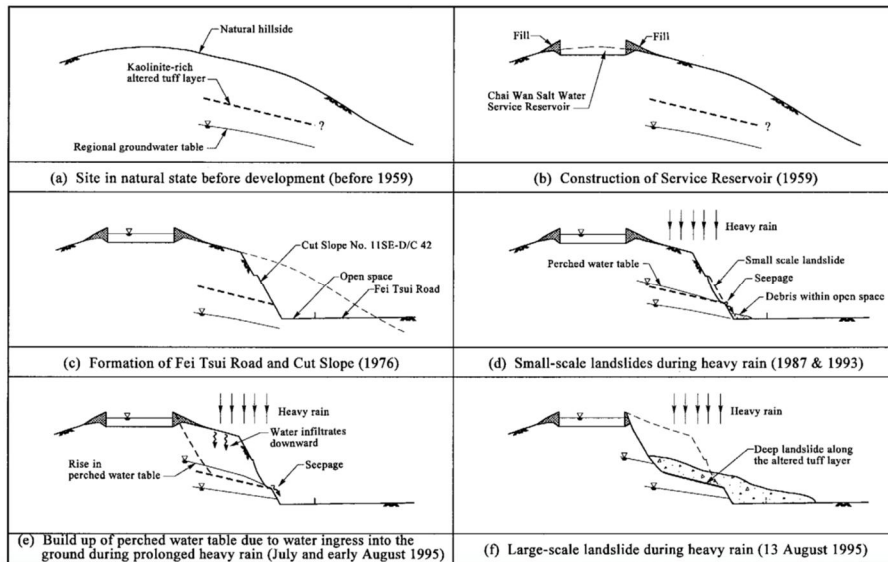


Figure 7-4 Probable sequence of the events ([122])

The average depth of the landslide was about 15 m, which is deep compared with other rain-induced slope failures in Hong Kong. About 14,000 m³ of debris were released in the landslide. The maximum horizontal travel distance of the debris was about 70 m, as measured from the crest of the landslide. The maximum width of the debris mound was about 90 m (Figure 7-1b).

Two groundwater regimes are recognised at the site: a deeper regional water table and a shallower perched water table retained by the kaolinitic clay layer at a higher level. The regional water table, as based upon observations in boreholes drilled after the landslide, is 4 to 8 m below the kaolinitic clay layer. The perched water table was unlikely to have built up to the level of the exposed back scarp, which is about 4 m to 5 m above the altered tuff layer, because of the lack of signs of significant seepage at the back scarp exposed in the landslide. As a best estimate, the perched water level was in the range of 1 m to 4 m above the altered tuff layer when the landslide took place, as shown in Figure 7-5.

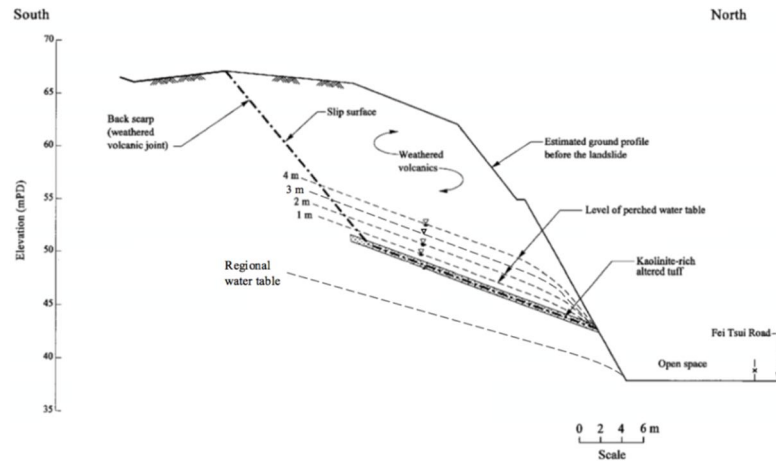


Figure 7-5 Groundwater regime ([122])

The geology at the landslide area comprises weathered volcanic rock overlain by a layer of fill up to about 3 m thick at the top of the slope. The presence of kaolinite is not unusual in altered or weathered rocks in Hong Kong. In this case, unusual is that the kaolinite was present as a relatively thick, continuous layer.

Referring to the main scheme that is used in Hong Kong for the classification of rock mass weathering, that is the Partial Weathering or 'PW' scheme (GCO, 1988a), six grades can be used to classify the decomposed volcanic rocks in Hong Kong. Normally, the first three grades (Grade VI to Grade IV) are considered as soils and the other grades (Grade III to Grade I) are considered as rocks for practical purposes. The weathered rock in the site consists of completely to slightly decomposed tuff. Across the site, the lower 5 m to 7 m of the cut slope is predominantly composed of moderately to slightly decomposed tuff and it did not form part of the landslide.

The typical permeability ranges for completely decomposed tuff in Hong Kong is between 10^{-5} ÷ 10^{-7} m/s (GEO, 1993).

7. SIMULATION OF A RAINFALL-INDUCED LANDSLIDE IN HONG KONG

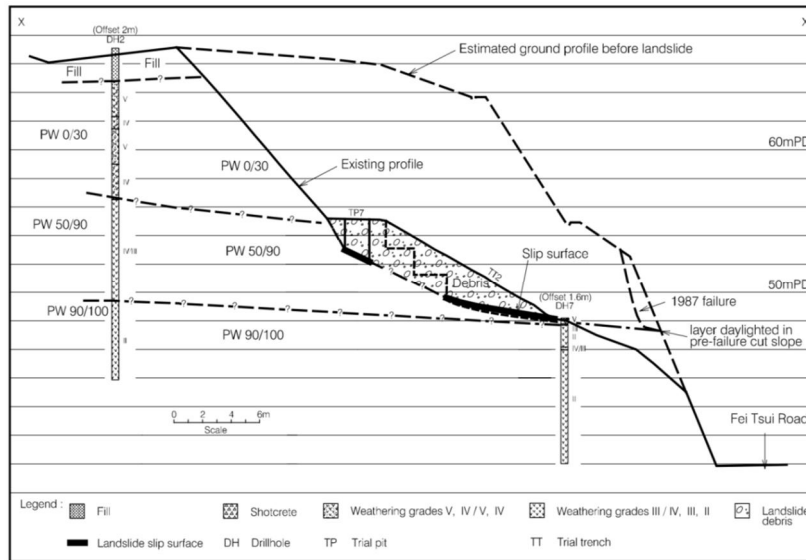


Figure 7-6 Geological cross section of the slope before that landslide occurred ([122])

A comprehensive series of classification, strength and consolidation tests has been carried out on the materials within the landslide that are relevant to the stability of the slope. These tests aimed to determine the geotechnical properties of the kaolinite-rich altered tuff and the weathered volcanic joints, which formed the basal slip surface and the back scarp respectively.

A range of shear strength values has been established dependent on the relative proportion of kaolinite, and associated veining, with the altered tuff. The lower bound value of $\varphi' = 22^\circ$, $c' = 0$ was assigned to the situation where shearing was through soil with a higher kaolinite content and $\varphi' = 29^\circ$, $c' = 0$ was considered representative of the kaolinite-rich altered tuff layer which formed the basal failure surface of the landslide. The average φ' for weathered volcanic joints was found by direct shear tests to be 35° , with zero cohesion. The shear strength of the two soils are represented in Figure 7-7.

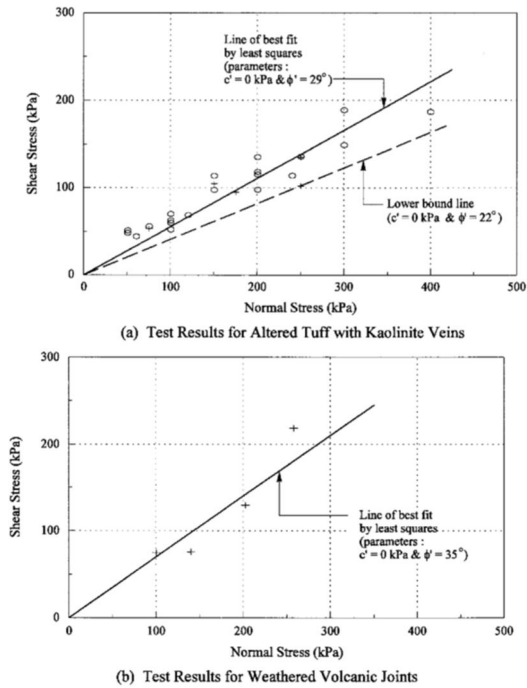


Figure 7-7 Direct shear test results for altered tuff with kaolinite veins (a) and for weathered volcanic joints (b) ([122]).

Table 7-1 Soil materials properties (data from [122]).

Soil material	Weathered volcanic joints	Altered tuff with kaolinite veins
Unit weight (γ)	19 kN/m ³	19 kN/m ³
Average fines (clay and silt)	71%	92%
Plasticity index (PI)	9 ÷ 18	9 ÷ 18
Liquid limit (w_L)	29 ÷ 50	29 ÷ 50
Cohesion (c')	0 kPa	0 kPa
Internal friction angle (ϕ')	35°	22° ÷ 29°
Saturated hydraulic conductivity (k_{sat}) *	10 ⁻⁵ ÷ 10 ⁻⁷ m/s	10 ⁻⁵ ÷ 10 ⁻⁷ m/s

7. SIMULATION OF A RAINFALL-INDUCED LANDSLIDE IN HONG KONG

*typical ranges of Hong Kong completely decomposed tuff, from GEO (1993)

It is difficult to establish the unsaturated characteristics of the soil materials in the landslide site, because there is no so much data available. For this reason, the characteristic curves were obtained from GeoStudio software, referring to previous studies, in which completely decomposed tuff (CDT) properties are described. GeoStudio uses the [124] method to predict the volumetric water content function using some parameters, that are porosity, diameter (mm) at 10% and 60% passing and liquid limit.

Four CDT samples have been compared, each of them was taken from a different article. In synthesis, storage water content curves are shown in Figure 7-8.

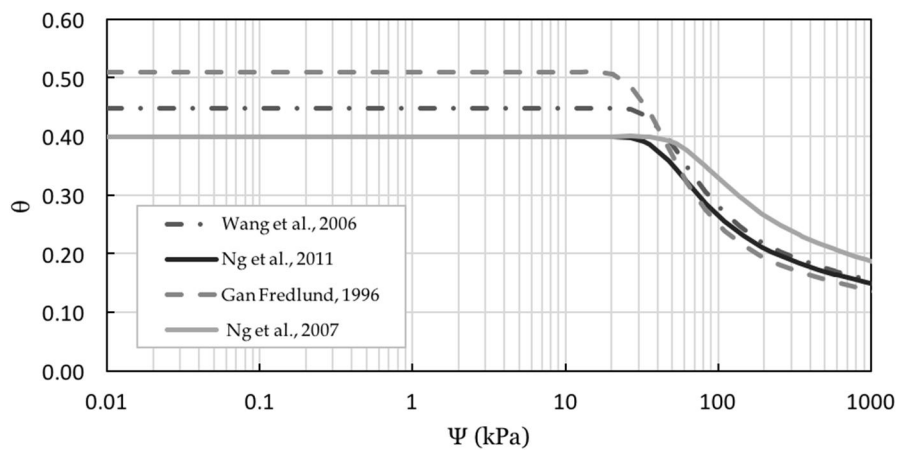


Figure 7-8 Water retention curves ([125])

7.2 SPH MODELLING OF LANDSLIDE PROPAGATION

7.2.1 The adopted procedure and data set

As it mentioned before, the aim of this research is to show the possibility of using the geometrical observations to back-analysing the landslide and to figure out the geo-mechanical or hydraulically soil characteristics based on geometrical response. This kind of data is particularly useful for the simulation of the propagation stage of landslides. Concerning that, for a well-posed inverse analysis problem, it is very important to choose proper sets of observations-not always an easy task to perform. In this section the roles of observation in inverse analysis procedure would be addressed. The aim is to find a most relevant set of observation consists of minimum required information that is sufficient to obtain the soil characteristics thorough an inverse analysis procedure.

To this aim, this section proposes an original procedure to optimize the calibration of a landslide propagation model when observations of the deposition heights are available. The procedure is organised in two sequential steps and it includes both parametric and optimisation analyses, wherein the results of the first ones provide relevant information for the second ones. The observation sets employed in the definition of the inverse problem always refer to the values of soil deposit thickness, yet they differ for both the location and the number of adopted field values. During the first step of the procedure, when the analyses are conducted using a simpler rheology to model the propagating soil, many observation sets are tested with the aim of defining the ones that are most suitable to be used for the back-analysis of the landslide. Those sets are then used, in the second step of the procedure, to calibrate the model parameters of a more complex two-phase soil model.

Figure 7-9 shows the procedure employed herein to calibrate the input parameters of a numerical model that simulates the propagation of a landslide, when observations of the deposition heights are available. It is assumed that landslide propagation is simulated by two different mathematical models: mixed-phase or two-phase. In the former, one single input parameter is needed; in the latter, multiple input parameters

7. SIMULATION OF A RAINFALL-INDUCED LANDSLIDE IN HONG KONG

are required. The procedure is essentially based on a series of back-analyses - i.e. parametric and optimisation analyses - organised in two sequential steps, one for each model. The observation sets used in the analyses are always defined using in-situ records of deposition heights of the soil mass above the original ground surface. During the first step of the procedure, when the analyses are conducted using the mixed-phase model, many observation sets are tested with the aim of defining the ones that are most suitable to be used for the back-analysis of the considered debris flow. Those sets are then used, in the second step of the procedure, to calibrate the model parameters of the two-phase model.

The parametric analyses are conducted, in both steps, to evaluate the effect of the model parameters' values on the values of error functions quantifying the difference between simulated and observed landslide behaviour, such as the model error variance (s). The number of error functions to compute, for each analysis, is equal to the number of observation sets considered. The values assumed by each error function depend on the values assumed by the model parameters; to this aim, the analyst needs to define a range of values, by specifying a minimum, a maximum and a number of intermediate discrete values, for each model parameter to be tested within the parametric analysis. While in the first step of the procedure the model parameter to calibrate is only one, in the second step the model parameters are many. For the latter case, the parametric analysis is conducted using pairwise combinations of the parameters so that the results are easily representable by means of charts showing the value of the model error variance as a function equation (3-27) of the values of the parameters. In the first step, aim of the parametric analysis is to compare the effect on the results of the values assumed by the (single) model parameter, when different sets of observations are used to quantify the model error variance. To this aim, an observation set is assumed to be relevant for subsequent analyses if the minimum value of the model error variance does not occur when the parameter assumes either the minimum or the maximum value of the specified range. In other words, a set of observations is deemed adequate for back-analysis purposes if the error function is not monotonically increasing or decreasing as the model parameter changes within a reasonable range of values. In the second step, the aim of the parametric analysis is to identify, among the many input parameters of the model, the relevant ones to be used within the final optimisation analysis. To

this aim, an input parameter is assumed to be irrelevant for the performance of the model if the model error variance does not change significantly considering the parameter's adopted range of values.

The optimisation analyses are conducted, in both steps of the procedure, employing the regression algorithm described in the previous section. In the first step, the aim of the optimisation analysis is the identification of the observation sets most suitable for the quantification of the model error variance and for its minimization by means of an automated inverse analysis algorithm. To this aim, the following items are considered: consistency with the results of the parametric analysis; number of iterations needed for convergence; stability of the regression results for different initial values of the model parameter. In the second step, the aim of the optimisation analysis is the final calibration of the two-phase model relevant parameters, i.e. the definition of the parameters' values optimising the performance of the numerical model in relation to the observed deposition heights. To this aim, the initial values of the parameters are retrieved from the results of the parametric analysis. In this final step, the values of the regression input parameters must be "tuned" to ensure that the optimisation analysis converges towards reasonable values of the model parameters within a reasonable number of iterations. In other words, the minimisation of the model error variance must be always be coupled with an assessment (i.e. engineering judgment) of the soundness of the results obtained by the employed optimisation algorithm.

7. SIMULATION OF A RAINFALL-INDUCED LANDSLIDE IN HONG KONG

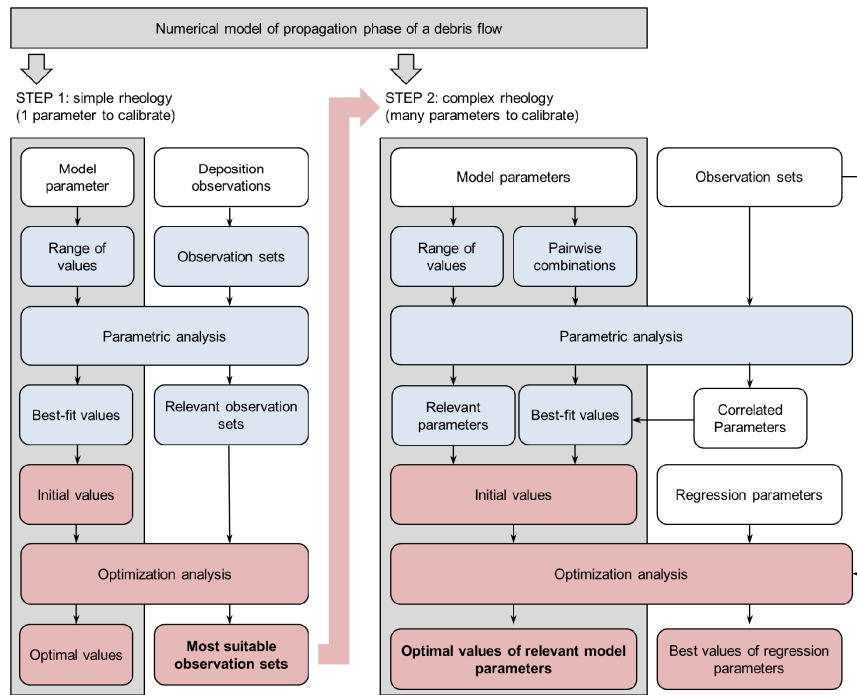


Figure 7-9 Procedure employed to calibrate the input parameters of a numerical model that simulates the propagation of a landslide.

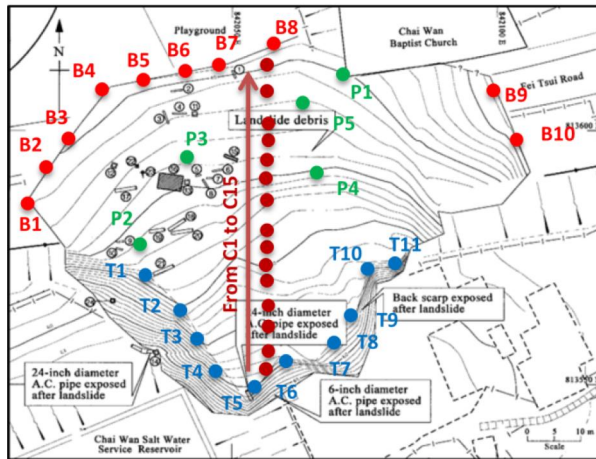
Figure 7-10 shows the plan view and the cross section of the landslide debris ([122]). The height of soil deposition in different points of the landslide was obtained from field evidence. Four classes of deposition height observations, completely covering the main geometric features of the landslide, have been chosen to compute a number of different objective functions for model calibration (Table 7-2): points lying at the bottom boundary of the deposition zone (indicated with the letter B); points located at the topmost boundary of the displaced mass (indicated with the letter T); points situated along the most representative cross-section of the landslide (indicated with the letter C); and other characteristic points where information on the deposition height is available (indicated with the letter P). To perform the analyses, a total of 40 observations have been selected (B1 to B10, T1 to T10, C1 to C15, P1 to P5), from which 13 observation sets have been derived. The

adopted sets of observations correspond to different strategies that can be used to compute the objective function to minimise by inverse analysis, considering: one or multiple classes of observations; or a few or many points within each class of observations.

Table 7-2 Sets of observations used for model calibration.

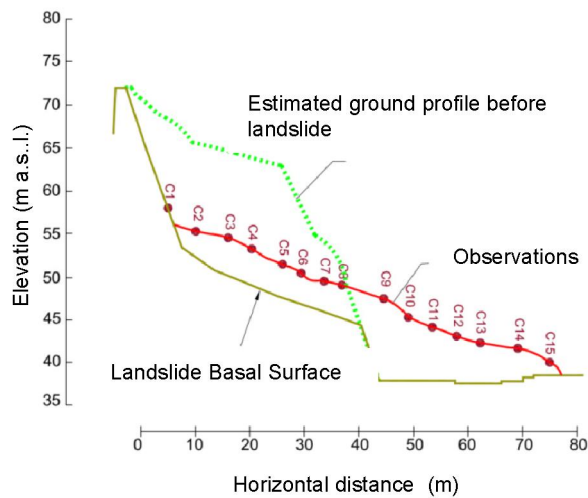
No	Observations	Description of deposition height observations
1	C1 to C15	15 points along main cross section
2	P1 to P5	5 characteristic points in the deposition zone
3	B1 to B10	10 points along bottom boundary of deposition zone
4	T1 to T10	10 points along topmost boundary of the displaced mass
5	B1 to B10, T1 to T10	Set 3 + Set 4
6	B1 to B10, P3	Set 3 + one characteristic point (max height)
7	B1 to B10, P1	Set 3 + one characteristic point (building)
8	T1 to T10, P3	Set 4 + one characteristic point (max height)
9	T1 to T10, P1	Set 4 + one characteristic point (building)
10	B1 to B10, P1, P3	Set 3 + two characteristic points (max height, building)
11	B1 to B10, T1 to T10, P3	Set 3 + Set 4 + one characteristic point (max height)
12	B1-3-5-7-9, T1-3-5-7-9, P3	5 points from Sets 3 and 4 + one characteristic point (max height)
13	All	Set 1 + Set 2 + Set 3 + Set 4
No	Observations	Description of deposition height observations

7. SIMULATION OF A RAINFALL-INDUCED LANDSLIDE IN HONG KONG



- Bottom Boundary point ● Top Boundary point
- Cross-Section point ● Point on the deposit zone

(a)



(b)

Figure 7-10 Location of the landslide deposition height observations used to compute the objective functions for model calibration: a) plan view (modified from [122]); b) cross-section.

7.2.2 Definition of parametric studies

The parametric analyses are conducted, as previously described, in both steps of the proposed procedure to evaluate the effect of the model input parameters on the model error function, i.e. the difference between computed and observed landslide behaviour considering a set of observations. Table 7-3 shows the model adopted, the rheological laws, the values of the input parameters and the number of simulations performed for the parametric analyses. Study 1 refers to the analysis performed within the first step of the procedure, when the landslide is modelled using a mixed-phase model and the adopted frictional rheology is based on a single input parameter, the basal friction angle (ϕ_b). Studies 2 to 4 refer to the analyses performed within the second step of the procedure, when the landslide is modelled using a two-phase model and the adopted frictional rheology is based on four input parameters: the friction angle (ϕ_b); the consolidation factor (c_v); the ratio between the initial basal pore-water pressure and the liquefaction pressure (p_w^{rel}); and the relative water height (h_w^{rel}). These three studies are defined considering pairwise combinations of the four input parameters. In all cases, the values assumed by the error functions depend on the values assumed by the model parameters, therefore a minimum, a maximum and a number of intermediate discrete values have been specified, in each study, for each model parameter. The number of error functions computed for each simulation is 13, i.e. equal to the number of observation sets considered (see Table 7-2).

7. SIMULATION OF A RAINFALL-INDUCED LANDSLIDE IN HONG KONG

Table 7-3 Material schematization, rheological laws, values of the input parameters and number of simulations performed for the parametric analyses.

	Study 1	Study 2	Study 3	Study 4
Model	mixed-phase model	two-phase model	two-phase model	two-phase model
Rheology	Frictional (Eq.1)	Frictional (Eq. 2, 3)	Frictional (Eq. 2, 3)	Frictional (Eq. 2, 3)
No. of parameters	1	4	4	4
$\tan \phi_b$	0.40,0.42, 0.44, 0.46,0.48, 0.50, 0.52,0.54, 0.56, 0.58, 0.60	0.45,0.50, 0.55, 0.60,0.65, 0.70, 0.75	0.45,0.50, 0.55, 0.60,0.65, 0.70, 0.75	0.45,0.50, 0.55, 0.60,0.65, 0.70, 0.75
c_v	-	0.001,0.005, 0.01, 0.05, 0.10	0.01	0.01
p_w^{rel}	-	0.1	0.01,0.05, 0.10, 0.15, 0.20	0.1
h_w^{rel}	-	0.33	0.33	0.074, 0.14, 0.33, 0.44, 0.51
No. of simulations	11	35	35	35

Table 7-4 Linear correlation coefficients between the parameters of the rheological law, computed from the variance-covariance matrix for the following values of the parameters:

$\tan \phi_b = 0.55$, $c_v = 0.01$, $p_w^{rel} = 0.1$, $h_w^{rel} = 0.33$.

	$\tan \phi_b$	c_v	p_w^{rel}	h_w^{rel}
$\tan \phi_b$	1.00	0.26	0.90	0.23
c_v	0.26	1.00	0.55	0.90
p_w^{rel}	0.90	0.55	1.00	0.52
h_w^{rel}	0.23	0.90	0.52	1.00

7.2.3 Observations Selection

In the first step of the adopted procedure, the model used to simulate the propagating mass of the landslide employs one input parameter, $\tan \phi_b$. This step of the procedure comprises, as shown in Figure 1, a parametric analysis and an optimisation analysis. The parametric analysis adopts a large number of observations - grouped in 13 observation sets - to quantify the model error variance (see Table 7-2). The aim of this analysis is to define the observation sets most relevant for the subsequent analyses. An observation set is assumed to be relevant for back-analysis purposes if the error function is not monotonically increasing or decreasing as the model parameter changes within a reasonable range of values. Herein, the parametric analysis is executed by means of a single study (indicated as study 1 in Table 7-3) using 11 simulations evaluating the effects of the variations of $\tan \phi_b$ within the range of values 0.4-0.6 ($22^\circ \leq \phi_b \leq 31^\circ$). For each simulation, 13 error functions are computed, being equal in number to the number of observation sets considered. The main results of the parametric analysis are reported in Figure 7-11 and Figure 7-12.

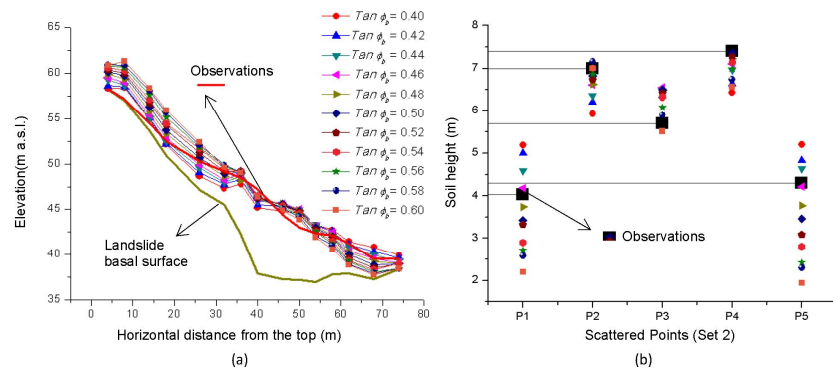


Figure 7-11 Parametric study 1: comparison between observations and computed results for observation set 1 (a) and observation set 2 (b).

7. SIMULATION OF A RAINFALL-INDUCED LANDSLIDE IN HONG KONG

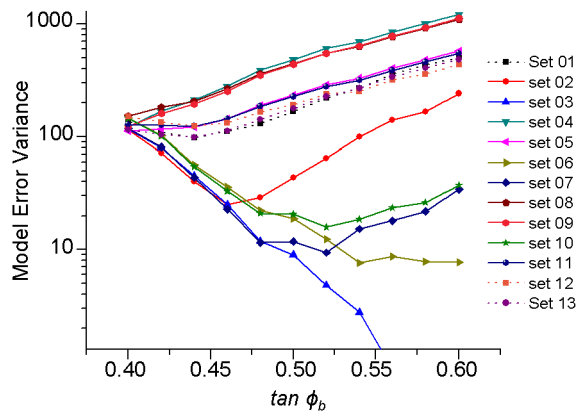


Figure 7-12 Parametric study 1: model error variance vs. value of model parameter, $\tan \phi_b$, for the 13 observation sets employed in the analysis.

Figure 7-11a shows a comparison between the soil height observations along the main cross section of the landslide - i.e. observation set No. 1 - and the results of the 11 performed simulations. The agreement between observations and simulated results appears to be good in the middle of the cross section, yet most of the simulations over predict the soil heights at the top of the cross section and under predict them at the bottom of the section. As expected, an inverse relationship exists between the value of the basal friction angle and the height of the soil in the lowermost deposition zone. In Figure 7-11b, the comparison focuses on 5 characteristic points selected within this zone, i.e. observation set No. 2. It can be clearly seen that the dispersion of the 11 errors computed for the three points at the summit of this zone - i.e. P2, P3 and P4 - is much lower than the one for the other two points - i.e. P1 and P5 - indicating that the observations located in the lowermost part of the landslide are more important for model calibration purposes. A numerical comparison of the error distribution for the 11 performed simulations and for the 13 considered error functions is shown in Figure 7-12. The results depict different trends for the variations of model error variance, for each observation set, in relation to the value assumed by the model input parameter $\tan \phi_b$. When only the boundary observations are used, the trend of error variance is monotonically

increasing or decreasing. If one assumes that the chosen range of values for parameter $\tan \phi_b$ contains all the reasonable values of the parameter, this behaviour is the symptom of a wrongly-defined error function. In particular, for observation set 3 - i.e. 10 observations along the bottom boundary of the deposition zone - the model error variance assumes, as expected, very low values when the displaced mass does not reach the location of the observation points (high values of $\tan \phi_b$). Conversely, for observation set 4, i.e. the 10 observations along the topmost boundary of the deposited mass, the model error variance increases with the reduced mobility of the landslide. The same behaviour is also registered for the simulations considering the observation sets 8 and 9, wherein the 10 observations along the topmost boundary of the deposited mass are combined with another characteristic soil height inside the mass. In the other cases, however, the model error variance shows a minimum value within the chosen range of values for parameter $\tan \phi_b$ that occurs, for different assumptions, at different values of the parameter. To compare and evaluate all the results of the parametric analysis, the simulation related to the observation set 13, i.e. when all 40 observations are used, is assumed to be the reference providing the best estimate of the model parameter ($\tan \phi_b = 0.44$). The three simulations yielding the same parameter estimate of the reference simulation are observation sets 1, 11 and 12. Therefore, these observations sets can be considered as the most relevant for the back-analysis of the considered landslide. Among them, the best performing simulation is the one using 15 observation points along the main cross section, i.e. observation set 1, as it produces a minimum value of model error variance almost coincident with the one produced by the reference simulation. It's worth commenting, however, that soil heights data along the main path of a landslide are not always available from in-situ surveys. On the contrary, the identification of the boundaries of debris flows from post-event topographic surveys is, typically, a relatively easy task to perform. In this respect, observation set 12 is convenient to use because it employs a limited number of easy accessible observations. For these reasons, the following three observations sets are chosen as relevant for the optimisation analysis: set 1, set 12 and set 13.

The aim of the optimisation analysis of the first step of the procedure is the identification of the observation sets most suitable for the

7. SIMULATION OF A RAINFALL-INDUCED LANDSLIDE IN HONG KONG

minimisation of the model error variance by means of an automated inverse analysis algorithm. Model calibration by inverse analysis is herein conducted employing UCODE and using the three observations sets previously identified as relevant. The results of the performed analysis are shown in Figure 7-13, which reports the values of model parameter and model error variance (Equation (3-27)) at each iteration of the six performed regressions. For each observation set, two different initial values of the model parameter $\tan\phi_b$ - respectively equal to 0.4 and 0.6 - have been considered to evaluate the stability of the regression results. All six regressions converge very quickly, in two or three iterations, and lead to similar values of the model parameter, ranging from 0.4293 to 0.4378. These values are consistent with the results of the parametric analysis, for which the best estimate of $\tan\phi_b$ was 0.44. The slightly different results achieved in terms of model error variance indicate that observation set 1 performs, as expected, slightly better than observation set 12 in relation to the reference simulation employing all 40 observations, i.e. observation set 13. Notwithstanding this, all three observation sets may be considered suitable for the analyses to be conducted in the following step of the procedure.

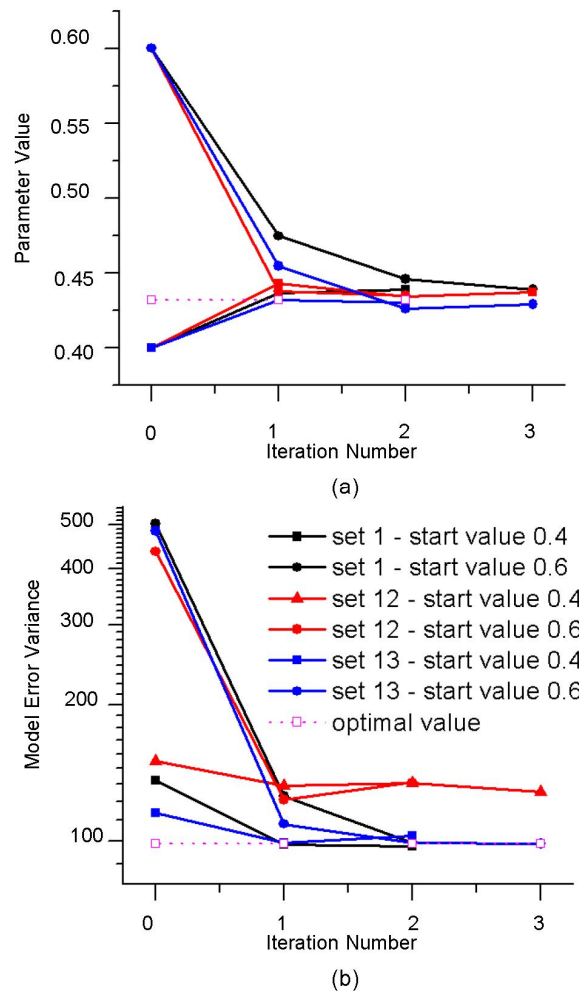


Figure 7-13 Step 1 optimization analysis: value of model parameter (a) and model error variance (b) at each iteration of performed regression.

7.2.4 Two phase propagation analysis

The second step of the procedure is used to calibrate the parameters of a complex two-phase model employing the most suitable observation sets for the considered landslide, as determined in the previous step. As already mentioned, in this model the frictional rheology is based on four

7. SIMULATION OF A RAINFALL-INDUCED LANDSLIDE IN HONG KONG

input parameters: the basal friction angle (ϕ_b); the consolidation factor (c_v); the ratio between the initial basal pore-water pressure and the liquefaction pressure (p_w^{rel}); and the relative water height (h_w^{rel}). This step comprises, as in the previous one, a parametric analysis and an optimisation analysis.

The parametric analysis is used to identify the relevant input parameters of the model to be used within the final optimisation analysis. The analysis is herein performed by means of three studies (indicated as study 2, study 3 and study 4 in Table 7-3 using 35 simulations for each one of them. The studies have been defined considering pairwise combinations of the four input parameters and ranges of values defined by heuristic expert judgement. In all three cases, the parameter $\tan\phi_b$ has been considered variable within the range of values 0.45-0.75 ($24^\circ \leq \phi_b \leq 37^\circ$). The values of the other input parameters are assumed to vary as follows: between 0.001 and 0.10 for c_v , within study 2; between 0.01 and 0.20 for p_w^{rel} , within study 3; and between 0.074 and 0.51 for h_w^{rel} , within study 4. The number of error functions computed for each simulation is equal to the number of observation sets considered in this step, i.e. sets 1, 12 and 13. The main results of the parametric analysis are reported in Figure 7-14 to Figure 7-15

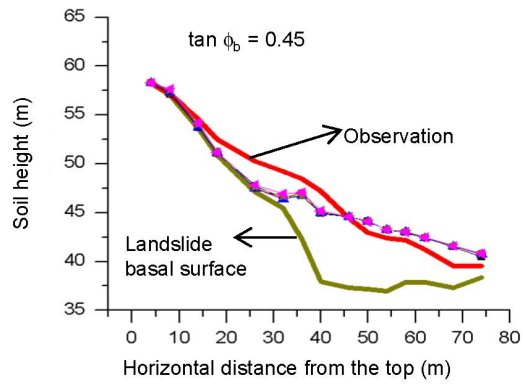
Figure 7-14 shows a comparison between the observations along the main cross section of the landslide -i.e. observation set 1 - and the results of study 2. The comparison is reported considering the five values adopted in the analysis for parameter c_v and three of the seven values adopted for parameter $\tan\phi_b$, including the value providing the best model fit within the assumed range of values (Figure 7-16b), and the minimum (Figure 7-14a) and maximum (Figure 7-14c) parameter values. The graphs clearly indicate that the results are almost insensitive to variations of the consolidation factor (c_v) while the effects of changes in the value of the basal friction angle $\tan\phi_b$ are clearly visible. In particular, the agreement between observations and simulated results is satisfactory when $\tan\phi_b$ is equal to 0.55. The values of model error variance reported in Figure 7-15 for all the three adopted observation sets, as a function of both the input parameters $\tan\phi_b$ and c_v , confirm these findings. Indeed, the model error changes only very slightly for values of c_v spanning two orders of magnitude, from 0.001 to 0.1. In all three cases, the best fit is reported for the same value of $\tan\phi_b$, equal to

0.55 and corresponding to a friction angle of 28.8° . It's worth highlighting that this value is very different from the value of friction angle providing the best model fit in the previous step of the procedure, i.e. when the landslide was modelled using a mixed-phase model. This difference does not come as a surprise if one considers that the parameter $\tan\phi_b$ adopted in the two models is not an inherent property of the landslide material but rather a way of considering, within each one of the two schematisations, an average frictional energy loss per unit length during the landslide propagation.

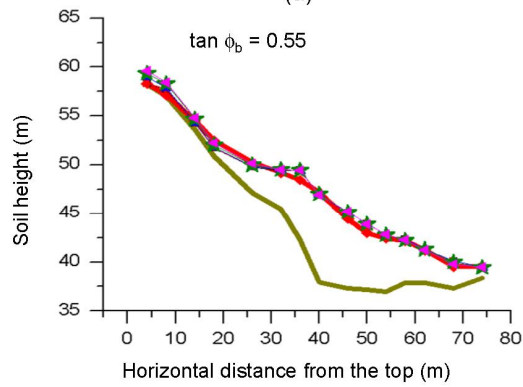
The results from studies 3 and 4 are shown in Figure 7-16. In this case, only the results related to observation set 1 are reported, both as a comparison between observed and computed soil heights in the main cross section when $\tan\phi_b$ is equal to 0.55 (Figure 7-16a), and as changes in model error variance in relation to the values of the model parameters (Figure 7-16b). The results from the two studies are significantly different from each other. Indeed, in the first case, i.e. study 3, considering parameters $\tan\phi_b$ and p_w^{rel} more than one combination of parameter values minimizes the model error function; while in the second case, i.e. study 4, considering parameters $\tan\phi_b$ and h_w^{rel} the minimum values of the model error function always occur when $\tan\phi_b$ is equal to 0.55. In the latter case, similar to what occurred for study 2, the sensitivity of the results to changes in the parameter values is very low. The results from study 3 seem to indicate a correlation between the two investigated parameters. The correlation between these parameters derives from the structure of Eq. 3, in which we can see that the effect of increasing values of pore pressures is similar to decreasing values of the basal friction angle, as both those changes decrease the basal shear stress τ_b . The significant correlation between $\tan\phi_b$ and p_w^{rel} was confirmed by computing the variance-covariance matrix for all four model parameters by means of a perturbation sensitivity analysis, under the following assumptions: observations from set 13; $\tan\phi_b=0.55$; $c_v=0.01$; $p_w^{rel}=0.1$; $h_w^{rel}=0.33$; 1% perturbation of the parameter values; forward sensitivity estimation; and constant error variance for all observations. Table 7-4 reports the linear correlation coefficients, $cor(i,j)$, retrieved from the elements of the variance-covariance matrix equation (3-17).

7. SIMULATION OF A RAINFALL-INDUCED LANDSLIDE IN HONG KONG

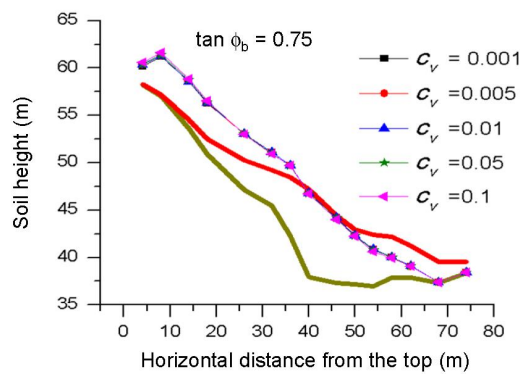
The optimisation analysis is conducted, in this step of the procedure, to perform the final calibration of the model input parameters. To this aim, the regression algorithm (described in Sec. 3.1.2.1) is used to fine-tune the values of the parameters resulting from the parametric analysis, which are thus used as initial values. In this step, one must ensure that the optimisation converges towards reasonable parameter values within a reasonable number of iterations. The parametric analysis indicated that: i) the model results are very sensitive to variations of parameter $\tan \phi_b$; ii) the results are not sensitive to variations of parameters c_v and h_w^{rel} ; and iii) parameters $\tan \phi_b$ and ρ_w^{rel} are highly correlated. Based on these findings two different regressions have been performed and compared. In the first one, only the most important parameter, i.e. $\tan \phi_b$, is calibrated (Figure 7-17a and Figure 7-18a); in the second one, both $\tan \phi_b$ and ρ_w^{rel} are calibrated (Figure 7-17b and Figure 7-18b). In the latter case, following a recommendation by [126] dealing with regression convergence in the presence of correlated parameters, the parameter ρ_w^{rel} is not directly estimated but it is linked to a coefficient R, included in the regression, herein defined as the ratio between ρ_w^{rel} and $\tan \phi_b$. In both cases, the values of the parameters that are not calibrated are equal to the mean values assumed in the parametric analysis, i.e. $c_v=0.01$; $\rho_w^{rel}=0.1$; and $h_w^{rel}=0.33$. Two convergence criteria are adopted in the regression, which is said to converge if: i) the maximum parameter change of a given iteration is less than 1% of the value of the parameter at the previous iteration; or ii) the objective function Eq. (3-8) changes less than 5% for three consecutive iterations. The other assumptions adopted to perform the regressions presented in Figure 9 are: adoption of observation set 1; perturbation of the parameter values equal to 1%; and sensitivity estimation by forward difference.



(a)



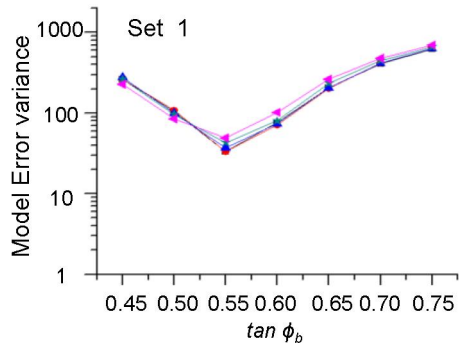
(b)



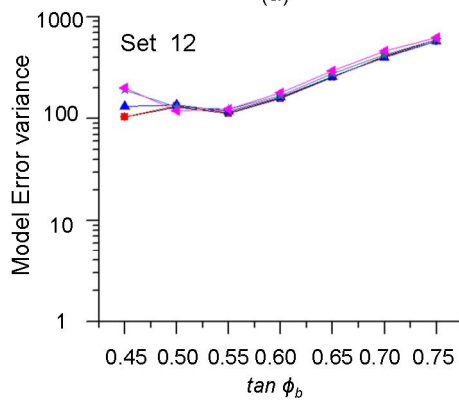
(c)

Figure 7-14 Parametric study 2: comparison between observation set 1 and computed results for three values of model parameter $\tan \phi_b$ and five values of model parameter c_v .

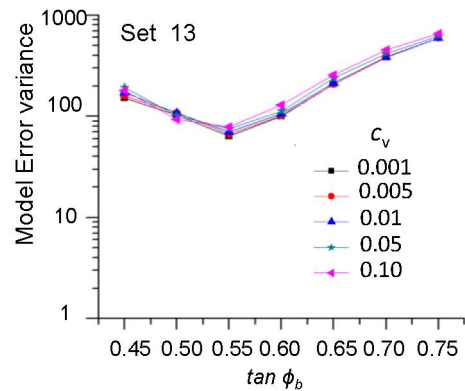
7. SIMULATION OF A RAINFALL-INDUCED LANDSLIDE IN HONG KONG



(a)



(b)



(c)

Figure 7-15 Parametric study 2: model error variance vs. value of model parameters, $\tan \phi_b$ and c_v , for observation sets 01 (a), 12 (b) and 13 (c).

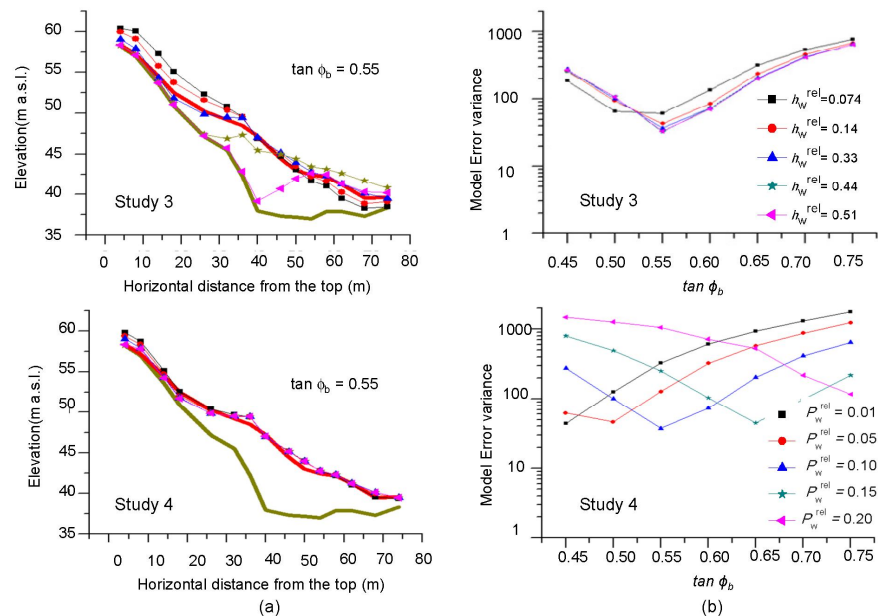


Figure 7-16 Parametric studies 3 and 4: (a) comparison between observation set 1 and computed results considering $\tan \phi_b = 0.55$ and five values of model parameters ρ_w^{rel} and h_w^{rel} ; (b) model error variance vs. values of model parameters for observation set 1.

Figure 7-17a shows the results of the first performed regression, reporting the values of the calibrated parameter and the model error variance at each iteration of the regression. The regression converges in four iterations. The model error variance is reduced by about 10% for a change in the value of the calibrated parameter of less than 3% - i.e. $\tan \phi'$ changes from 0.55 to 0.5642. Figure 7-18a shows the soil height contour lines for the best-fit parameter estimate. Figure 7-17b and Figure 7-18b show the results of the second performed regression, where both $\tan \phi_b$ and ρ_w^{rel} (by means of the coefficient R) are calibrated. In this case, a higher number of iterations is needed for the regression to converge, yet the outcome of the optimisation is similar: i) the optimal values of $\tan \phi_b$ and ρ_w^{rel} are, respectively, 0.57 and 0.103; ii) the final value of the model error variance, equal to 430.43, is very close to the value of the previous case; and iii) the contour map looks, at the scale of the figure, identical to the previous one. It's worth mentioning that two

7. SIMULATION OF A RAINFALL-INDUCED LANDSLIDE IN HONG KONG

other runs of the regression algorithm conducted considering, respectively, all the four parameters at once or $\tan \phi_b$ and ρ_w^{rel} (without adopting the coefficient R), do not converge within 20 iterations. This behaviour, sign of an ill-posed regression problem, does not come as a surprise considering that the two input parameters $\tan \phi_b$ and ρ_w^{rel} are highly correlated (see Table 3) and the model results, at the location of the employed observations, are rather insensitive to the values of the other two parameters, c_v and h_w^{rel} (see Figure 7-14 and Figure 7-16).

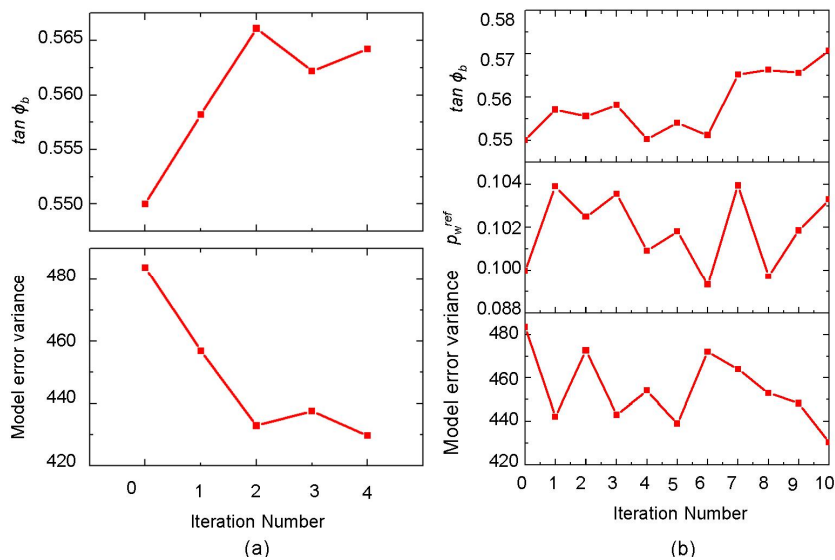


Figure 7-17 Values of calibrated parameters and model error variance at each iteration of the regression: (a) calibration of parameter $\tan \phi_b$; (b) calibration of parameters $\tan \phi_b$ and ρ_w^{rel} .

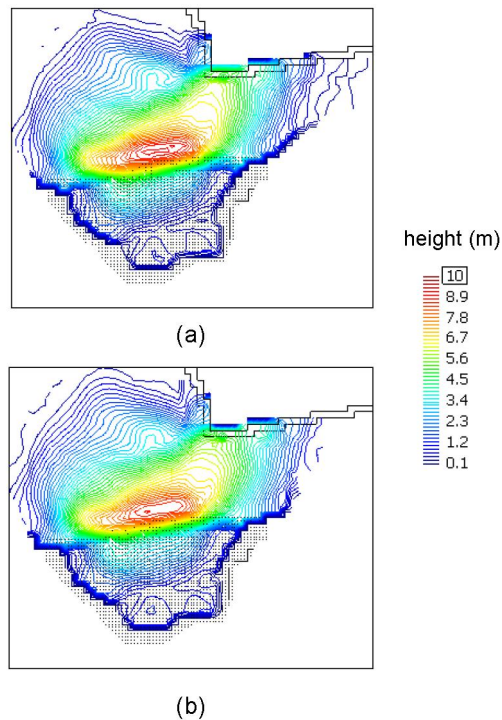


Figure 7-18 Soil height contour lines for the best-fit parameter estimates: (a) calibration of parameter $\tan\phi_b$; (b) calibration of parameters $\tan\phi_b$ and ρ_w^{rel} .

7.3 SLOPE STABILITY ANALYSIS USING LEM

The limit equilibrium analysis (LEM) was essential to assess some uncertain parameters (e.g. saturated hydraulic conductivity and initial suction), since the available data were few, as it frequently happens for most landslides triggered in nature. The limit equilibrium analysis used pore pressures computed by a seepage analysis conducted using the Seep/W software, employing the calculation mesh shown in. A transient analysis was carried out in order to simulate the rise of the perched water table during the heavy rainfall before the landslide triggering and to estimate some undetermined parameters, mainly the saturated hydraulic conductivity, the critical depth of the water table and the suction value before the landslide occurred.

7. SIMULATION OF A RAINFALL-INDUCED LANDSLIDE IN HONG KONG

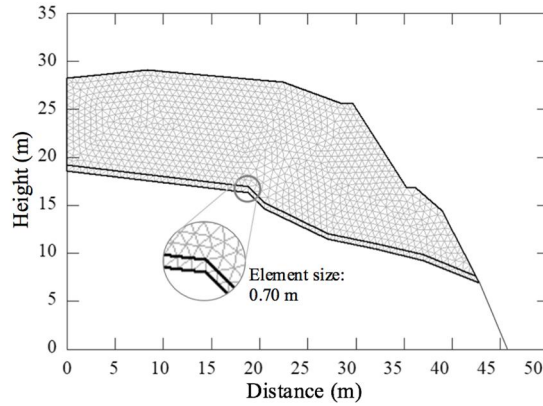


Figure 7-19, The Calculation mesh used in the seepage analysis

The general governing differential equation for two-dimensional seepage can be expressed as:

$$\frac{\partial}{\partial x} \left(k_x \frac{\partial H}{\partial x} \right) + \frac{\partial}{\partial y} \left(k_y \frac{\partial H}{\partial y} \right) + Q = \frac{\partial \theta}{\partial t} \quad (7-1)$$

in which H is the total head, k_x the hydraulic conductivity in the x -direction, k_y the hydraulic conductivity in the y -direction, Q is the applied boundary flux and θ is the volumetric water content.

The characteristic curves were obtained to establish the unsaturated characteristics of the soil materials in the landslide site. For this reason, the volumetric content curve was achieved through the [124] method, The permeability curve was deduced from the volumetric water content function, employing the Van Genuchten method:

$$k(\Psi) = k_{\text{sat}} \cdot \frac{[1 - (a\Psi^{n-1})(1 + (a\Psi^n)^{-m})]^2}{(1 + a\Psi)^{nm/2}} \quad (7-2)$$

where k_{sat} is the saturated hydraulic conductivity, Ψ is the matric suction, a , n and m are curve fitting parameters.

Regarding the saturated hydraulic conductivity, two different values were considered for the thin kaolinitic layer and the weathered volcanics. [127] report that the typical permeability for the completely altered tuff is between $10^{-4} \div 10^{-7}$ m/s. For this reason, a value of hydraulic conductivity equal to 10^{-7} m/s was assumed for the material with a high content of kaolinite and a variable permeability ($10^{-4} \div 10^{-5}$ m/s) was

considered for the soil above it. The permeability value of the latter is better calibrated through the analysis itself.

The slope stability analysis was carried out in order to show the change in time of the safety factor during the infiltration of the rain, using the Morgenstern-Price method (1965). Furthermore, the influence of initial suction and soil permeability on the safety factor trend over time is highlighted. The input data of the analyses are shown in Table 7-5.

The slope analysis, together with the seepage analysis results, allows to assess the initial value of suction (s_0) and the permeability value that enable to obtain the factor of safety closest to one at failure time. To achieve this goal, the trend of safety factor over time has been evaluated, considering also the dependence with the initial suction and the permeability of the weathered tuff. This allowed estimating the most probable values of these parameters, which are equal to 51 kPa and $5 \cdot 10^{-5}$ m/s respectively (Figure 7-20).

Such result is in agreement with the slip surface observed on site and also with the depth of the perched water table (Figure 7-21a). Indeed, the GEO report n°188 ([122]) states that "as there was no evidence of significant seepage at the toe of the back scarp of the landslide, about 5 m above the kaolinitic clay layer, the perched water level was probably in the range 1 to 4 m above the kaolinitic clay layer".

The distribution of suction at failure time, as shown in Figure 4b, demonstrates that suction plays an essential role in the evolution of the slope instability. The additional soil strength due to suction (c_{add}) can be expressed as:

$$c_{add} = s \cdot S_r \cdot \tan\phi' \quad (7-3)$$

Where s is the suction value, S_r is the degree of saturation. The results of the seepage analysis furnished an average suction value (\underline{S}) at failure equal to about 30 kPa and also an average degree of saturation (\underline{S}_r) equal to about 95%. Considering that is equal to 0.7, the additional strength c_{add} is about 20 kPa.

7. SIMULATION OF A RAINFALL-INDUCED LANDSLIDE IN HONG KONG

Table 7-5, Seepage and slope analyses inputs

	Input	Symbol	Altered tuff with kaolinite veins	Weathered volcanics
Hydraulic functions	Unit weight	γ (kN/m ³)	19	19
	Cohesion	c' (kPa)	0	0
	Friction angle	ϕ' (°)	22	35
	Saturated hydraulic conductivity	k_{sat} (m/s)	10^{-7}	$10^{-4}; 5 \cdot 10^{-5}; 10^{-5}$
Hydraulic functions	Hyetograph	$i(t)$	In-situ measured rainfall	
	Volumetric water content	$\theta(\Psi)$	$\theta_{sat}=0.4; w_L=34\%; D_{10}=0.00175$ mm; $D_{60}=0.0182$ mm	
	Hydraulic conductivity	$k(\Psi)$	$\theta_{sat}=0.4; \theta_r=0.11; \alpha=0.015;$ $n=1.892$	

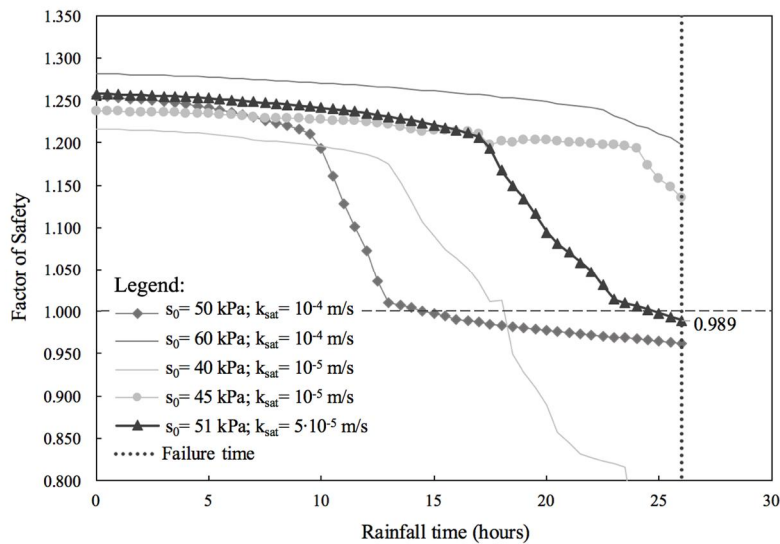


Figure 7-20, Factor of safety changing in time with different suction and permeability values

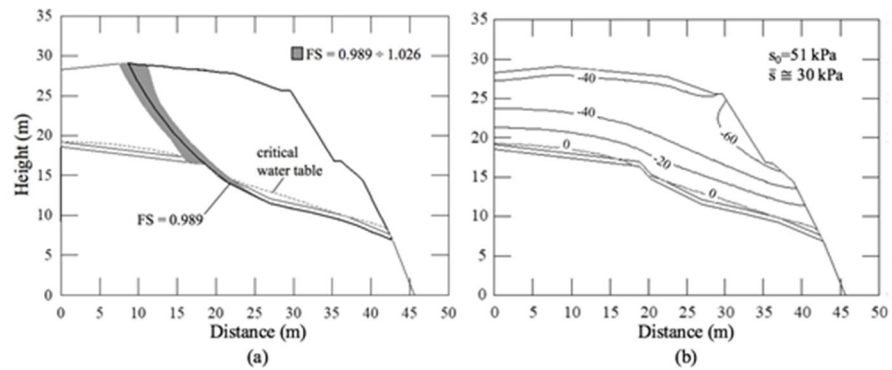


Figure 7-21, (a) Critical slip surface at failure time; (b) Suction distribution at failure time

7.4 MPM ANALYSIS USING TWO PHASE FORMULATION

7.4.1 Effect of soil cohesion

The MPM analysis focuses the attention on the slope evolution from the onset of failure until the final slope configuration. The calculation mesh is shown in Figure 5a, while the soil materials are reported in Figure 5b, representing the output water table of the limit equilibrium analysis. The input parameters used in the analysis are shown in Table 7-3.

A contact algorithm is introduced at the boundary between the kaolinitic layer, simulated as a linear elastic material, and the overlying soil, since the site observations showed that the slip surface of the landslide is located there. In the weathered volcanics, the use of cohesion (c') is a simplified way of modeling the additional strength due to the presence of suction, since a Mohr Coulomb constitutive model was adopted ([81]; [128]).

In order to simulate a more realistic mechanical soil behavior, a gradual loss of suction is taken into account. A linear reduction of cohesion (c') with increasing deviatoric strain (ϵ_d) is adopted, including a fixed threshold (ϵ_t) that represents the value of deviatoric strain beyond which

the cohesion is set to zero, starting from an initial cohesion (c_0) that is the additional strenght value (c_{add}) derived from the seepage analysis at failure time.

The function adopted for the analysis is better explained through Equation 4:

$$\begin{cases} c' = c_0 - \alpha \epsilon_d & \text{for } \epsilon_d < \epsilon_d^t \\ c' = 0 & \text{for } \epsilon_d \geq \epsilon_d^t \\ \epsilon_d = \frac{2}{3} \sqrt{\epsilon_x^2 + \epsilon_y^2 + \epsilon_x \epsilon_y} \end{cases} \quad (7-4)$$

where α represents the gradient of the reduction, that is c_0/ϵ_d^t .

The MPM analysis has enabled to understand the importance of considering the presence of suction, in particular its decrease with large deformations of the soil, for a better estimate of the soil mechanical behaviour during the propagation stage (Figure 7-23). In fact, if no additional cohesion is considered, the final shape of the landslide is well-simulated only in the central part of the slope, but not in the upper part, which has to be stable according to the landslide report (case 1 in Figure 7-23). Conversely, the presence of a constant cohesion simulates well the part of the slope that remains stable during the whole process evolution, but the other slope zones are completely inconsistent to the observed one (case 2 in Figure 7-23).

The results from these two cases suggest that the best model response might be obtained by considering a soil mechanical behaviour as something intermediate between the two. Indeed, case 3 in Figure 7-23 represents the model producing the final soil configuration that is the closest to the observed one.

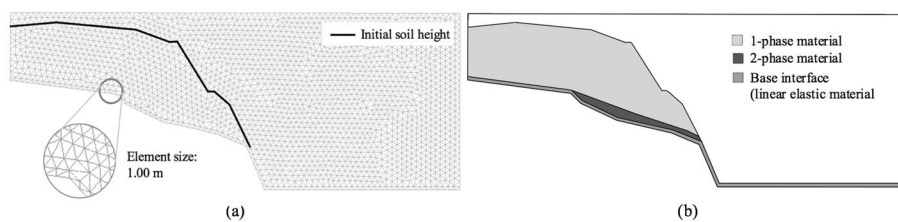


Figure 7-22, (a) Calculation mesh for the MPM analysis; (b) Geometry of the slope for the MPM simulations.

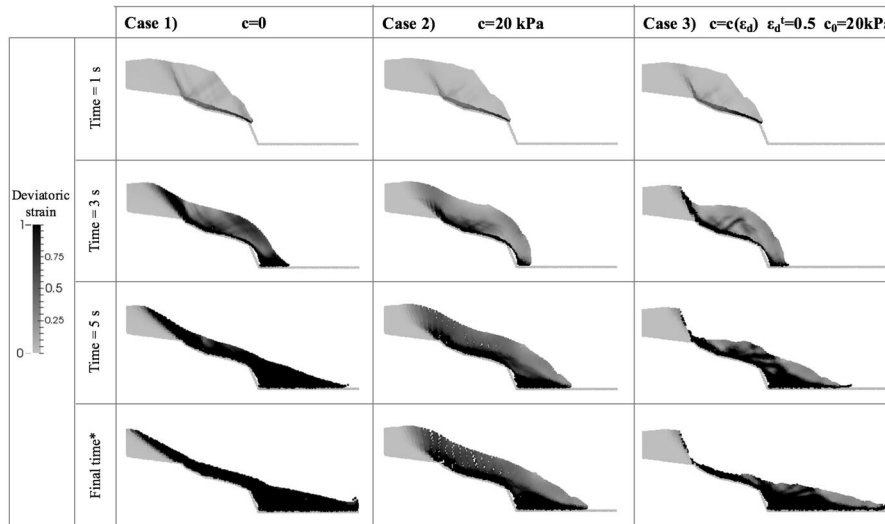
In terms of deviatoric strain values, the difference between these three cases is also considerable. At failure, the deviatoric strain is more than

one on the whole dislocated mass for the case1, and especially around the sliding surface for the second case. The third case turns out to be a combination of the two aforementioned distributions.

Table 7-6, Initial input parameters in the MPM simulation of the slope

	Parameter	Symbol	1-phase material	2-phase material	Elastic material
Solid properties	Density solid	ρ_s (kg/m ³)	2,650	2,650	2,650
	K0-value	K_0 (-)	0.5	0.5	0.5
	Initial porosity	n (-)	0.45	0.45	0.45
	Saturated hydraulic conductivity	k_{sat} (m/s)	$5 \cdot 10^{-5}$	$5 \cdot 10^{-5}$	-
	Young modulus	E (kPa)	50,000	50,000	10,000
	Poisson ratio	ν (-)	0.3	0.3	0.3
	Cohesion	c' (kPa)	0; 20; variable	0	-
	Friction angle	ϕ' (°)	35	35	22*
	Dilatancy angle	ψ (°)	0	0	0
Liquid properties	Density of water	ρ_w (kg/m ³)	-	1,000	-
	Liquid bulk modulus	K_w (kPa)	-	20,000	-
	Liquid dynamic viscosity	μ (kPa · s)	-	10^{-3}	-
* this value is applied considering a contact algorithm					

7. SIMULATION OF A RAINFALL-INDUCED LANDSLIDE IN HONG KONG



*The final time of propagation is reached when the soil mass stops. It is 9.0 s for case 1, 6.7 s for case 2 and 7.1 for case 3

Figure 7-23, Deviatoric strain distribution for three simulations with different cohesion values

7.4.2 Effect of basal friction angle

In the previous section it was shown that using a simple strength reduction approach could well simulate the vanishing of the apparent cohesion (caused by suction) and at the end the general agreement between simulated and observed final scheme of landslide was achieved. Yet, still there is a considerable mismatch in the terms of landslide run out. The simulation shows a larger run out distances with respect to the reality. As it can be seen in Figure 7-24, the predicted soil height in the deposition zone is over estimated, whilst the soil height in the transition zone is underestimated. This mismatch could be related to the one of these reasons: lack of the viscosity in Mohr-Coulomb constitutive model as it was explained in detail in Sec.6.1 2) in the created model, the adopted value for friction angle between elastic base and the soil, i.e. $\phi_\beta=22^\circ$ was interpreted from the internal friction angle of the bottom weak layer of the slope, while the friction between debris and the road surface might be a different value. Thus, in order to improve the fit between simulation and observation, the contact between soil and elastic base would be divided into the two parts. The upper part I represents the internal friction angle of thin weak layer of the slope (stable zone and

transition zone) , and the lower part II represents the friction between debris and the road in front of the slope (Deposition zone). In order to obtain the optimal value of the friction angle of both part, the inverse analysis procedure identical to Sec.6.1. was carried out. herein the variable parameters are the basal friction angle of part I, ϕ_b^I , The basal friction angle of partII, ϕ_b^{II} , and the parameters ϵ_d^t . The rest of the parameters of the model are remained fixed. 15 points located on the cross section of the landslide are employed as observation Figure 7-24. The soil height extraction algorithm explained in Sec.6.1 helps to carry out this inverse analysis. The starting value for the basal friction angle, for both part, is 22° and the starting value of ϵ_d^t is 0.5. Figure 7-25 shows the results of the inverse analysis. As it can be seen, the optimisation procedure converged after 7 iterations. The optimal value for the friction of part II is obtained as $\phi_b=34$. This value is relatively close to the internal friction angle of the weathered rock of the slope. The higher obtained value for this basal friction angle is in accordance to the conclusion of Sec.6.1 implies that, in the case of the usage of Mohr-Coulomb constitutive model higher value of basal friction angle could be considered to reproduce the run out distance of landslide propagation. The obtained friction is also higher from the value of 29° achieved from inverse analysis of SPH model in Sec.0.

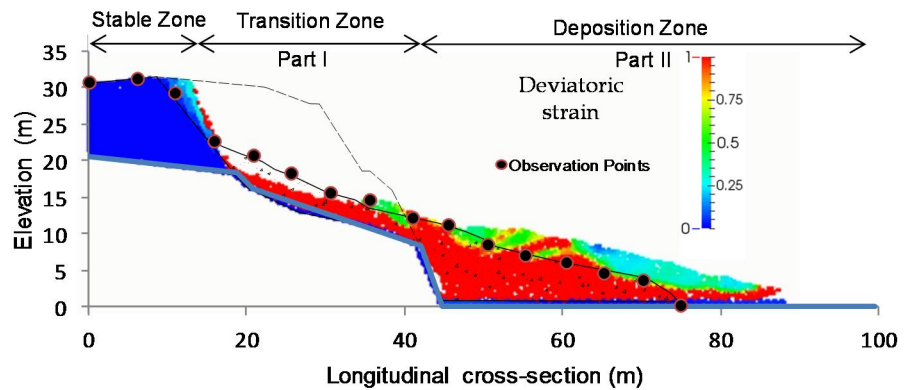


Figure 7-24, comparison of the outcome of case 3 with final the geometry of landslide

7. SIMULATION OF A RAINFALL-INDUCED LANDSLIDE IN HONG KONG

The final geometry of the optimal model is shown in Figure 7-26 and Figure 7-27 . The figures imply better matches between simulations and real observed cross-section. As it can be seen in the figure the predicted soil height in the deposition zone are close to the observations. In the contrary of the initial parameters value, the predicted soil heights in the transition zone are underestimated with respect to the reality. The optimal model also simulated well the stable part of the slope. More importantly in terms of propagation analysis, the predicted run-out distance is comparable with observation.

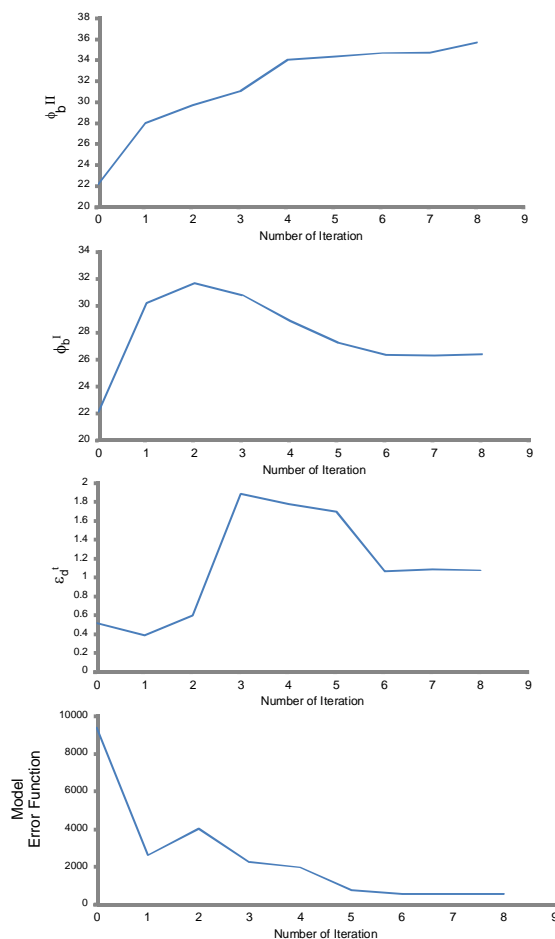


Figure 7-25 Results of the inverse analysis

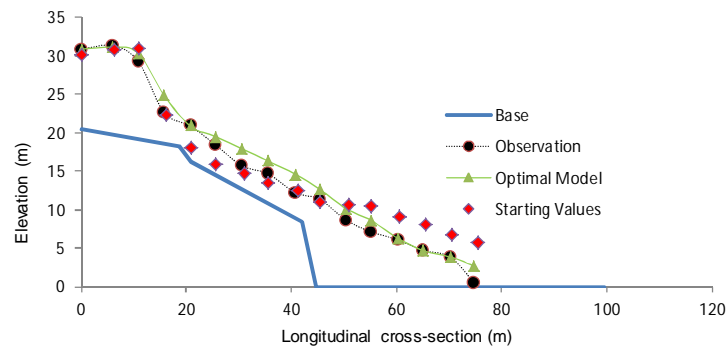


Figure 7-26, optimal model obtained through the inverse analysis and comparison with initial one.

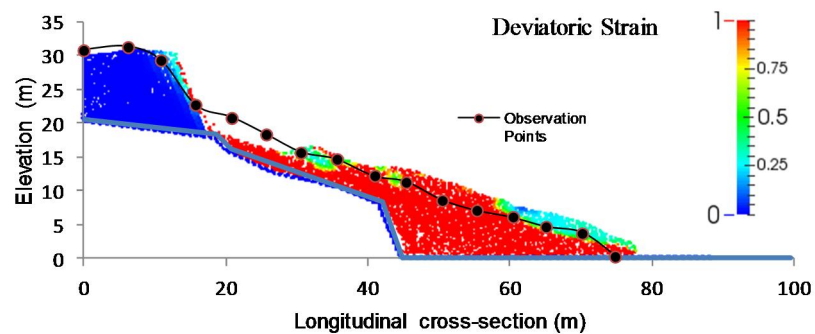


Figure 7-27, comparison of the optimal model with final geometry of landslide

7.5 CONCLUSIONS

In this chapter, the simulation and back-analysis of a complex fast rainfall-induced landslide in Hong Kong was addressed. A comprehensive series of analysis consists of LEM, SPH, and MPM were carried out to get an insight on various aspects of the landslide characteristics. First of all back-analysis of the propagation stages using SPH modelling were addressed, it showed that, adopting a cross-section of the landslide is quite sufficient to perform reliable inverse analysis. Throughout the inverse analysis of the SPH model, Rheological parameters of debris flow were estimated.

7. SIMULATION OF A RAINFALL-INDUCED LANDSLIDE IN HONG KONG

In the next stage, special attention was paid to the triggering stage of landslide in which the hydraulic properties as well as matric of the suction of the material were estimated via the back-analysis of the observed failure surface and the water table level at the onset of the failure.

Last stage of the study consists in an attempt to simulate the cross-section of the landslide from onset of the failure till end of the propagation using two phase material point method. The initial suction of the slope was simply simulated by considering an apparent cohesion. A simple approach in order to model the vanishing of the suction with respect to the shear strain of the soil element was adopted. i.e. linear reduction of the apparent cohesion versus increment of deviatoric strain. It was shown that this approach is able to properly reproduce the general features of the final geometry of the landslide, however, the run out distance and shape of the deposition zone had slightly differences with reality. Therefore again inverse analysis algorithm was adopted to fine-tune the value of basal friction angle. The parameters were recalibrated through the regression and the optimal model parameters were introduced. The final outcome of the analysis is in very good agreement with field observation. This shows that, the correct selection of the input parameters regarding the adopted model could reproduce the main features of the landslide properly, even if a simple Mohr Coulomb constitutive model is adopted to model the soil in MPM.

8 CONCLUDING REMARKS

In the present study, the attention focused on the soil parameter estimation in order to large deformation modelling of geotechnical problems. Compatibility of the inverse analysis along with positive and negative points of this approach was discussed. This chapter draws some conclusions from this study.

An extended literature review was performed on the application of inverse analysis to geotechnical problem, it was concluded that, the majority of research were aimed to soil estimation for small deformation problems and particularly excavation. While a review on the researches on the simulation of large deformation showed that the parameters estimation for reproducing soil behaviour in large strains are challenging since the advanced constitutive model are required to simulate the correct soil condition in critical state.

The ingredients employed in this study were explained in chapter 3, consist of the optimisation algorithms, numerical models and adopted constitutive models. Two phase material point method for 3D problem was described. Then, the axisymmetric material point method formulation was explained. Three different constitutive models, from the simple one of Mohr- coulomb, a semi advanced one, Hardening soil and the advanced one of Hypo plastic model were elaborated. It was shown that, although Hypoplastic model shows proper performance to reproduce the results of monotonic tests, the model suffering from some problem in cyclic loading modelling. Furthermore, one may find many challenges when using the model with an explicit numerical scheme which involves high oscillations in the state variables, which is the case in adopting Material Point Method due to Grid Crossing Error, this leads to instability of the model, even when the static problem is being simulated. It was shown that, considering a larger range of elastic strain for the material may mitigate this difficulty.

Chapter 4 of the thesis stated by determination of the hypoplastic model parameters using the automatic algorithm. It was shown that, the

8. CONCLUDING REMARKS

SQPSO curve fitting algorithm was able to determine a set of parameters by which the simulated soil behaviour was closer to the experimental result than the response computed using parameters values reported in the literature. Secondly, the importance of the right selection of the type of tests used to provide the observations for the inverse analysis algorithm was shown. In another word, the obtained set of calibrated parameters significantly depends on the observations used to calibrate them. For example, it appears that performing the inverse analysis employing triaxial tests conducted on specimens subjected to higher confining pressures more likely leads to a correct estimate of the parameters. However, it should also be stated that a set of parameters providing good predictions of triaxial tests does not necessarily allow simulating oedometer tests properly. It entails that combinations of different types of laboratory tests should be used for a general calibration of constitutive model along different stress paths.

In the next step, the performance of inverse analysis to the calibration of cyclic triaxial tests were investigated, a 5-step procedure has been introduced in order to determine all of the hypoplastic model parameters including the small strain ones. Three kinds of laboratory tests were adopted in the calibration procedures, which consist of drained and undrained monotonic triaxial tests as well as cyclic undrained triaxial tests performed on samples of Northsea sand (Kreftenheye sand).

In each step of the procedure, the most relevant observations for the estimation of a certain group of parameters were used. The shortcoming of the hypoplastic model in the prediction of each adopted experimental curve was highlighted. As it was shown, the model suffers from the wrong prediction of material behaviour at low stress levels, close to instability points, and for the "close-to-failure" behaviour during load control cyclic tests.

In order to calibrate the cyclic triaxial tests, the S-N cyclic resistance curve was employed. Regarding the shortcoming of the hypoplastic model in the proper prediction of cyclic mobility and axial strain, a new failure criterion in order to identify the numerical instability was proposed, based on a new type of curve named artificial S-N curve. The slope of this curve can be compared with the one obtained by experimental data and, by matching the slopes of these two curves, the most relevant model parameters which represent liquefaction resistance of the soil can be obtained.

In Chapter 5, simulation of the pile penetration using material point method was addressed. The idea was to determine the soil parameters value which represents the in-situ soil characters. First of all a simple exercise to back analysis of Mohr-coulomb model parameters using syntactic data was performed and it was revealed that; the regression problem must be well-posed, which means: the observations must be significant for the adopted constitutive law and the numerical implementation of the CPT boundary value problem; the computed results must be sensitive to the parameters being calibrated; the parameters do not have to be highly correlated. When this happens, a gradient-based optimization algorithm, such as the one adopted herein, can be effectively used to optimize the model parameters so that the computed results match CPT observations.

In the next step, back analyses of chamber tests were aimed. The section mainly focused on the accuracy of MPM Forward model by sensitivity analysis on the mesh size and also the alternative numerical mitigation for coping with grid crossing error.

The result of that section showed the capability and shortcoming of Mohr-coulomb model to simulate CPT granted that, stiffness dependency on the pressure in the constitutive model is extremely needed. Therefore, the hardening soil model was employed in the second place. However, in the second case the numerical instability was observed while MPM-Mixed was used for the integration. Whilst adopting original MP with averaging only the volume of particles inside the element depicted more stable results. Mesh dependency of the model in terms of hardening soil model were also observed. As a result, finer mesh have should be adopted.

Another outcome of chapter 5 was the fact of necessity of the parameters recalibration. Admitting that, the parameters determined through lab data interpretation are unlikely to fit the material point method model of CPT with Chamber or field data this was proved for to advanced constitutive model of hardening soil and hypo plastic model.

The first part of Chapter 6 presented the calibration by inverse analysis of the MPM model of a debris flow experiment conducted in a small-scale flume. The results of the optimized model demonstrated the ability of a MPM schematization of the test to simulate, in space and time, the behaviour of a dry sand flow. First of all, it was observed that, to get the best fit with experimental results, higher value of friction between materials and basal of the flume is needed, this could be attributed to the

8. CONCLUDING REMARKS

lack of viscosity in the adopted constitutive model (Mohr-coulomb). On the other hand, it was shown that the deposited soil heights at the end of the propagation are sufficient to adequately calibrate the numerical model. This should be considered very good news because, differently to what happens for laboratory experiment, it is very difficult to get in-situ observations of debris flows related to the propagating soil mass.

In the second part of chapter 6, Material Point Method modelling of complex slope instability induced by seepage flow and characterised by retrogressive failure and static liquefaction was carried out. The hypoplastic constitutive model was used to reproduce liquefiable behaviour of the material as observed in REV laboratory tests and in the slope experiment.

Adopting inverse analysis techniques alongside with advanced curve fitting techniques allowed evaluating the proper parameters for the loose cohesion less material, in a way that the results of REV simulations were in good agreement with those measured in triaxial tests and the liquefiable behaviour was also well reproduced.

The performance of the estimated parameters in the slope MPM simulation was appreciable as the results are in good agreement with those observed in the experiment. The retrogressive slides involving static liquefaction were well captured in the simulation. The outcomes of a parametric study on the initial density of the slope testified a lower liquefaction potential for a denser soil. It was also shown that increasing the mobilized friction angle at earlier strain levels at low stress states would make the simulation results more close to the observed ones. The chapter also highlighted the capability of the combination of MPM and an advanced hypoplastic model to simulate important aspects of static liquefaction within slopes, such as: early building up of excess pore water pressure and dropping of effective stress associated to slope instability; regaining of the effective stresses in the post-failure stage. The full simulation of onset, progress and vanishing of static liquefaction corresponding to a transition from solid-like to fluid-like behaviour and vice versa is thought one of the relevant novelties achieved through the proposed procedure.

In the last chapter, the simulation and back-analysis of a complex fast rainfall-induced landslide in Hong Kong was addressed. A comprehensive series of analysis consists of LEM, SPH, and MPM were

carried out to get an insight on various aspects of the landslide characteristics. The first step of the procedure aims at identifying the observation sets most suitable for the minimisation of the model error variance by means of an automated inverse analysis algorithm. In this step SPH simulation of the propagation step of the landslide was used as the forward model. The second step aims at calibrating the parameters of a complex soil model employing the most suitable observation sets for the considered landslide, as determined in the previous step. In each step of the procedure both parametric analyses and automatic optimisation analyses are used. The study proved that using more observations does not always lead to more accurate results. In fact, it was the location of the adopted points that had the greatest influence on model accuracy. For instance, using 20 boundary points did not lead to a successful minimisation of the objective function, while the set of observations which consisted of only 10 points located on the boundary in addition to one point at the summit of deposition zone was able to lead to a unique optimal estimated value of the input parameter. It was also observed that, 15 points located on the cross-section of the landslide are also sufficient to calibrate the model. Therefore, Last stage of the study consists in an attempt to simulate the cross-section of the landslide from onset of the failure till end of the propagation using two phase material point method. The initial suction of the slope was simply simulated by considering an apparent cohesion. A simple approach in order to model the vanishing of the suction with respect to the shear strain of the soil element was adopted, i.e. linear reduction of the apparent cohesion versus increment of deviatoric strain.

It was shown that this approach is able to properly reproduce the general features of the final geometry of the landslide, however, the run out distance and shape of the deposition zone had slightly differences with reality.

More in general, the proposed approach is fully promising and more attention should be devoted to further geotechnical engineering applications. The proposed methodology in this thesis could be the basic of the idea of adopting artificial intelligence (AI) in soil parameter estimation and site characterisations, to do this this aim, further researches in order to develop optimisation algorithms compatible with time consuming black box functions are needed.

9 BIBLIOGRAPHY

- [1] G. Gioda and G. Maier, "Direct search solution of an inverse problem in elastoplasticity: Identification of cohesion, friction angle and in situ stress by pressure tunnel tests," *International Journal for Numerical Methods in Engineering*, vol. 15, no. 12, pp. 1823-1848, 12 1980.
- [2] A. Cividini, G. Maier and A. Nappi, "Parameter estimation of a static geotechnical model using a Bayes' approach," *International Journal of Rock Mechanics and Mining Sciences & Geomechanics Abstracts*, vol. 20, no. 5, pp. 215-226, 10 1983.
- [3] A. Cividini, L. Jurina, G. G. -. I. J. o. R. M. And and U. 1981, "Some aspects of 'characterization' problems in geomechanics," *Sci. & Geomech*, vol. 18, pp. 487 -503, 1981.
- [4] G. Gioda, "Some remarks on back analysis and characterization problems in geomechanics," in *5th international conference on numerical methods in geomechanics*, 1985.
- [5] S. Sakurai and K. Takeuchi, "Back analysis of measured displacements of tunnels," *Rock Mechanics and Rock Engineering*, vol. 16, no. 3, pp. 173-180, 8 1983.
- [6] J. N. Hutchinson, "A sliding-consolidation model for flow slides," *Canadian Geotechnical Journal*, vol. 23, no. 2, pp. 115-126, 5 1986.
- [7] K. ARAI, H. OHTA, K. KOJIMA and M. WAKASUGI, "Application of back-analysis to several test embankments on soft clay deposits.," *SOILS AND FOUNDATIONS*, vol. 26, no. 2, pp. 60-72, 15 6 1986.
- [8] M. Calvello and R. Finno, "Selecting parameters to optimize in model calibration by inverse analysis," *Computers and Geotechnics*, vol. 31, no. 5, pp. 410-424, 2004.
- [9] R. F. Obrzud, L. Vulliet and A. Truty, "Optimization framework for calibration of constitutive models enhanced by neural

- networks," *International Journal for Numerical and Analytical Methods in Geomechanics*, 2009.
- [10] T. Knabe, M. Datcheva, T. Lahmer, F. Cotecchia and T. Schanz, "Identification of constitutive parameters of soil using an optimization strategy and statistical analysis," *Computer and Geotechnics*, vol. 49, pp. 143-157, 2013.
- [11] R. J. Finno and M. Calvello, "Supported Excavations: Observational Method and Inverse Modeling," *Journal of Geotechnical and Geoenvironmental Engineering*, vol. 131, no. 7, pp. 826-836, 7 2005.
- [12] Y. M. A. Hashash, S. Levasseur, A. Osouli, R. Finno and Y. Malecot, "Comparison of two inverse analysis techniques for learning deep excavation response," 2009.
- [13] S. Rodríguez, V. Ledesma and S. Gens , "Hybrid minimization algorithm applied to tunnel back analysis.," in *In Computer Methods and Recent Advances in Geomechanics-Proceedings of the 14th Int. Conference of International Association for Computer Methods and Recent Advances in Geomechanics*, Barcelona, 2014.
- [14] R. J. Chandler, "Back analysis techniques for slope stabilization works: a case record," *Géotechnique*, vol. 27, no. 4, pp. 479-495, 25 12 1977.
- [15] F. Tavenas and S. Leroueil, "Creep and failure of slopes in clays," *Canadian Geotechnical Journal*, vol. 18, no. 1, pp. 106-120, 2 1981.
- [16] R. Deschamps and G. Yankey, "Limitations in the Back-Analysis of Strength from Failures," *Journal of Geotechnical and Geoenvironmental Engineering*, vol. 132, no. 4, pp. 532-536, 4 2006.
- [17] L. L. Zhang, L. M. Zhang and W. H. Tang, "Rainfall-induced slope failure considering variability of soil properties," *Géotechnique* , vol. 55, no. 2, pp. 183-188, 2005.
- [18] M. Calvello, L. Cascini and G. Sorbino, "A numerical procedure for predicting rainfall-induced movements of active landslides along pre-existing slip surfaces," *International Journal for Numerical and Analytical Methods in Geomechanics*, vol. 32, no. 4, pp. 327-351, 1 3 2008.
- [19] L. Wang, J. H. Hwang, Z. Luo, C. H. Juang and J. Xiao, "Probabilistic back analysis of slope failure – A case study in Taiwan," *Computers and Geotechnics*, vol. 51, pp. 12-23, 1 6 2013.

9. BIBLIOGRAPHY

- [20] P. J. Vardon, K. Liu and M. A. Hicks, "Reduction of slope stability uncertainty based on hydraulic measurement via inverse analysis," *Georisk: Assessment and Management of Risk for Engineered Systems and Geohazards*, vol. 10, no. 3, pp. 223-240, 27 2016.
- [21] L. M. Zhang, X. Li, J. H. Wang, L. L. Zhang, Y. F. Zh Eng, L. M. Z. Ang and X. Li, "Probabilistic model calibration for soil slope under rainfall: Effects of measurement duration and frequency in field monitoring," *Geotechnique*, vol. 64, no. 5, pp. 365-378, 2014.
- [22] P. Arnold, M. H. -. S. o. G. S. a. R. ... and u. 2011, "A stochastic approach to rainfall-induced slope failure," in *Third International Symposium on Geotechnical Safety and Risk (ISGSR)*, Munich, Germany, , 2011.
- [23] H. Chen and C. F. Lee, "Numerical simulation of debris flows," *Canadian Geotechnical Journal*, vol. 37, no. 1, pp. 146-160, 2 2000.
- [24] F. Federico and C. Cesali, "An energy-based approach to predict debris flow mobility and analyze empirical relationships," *Canadian Geotechnical Journal*, vol. 52, no. 12, pp. 2113-2133, 12 2015.
- [25] F. Frank, B. W. Mcardell, N. Oggier, P. Baer, M. Christen and A. Vieli, "Debris-flow modeling at Meretschibach and Bondasca catchments, Switzerland: sensitivity testing of field-data-based entrainment model," *Hazards Earth Syst. Sci.*, vol. 17, pp. 801-815, 2017.
- [26] S. Cuomo, M. Calvello and V. Villari, "Inverse analysis for rheology calibration in SPH analysis of landslide run-out," in *Engineering Geology for Society and Territory-Volume*, L. Giorgio, Ed., Rome, Springer, Cham, 2015, pp. 1635-1639.
- [27] S. Fan, B. Bienen and M. F. Randolph, "Stability and efficiency studies in the numerical simulation of cone penetration in sand," *Géotechnique Letters*, 2018.
- [28] I. Al_Kafaji, Formulation of a dynamic material point method (MPM) for geomechanical problems, Stuttgart, Germany: Univ. of Stuttgart, 2013.
- [29] N. Phuong, A. Van Tol, A. Elkadi and A. Rohe, "Numerical investigation of pile installation effects in sand using material point method," *Computers and Geotechnics*, vol. 73, pp. 58-71, 2015.
- [30] J. Grabe, S. Henke, S. Kinzler and T. Pucker, "Inverse

- determination of soil density and stress state using dispersion wave measurements and cone penetration tests in a non-layered soil," *Soil Dynamics and Earthquake Engineering*, vol. 30, no. 6, pp. 481-489, 16 2010.
- [31] L. Cascini, S. Cuomo, M. Pastor and S. Sacco, "Modelling the post-failure stage of rainfall-induced landslides of the flow type," *Canadian Geotechnical Journal*, pp. 924-934, 2013.
- [32] D. Eckersley, "Instrumented laboratory flowslides," *Geotechnique*, vol. 40, no. 3, pp. 489-502, 1990.
- [33] S. Lourenco, K. Sassa and H. Fukuoka, "Failure process and hydrologic response of a two layer physical model : implications for rainfall-induced landslides," *Geomorphology*, vol. 73, no. 1-2, pp. 115-130, 2006.
- [34] W. H. TANG, T. D. STARK and M. ANGULO, "Reliability in Back Analysis of Slope Failures.," *SOILS AND FOUNDATIONS*, vol. 39, no. 5, pp. 73-80, 15 10 1999.
- [35] Y. S. Lee, C. Y. Cheuk and M. D. Bolton, "Instability caused by a seepage impediment in layered fill slopes," *Canadian Geotechnical Journal*, vol. 45, no. 10, pp. 1410-1425, 2008.
- [36] W. NG, "What is Static Liquefaction Failure of Loose Fill Slopes," in *In Conf., The first Italian Workshop on Landslides.*, Napoli, 2009.
- [37] P. Lade, "Static instability and liquefaction of loose fine sandy slopes," *Journal of Geotechnical Engineering*, vol. 118, no. 1, pp. 51-71, 1992.
- [38] M. Konstadinou and V. N. Georgiannou, "Cyclic behaviour of loose anisotropically consolidated Ottawa sand under undrained torsional loading," *Géotechnique*, vol. 63, no. 13, pp. 11-44, 2013.
- [39] L. Cascini, S. Cuomo, M. Pastor and G. Sorbino, "Modeling of rainfall-induced shallow landslides of the flow-type," *Journal of Geotechnical and Geoenvironmental Engineering*, vol. 136, no. 1, pp. 85-98, 2010.
- [40] N. Janbu, "Application of composite slip surfaces for stability analysis," in *Proc., Of European conference on stability of earth slopes*, Stockholm, 1955.
- [41] M. Pastor, M. Quecedo, J. A. Fernández Merodo, M. I. Herrores, E. González and P. Mira, "Modelling tailings dams and mine

9. BIBLIOGRAPHY

- waste dumps failures," *Géotechnique*, vol. 52, no. 8, pp. 579-591, 10 2002.
- [42] S. Cuomo, N. Prime, A. Iannone, F. Dufour, L. Cascini and F. Darve, "Large deformation FEM-LIP drained analysis of a vertical cut," *Acta Geotechnica*, vol. 8, no. 2, pp. 125-136, 2013.
- [43] N. Prime, F. Dufour and F. Darve, "Solid–fluid transition modelling in geomaterials and application to a mudflow interacting with an obstacle," *International Journal for Numerical and Analytical Methods in Geomechanics*, vol. 38, no. 13, pp. 1341-1361, 2014.
- [44] M. Pastor, B. Haddad, G. Sorbino, S. Cuomo and V. Drempetic, "A depth-integrated, coupled SPH model for flow-like landslides and related phenomena," *INTERNATIONAL JOURNAL FOR NUMERICAL AND ANALYTICAL METHODS IN GEOMECHANICS Int. J. Numer. Anal. Meth. Geomech*, 2008.
- [45] K. Soga, E. Alonso, A. Yerro, K. Kumar and S. Bandara, "Trends in large-deformation analysis of landslide mass movements with particular emphasis on the material point method," *Géotechnique*, vol. 66, no. 3, pp. 248-273, 2015.
- [46] C. Yuan and B. Chareyre, "A pore-scale method for hydromechanical coupling in deformable granular media," *Computer Methods in Applied Mechanics and Engineering*, vol. 318, pp. 1066-1079, 2017.
- [47] S. Bandara, "Coupling of soil deformation and pore fluid flow using material point method," *Computers and Geotechnics*, vol. 63, pp. 199-214, 2015.
- [48] F. Wang and K. Sassa, "Landslide simulation by a geotechnical model combined with a model for apparent friction change," *Physics and Chemistry of the Earth, Parts A/B/C*, vol. 35, no. 3-5, pp. 149-161, 1 1 2010.
- [49] A. Yerro, N. Pinyol and E. Alonso, "Internal progressive failure in deep-seated landslides," *Rock Mechanics and Rock Engineering*, vol. 49, no. 6, pp. 2317-2332, 2016.
- [50] X. Zhao, D. Liang and M. Martinelli, "Numerical simulations of dam-break floods with MPM," Delft, 2017.
- [51] F. Ceccato and P. Simonini, "Granular flow impact forces on protection structures: MPM numerical simulations with different

- constitutive models," in *Geotechnical Engineering in Multidisciplinary Research*, Bologna, 2016.
- [52] P. v. d. Berg, *Analysis of soil penetration*, Delft University Press, 1994, p. 175.
- [53] G. Qiu, S. Henke and J. Grabe, "Application of a Coupled Eulerian–Lagrangian approach on geomechanical problems involving large deformations," *Computers and Geotechnics*, vol. 38, no. 1, pp. 30-39, 1 1 2011.
- [54] D. Wang, B. Bienen, M. Nazem, Y. Tian, J. Zheng, T. Pucker and M. F. Randolph, "Large deformation finite element analyses in geotechnical engineering," *Computers and Geotechnics*, vol. 65, pp. 104-114, 1 4 2015.
- [55] Beuth, L and Vermeer, P. A. (, "Large deformation analysis of cone penetration testing in undrained clay," Rotterdam (pp. 1-7)., 2013.
- [56] A. Tolooiyan and K. Gavin, "Modelling the Cone Penetration Test in sand using Cavity Expansion and Arbitrary Lagrangian Eulerian Finite Element Methods," *Computers and Geotechnics*, vol. 38, no. 4, pp. 482-490, 1 6 2011.
- [57] F. Ceccato, L. Beuth, P. A. Vermeer and P. Simonini, "Two-phase Material Point Method applied to the study of cone penetration," *Computers and Geotechnics*, vol. 80, pp. 440-452, 1 12 2016.
- [58] G. P. Kouretzis, D. Sheng and D. Wang, "Numerical simulation of cone penetration testing using a new critical state constitutive model for sand," *Computers and Geotechnics*, vol. 56, pp. 50-60, 1 3 2014.
- [59] V. Galavi, F. Tehrani, M. Martinelli, A. Elkadi and D. Luger, "Axisymmetric formulation of the material point method for geotechnical engineering applications," in *Proc., of 9th NUMGE Conf*, Porto, Portugal, 2018.
- [60] S. Rao, *Engineering optimization: theory and practice*, John Wiley & Sons, 2009.
- [61] Z. Yin, . Y. F. Jin, S. Shen and H. Huang, "An efficient optimization method for identifying parameters of soft structured clay by an enhanced genetic algorithm and elastic–viscoplastic model," *Acta Geotechnica*, vol. 12, no. 4, pp. 849-867, 2017.
- [62] M. Calvello, "Calibration of soil constitutive laws by in-verse

9. BIBLIOGRAPHY

- analysis," in *ALERT Doctoral School 2014 Stochastic Analysis and Inverse Modelling*, J. C. Hicks M.A., Ed., Delft, Alert Geomaterials, 2014, pp. 239-262.
- [63] J. Meier, W. Schaedler, L. Borgatti, A. Corsini and T. Schanz, "Inverse parameter identification technique using PSO algorithm applied to geotechnical modeling," *Journal of Artificial Evolution and Applications*, pp. 1-14, 2008.
- [64] H. Zhao and S. Yin, "Geomechanical parameters identification by particle swarm optimization and support vector machine," *Applied Mathematical Modelling*, vol. 33, no. 10, pp. 3997-4012, 2009.
- [65] Y. Zhang, D. Gallipoli and C. Augarde, "Parameter identification for elasto-plastic modelling of unsaturated soils from pressuremeter tests by parallel modified particle swarm optimization," *Computer and Geotechnics*, pp. 293-303, 2013.
- [66] E. Poeter, M. Hill, E. Banta and S. Christensen, "UCODE_2005 and six other computer codes for universal sensitivity analysis, calibration, and uncertainty evaluation constructed using the JUPITER API," USGS, 2006.
- [67] J. E. Dennis, D. M. Gay and R. E. Welsch, "Algorithm 573: NL2SOL---An Adaptive Nonlinear Least-Squares Algorithm [E4]," *ACM Transactions on Mathematical Software*, vol. 7, no. 3, pp. 369-383, 1981.
- [68] V. Hosseinnezhad, M. Rafiee, M. Ahmadian and M. T. Ameli, "Species-based quantum particle swarm optimization for economic load dispatch," *International Journal of Electrical Power and Energy Systems*, vol. 63, pp. 311-322, 2014.
- [69] Jun Sun, Bin Feng and Wenbo Xu, "Particle swarm optimization with particles having quantum behavior," in *Proceedings of the 2004 Congress on Evolutionary Computation (IEEE Cat. No.04TH8753)*.
- [70] V. Hosseinnezhad, M. Rafiee, M. Ahmadian and P. Siano, "Optimal day-ahead operational planning of microgrids," *Energy Conversion and Management*, vol. 126, pp. 142-157, 15 10 2016.
- [71] V. Hosseinnezhad, M. Rafiee, M. Ahmadian and P. Siano, "Optimal island partitioning of smart distribution systems to improve system restoration under emergency conditions," *International Journal of Electrical Power & Energy Systems*, vol. 97, pp. 155-164, 14 2018.

-
- [72] J. Fern, A. Rohe, K. Soga and E. E. Alonso, The material point method for geotechnical engineering : a practical guide.
- [73] O. Zienkiewicz, A. Chan, M. Pastor, B. Schrefler and T. Shiomi, Computational geomechanics., Wiley Chichester, 1990.
- [74] A. Verruijt, Soil dynamics, Technische Universiteit, Faculteit Civiele Techniek., 1996.
- [75] A. Gens and D. Potts, "Formulation of quasi-axisymmetric boundary value problems for finite element analysis," *Engineering Computations*, vol. 1, no. 2, pp. 144-150, 1984.
- [76] J. Van Esch, D. Stolle and I. Jassim, "Finite element method for coupled dynamic flow-deformation simulation," in *In 2nd International Symposium on Computational Geomechanics (ComGeo II)*, Cavtat-Dubrovnik, 2011.
- [77] James Fern, Alexander Rohe, Kenichi Soga and Eduardo Alonso, Eds., MATERIAL POINT METHOD FOR GEOTECHNICAL ENGINEERING A PRACTICAL GUIDE., CRC PRESS, 2019.
- [78] A. G. Acosta, L. ; Vardon and P. ; Hicks, "An evaluation of MPM, GIMP and CPM in geotechnical problems considering large deformations," in *Proceedings of the 15th International Conference of the International Association for Computer Methods and Advances in Geomechanics*, 2017.
- [79] K. Terzaghi, Theoretical soil mechanics, New York: John Wiley & Sons, 1943.
- [80] A. Bishop, "Discussion on measurement of shear strength of soils," *Géotechnique*, vol. 2, no. 2, p. 108–116, 1950.
- [81] J. E. Fern and K. Soga, "The role of constitutive models in MPM simulations of granular column collapses," *Acta Geotechnica*, pp. 659-678, 2016.
- [82] F. Richard , J. Hall and R. Wood, Vibrations of soils and foundations, New Jersey: Princeton-Hall Inc, Inglewood Cliffs, 1970.
- [83] T. Schanz, P. Vermeer and P. Bonnier, "The hardening soil model: formulation and verification," in *Beyond 2000 in computational geotechnics*, Rotterdam, 1999.
- [84] T. Benz, Small – strain stiffness of soils and, Stuttgart: PhD thesis, University of Stuttgart, Germany., 2007.

9. BIBLIOGRAPHY

- [85] R. Brinkgreve, E. Engin and H. Engin, "Validation of empirical formulas to derive model parameters for sands," in *Numerical methods in geotechnical engineering*, Oslo, 2010.
- [86] M. Jefferies and K. Been, *Soil Liquefaction: A Critical State Approach*, Abingdon, UK.: Taylor & Francis, 2006.
- [87] H. Stutz, D. Mašín and F. Wuttke, "Enhancement of a hypoplastic model for granular soil–structure interface behaviour," *Acta Geotechnica*, vol. 29, no. 2, pp. 1249-1261, 2016.
- [88] C. Abril, *Numerical simulations of static liquefaction in submerged slopes*, Delft: Msc Thesis, TU Delft, 2017.
- [89] A. Niemunis and I. Herle, "Hypoplastic model for cohesionless soils with elastic strain range," *Mechanics of Cohesive-frictional Materials*, vol. 2, no. 4, pp. 279-299, 1997.
- [90] D. Wegener and I. Herle, "Prediction of permanent soil deformations due to cyclic shearing with a hypoplastic constitutive mode," *Geoteknik*, vol. 37, no. 2, pp. 113-122, 2013.
- [91] D. Mašín, "Hypoplasticity for practical applications part 4: determination of material parameters," 3 March 2015. [Online]. Available:
<<https://web.natur.cuni.cz/uhigug/masin/hypocourse>>.
[Accessed 3 March 2015].
- [92] T. Wichtmann and T. Triantafyllidis, "An experimental database for the development, calibration and verification of constitutive models for sand with focus to cyclic loading: part I—tests with monotonic loading and stress cycles," *Acta Geotechnica*, vol. 11, no. 4, pp. 739-761, 6 8 2016.
- [93] S. Ma, X. Zhang and X. Qiu, "Comparison study of MPM and SPH in modeling hypervelocity impact problems," *International Journal of Impact Engineering*, vol. 36, no. 2, pp. 272-282, 1 2 2009.
- [94] L. B. Lucy, "A numerical approach to the testing of the fission hypothesis," *THE ASTRONOMICAL JOURNAL*, vol. 82, no. 12, 1977.
- [95] R. A. Gingold and J. J. Monaghan, "Smoothed particle hydrodynamics: theory and application to non-spherical stars," *Monthly Notices of the Royal Astronomical Society*, vol. 181, no. 3, pp. 375-389, 1 12 1977.

-
- [96] M. Pastor, T. Blanc, B. Haddad, S. Petrone, M. Sanchez Morles, V. Dremptic, D. Issler, G. B. Crosta, L. Cascini, G. Sorbino and S. Cuomo, "Application of a SPH depth-integrated model to landslide run-out analysis," *Landslides*, vol. 11, no. 5, pp. 793-812, 6 10 2014.
- [97] Q. Xu, Y. Shang, T. van Asch, S. Wang, Z. Zhang and X. Dong, "Observations from the large, rapid Yigong rock slide – debris avalanche, southeast Tibet," *Canadian Geotechnical Journal*, vol. 49, no. 5, pp. 589-606, 5 2012.
- [98] T. van Asch, Q. Xu and X. Dong, "Unravelling the multiphase run-out conditions of a slide-flow mass movement," *Geomorphology*, vol. 230, pp. 161-170, 1 2 2015.
- [99] N. Anaraki, Hypoplasticity investigated: parameter, Delft: Msc, Thesis, TU Delft , 2008.
- [100] E. Bauer, "Calibration of a comprehensive hypoplastic model for granular materials," *Soils and foundations*, vol. 36, no. 1, pp. 13-26, 1996.
- [101] Fugro, "Geotechnical Report Laboratory Test Data Wind Farm Site I&II Borssele Wind Farm Zone Dutch Sector, North Sea," Rijksdienst voor Ondernemend Nederland, Noordrop, 2015.
- [102] D. Eckersley, "Flowslides in stockpiled coal," *Engineering Geology*, vol. 22, no. 1, pp. 13-22, 1986.
- [103] G. Mesri and M. Ajlouni, "Engineering properties of fibrous peats," *Journal of Geotechnical and Geoenvironmental Engineering*, vol. 133, no. 7, pp. 850-866, 2007.
- [104] J. Yamamuro and P. Lade, "Steady-state concepts and static liquefaction of silty sands," *Journal of Geotechnical and Geoenvironmental Engineering*, vol. 124, no. 9, pp. 868-877, 1998.
- [105] I. Herle and G. Gudehus, "Determination of parameters of a hypoplastic constitutive model from properties of grain assemblies," *Mechanics of Cohesive-frictional Materials*, vol. 4, no. 5, pp. 461-486, 1999.
- [106] R. Boulanger, R. Arulnathan, L. .. Harder Jr, R. A. Torres and M. W. Driller, "Dynamic properties of Sherman Island peat," *Journal of Geotechnical and Geoenvironmental Engineering*, vol. 124, no. 1, pp. 12-20, 1998.
- [107] T. Kishida, R. V. Boulanger, N. A. Abrahamson, T. M. Wehling

9. BIBLIOGRAPHY

- and M. Driller, "Regression models for dynamic properties of highly organic soils," *Journal of geotechnical and geoenvironmental engineering*, vol. 153, no. 4, pp. 533-543, 2009.
- [108] P. von Wolffersdorff, "A hypoplastic relation for granular materials with a predefined limit state surface," *Mechanics of Cohesive-frictional Materials banner*, vol. 1, no. 3, pp. 251-271, 1996.
- [109] F. S. Tehrani, M. I. Arshad, M. Prezzi and R. Salgado, "Physical Modeling of Cone Penetration in Layered Sand," *Journal of Geotechnical and Geoenvironmental Engineering*, vol. 144, no. 1, p. 040171101, 1 2018.
- [110] R. Stoevelaar, A. Bezuijen and H. Van Lottum, "Effects of crushing on pile point bearing capacity in sand tested in a geotechnical centrifuge," *15th European Conference on Soil Mechanics and Geotechnical Engineering*, pp. 939-944, 2011.
- [111] M. Arshad, Experimental study of the displacements caused by cone penetration in sand, Doctoral dissertation, Purdue University, 2014.
- [112] J. Rietdijk, F. M. Schenkeveld, P. E. L. Schaminée and A. Bezuijen, "The drizzle method for sand sample preparation," in *Proceedings of the International Conference on Physical Modelling in Geotechnics 2010*, 2010.
- [113] Fugro, "Geotechnical Report Laboratory Test Data Wind Farm Site I&II Borssele Wind Farm Zone Dutch Sector, North Sea," Rijksdienst voor Ondernemend Nederland, 2015.
- [114] P. Huang, X. Zhang, S. Ma and X. Huang, "Contact algorithms for the material point method in impact and penetration simulation," *International Journal for Numerical Methods in Engineering*, vol. 85, no. 4, pp. 498-517, 28 1 2011.
- [115] J. Ma, D. Wang and M. Randolph, "A new contact algorithm in the material point method for geotechnical simulations," *International Journal for Numerical and Analytical Methods in Geomechanics*, vol. 38, no. 11, pp. 1197-1210, 10 8 2014.
- [116] E. J. Murray and J. D. Geddes, "Uplift of Anchor Plates in Sand," *Journal of Geotechnical Engineering*, vol. 113, no. 3, pp. 202-215, 3 1987.
- [117] T. Van der Linden, Influence of multiple thin soft layers on the

- cone resistance in intermediate soils, Delft: TU Delft, Ms.c. Thesis, 2016.
- [118] R. Salgado and M. Prezzi, "Computation of Cavity Expansion Pressure and Penetration Resistance in Sands," *International Journal of Geomechanics*, vol. 7, no. 4, pp. 251-265, 7 2007.
- [119] M. D. Bolton, "The strength and dilatancy of sands," *Geotechnique*, vol. 36, no. 1, pp. 65-78, 1986.
- [120] . F. H. Kulhawy and P. Mayne, "Manual on estimating soil properties for foundation design," Cornell Univ., Ithaca, NY (USA), Palo Alto CA (USA), 1990.
- [121] R. Denlinger and R. Iverson, "Flow of variably fluidized granular masses across three-dimensional terrain: 2. Numerical predictions and experimental tests," *Journal of Geophysical Research: Solid Earth*, vol. 106, no. B1, pp. 553-566, 2001.
- [122] S. Knill, "Report on the Fei Tsui road landslide of 13 August 1995," 1996.
- [123] M. E. Sanchez, M. Pastor and M. G. Romana, "Modelling of short runout propagation landslides and debris flows," *Georisk: Assessment and Management of Risk for Engineered Systems and Geohazards*, vol. 7, no. 4, pp. 250-266, 12 2013.
- [124] M. Aubertin, M. Mbonimpa, B. Bussière and R. P. Chapuis, "A model to predict the water retention curve from basic geotechnical properties," *Canadian Geotechnical Journal*, vol. 40, no. 6, pp. 1104-1122, 12 2003.
- [125] A. Di Perna , Application of the Material Point Method, Salerno: Ms.c. Thesis , University of Salerno, 2018.
- [126] M. C. Hill and O. Østerby, "Determining extreme parameter correlation in ground-water models," 2002.
- [127] C. W. W. Ng and E. H. Y. Leung, "Determination of Shear-Wave Velocities and Shear Moduli of Completely Decomposed Tuff," *Journal of Geotechnical and Geoenvironmental Engineering*, vol. 133, no. 6, pp. 630-640, 6 2007.
- [128] M. Calvello, P. Ghasemi, S. Cuomo and M. Martinelli, "Optimizing the MPM model of a reduced scale granular flow by inverse analysis," in *Proc., of 9th NUMGE Conf*, Porto Portugal, 2018.
- [129] M. Calvello, "From the Observational Method to "Observational

9. BIBLIOGRAPHY

- Modelling" of Geotechnical Engineering Boundary Value Problems," in *International Symposium on Geotechnical Safety and Risk*, Denver, Colorado, 2017.
- [130] M. Calvello, S. Cuomo and P. Ghasemi, "The role of observations in the inverse analysis of landslide propagation," *Computers and Geotechnics*, vol. 92, pp. 11-21, 2017.
- [131] S. Cuomo, P. Ghasemi, M. Calvello and V. Hosseini-zhad, "Hypoplasticity model and inverse analysis for simulation of triaxial tests," in *Proc., of 9th NUMGE Conf.*, 2018.
- [132] S. Cuomo, M. Moscariello, D. Manzanal, M. Pastor and V. Foresta, "Modelling the mechanical behaviour of a natural unsaturated pyroclastic soil within Generalized Plasticity framework," *Computers and Geotechnics*, vol. 99, no. 1, pp. 191-202, 2018.
- [133] P. Ghasemi, Martinelli, M., Calvello, M. and Cuomo, S., "MPM modelling of static liquefaction in reduced-scale slope," in *Proc., of 9th NUMGE Conf.*, Porto, 2018.
- [134] G. Gudehus, "A visco-hypoplastic constitutive relation for soft soils," *Soils and Foundations*, vol. 44, no. 4, pp. 11-25, 2004.
- [135] D. Kolymbas, "A generalized hypoelastic constitutive law," in *Proc., XI Int. Conf., Soil Mechanics and Foundation Engineering*, San Francisco, 1985.
- [136] M. Pastor, J. Fernandez-Merodo, E. Gonzalez, P. Mira, T. Li and X. Liu, "Modelling of landslides: I. Failure mechanisms," in *Degradations and Instabilities in Geomaterials, CISM Course and Lectures No. 461, Darve F. and Vardoulakis I. ed.*
- [137] R. Boulanger and R. Arulnathan, *Dynamic properties of Sherman Island peat*.
- [138] K. Abe, S. Nakamura, H. Nakamura and K. Shiomi, "Numerical study on dynamic behavior of slope models including weak layers from deformation to failure using material point method," *Soils and Foundations*, vol. 57, no. 2, pp. 155-175, 2017.
- [139] S. G. Bardenhagen, J. E. Guilkey, K. M. Roessig, J. U. Brackbill, W. M. Witzel and J. C. Foster, "An improved contact algorithm for the material point method and application to stress propagation in granular material," *CMES: Computer Modeling in Engineering & Sciences*, vol. 2, no. 1, pp. 509-522, 2001.

- [140]
- [141] M. Calvello, "From the observational method to "observational modelling" of geotechnical engineering boundary value problems," in *Geotechnical Special Publication No. 286, Geotechnical Safety and Reliability: Honoring Wilson H.,* Geotechnical Special Publication No. 286, Geotechnical Safety and Reliability: Honoring Wilson H. Tang, 2017.
- [142] F. Ceccato and P. Simonini, "Study of landslide run-out and impact on protection structures with the Material Point Method," Lecerne, 2016.
- [143] S. Cuomo,, M. Pastor, S. Vitale and L. Cascini, "Improvement of irregular DTM for SPH modelling of flow-like landslides," in *Proceedings of the XII International Conference on Computational Plasticity. Fundamentals and Applications*, E. Oñate, D. Owen, D. Peric and B. Suárez, Eds., Barcelona, COMPLAS XII, 2013, pp. 3-5.
- [144] R. Fell, J. Corominas, C. Bonnard, L. Cascini, E. Leroi and W. Z. Savage, "Guidelines for landslide susceptibility, hazard and risk zoning for land-use planning.," *Engineering Geology*, vol. 102, no. 3, pp. 99-111, 2008.
- [145] W. Shin, Numerical simulation of landslides and debris flows using an enhanced material point method, Ph.D. thesis, University of Washington, 2009.
- [146] D. Sulsky,, Z. Chen and H. L. Schreyer, "A particle method for history-dependent materials," *Computer methods in applied mechanics and engineering*, vol. 118, no. 1-2, pp. 179-196, 1994.
- [147] A. M. Puzrin and I. Sterba, "Inverse long-term stability analysis of a constrained landslide," *Géotechnique*, vol. 56, no. 7, pp. 483-489, 9 2006.
- [148] E. P. Poeter and M. C. Hill, "Inverse Models: A Necessary Next Step in Ground-Water Modeling," *Ground Water*, vol. 35, no. 2, pp. 250-260, 1 3 1997.
- [149] C. Kim, E. Medley, C. Snell and C. E. Medley, "Shear Strength of Franciscan Complex Melange as Calculated from Back-Analysis of a Landslide," 2004.
- [150] M. Hill, O. Ø. -. Groundwater and u. 2003, "Determining extreme parameter correlation in ground water models," *Wiley Online*

9. BIBLIOGRAPHY

Library.

- [151] M. C. Hill, *Methods and guidelines for effective model calibration [electronic resource]*, Branch of Information Services [distributor], 1998.
- [152] DUNCAN and J. M., "Soil strengths from back-analysis of slope failures," *Proc. of Specialty Conf. Stability and Performance of Slopes and Embankments-II*, vol. 1, pp. 890-904, 1992.
- [153] H. X. Chen and L. M. Zhang, "EDDA 1.0: integrated simulation of debris flow erosion, deposition and property changes," *Geoscientific Model Development*, vol. 8, no. 3, pp. 829-844, 27 3 2015.
- [154] P. J. N. Pells, "Indirect identification of the average elastic characteristics of rock masses.," in *Structural foundations on rock : proceedings of the International Conference on Structural Foundations on Rock*, Sydney, 1980.
- [155] F. Oka, A. Murakami, R. Uzuoka and S. Kimoto, "Hybrid minimization algorithm applied to tunnel back analysis," in *Computer Methods and Recent Advances in Geomechanics - Proceedings of the 14th Int. Conference of International Association for Computer Methods and Recent Advances in Geomechanics, IACMAG 2014*, 2014.
- [156] M. Hisataki and T. Ito, "Back analysis for tunnels by optimization method," in *International conference on numerical methods in geomechanics*, 1985.
- [157] J. T. YI, S. H. GOH, F. H. LEE and RANDOLPH. M.F., "A numerical study of cone penetration in fine-grained soils allowing for consolidation effects," *Geotechnique*, vol. 62, no. 8, p. 707-719, 2012.
- [158] K. Gavin and A. Tolooyan, "An investigation of correlation factors linking footing resistance on sand with cone penetration test results," *Computers and Geotechnics*, vol. 46, pp. 84-92, 1 11 2012.
- [159] R. J. Jardine, B. M. Lehane and S. J. Everton, "Friction Coefficients for Piles in Sands and Silts," Springer, Dordrecht, 1993, pp. 661-677.
- [160] R. W. Boulanger, R. Arulnathan, L. F. Harder, R. A. Torres and M. W. Driller, "Dynamic Properties of Sherman Island Peat," *Journal of Geotechnical and Geoenvironmental Engineering*, vol. 124, no. 1, pp. 12-20, 1 1998.
- [161] S. Cuomo, M. Pastor, L. Cascini and G. C. Castorino, "Interplay of

rheology and entrainment in debris avalanches: a numerical study," *Canadian Geotechnical Journal*, vol. 51, no. 11, pp. 1318-1330, 11 2014.